COOL 2021

01 – 05 November, 2021.
Budker INP, Novosibirsk, virtual mode

*The bi-annual 13th International Workshop **COOL'21** will be held on November 1 - 5, 2021, organized by the Budker Institute of Nuclear Physics SB RAS in virtual mode. The workshop will be focused on the various aspects of the cooling methods and technics of charged particles.*

Workshop Topics: electron cooling, stochastic cooling, muon cooling, cooled beam dynamics, new concepts and theoretical advancements in beam cooling, facility status updates and beam cooling reviews.

International Advisory Commitee

Derbenev, Yaroslav	JLAB
Dietrich, Jürgen	Univ. Dortmund
Fedotov, Alexei	BNL
Kaplan, Daniel	Illinois Institute of Technology
Katayama, Takeshi	Nihon Univ.
Katsuya, Yonehara	FNAL
Litvinenko, Vladimir	Stony Brook Univ.
Meshkov, Igor	JINR
Nagaitsev, Sergei	FNAL
Parkhomchuk, Vasily	BINP
Prasuhn, Dieter	Forschungszentrum Jülich
Steck, Markus	GSI
Shirai, Toshiyuki	QST NIRS
Tranquille, Gerard	CERN
Trubnikov, Grigory	JINR
Wakasugi, Masanori	RIKEN
Wolf, Andreas	MPI Heidelberg
Yang, Xiaodong	IMP Lanzhou
Zhang, Yuhong	JLAB

Local Organizing Committee

Vassily Parkhomchuk,
Vladimir Reva,
Andrey Prokopenko,
Maksim Kuzin,
Alex Marukov

Workshop Web:
https://indico.inp.nsk.su/e/COOL21/

Deadline for Delegate registration - October, 25th, 2021
Deadline for Abstract submission - September, 15th, 2021

On the photo - Novosibirsk Opera and Ballet Theater


Andreas Wolf
Kuzin
Alexei Fedotov
Rolf Stassen
Bruno Galante
Fritz Caspers
Evgeny Syresin
Davide Gamba
Igor Meshkov
He Zhang
Jonathan Jarvis
Parkhomchuk Vasily
Oleksii Khelemelia
Lijun Mao (IMP,Lanzhou)
Claude Krantz
Rogers, Chris (STFC,RAL,ISIS)
Vladimir Shiltsev
Gerard Alain Tranquille
Takeshi Katayama
Skrinsky
Fanglei Lin
Yangxd
Vladimir Reva
Kurt Aulenbacher
C Dimopoulou
Sergei Nagaitsev
Will Bergan
wolfganghofle
Stephen Benson
Ilya Pogorelov
Markus Steck
grieser
Lars Varming Joergensen
David Bruhwiler (he/him)
J. Li
Nilanjan Banerjee
Haipeng Wang, Jefferson Lab
Rainer Hettrich
Sergei Seletskiy
Bryzgunov Maxim
Claudius Peschke
Fu Ma
Boris Skarbo
Rui Li
Rolf Stassen

PREFACE

The bi-annual 13th International Workshop COOL'21 will be held on November 1 - 5, 2021 by the Budker Institute of Nuclear Physics SB RAS in virtual mode using ZOOM. The workshop was focused on the various aspects of the cooling methods and techniques of charged particles. The conference was participated by 138 physicists from 17 countries (Russia, China, Germany, USA, Switzerland, Japan, England, India, Iran, Serbia, Korea, France, Spain, Sweden, Turkey, Ukraine and Brazil). 24 oral and 19 poster presentation were made at ten sections of the conference which covered a wide range of problem related to the physics of cooling of charged particles at all energies: from low to relativistic.

The scientific program covered the conventional topics:

- electron cooling
- stochastic cooling
- muon cooling
- cooled beam dynamics
- new concepts and theoretical advancements in beam cooling
- facility status updates and beam cooling reviews

Traditionally Dieter Möhl medals are awarded at conferences. In this year the medal was awarded Dr. Fritz Caspers for his lifetime work on the development of RF engineering devices for the stochastic cooling systems of CERN storage rings and international projects, Dr. Alexei Fedotov for the successful demonstration of electron cooling of ion beams in a collider with an RF accelerated electron beam and Dr. Andreas Wolf for his pioneering work in the use of low energy electron coolers in merging electron beams for atomic and molecular physics studies. The medal of best young researcher was award Dr. Chris Rogers for the successful demonstration of muon ionization cooling on the MICE muon cooling experiment.

The success of the COOL 2021 can be attributed to the collaborative efforts of the Program and Organizing Committees, and, of course, to all of the participants themselves.

Participants of the Conference from Russian and from several foreign accelerator centers enjoyed fruitful discussions at oral and poster presentations regardless to the coronavirus infection (COVID-19). At the end of the conference the Chairman of the International Advisory Committee V. V. Parkhomchuk informed the participants that the next conference of this series (2023) will be held in the CERN by the decision of IAC.

Reva Vladimir, Chairman of the Organizing Committee

ORGANIZED BY

Budker Institute of Nuclear Research SB RAS

INTERNATIONAL ADVISORY COMMITTEE

Chairman — V. Parkhomchuk (BINP SB RAS)
Y. Derbenev (JLAB)
D. Juergen (Univ. Dortmund)
A. Fedotov (BNL)
D. Kaplan (Illinois Institute of Technology)
T. Katayama (Nihon Univ)
V. Litvinenko (Stony Brook Univ.)
I. Meshkov (JINR)
S. Nagaitsev (FNAL)
D. Prasuhn (Forschungszentum Julich)
M. Steck (GSI)
T. Shirai (QST NIRS)
G. Tranquille (CERN)
G. Trubnikov (JINR)
M. Wakasugi (RIKEN)
A. Wolf (MPI Heidelberg)
X. Yang (IMP Lanzhou)
Y. Zhang (JLAB)

LOCAL ORGANISING COMMITTEE

V. Reva
M. Kuzin
V. Parkhomchuk
A. Marukov
A. Prokopenko

Contents

ISBN: 978-3-95450-243-1 ISSN: 2226-0374 doi:10.18429/JACoW-COOL2021-S101

NICA SYNCHROTRONS AND THEIR COOLING SYSTEMS

E.Syresin, A. Baldin, A. Butenko, I. Gorelyshev, A. Kobets, S.Melnikov, I. Meshkov, K. Osipov, S. Semenov, A. Sergeev, A. Sidorin, G. Trubnikov, Joint Institute for Nuclear Research, Dubna, Russia,
A. Bubley, N. Mityanina, V. Parkhomchuk, V. Reva, Budker Institute for Nuclear Physics SB RAS, Novosibirsk, Russia

Abstract

The Nuclotron-based Ion Collider fAcility (NICA) is under construction at JINR. The NICA goal is to provide of colliding beams for studies of hot and dense strongly interacting baryonic matter and spin physics. The ion mode accelerator facility of the NICA Collider consists of the following accelerators: The new operating Heavy Ion Linac (HILAC) with RFQ and IH DTL sections at energy 3.2 MeV/u, new operating superconducting Booster synchrotron at energy up 600 MeV/u, operating superconducting synchrotron Nuclotron for the gold ion energy 3.9 GeV/u and two Collider storage rings with two interaction points. There is the electron cooling system in the Booster synchrotron, the Collider has electron and stochastic cooling systems. The status of the NICA acceleration complex and its cooling systems is presented. The application of the cooling systems to the operation of the NICA accelerators – the Booster and the Nuclotron are discussed.

NICA INJECTION COMPLEX

The NICA accelerator complex [1,2] is constructed and commissioned at JINR. NICA experiments will be aimed at searching of the mixed phase of baryonic matter and studying the nature of the nucleon/particle spin. The new NICA accelerator complex will permit implementing experiments in the following modes: with the Nuclotron ion beams extracted to a fixed target; with colliding ion beams in the Collider; with colliding ion-proton beams; with colliding beams of polarized protons and deuterons. The main elements of the NICA complex are an injection complex, which includes a set of ion sources and two linear accelerators, the superconducting operating Booster, the superconducting operating synchrotron Nuclotron, a Collider composed of two superconducting rings with two beam interaction points, a Multi-Purpose Detector (MPD) and a Spin Physics Detector (SPD) and the beam transfer lines.

The heavy ion injection chain consists from electron string ion source, the laser ion source, the plasma ion source, the operating HILAC, the transfer line HILAC-Booster, the superconducting operating synchrotron Booster, the transfer line Booster-Nuclotron and the operating superconducting synchrotron Nuclotron.

The HILAC constructed by the JINR-Bevatech collaboration is under exploitation since 2016. It is aimed to accelerate the heavy ions injected from KRION-6T, a superconducting electron-string heavy ion source. At the present time KRION-6T produces 5×10^{8} ^{197}Au^{31+} and 2×10^{8} ^{209}Bi^{27+} ions per pulse.

Especially for the test of the Booster [3] the plasma source generating a single component He^{1+} beam was created. The efficiency of the beam transportation through second and third IH sections was 78.5%. The maximal ion ^{4}He^{1+} beam current at HILAC entrance during first Booster runs corresponds to the project value of 10 mA. During second Booster run the ^{4}He^{1+}and ^{56}Fe^{14+} ions produced in the plasma and the laser ion sources were accelerated in HILAC and injected in Booster.

The transfer line from HILAC to Booster [1] consists of 2 dipole magnets, 7 quadrupole lenses, 6 stirrer magnets, debuncher, collimator, vacuum and diagnostic equipment. The assembling of transfer line was done in 2020. The achieved efficiency of the beam transportation during first Booster beam run was of 90% at the beam current at the HILAC exit of 4 mA, this value was sufficient for the first experiments.

The Booster [1-3] (Fig. 1) is a superconducting synchrotron intended for accelerating heavy ions to an energy of 600 MeV/u. The magnetic structure of the Booster with a 211-m-long circumference is mounted inside the yoke of the Synchrophasotron magnet.

Figure 1: Booster ring inside Synchrophasatron yoke.

The main goals of the Booster are accumulation of 2·10^{9} ^{197}Au^{31+} ions, acceleration of the heavy ions up to the energy 578 MeV/u required for effective stripping, and forming of the required beam emittance with the electron cooling system. The Booster has a four-fold symmetry lattice with DFO periodic cells. Each quadrant of the Booster has ten dipole magnets, six focusing and six defocusing quadrupole lenses, and multipole corrector magnets. All Booster dipole magnets and quadrupole lenses were fabricated and tested at JINR.

The beam injection system of the Booster consists of an electrostatic septum and three pulsed electric kickers.

The Booster RF system designed and constructed by Budker Institute of Nuclear Physics (BINP), Siberian Branch, Russian Academy of Sciences, provides 10 kV of acceleration voltage. The operating frequency range of the stations is from 587 kHz to 2526 kHz.

The electron cooling system (Fig. 2) designed and manufactured by BINP SB RAS has the maximal electron energy of 60 keV. The Booster electron cooling will be used at first at an energy of 3.2 MeV/u for multiple or multiturn injection. The application of the electron cooling permits to increase in accordance to BETACOOL simulations the intensity of $^{197}Au^{31+}$ stored ion beam by factor of 5 (Fig. 3) at the cooling time of 150 ms, the injection repetition frequency of 10 Hz, the vacuum pressure life time of 5 s and the electron recombination life time of 2 s. A reduction of the beam emittance and the momentum spread will be done by the electron cooling at the ion energy of 65 MeV/u and the cooling time of 1 s. This allows to provide acceptable beam parameters after acceleration to 578 MeV/u and the stripping on a target at extraction from the Booster.

Figure 2: Booster electron cooling system.

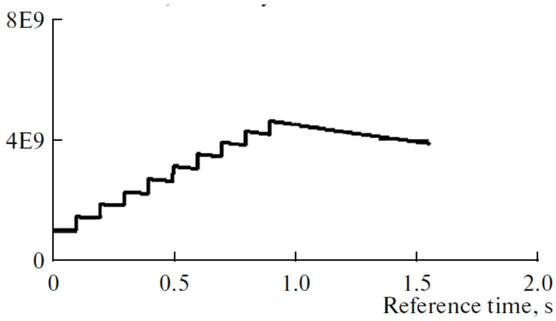

Figure 3: Dependence of stored Au^{31+}ion intensity on time at multiple injection with electron cooling.

The first technical Booster run was performed in November-December 2020. After the orbit correction and tuning of the injection system the intensity of the $^4He^{1+}$ circulating beam was increased up to 7×10^{10} ions. This is equivalent to the charge of 2×10^9 Au^{31+} ions. The lifetime of ions corresponds to 1.3 s at the equivalent average residual gas pressure 2×10^{-8} Pa.

During second run in September 2021 the beams of ions $^4He^{1+}$ and $^{56}Fe^{14+}$ (mass-to-charge ratio A/Z=4) and intensity up to 4×10^{10} and 4×10^9 respectively were injected in Booster, bunched on the injection plateau of the magnetic field on fifth RF harmonic and then accelerated up energy 65 MeV/u, where they were rebunched on the first RF harmonic and again accelerated. The $^{56}Fe^{14+}$ ions were accelerated in Booster up to the project energy of 578 MeV/u (Fig. 4).

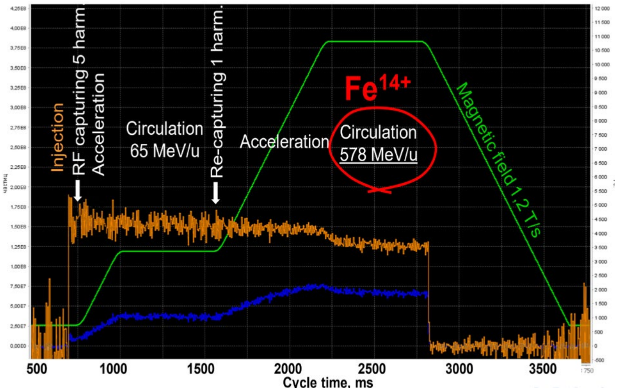

Figure 4: Beam current transformer signal at $^{56}Fe^{14+}$ ion acceleration.

The main results of the second Booster run are the following: the beam injection efficiency is larger than 95% with adiabatic capturing at 5th harmonic; acceleration up to the energy 65 MeV/u with recapturing from the 5th harmonic to the 1th one with efficiency close to 100%; acceleration up to energy of 578 MeV/u with dB/dt = 1.2 T/s; ultrahigh vacuum at $^4He^{+1}$ ion life-time longer than 10 s; the electron cooling of ions at energy of 3.2 MeV/u; the beam extraction in to the Booster-Nuclotron transfer line and the beam transportation in this transfer line with total efficiency of 70%.

The $^4He^{1+}$ ion lifetime (Fig. 5) during second Booster run corresponds to 10.8 s. The equivalent residual gas pressure is about 5×10^{-9} Pa.

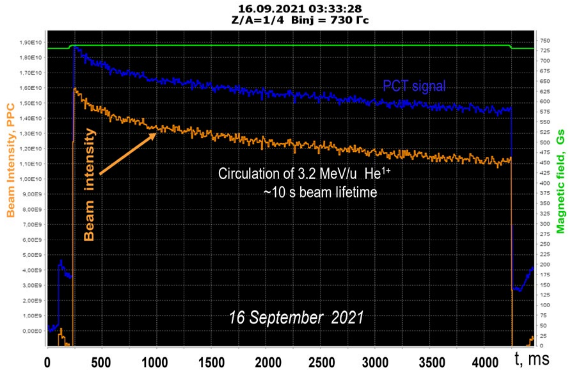

Figure 5: Parametric current transformer (PCT) signal at $^4He^{1+}$ ion energy 3.2 MeV/u.

The cryomagnetic and the power supply systems were tested at the design magnetic field cycle during first Booster run (Fig. 6). The magnetic cycle has three plateaus: for injection, electron cooling and beam extraction. The achieved magnetic field ramping rate of 1.2 T/s corresponds to the project value (Fig. 6). The achieved maximum magnetic field of 1.8 T is also equal to the project value.

The electron cooling of $^{56}Fe^{14+}$ ions was first done during second Booster run. The ion beam circulation and acceleration were performed from injection energy 3.2 MeV/u up 65 MeV/u, corresponding to designed energy range of electron cooling system (ECS), at ECS solenoid magnetic field 0.7 kGs. Operation of ECS was done with an effective recuperation at the electron beam current range of 30 - 150 mA.

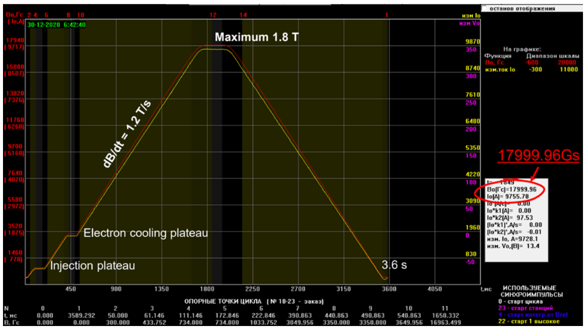

Figure 6: The Booster magnetic field cycle at design parameters.

The FWHM relative momentum spread of uncooled circulated beam corresponds to $1.2 \cdot 10^{-3}$ (Fig. 7a). The FWHM relative momentum spread of cooled ions is equal to 4×10^{-4} (Fig. 7b).

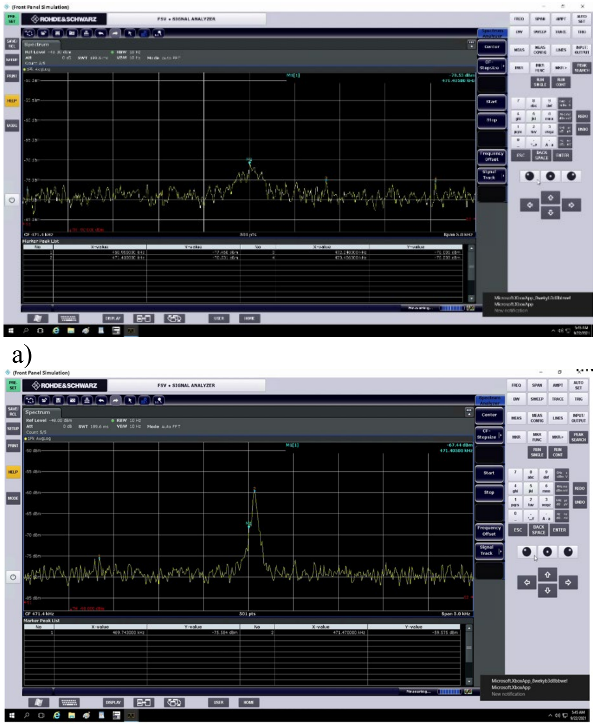

a)

b)

Figure 7: Schottky noise signal at 4 harmonic of revolution frequency and $^{56}Fe^{14+}$ ion energy of 3.2 MeV/u.

The horizontal and vertical beam profiles were measured by Micro Channel Plate ionization profilometer. The root-mean-square (rms) emittance of circulated beam was rather large $\varepsilon_x/\varepsilon_z$=14/8 π·mm·mrad at a mismatched and not optimized injection during first run with electron cooling. The horizontal cooling time corresponds to 3,1 s at the e-times reduction in the beam emittance (Fig. 8a).

The BETACOOL simulated horizontal cooling time is 2.1 s at these emittances (Fig. 9).

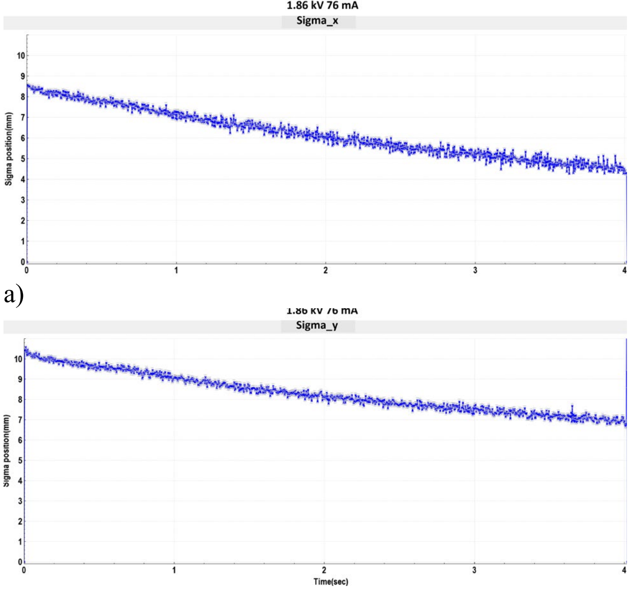

a)

b)

Figure 8: Dependence of MCP measured rms horizontal (a) and vertical (b) of $^{56}Fe^{14+}$ ion beam on time at ion energy 3.2 MeV/u and electron beam current of 76 mA.

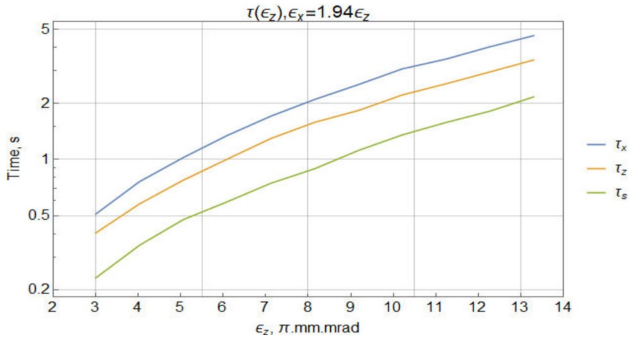

Figure 9: Dependence of horizontal, vertical and longitudinal cooling time on vertical emittance ε_z at horizontal emittance ε_x=1.94ε_z and electron beam current of 76 mA.

The effects of electron heating were observed at an electron energy shifted from the corresponding ion energy related to the electron cooling. At a higher electron beam current and a high ion intensity the coherent longitudinal oscillations were observed (Fig. 10). The coherent oscillations disappeared at a threshold value of the electron beam current multiplied on the ion intensity $(I_e \times N_i)_{th}$ (Fig. 11). The $^{56}Fe^{14+}$ ion lifetime is reduced at switch on the electron beam current (Fig. 12). The $^{56}Fe^{14+}$ ion lifetime corresponds to 4.9 s at the intensity of $4 \cdot 10^9$ ions and zero electron beam current (Fig. 12a). It is reduced to the value of 1.35 s at the electron beam current of 100 mA (Fig. 12b).

ISBN: 978-3-95450-243-1 ISSN: 2226-0374 doi:10.18429/JACoW-COOL2021-S101

Figure 10: Signal of coherent longitudinal oscillations at 5th harmonic of revolution frequency and ^{56}Fe^{14+} ion energy 3.2 MeV/u.

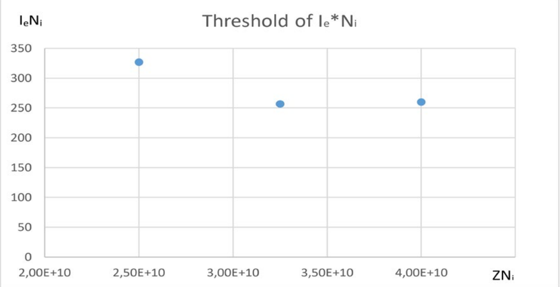

Figure 11: Dependence of threshold value $(I_e \times N_i)_{th}$ (relative units), at which coherent longitudinal oscillations disappeared, on the ion intensity multiplied by the ion charge (total ion beam charge).

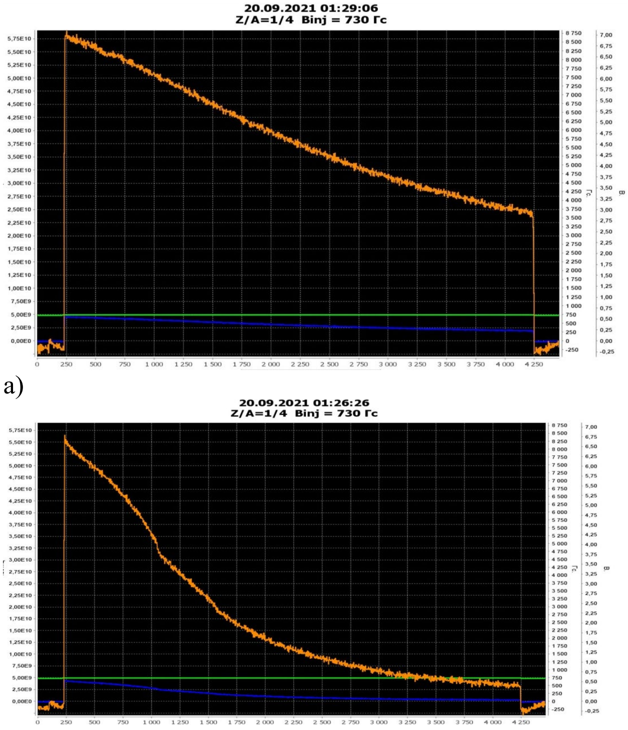

a)

b)

Figure 12: PCT signal for ^{56}Fe^{14+} ions at electron beam current I=0 mA (a) and I=100 mA (b).

The Booster beam extraction system [1] consists of a magnetic kicker, two magnetic septa, a stripping station and a closed orbit bump subsystem including four lattice dipoles with five additional HTS current leads. The Booster beam extraction system together with the transfer line Booster-Nuclotron were fabricated by BINP. The first beam experiments with extracted ^{4}He^{1+} and ^{56}Fe^{14+} ion beams were performed during second Booster beam run.

The upgraded Nuclotron [4] accelerates protons, polarized deuterons and ions to a maximum energy depending of the sort of particles. The maximum ion energy corresponds to 5.2 GeV/n at present time.

The installation in the Nuclotron of the Booster beam injection system and the Collider fast extraction system are required for its operation as the main synchrotron of the NICA complex. The kicker and the Lambertson magnet should be installed in the injection section in end 2021 or in beginning 2022.

COLLIDER RINGS

The Collider [1,2,5] consists of two storage rings with two interaction points (IPs). Its main parameters are as follows: the magnetic rigidity is up to 45 T·m; the residual gas pressure in the beam chamber is not high than 10^{-10} Torr; the maximum field in dipole magnets is 1.8 T; the kinetic energy of gold nuclei ranges from 1 to 4.5 GeV/u; the beam axes coincide at the interaction section (zero intersection angle); the average luminosity is 10^{27} cm^{-2} s^{-1} for gold ions. The rings of the Collider are identical in shape to a racetrack — two arcs are connected by two long straight section (109 m each). The circumference of each ring is 503.04 m.

Methods for cooling charged particle beams represent the key accelerator technologies, which are critical for achieving the design parameters of the complex. The electron cooling system [1] for the NICA Collider at an electron energy of 2.5 MeV is intended for accumulation and bunch formation at the ion kinetic energies in the range of 1.0–4.5 GeV/u. The cooling time of Au^{79+} ions corresponds to 20-100 s at ion energy 3-4.5 GeV/u (Fig. 13). The solenoid cooling section has the length of 6 m, the magnetic field is of 1 kGs. The maximum electron beam current corresponds to 1 A. Construction of the electron cooling system was started in BINP in 2016. The commissioning of the cooling system in JINR will be in end of 2022.

The stochastic cooling system (SCS) [1] of the NICA Collider (Table 1) must provide ion cooling up to 3.1 × 10^{9} ^{197}Au^{79} ions in a bunch. To achieve the design cooling time, an SCS with the frequency bandwidth 0.7–3.2 GHz is necessary. The Collider SCS uses pickup electrodes and kickers. The main elements of the stochastic cooling system also include signal delay system blocks, solid-state amplifier and preamplifier cascades, and a rejector (comb) filter system.

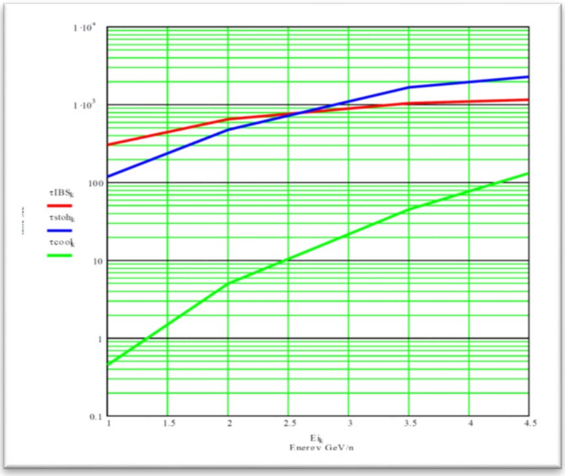

Figure 13: Dependence of electron, stochastic cooling time and IBS time on ion energy.

Table 1: Parameters of Stochastic Cooling System

Longitudinal cooling method	Filter
Passband, GHz	0,7 – 3,2
Beam distance pickup -kicker, m	183,5-191,5
Phase from pickup to kicker, deg	1340-1360
Ion Energy Au^{79+}, GeV/u	3,0
Slip-factor from pickup to kicker	0.0294
Revolution slip-factor	0.0362
Pickup/kicker coupling impedance, Ω	200/800
Gain, dB	75 – 79
Peak power at kicker, W	3×200
Pickup/noise temperature, K	300/40

Three RF systems with 26 cavities of the acceleration radio-frequency voltage will be applied for ion accumulation and formation of ion bunches [1,5]. Accumulation of the beam of the required intensity is planned to be realized in the longitudinal phase space with the use of the 'technique of barrier RF1 voltages' and of stochastic or electron cooling of the particles being accumulated. The barrier bucket technique also will be used for ion acceleration in the rings.

The rms longitudinal emittance of injected beam in the Booster corresponds to $\varepsilon_B=\beta_{inj}(\Delta p/p)_{inj}\sigma_{inj}=0,0048$ m, where $(\Delta p/p)_{inj}=10^{-3}$ is the relative momentum spread after the HILAC debuncher, $C_B=210$ m is the Booster circumference, $\sigma_{inj}=C_B/(2\times3^{1/2})=66$ m is the rms length of injected beam. The total longitudinal emittance of the ion beams corresponds to $\varepsilon_{inj}=n_{inj}\varepsilon_B=0.39$ m at $n_{inj}\approx80$ Collider injection cycles.

The longitudinal acceptance of RF barriers is equal to $\varepsilon_c=\gamma_c\beta_c(\Delta p/p)\sigma_c=0.06$ m at $\gamma_c=3$, $(\Delta p/p)_c=3\cdot10^{-4}$ is the relative rms momentum spread related to RF barrier acceptance, $\sigma_c=C_c/(4\times3^{1/2})=72$ m is the rms stack length. The ratio of total longitudinal rms beam emittances at $n_{inj}\approx80$ Collider injection cycles to acceptance of RF barriers corresponds to $\varepsilon_{inj}/\varepsilon_c=6.5$. The electron cooling time should be shorter $\tau_{cool}=\tau_{inj}\ \varepsilon_c/\varepsilon_B\approx100$ s, where $\tau_{inj}=8$ s is the repetition injection time in each Collider ring. The Booster ion precooling permits to reduce by a factor of 3 the relative rms momentum spread $dp/p\approx4\cdot10^{-4}$. In this case the cooling time of $\tau_{cool}=300$ s provides the stack storage with required intensity.

When the necessary intensity is achieved, the beam is bunched the RF2 system at voltage up to 25 kV of the 22nd harmonics of the rotation frequency with the subsequent takeover by the RF3 system of the 66th harmonics. This permits 22 short bunches with rms length of 0.6 m to be formed (Fig. 14), which is necessary for achieving high luminosity.

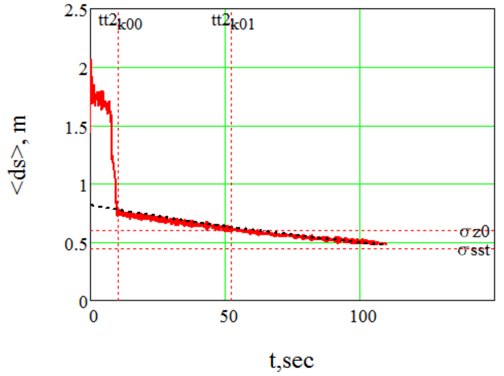

Figure 14: Dependence of bunch length on time at cooling time of 100 s.

The maximal RF3 voltage corresponds to 125 kV. The RF solid state amplifiers developed by Russian firm TRIADA are used for RF2 and RF3 cavities. The construction of three RF systems was started in 2016-2017 in BINP. Two RF1 stations, 8 RF2 and 16 RF3 cavities will be installed in Collider in 2022.

REFERENCES

[1] Technical Project of NICA Acceleration Complex (Dubna, 2015).

[2] V.D. Kekelidze R. Lednicky, V.A. Matveev *et al.*, "Three stages of the NICA accelerator complex", *Eur. Phys. J. A*, v.52:211, p.390, 2016. `doi:10.1088/1742-6596/668/1/012023`

[3] A. Butenko, N. Agapov, A. Alfeev *et al.*, "First Experiments with Accelerated Ion Beams in the Booster of NICA Accelerator Complex", *in Proc. 12th Int. Particle Accelerator Conf. (IPAC'21),* Campinas, Brazil, May 2021, pp.123-125. `doi:10.18429/JACoW-IPAC2021-MOPAB025`.

[4] E.M. Syresin, N.N. Agapov, A.V. Alfeev *et al.*, "Nuclotron Development for NICA Acceleration Complex", in *Proc. IPAC 19*, Melbourne, Australia, May 2019, paper THXXPLM1, pp.3396-3398. `doi: 10.18429/JACoW-IPAC2019-THXXPLM1`

[5] E. Syresin, O.Brovko, A.Butenko *et al.*, "Status of Accelerator Complex NICA", in *Proc. 26th Russian Particle Accelerator Conf. (RuPAC'18)*, Protvino, Russia, Oct. 2018, pp. 12-16. `doi:10.18429/JACoW-RUPAC2018-MOXMH03`.

ISBN: 978-3-95450-243-1 ISSN: 2226-0374 doi:10.18429/JACoW-COOL2021-S102

ELEMENTS OF HIGH VOLTAGE ELECTRON COOLING SYSTEM FOR NICA COLLIDER

M. Bryzgunov, A. Bubley, A. Denisov, A. Goncharov, V. Gosteev, V. Panasyuk, V. Parkhomchuk, V. Reva[1], A. Batrakov, E. Bekhtenev[1], O. Belikov, V. Chekavinskiy, M. Fedotov, K. Gorchakov, I. Gusev, I. Ilyin, A. Ivanov[1], G. Karpov, M. Kondaurov, N. Kremnev[1], D. Pureskin, A. Putmakov, D. Senkov, K. Shtro, D. Skorobogatov, R. Vakhrushev, A. Zharikov,
Budker Institute of Nuclear Physics, Novosibirsk, Russia
[1]also at Novosibirsk State University, Novosibirsk, Russia

Abstract

Beam cooling plays a key role in the project of the NICA collider. In order to achieve needed luminosity it is important to provide effective cooling during beam accumulation and during experiment. For this purpose, the ring will be equipped with both electron and stochastic cooling systems. The article describes construction of the electron cooler and status of its production by Budker INP.

INTRODUCTION

The collider ring will be the main element of the future NICA complex (JINR, Russia), where experiments with colliding ion beams in the energy range 1÷4.5 GeV/u will be provided in order to investigate properties of dense baryonic matter at extreme values of temperature and density with planned luminosity 10^{27} $cm^{-2}s^{-1}$. In order to achieve such luminosity the collider ring will be equipped with two cooling systems: stochastic and electron. The systems will provide increase of beam intensity during accumulation and decrease bunch length and emittance during experiments. The electron cooling system for the NICA collider now is under construction in the Budker Institute of Nuclear Physics (Novosibirsk, Russia).

In order to provide electron cooling in full range of ion energy the electron cooling system must produce electron beam with energy up to 2.5 MeV. Experience, achieved during experiments on the high voltage electron cooling system of the COSY synchrotron [1] and results of operation of electron cooler of the Recycler ring [2] in Fermilab (USA) show, that for effective cooling it is enough to have electron beam with current about 1 A.

Main parameters of the system are shown in Table 1.

Table 1: Electron Cooling System Parameters

Parameter	Value
Electron energy	0.2 ÷ 2.5 MeV
Energy stability	$<10^{-4}$
Electron current	0.1 ÷ 1 A
Cooling section length	6 m
Magnetic field in the cooling section	0.5 ÷ 2 kG
Vacuum presure	10^{-11} mbar

SYSTEM OVERVIEW

Figure 1 shows 3-d layout of the NICA high voltage electron cooling system. The construction is based on high voltage electron cooling system for the COSY synchrotron. In order to cool both ion beams simultaneously, the system consists of two independent coolers. Every cooler contains independent high voltage system, cooling section and transport channels.

Electron beam, emitted by electron gun, is accelerated by electrostatic tube to working energy and moves (through transport cannel) to the cooling section, where it interacts with ion beam. After the cooling section electrons move back to high voltage system where they are decelerated and absorbed by collector surface. On whole trajectory from gun to collector electron beam moves in longitudinal magnetic field, which provides transverse focusing of the beam.

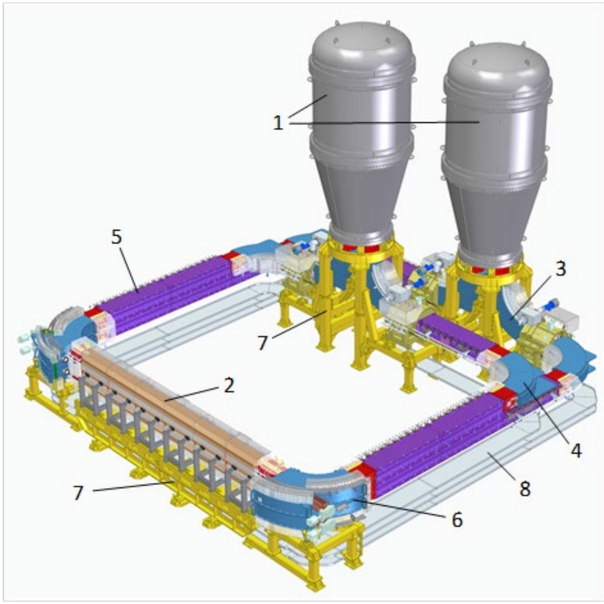

Figure 1: 3D model of the electron cooling system for the NICA collider. 1 – high-voltage vessels, 2 – cooling section, 3 – vertical bend, 4 – horizontal bends, 5 – linear sections, 6 – toroid magnet, 7 – supports, 8 – cable channels.

Figure 2 shows construction of the high voltage system. Its main parts are high voltage column (which generates accelerating voltage and provides electron acceleration to working energy) and high voltage terminal (which contains electron gun [3], electron collector and electronics for their control). For high voltage insulation the system is placed in hermetic vessel with SF_6 gas under pressure of up to 8 bar.

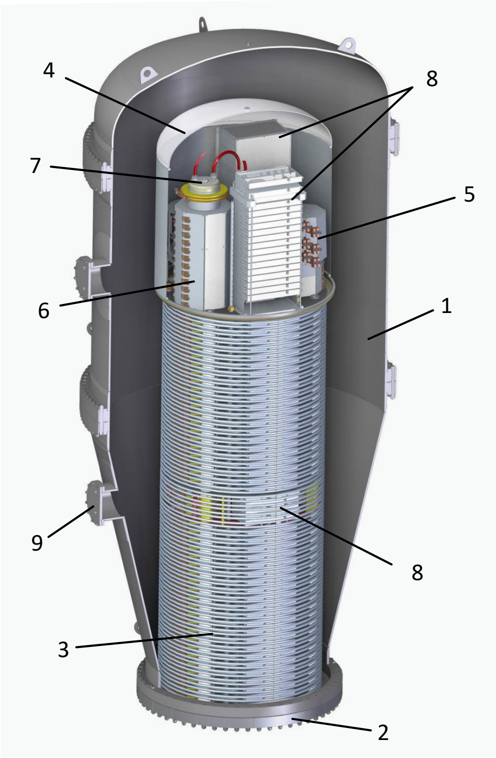

Figure 2: High voltage system of the electron cooler for NICA collider. 1 – pressure vessel, 2 – bottom flange, 3 – high voltage column, 4 – high voltage terminal, 5 – electron gun solenoid, 6 – electron collector solenoid, 7 – collector, 8 – middle section, 9 – side flange.

Length of the high voltage column is 3 m and it consists of 42 high voltage sections (Fig. 3) and one special middle section (Fig. 4).

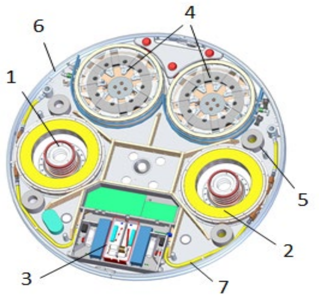

Figure 3: High voltage section. 1 – electrostatic tube, 2 – magnetic coil, 3 – electronics unit, 4 – sections of cascade transformers, 5 – insulating supports, 6 – external ring, 7 – oil tubes

Each high voltage section contains 2 high voltage power supplies (up to 30 kV), connected in series, magnetic coils for longitudinal field, power supplies for coils and control electronics. The sections are separated from each other with insulating (plastic) supports. Section height is 48 mm, period is 64 mm. High voltage power supplies of all sections are connected in series in order to form full accelerating voltage. Connection of every section with control computer is realized with the help of wireless interface ZigBee. All sections are powered with the help of cascade transformer [4]. For this purpose each section of the transformer has additional small winding.

Two electrostatic tubes for beam acceleration and deceleration are installed in magnetic coils.

The middle section of the column is intended for additional vacuum pumping and beam position measurement with the help of pickup electrodes (BPM). The section does not contain high voltage power supplies, but it has magnetic coils in order to provide homogeneous magnetic field in whole electrostatic tube. Coils support allows to incline them mechanically in order to improve beam transition through the electrostatic tube in case of tube and coils misalignment.

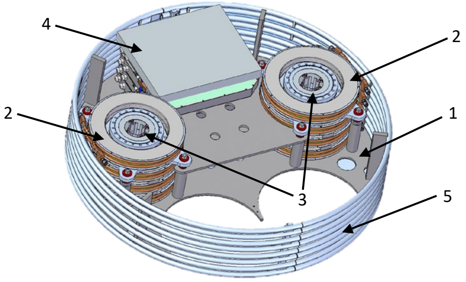

Figure 4: Middle section of the high voltage column. 1 – section's base, 2 – magnetic coils, 3 – vacuum chambers, 4 – electronics, 5 – external rings.

In Fig. 5 a vacuum chamber of the middle section is shown. Top and bottom vacuum flanges are used for connection with 2 parts of electrostatic tube. In order to avoid mechanical load on tubes, there is a bellow, installed in bottom of the chamber. BPM consists of 4 electrodes, and its construction is usual for electron coolers, produced in BINP. For vacuum pumping 4 side flanges can be used. It is planned to install there small getter pumps (NEG).

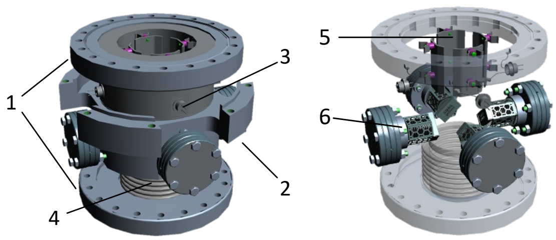

Figure 5: Vacuum chambers of the middle section: left – outer view, right – inner view. 1 – flanges for electrostatic tubes connection, 2 – mechanical support, 3 – BPM's feedthough, 4 – bellow, 5 – BPM's electrodes, 6 – NEGs.

During assembling of the COSY high voltage cooler it was recognized, that electrostatic tubes, with length of more than 2 m, which are fixed only on the bottom flange of vessel, need very careful work with surrounding devices in order not to damage the tubes. Electrostatic tubes of the

ISBN: 978-3-95450-243-1 ISSN: 2226-0374 doi:10.18429/JACoW-COOL2021-S102

NICA high voltage cooler have length more than 3 m, that worsens this problem. Another problem is cascade transformer of big length. During assembling of the transformer one needs first to connect all electrical circuits and after that it is tightened in order to make it hermetic. The tightening is very complicated process and its complexity significantly increases with length increase. In the NICA high voltage cooler length of the transformer is higher and it was decided to divide it to 2 parts.

Because of this another important goal of the middle section is to simplify system assembling providing place, where two parts of electrostatic tubes and 2 parts of cascade transformers can be connected.

As it was said above, electrostatic tubes are connected via vacuum chamber of the middle section, which also provides intermediate support for the electrostatic tubes. The cascade transformer connection is shown in Fig. 6. Supports for the top transformers are installed on the bottom transformers and have units for transformers alignments. Since transformers are cooled with oil, there are tubes (bellows) for their oil connection. Electrical connection is made with additional wires (not shown).

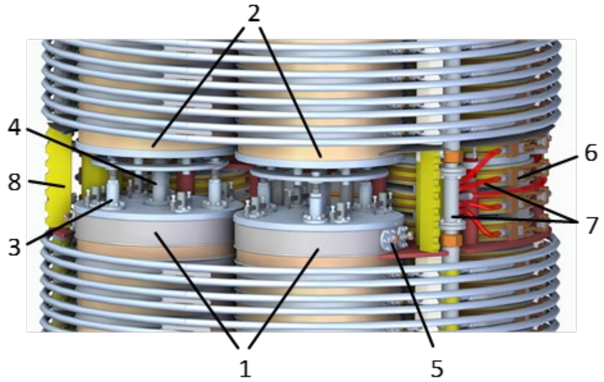

Figure 6: Connection of transformers in the middle section. 1 – bottom transformers, 2 – top transformers, 3 – supports for top transformers, 4 – oil connector, 5 – feeed-through for final winding of transformer, 6 – magnetic coils, 7 – tubes for cooling, 8 – support for external rings.

MAGNETIC MEASUREMENTS

As it was said, for transverse focusing the electron beam moves in longitudinal magnetic field on whole trajectory from gun to collector. For this purpose, the transport channel of the cooler consists of a set of linear and bent solenoids. Before assembling of the cooler its all magnetic elements will be tested. New magnetic measurement system, based on 3-d Hall probe, was produced. The Hall probe is installed on carriage, which moves inside magnetic element along special aluminium rail with the help of stepping motor by special tape. The rail consists of set of different linear and bent segments, which can be assembled in different way in order to install it in part of transport channel of the electron cooler. In Fig. 7 the measurement system, installed in part of transport channel is shown. The part consists of 3 elements (2 linear solenoids and 1 bend solenoid).

Figure 7: Part of cooler's transport channel during magnetic measurements. The assembling consists of 3 solenoids (called “INSERT” (red), ”BEND” (blue) and ”LINE-08” (yellow)). Aluminium rail of needed bent shape is installed inside the solenoids.

Figure 8 shows first results of field measurements. Here one can see 3 graphs corresponding to longitudinal field measurements in cases, when only one element is powered. Such measurements allow us to obtain elements field map and to find error in elements production and connection.

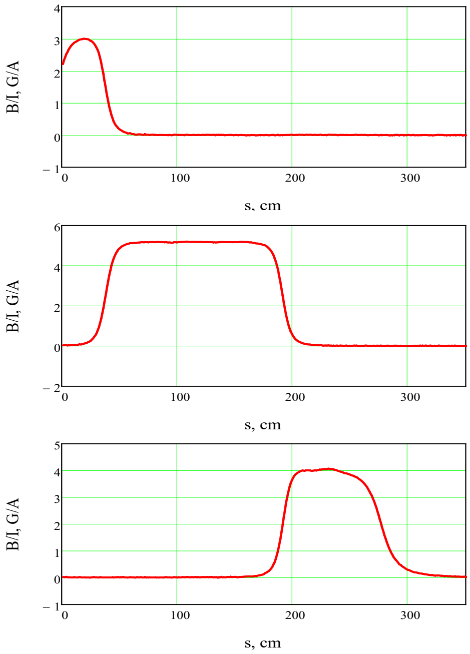

Figure 8: longitudinal magnetic field in the system with current only in “INSERT” solenoid (top), in “BEND” solenoid (middle) and in “LINE-08” solenoid (bottom).

In addition to Hall measurement system a high precision, compass-based system [5] is also being prepared. The system is needed for magnetic field line measurements in the cooling section. It is based on special compass probe, which moves along the cooling section through the special segmented titanium rail of round shape (Fig. 9). Maximum length of the rail is 10 m, that is enough for measurement in whole solenoid.

ISBN: 978-3-95450-243-1 ISSN: 2226-0374 doi:10.18429/JACoW-COOL2021-S102

Figure 9: titanium rail for compass-based measurements

For probes testing and adjustment and for new measurement electronics testing a test bench was prepared.

ELECTRON GUN TESTS

Since ion beam diameter in the NICA is small In comparison with accelerators with low energy electron coolers, it was decided to decrease cathode diameter from 3 cm (as it was in previous coolers, produced by BINP) to 1 cm. For this purpose a new gun was constructed [3] and special test bench was built for its testing (Fig. 10). The main magnetic element of the test bench is straight solenoid. Vacuum chamber with gun and collector is installed along solenoid's axis. For beam property measurements the vacuum chamber contains special diagnostic node with wire profile monitor and BPM inside. The monitor provides measurements of both electrical and optical signals (due to wire heating by electron beam).

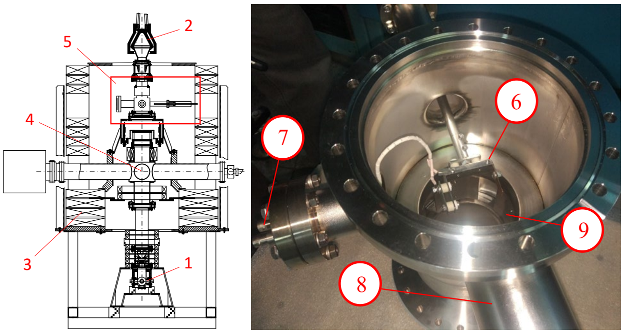

Figure 10: "Gun-collector" test bench (left) and diagnostic node of the test bench (right). 1 – electron gun, 2 – electron collector, 3 – solenoid, 4 – vacuum chamber, 5 – diagnostic node, 6 – wire support of the monitor, 7 – electric feedtroughs for the monitor, 8 – tube for vacuum window, 9 – BPM.

Figure 11 shows results of profile measurement for different regimes of the gun work. One can see, that (depending on gun electrodes voltage) it is possible to obtain narrow beam, hollow beam, or beam with homogeneous current distribution. Such profile variability will be useful for effective cooling adjustment in future [6].

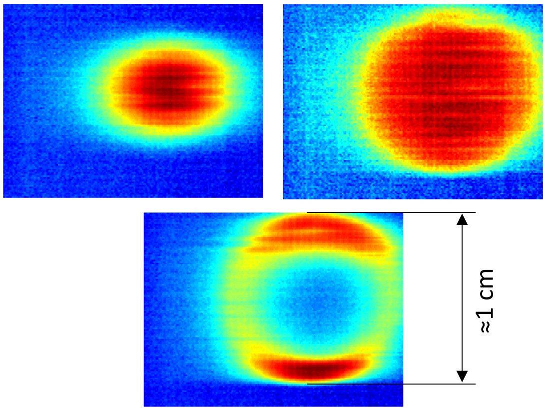

Figure 11: beam profiles for different gun regimes, measured on the test bench.

CONCLUSION

High voltage electron cooling system is important part of the NICA collider, which is needed for achieving of project luminosity in ion-ion collision experiments. Now the Budker INP is produces elements of the cooler and starts testing of already produced elements. Gun prototype testing shows possibility of beam shape control in wide range from narrow to hollow beam. Hall magnetic measurement system is ready for active work and first measurements were started.

REFERENCES

[1] V. B. Reva *et al.*, "COSY 2 MeV Cooler: Design, Diagnostic and Commissioning", in *Proc. 5th Int. Particle Accelerator Conf. (IPAC'14)*, Dresden, Germany, Jun. 2014, pp. 777-779. `doi:10.18429/JACoW-IPAC2014-MOPRI075`

[2] S. Nagaitsev, L. Prost, A. Shemyakin, "Fermilab 4.3 MeV electron cooler", `https://arxiv.org/abs/1411.6994`

[3] A. P. Denisov *et al.*, "Design of a Compact Electron Gun for the High-Voltage Electron Cooling System of the NICA Collider", in *Proc. 12th Workshop on Beam Cooling and Related Topics (COOL'19)*, Novosibirsk, Russia, Sep. 2019, pp. 18-21. `doi:10.18429/JACoW-COOL2019-MOA02`

[4] M. Bryzgunov *et al.*, "Energy transfer in the high-voltage electron cooler for the COSY synchrotron ring", *Instruments and Experimental Technics*, vol. 58, pp. 181-189, 2015. `doi: 10.1134/S0020441215020165`

[5] V.N. Bocharov *et al.*, "Precision Measurements and Compensation for the Transverse Components of the Solenoids Magnetic Field". *Instruments and Experimental Technics*, vol.48, No. 6, p. 772, 2005. `doi:10.1007/s10786-005-0139-2`

[6] V. V. Parkhomchuk, "Development of a new generation of coolers with a hollow electron beam end electrostatic bending", in *Proc. of International Workshop on Beam Cooling and Related Topics (COOL05)*, Galena, Illinois, U.S.A., September 2005, paper CP821, pp. 249-258

ISBN: 978-3-95450-243-1 ISSN: 2226-0374 doi:10.18429/JACoW-COOL2021-S103

DEVELOPMENT OF ELECTRON COOLER COMPONENTS FOR HIAF ACCELERATOR*

L. J. Mao†, J. Li, M. R. Li, H. J. Lu, F. Ma, X. M. Ma, X. P. Sha, M. T. Tang, K. M. Yan, X. D. Yang, H. Zhao, L. X. Zhao, Y. B. Zhou, IMP CAS, Lanzhou, China

Abstract

The High Intensity heavy-ion Accelerator Facility (HIAF) is under constructed at IMP in China, which is used to provide high intensity heavy ion beam pulse. A 450 keV electron cooler was proposed to boost the luminosity of high-density internal targets experiment in the spectrometer ring (SRing) at HIAF. The cooler is designed based on changes of the 300 keV cooler at IMP, which was made by BINP in 2004. In this paper, experimental testing results of the prototypes of the coils, the electron gun and the collector are reported. The technical challenges and solutions on the 450 keV high voltage system are discussed.

INTRODUCTION

The High Intensity heavy-ion Accelerator Facility (HIAF) is a new accelerator under construction at the Institute of Modern Physics (IMP) in China [1]. It is designed to provide intense primary heavy ion beams for nuclear and atomic physics. The facility consists mainly of a superconducting electron-cyclotron-resonance (SECR) ion source, a continuous wave (CW) superconducting ion linac (iLinac), a booster synchrotron (BRing) and a high precision spectrometer ring (SRing). A fragment separator (HFRS) is also used as a beam line to connect BRing and SRing. Six experimental terminals will be built in phase-I at HIAF. The layout of the HIAF accelerator was shown in Fig. 1. The main parameters are listed in Table 1.

The construction of the HIAF project was started officially in December 23rd, 2018. Up to now, roughly 50% of civil construction is finished. The first component of SECR is planned to equip in the tunnel in the middle of 2022. The first beam will be accelerated at BRing in the middle of 2025. A Day-one experiment is proposed before the end of 2025.

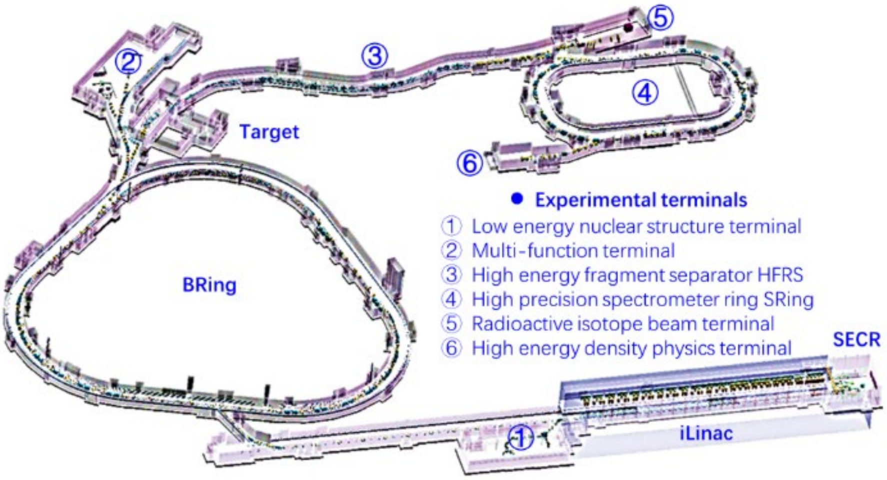

● Experimental terminals
① Low energy nuclear structure terminal
② Multi-function terminal
③ High energy fragment separator HFRS
④ High precision spectrometer ring SRing
⑤ Radioactive isotope beam terminal
⑥ High energy density physics terminal

Figure 1: Layout of the HIAF project.

Table 1: Main Parameters of the HIAF Accelerators.

	SECR	iLinac	Bring	HFRS	SRing
Length / circumference (m)	---	114	569	192	277
Final energy of U (MeV/u)	0.014 (U^{35+})	17 (U^{35+})	835 (U^{35+})	800 (U^{92+})	800 (U^{92+})
Max. magnetic rigidity (Tm)	---	---	34	25	15
Max. beam intensity of U	50 pμA (U^{35+})	28 pμA (U^{35+})	10^{11}ppp (U^{35+})		10^{10}ppp (U^{92+})
Operation mode	DC	CW or pulse	fast ramping (12T/s, 3Hz)	Momentum-resolution 1100	DC or deceleration
Emittance or Acceptance (H/V, π·mm·mrad, dp/p)		5 / 5	200/100, 0.5%	±30mrad(H)/±15 mrad(V), ±2%	40/40, 1.5%, normal mode

SRing is a versatile storage ring employed in nuclear and atomic experiments with stored stable or radioactive ion beams. Especially, the highly-charged stable ions can be used either at the injection energies or at lower energies

---

* Work supported by the National Development and Reform Commission, China
†maolijun@impcas.ac.cn.

after deceleration. A powerful electron cooling system is needed for the stable ion beams in the energy range of 800 to 30 MeV/u [2]. It also allows few intermediate energies cooling in the deceleration operation mode, to obtain a high efficiency and low losses during the deceleration of ion beams. The electron beam should be turned off during the ramping of the high voltage deceleration. In addition, the electron cooling involves isotopes beam cooling together with the stochastic cooling system. The electron cooler will be installed in the 16 meter-straight section of SRing. The total length of the cooler in ion beam direction is 11.2 m. the height is limited by the tunnel up to 6 m. The high voltage tank is equipped on the side of the cooler. Figure 2 shows a general model of SRing electron cooler.

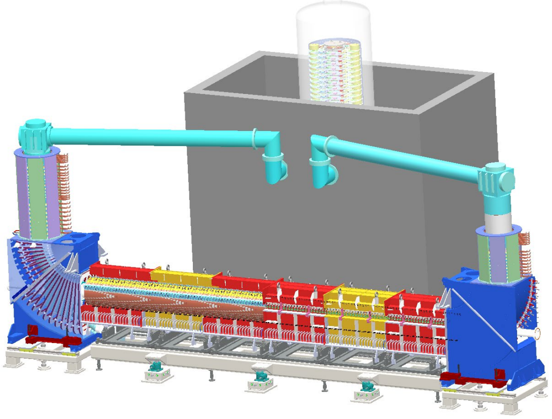

Figure 2: 3-D structure of SRing electron cooler.

DESIGN PARAMETERS

The ion beam $^{238}U^{92+}$ is taken as a reference for the design work of SRing electron cooler. The ion energy ranges from 800 MeV/u to 30 MeV/u (deceleration) that corresponds to the electron energy range of 450 keV and 15 keV. The cooling time around 10 sec is needed at the top energy. Therefore, a DC magnetized electron cooler with the electron beam current up to 2.0 A is required. According the cooling process simulation performed by a multi particle tracking code, the main parameters of the cooler was fixed as shown in Table 2.

Table 2: Technical Parameters of SRing Cooler.

Parameters	Value
Maximum acceleration voltage	450 kV
Voltage ripple	$<5.0\times10^{-5}$
Cathode radius	1.5 cm
Maximum electron current	2.0 A
Gun solenoid field	4.0 kGs
Cooling solenoid field	1.5 kGs
Collector solenoid field	2.0 kGs
Effective cooling length	7.4 m
Vacuum chamber diameter	200 mm
Vacuum	2.0×10^{-11}
Total power consumption	700 kW

MAGNETIC SYSTEM

A high-quality magnetic field is required, the allowable magnetic field homogeneity is estimated to be less than 10^{-4} in the cooling section and 10^{-3} in other sections, respectively. To satisfy these requirements cooling solenoids is made from pancake coils with possibility to incline each on the down support points [3]. In addition, based on the experience of COSY cooler [4], two types of coils with opposite direction of winding are used to decrease the transverse magnetic field components. Photo of coils is shown in Fig. 3.

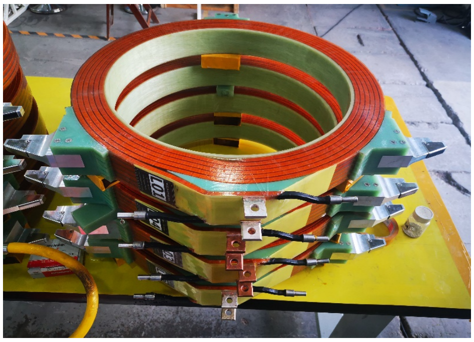

Figure 3: cooling section coils.

To achieve the magnetic field homogeneity requirement, the relative angle between the magnetic field axis and the geometric symmetrical axis must be smaller than 2.0 mrad [5]. A device with two orthogonal Hall probes was developed to measure the angle of coil, as shown in Fig. 4. The longitudinal and radial magnetic field components can be measured Hall probes respectively. Generally, the longitudinal magnetic field is a constant value. The radial magnetic field distribution can be measured by rotating the probes. The angle is calculated by the ratio of the radial magnetic field amplitude to the longitudinal magnetic field component. The direction of the angle is determined by the position of the maximum radial magnetic field.

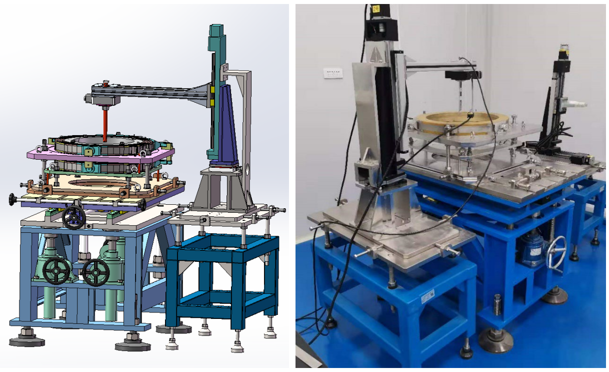

Figure 4: 3-D structure design of the magnetic field measurement platform (left) and photo of device (right).

Figure 5 shows a magnetic field measurement of one coil with the current of 150 A. It was measured ten times at each position, then calculated the average value and its deviation. The probe rotates with the step of 15°. In this measurement, the radial magnetic field amplitude is B_r=0.167 82 ± 0.000 61 Gs, the longitudinal magnetic field is B_s=130.859 ± 0.0023 Gs, the maximum radial magnetic field is appeared at the position of 101°. Therefore, the calculated angle between the magnetic field axis and the geometric symmetrical axis of the coil is θ=1.28 ± 0.10 mrad. In the SRing electron cooler, the measurement would be done for each coils of the cooling section, then an arrangement of all coils will be made according to the measurement results to minimum the transverse magnetic field component in the cooling section.

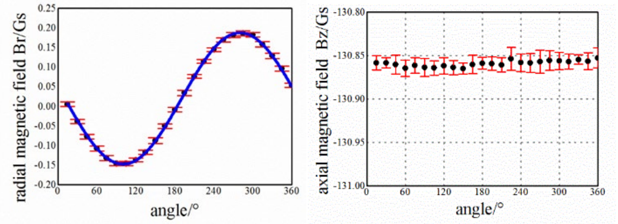

Figure 5: the measurement of the radial (left) and longitudinal (right) magnetic field components of the coil with current of 125 A.

GUN AND COLLECTOR

Electron beam up to 2.0 A is required in SRing cooler. An electron gun with a thermionic cathode is designed which is like the guns for CSR electron coolers from BINP. It can provide a variable profile electron beam to supress an "electron heating" caused by a small fractions of intensive cooled ion beam in centre [6].

A oxide cathode coated BaSrCa(CO_3) on the surface of Ni base is used for the gun [7], as shown in Fig. 6. The diameter of cathode is 29 mm. The maximum electron emission current density up to 1.3 A/cm^2 with the temperature of 800°C was achieved at a test bench. A lifetime measurement is given in Fig. 7. An estimate of cathode lifetime with 0.5 A/cm^2 (for HIAF cooler requirement) would be larger than 10^5 hours.

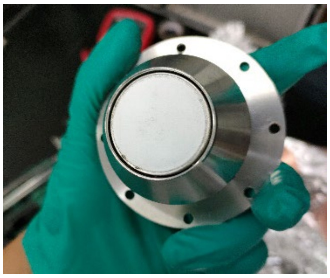

Figure 6: the assembling cathode for HIAF cooler.

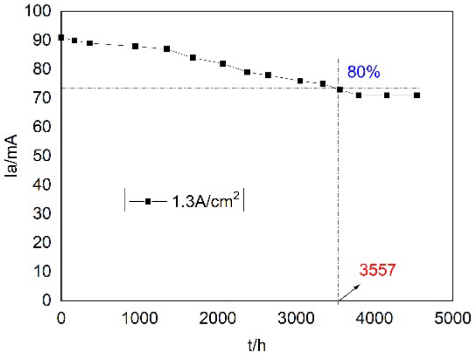

Figure 7: the lifetime measurement of the cathode (it was measured with a Φ3mm cathode NOT the real cooler cathode).

It is necessary to check the vacuum property of the gun and collector before the installation. A heat chamber is used to make a uniform temperature distribution on the ceramic rings during heating process, as shown in Fig. 8. The gun and collector were heated from 20°C to 180°C linearly within 30 hours, and then keep it for 48 hours. Finally, return to the room temperature with a rate of -5°C/h. A titanium getter pump is turned on for few minutes at last. A vacuum condition of 4.3×10^{-12} is obtained, which is satisfy to the SRing requirement.

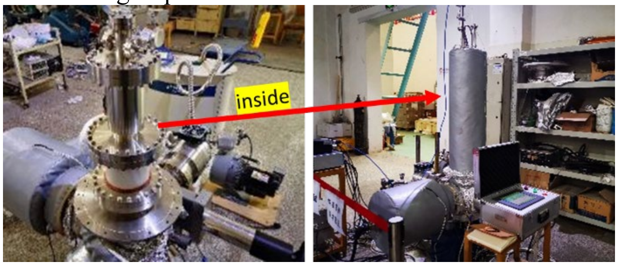

Figure 8: the assembling cathode for HIAF cooler.

The gun and collector have been operated in the test bench, as shown in Fig. 9. The test bench is built to measure the gun perveance, the collector efficiency, the electron beam profile and so on. The collector is installed on the top because it is much heavier than the gun. The electron beam is controlled by three groups of coils. A scanning wire is installed near the entrance of the collector.

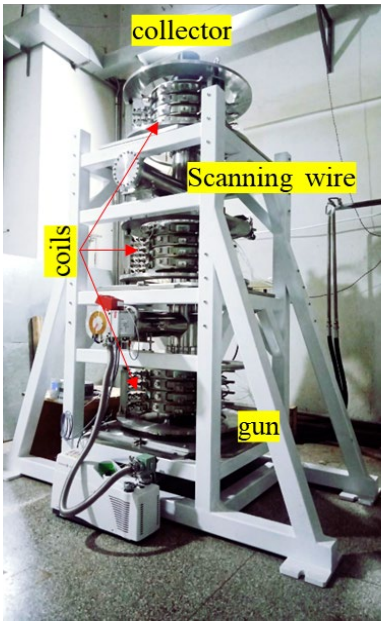

Figure 9: the gun and collector test bench for HIAF cooler.

The measured dependence of the gun perveance on the ratio of grid to anode voltages is shown in Fig. 10. The ratio means different electron beam profiles. A "hollow" electron beam can be obtained with a larger ratio. In the beginning, a 65 W heating power is used for the cathode activation. The measured perveance shows that the electron emission current density is much lower than the simulation results. After that, 120 W heating power is applied for a reactivation process. The final measurement shows an agreement with the simulation result.

ISBN: 978-3-95450-243-1 ISSN: 2226-0374 doi:10.18429/JACoW-COOL2021-S103

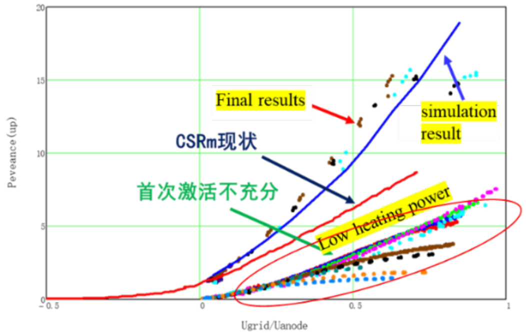

Figure 10: the gun perveance measurement on test bench.

The collector efficiency is measured with a small electron beam current on the test bench. As a device without bending magnetic field, electrons reflected from the collector can be collector again. Therefore, the measured collector efficiency is much better than the simulation results, as shown in Fig. 11. Both simulation and measurement show that the collector efficiency decrease with an increasing of suppressor voltages. The suppressor is used to create a voltage "bucket". Electrons reflected from the collector can be suppressed since the energies are smaller than primary electrons' energies [8]. However, deep "bucket" could reflect the primary electrons at the entrance of collector cup. Therefore, a drastic decreasing with a very lower suppressor voltages was observed.

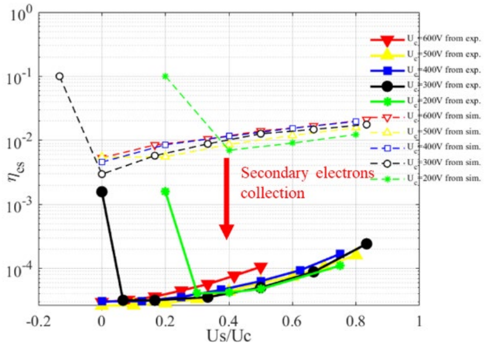

Figure 11: the collector efficiency measured on the test bench. The secondary electrons collection is not included in the simulation work.

CONCLUSION

The HIAF project is the biggest heavy ion accelerator project under-construction in China. A traditional DC magnetized electron cooler is used to improve luminosities for internal target experiments. Based on the CSR coolers designed by BINP, a 450 keV cooler is designed at IMP. The main components including coils, the electron gun and the collector are manufactured. The preliminary tests show that main parameters are satisfied to the SRing cooler requirements.

ACKNOWLEDGEMENTS

We thank all the colleagues working on the HIAF project for their valuable contributions on this article. The authors would like to thank Dr. Parkhomchuk, Dr. Reva and colleagues from BINP for their supports.

REFERENCES

[1] J.C.Yang *et.al., Nucl. Instr. Meth.* B 317, 263, 2013.

[2] L.J.Mao *et.al.,* "The Electron Cooling System for the HIAF Project in China", in *Proc. 12th Workshop on Beam Cooling and Related Topics (COOL'19)*, Novosibirsk, Russia, Sep. 2019, pp. 4-17. `doi: 10.18429/JACoW-COOL2019-MOZ01`

[3] E.Behtenev *et.al.,* "Commission of Electron Cooler EC-300 for HIRFL-CSR", in *Proceedings of EPAC 2004*, Lucerne, Switzerland, 2004, pp. 1419-1421.

[4] J.Dietrich *et.al.,* "Development of Electron Cooler Components for COSY", in *Proceedings of RuPAC 2010*, Protvino, Russia, 2010, pp. 151-155.

[5] Sha Xiaoping *et.al., High Power Laser and Particle Beams*, Vol. 33, No.8, 0840.

[6] A.V.Bubley *et.al., Nucl. Instr. Meth.* A 532, 303, 2004.

[7] Xianheng Liao *et.al.,* "Study on the Oxide Cathode for HIRFL-CSR Electron Cooler", in *Proc. 7th Workshop on Beam Cooling and Related Topics (COOL'09)*, Lanzhou, China, Sep. 2009, pp. 160-163.

[8] Tang, MT *et. al., Nucl Sci Tech* 32, 116, 2021.

ISBN: 978-3-95450-243-1 ISSN: 2226-0374 doi:10.18429/JACoW-COOL2021-S201

ELECTRON COOLING WITH SPACE-CHARGE DOMINATED PROTON BEAMS AT IOTA

N. Banerjee*, M.K. Bossard, J. Brandt, Y-K. Kim, The University of Chicago, Chicago, USA
B. Cathey, S. Nagaitsev†, G. Stancari, Fermilab, Batavia, Illinois, USA

Abstract

We describe a new electron cooler being developed for 2.5 MeV protons at the Integrable Optics Test Accelerator (IOTA), which is a highly re-configurable storage ring at Fermilab. This system would enable the study of magnetized electron cooling in the presence of intense space-charge with transverse tune shifts approaching -0.5 as well as highly non-linear focusing optics in the IOTA ring. We present an overview of the design, simulations and hardware to be used for this project.

INTRODUCTION

The creation and stability of high-intensity hadron beams is very important to future projects such as heavy-ion facilities [1–3], Electron-Ion Colliders [4], etc. Electron cooling provides a well-established method of attaining high equilibrium beam intensities and have been demonstrated for a wide range of ion energies from $\gamma \sim 1.00011$ [5] up to $\gamma \approx 9.5$ [6]. The maximum intensity of ion beams achieved through electron cooling is limited by the additional heating processes of Intra-Beam Scattering (IBS) and resonance-driven transverse heating due to space-charge tune shifts. [7] In practice, the transverse size of the ion beam decreases under the influence of electron cooling until the betatron tune shift reaches a maximum value of 0.1-0.2. [8, 9] Studying the influence of ion space-charge forces on electron cooling at the high-intensity limit requires the development of a novel test platform and associated theoretical models.

The Integrable Optics Test Accelerator (IOTA) is a re-configurable 40 m storage ring built at Fermilab which acts as a test facility dedicated to research on intense beams including the areas of Non-linear Integrable Optics (NIO), beam cooling, space-charge, instabilities and more. [10, 11] It can circulate both electrons up to 150 MeV and protons with a kinetic energy of 2.5 MeV ($pc \approx 70$ MeV). The proton beam energy is limited by the existing injector RFQ. In this contribution, we discuss the design of the electron cooler which we will operate with 2.5 MeV protons as a part of our electron-lens research program. [12] Besides enabling experiments on non-linear integrable optics by reducing energy spread and improving the lifetime of the beam by compensating for transverse emittance growth, the primary motivation of research with this cooler is to study the effect of space-charge forces in the regime of large transverse incoherent tune shift of $\Delta\nu_{x,y} \approx -0.5$ and compare with theoretical models. In addition, we are also planning experiments which uses electron cooling as a knob to study the interplay between space-charge and instabilities [13] and also control the phase space distribution in order to facilitate the realization of NIO in the presence of space-charge forces.

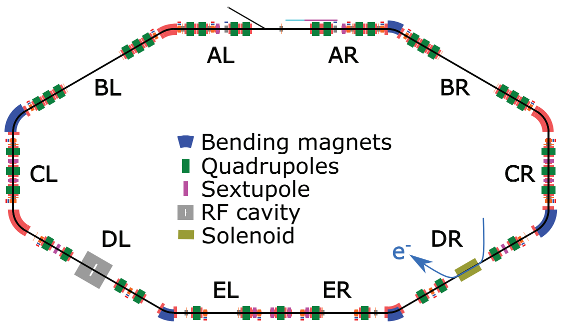

Figure 1: Layout of the Integrable Optics Test Accelerator (IOTA) at Fermilab. The machine is divided into multiple sections named AR (A right), BR (B right) and so on through AL (A left). The blue arrow represents the path of the electrons in the cooler.

In the next section, we detail the operation parameters of IOTA with protons and describe the electron cooler setup. Then we discuss a novel simulation model which includes electron cooling with transverse space-charge. In the last section, we summarize our results and present future plans.

ELECTRON COOLER SETUP

Figure 1 shows the layout of IOTA along with the planned location of the electron cooler. Protons with a kinetic energy of 2.5 MeV from the injector (not shown) enter into the ring in the A section, circulate clockwise and co-propagate with electrons in the DR section. Besides the coasting beam mode, an rf cavity operating at the 4th harmonic of the revolution frequency, placed in the DL section is used for bunched beam operation. In addition, non-linear magnets can be placed in the straight sections BL and BR to perform experiments on NIO. While the optics of the ring will be optimized for individual experiments, Table 1 shows some general parameters of operation with electron cooling. At the maximum design current corresponding to a vertical tune shift of -0.5, emittance growth times due to IBS are typically less than 10 seconds, thus limiting beam lifetime and constraining the experiments which

---

[*] nilanjan@uchicago.edu
[†] also at the University of Chicago

Table 1: Typical operation parameters for electron cooling of protons in IOTA. The last three rows list the emittance growth times due to Intra-Beam Scattering (IBS).

Parameter	Value		Unit
Circumference (C)	39.96		m
Kinetic energy (K_b)	2.5		MeV
Revolution time (τ_{rev})	1.83		μs
Emittances ($\epsilon_{x,y}$)	4.3, 3.0		μm
Momentum spread (σ_p/p)	1.32×10^{-3}		
	Coasting	Bunched	
Number of bunches	-	4	
Bunch length (σ_s)	-	0.79	m
Beam current (I_b)	6.25	1.24	mA
Bunch charge (q_b)	11.4	0.565	nC
Tune shifts ($\Delta\nu_{x,y}$)	-0.38, -0.50		
$\tau_{\mathrm{IBS},x}$	6.40	8.69	s
$\tau_{\mathrm{IBS},y}$	4.19	5.97	s
$\tau_{\mathrm{IBS},s}$	8.08	23.0	s

can be performed for intense proton beams at IOTA.[1] In addition, space-charge forces also create rapid emittance growth and beam loss especially in the first few 100 turns. Consequently electron cooling serves as an important tool to compensate for heating and is valuable for all research with proton beams in IOTA.

We have chosen a magnetized electron cooler configuration for IOTA with relevant parameters listed in Table 2. The electron beam energy and transverse beam size are chosen so that the electrons co-propagate with the protons at the same velocity in the cooler and forms an uniform distribution whose extent overlaps with 2σ of the transverse distribution of the protons. The maximum electron current is limited by the space-charge voltage depression at the center of the cooling beam. This is the dominant contribution to the longitudinal temperature $T_{\parallel,\mathrm{SC}}$ of the electrons given by,

$$T_{\parallel,\mathrm{SC}} = \frac{1}{k_B m_e c^2 \beta^2 \gamma^2}\left(\frac{1}{2}\frac{I}{4\pi\epsilon_0 c\beta}\right)^2, \qquad (1)$$

where I, β and γ are the electron beam current and relativistic parameters respectively and k_B, m_e, c and ϵ_0 are physical constants with their usual meaning. The transverse temperature of the electrons is dominated by the cathode temperature T_{cath}. In the case of a magnetized electron beam, perturbations to the field inside the solenoid manifests itself as an additional effective transverse temperature $T_{\perp,B_\perp}$ given by, [14]

$$T_{\perp,B_\perp} = \frac{m_e a^2 \omega_c^2}{4k_B}\left(\frac{B_\perp}{B_\parallel}\right)^2, \qquad (2)$$

Table 2: Baseline Electron Cooler Parameters for IOTA.

Proton parameters	
RMS Beam size ($\sigma_{b,x,y}$)	3.22 mm, 2.71 mm
Electron parameters	
Kinetic energy (K_e)	1.36 keV
Current (I_e)	10 mA
Temporal Profile	DC
Transverse Profile	Flat
Radius (a)	6 mm
Source temperature (T_{cath})	1400 K
Main solenoid parameters	
Magnetic field ($B_\parallel$)	0.1 T
Length (l_{cooler})	0.7 m
Field non-uniformity ($B_\perp/B_\parallel$)	2×10^{-4}
Electron beam temperatures	
Longitudinal ($T_\parallel \approx T_{\parallel,\mathrm{SC}}$)	22.3 K
Transverse ($T_\perp \approx T_{\mathrm{cath}} + T_{\perp,B_\perp}$)	1407.4 K
Effective ($T_{\mathrm{eff}} = T_{\perp,\mathrm{eff}} + T_\parallel$)	34.7 K
Cooling times ($\tau_{\mathrm{park,x,y,s}}$)	1.0 s, 0.9 s, 1.0 s

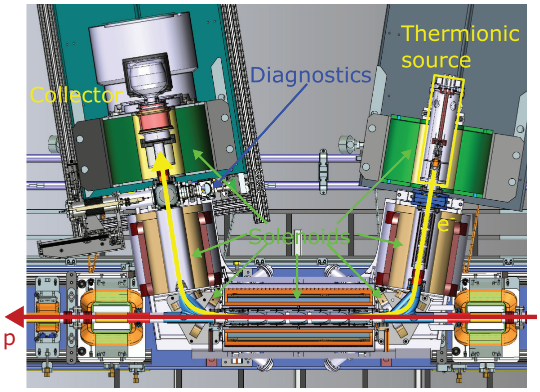

Figure 2: Electron lens setup for IOTA, which will also act as the electron cooler. The total beam power of the magnetized DC electron beam with a flat transverse profile is ≈ 13.6 W.

where a, B, $\omega_c \equiv eB/m_e$ and $B_\perp/B_\parallel$ are the electron beam radius, solenoid field, cyclotron frequency and the field non-uniformity of the cooler solenoid respectively. In the case of magnetized electron cooling, the cyclotron motion of the electrons effectively damps their transverse temperature as seen by the ions, giving rise to a much smaller effective transverse temperature referred to as $T_{\perp,\mathrm{eff}}$ under the *Parkhomchuk* model [15]. Since perturbations to the solenoid field in turn perturbs the cyclotron motion of the electrons, the field flatness of the solenoid must also be constrained and our design specification is such that the $T_{\perp,B_\perp} \lesssim T_{\perp,\mathrm{eff}}$. The initial cooling time with this configuration is about 1 second in all planes for bunched beam.

Figure 2 depicts a model of the electron cooler setup showing the thermionic source, collector and all the solenoids which keep the electron beam magnetized throughout the

---

[1] At an effective residual gas pressure of 10^{-10} Torr in the IOTA vacuum chamber, the typical emittance growth times due to small angle scattering are in excess of tens of minutes and the large angle scattering lifetime is in the order of 10 hrs. Hence residual gas scattering will not present a significant operational bottleneck for proton operations.

ISBN: 978-3-95450-243-1 ISSN: 2226-0374 doi:10.18429/JACoW-COOL2021-S201

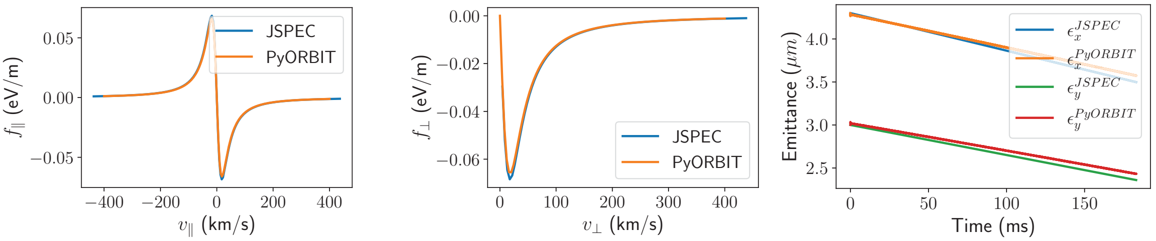

Figure 3: Comparison of the Parkhomchuk cooling force calculated using JSPEC and the `ecooler` extension for PyORBIT described in this paper. The first two panels show the longitudinal and transverse cooling force as a function of proton velocities and the third panel shows the evolution of transverse emittance as a function of time.

transport line. The structure of the thermionic source will be similar to others developed at Fermilab, including for the hollow electron lens at the HL-LHC [16]. While the strengths of the source and the main solenoid may be adjusted to provide a beam size expansion factor of 2, the baseline design assumes that both the source and the main solenoid are set to 0.1 T. Diagnostics for the electron beam include a Faraday cup to measure current and a scintillating screen to image the transverse profile at the entrance to the collector. Proton beam diagnostics include beam position monitors and a DC current transformer. Additionally, the radiative recombination rate of electrons and protons with the bunched beam parameters listed in Tables 1 and 2 is 6 kHz. This allows for a non-destructive but slow (compared to cooling time) diagnostic of the equilibrium transverse profile of the protons by placing a micro-channel plate detector and associated imaging system [17] at the downstream end of the DR section. The measurement of proton beam lifetime and equilibrium transverse profiles enable the realization of a variety of electron cooling experiments at IOTA.

SIMULATIONS

An intense ion beam undergoing electron cooling is subject to focusing from the lattice, cooling forces from the electrons, point-to-point Coulomb scattering with other particles of the beam i.e IBS and also forces due to mean-field contribution from the surrounding charge density i.e. space-charge. All these effects work in concert to limit the equilibrium phase space density which can be reached at the core of the beam. We used the JSPEC code [18] to obtain an initial estimate of electron cooling rates which are shown in Table 2 and also calculate the time evolution of the beam distribution and emittance. Using the Parkhomchuk model of electron cooling and the Martini model of IBS, our simulations indicate the formation of an un-physically dense core[2] which is ruled out by observations. [8, 9] In order to account for the effects of space-charge forces throughout the accelerator and particles crossing through betatron resonances of the storage ring during the cooling process, we implemented electron cooling as an extension to the particle tracking code PyORBIT. [19]

PyORBIT is an extendable particle tracking code implementing symplectic beamline elements and multiple Particle-in-Cell (PIC) space-charge models which allow for the simulation of dynamic space charge effects such as incoherent tune shifts [20], emittance growth [21] due to optics function mismatch and heating driven by particles crossing betatron resonances. Space-charge tracking in PyORBIT proceeds as follows, all magnetic lattice elements are divided into smaller segments which are implemented as thick-lens symplectic transfer maps called *nodes* after which thin-lens space-charge kick nodes are placed in between these segments. The beam is tracked through the lattice nodes and at the end of each node, the beam distribution is binned to a Cartesian grid. We use the `sc2p5d` model of space-charge which assigns transverse kicks to all particles by solving the Poisson's equation in 2D and calculating the total kick the particle receives while travelling through the same length as the last tracked thick-lens segment. In addition to these components we added a new extension to PyORBIT, which inserts a separate `ecooler` node after every cooler solenoid node. This node calculates a thin-lens kick which accounts for the total momentum change imparted by the cooling force and the static field of the electron beam as the ions travel through a small segment of the cooler. Our novel simulation model thus incorporates XY coupling from the solenoid, static space-charge from the electron beam and dynamic space-charge from the ion beam along with electron cooling.

The Parkhomchuk model [15] which is used to estimate the cooling force $\vec{F}_{\mathrm{cool}}$ on each particle in the center-of-momentum (CM) frame of the stored beam is defined as follows:

$$\begin{aligned}\vec{F}_{\mathrm{cool}} = -4 m_e n_e (Z r_e c^2)^2 \frac{\vec{V}}{\left[|\vec{V}|^2 + \vec{V}_{\mathrm{eff}}^2\right]^{3/2}} \\ \times \ln\left[\frac{\rho_{\max} + \rho_{\min} + \rho_L}{\rho_{\min} + \rho_L}\right],\end{aligned} \tag{3}$$

---

[2] The IBS models in JSPEC assume a Gaussian distribution of the beam. Hence, large deviations of the cooled beam from the initial Gaussian distribution is the likely cause for the un-physical results and a local model of IBS can alleviate the issue.

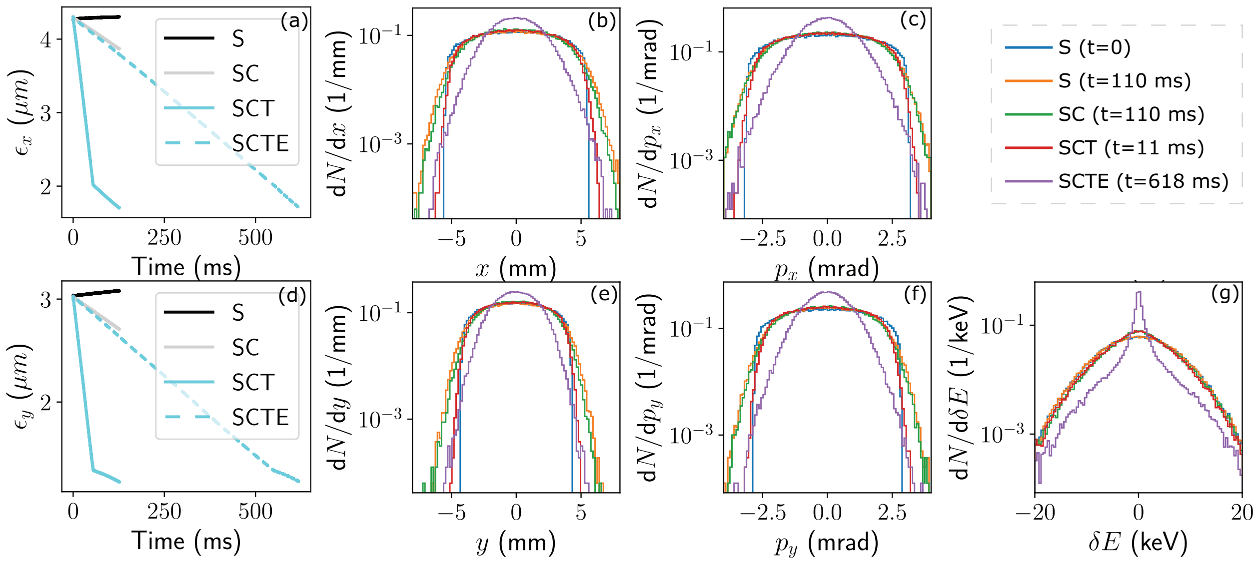

Figure 4: Electron cooling simulation results for IOTA with transverse space charge using the `eccoler` extension in PyORBIT. Panels (a) and (d) show the evolution of transverse emittance as a function of time for various runs listed in the text. Other panels show snapshots of particle distribution on various axes of phase space.

where n_e, r_e, ρ_L and Z are the electron beam density, classical radius, Larmor radius of electrons and the charge of the ions in the storage ring respectively. The cooling force on a single ion is a function of the relative velocity of the ion w.r.t to the electrons given by $\vec{V} \equiv \vec{v}_i - \langle \vec{v}_e \rangle$ and the effective velocity spread of the electrons $V_{\text{eff}}^2 \equiv \langle v_{e,\parallel}^2 \rangle + \Delta V_{e,\perp}^2$, where $\vec{v}_i$, $\vec{v}_e$, $v_{e,\parallel}$ and $\Delta V_{e,\perp}$ are the CM frame ion velocities, electron velocities, longitudinal component of electron velocities and *effective* transverse component respectively. The effective electron beam temperature listed in Table 2 is given by $T_{\text{eff}} \equiv m_e V_{\text{eff}}^2 / k_B$. The range of impact parameters of electron-ion scattering is constrained by $\rho_{\text{min}} \equiv Z r_e c^2 / (|\vec{V}|^2 + V_{\text{eff}}^2)$ and $\rho_{\text{max}} \equiv |\vec{v}_i| / (1/\tau_{\text{tof}} + \omega_p)$, where τ_{tof} and ω_p are the time-of-flight of the ion in the cooler and ω_p is the plasma frequency of the electrons. We assume that $\Delta V_{e,\perp}$ is dominated by the transverse drift velocity in the presence of crossed electric field E_ρ and magnetic field $B_\parallel$ of the cooling beam and the solenoid respectively. Therefore $\Delta V_{e,\perp} \equiv E_\rho(a)/B_\parallel$, where $E_\rho(a)$ is the maximum radial electric field generated by the electron beam. Figure 3 shows the cooling force estimated using this model in different codes as a function of transverse and longitudinal ion velocities. The third panel in Fig. 3 compares the evolution of transverse emittance in IOTA as a function of time between JSPEC and our `ecooler` extension in PyORBIT in the absence of space-charge and IBS. The results show that our implementation of the Parkhomchuk cooling force model agrees with JSPEC in turn-by-turn simulations.

The fidelity of the transverse space-charge model `sc2p5d` used in PyORBIT depends on the transverse grid size and the distance between each space-charge calculation node. In general, the transverse grid size must be much smaller than the Debye length $\lambda_{D,p}$ of the proton beam but also much larger than the mean distance d_p between individual protons. Further the distance between space-charge calculation nodes i.e the time step of the PIC calculation loop Δt_{PIC} must be much smaller than the plasma period τ_p of the proton beam. For the proton parameters listed in Table 1, $\lambda_{D,p} \approx 5$ mm, $d_p \approx 29.1\,\mu$m and $\tau_p \approx 127$ ns. In keeping with these constraints, we choose a 64×64 square grid with side length 50 mm which serves as a perfectly conducting boundary for the proton beam and keep the distance between space-charge nodes < 20 mm which corresponds to $\Delta t_{\text{PIC}} \approx 0.91$ ns. As the beam cools and the proton beam density increases, $\lambda_{D,p}$, d_p and τ_p all reduce in value. However in the simulations reported here, we use fixed discretization parameters. For a coasting beam at the design current of 6.25 mA, the space-charge forces dominate the dynamics over electron cooling with the baseline parameters listed in Table 2 and the simulations predict long term emittance growth. Simulations starting with a tune shift of $\Delta\nu_y = -0.1$ corresponding to a coasting beam current of 1.25 mA show interesting dynamics and some preliminary results are depicted in Fig. 4.

The electron cooling simulations reported here are named as follows: S represents a simulation with space-charge only without electron cooling, SC represents a run with space-charge and baseline parameters of electron cooling and SCT represents a run with space-charge and electron-cooling where the cooling force is scaled by a factor of 10 for the first 30000 turns ($\approx$ 54 ms) and then switched back to baseline values for the rest of the simulation. The transverse emittance grows for run S while it decays for the run SC, as seen in panels (a) and (d) of Fig. 4, indicating that electron cooling dominates the dynamics at the initial stage of the simulation. Looking at the 1D histograms of particle distribution in x, p_x, y and p_y at $t = 110$ ms in panels (b), (c), (e) and (f) respectively indicate that space-charge forces lead to the diffusion of particles from the core of the beam into the periphery as seen in the orange (run S) and green (run SC) traces which are very similar to each other and in general broader than the injected beam (K-V distribution in transverse) shown by the blue traces. In contrast, the energy distribution of particles in panel (g) shows a clear evidence of cooling for run SC (green) as evidenced by the increase of particles at low energy deviations δE when compared to the histogram for S (orange) at the same time. Even though the runs S and SC yield some insight into this initial stage of cooling when the space-charge forces are weak, longer term simulations are required to probe the intense space-charge regime.

In order to speed up the simulation in the initial weak space-charge regime, we introduce the run SCT where the cooling force is scaled by a factor of 10 during an initial period where space-charge forces are much smaller compared to the linear focusing provided by the lattice. The transverse emittance decays much faster for the run SCT compared to the run SC, but when the time axis is scaled by a factor of 10 (labelled SCTE in panels (a) and (d) of Fig. 4), the emittance decay closely follows SC. Comparing the distribution of particles in phase-space at $t = 110$ ms for SC (green) and $t = 11$ ms for SCT (red), we see very similar distributions in energy as shown by panel (g) and good agreement up to intermediate values of the transverse coordinates x, p_x, y and p_y in panels (b), (c), (e) and (f) respectively. Hence by suitably scaling the time for the run SCT, we can estimate the phase space distribution of the beam at $t = 618$ ms as shown in purple in Fig. 4. The results indicate reduction in transverse emittance by almost a factor of 2 in both planes and also significant reduction in energy spread.

CONCLUSION AND OUTLOOK

While electron cooling provides a mechanism to cool ions of low to intermediate kinetic energies, the maximum intensity of the ion beam attained through this method is limited by Intra Beam Scattering (IBS) and space-charge forces acting on the ion beam. A maximum incoherent space-charge tune shift of 0.1-0.2 has been achieved in practice. We are developing an electron cooling test bed for 2.5 MeV protons at the Integrable Optics Test Accelerator (IOTA) at Fermilab which is a 40 m storage ring operating up to a design current corresponding to a transverse space-charge tune shift of $\Delta\nu_y = -0.5$. We have developed the baseline design of a magnetized electron cooler which will enable the study of electron cooling for ion beams with intense space-charge, study the interplay between space-charge and instabilities and use cooling as a method of phase space control for Non-linear Integrable Optics.

With the baseline parameters, the cooling times are of the order of one second in all planes which is sufficient to compensate for emittance growth due to IBS at the planned proton beam parameters. To study the influence of intense space-charge with electron cooling, we developed an extension to the particle tracking code PyORBIT which uses the Parkhomchuk model of the cooling force, a static model of the electron beam space-charge and a transverse dynamic space-charge model of the proton beam. While we verified the cooling force with the simulation code JSPEC, efforts to validate long-term space-charge tracking in PyORBIT are still ongoing. Numerical simulations using our tool show that on starting with a coasting beam of 1.25 mA in IOTA corresponding to a tune shift of $\Delta\nu_y = -0.1$, the transverse emittances reduce by a factor of 2 in 618 ms. However the effect of space-charge is still weak and longer simulations covering multiple cooling times is required to adequately study the intense space-charge regime. This effort represents the first time electron cooling simulations have incorporated turn-by-turn space-charge tracking with all lattice elements enabling the analysis of non-linear dynamics of the particles, crossing of betatron resonances, etc.

Future simulation work will involve using an amplitude dependent model of IBS with electron cooling to compare with space-charge simulation results, studying the effect of a semi-hollow electron beam distribution on the cooling process and developing the thermionic electron source to generate the required beam. Based on these calculations, we will develop specific plans for experimental study in IOTA.

ACKNOWLEDGEMENT

We would like to thank Alexander Valishev, Alexander Romanov and Valeri Lebedev for discussions on proton operations in IOTA and helping develop the experimental parameters. We also want to acknowledge Alexey Burov and Alexei Fedotov for recognizing the need for a local model of IBS to prevent over-cooling in our JSPEC simulations. This manuscript has been authored by Fermi Research Alliance, LLC under Contract No. DE-AC02-07CH11359 with the U.S. Department of Energy, Office of Science, Office of High Energy Physics. This research is also supported by the University of Chicago.

REFERENCES

[1] P. Spiller *et al.*, “The FAIR Heavy Ion Synchrotron SIS100”, JINST **15**, no. 12, T12013, 2020

[2] J. C. Yang *et al.*, “High Intensity heavy ion Accelerator Facility (HIAF) in China”, Nucl. Instrum. Meth. B **317**, 263-265, 2021.

[3] V. D. Kekelidze., “NICA project at JINR: status and prospects”, JINST **12**, no. 06, C06012, 2017.

[4] F. Willeke *et al.*, “Electron Ion Collider Conceptual Design Report 2021”, United States, 2021. `https://www.bnl.gov/ec/files/EIC_CDR_Final.pdf`

[5] W. Bartmann *et al.* [ELENA and AD],“The ELENA facility”, Phil. Trans. Roy. Soc. Lond. A **376**, no.2116, 20170266, 2018

[6] S. Nagaitsev, *et al.*, “Experimental demonstration of relativistic electron cooling”, Phys. Rev. Lett. **96**, 044801, 2006

[7] V. Parkhomchuk, I. Ben-Zvi,, “Electron Cooling for RHIC”, BNL C-A/AP/47, 2001. `https://www.bnl.gov/isd/documents/79867.pdf`

[8] S. Nagaitsev *et al.*, “Space Charge Effects and Intensity Limits of Electron-Cooled Bunched Beams”, in *Proc. 16th Particle Accelerator Conf. (PAC’95)*, Dallas, TX, USA, May 1995, paper RAP22, pp. 2937–2939.

[9] M. Steck, *et al.*, “Beam accumulation with the SIS electron cooler”, Nucl. Instrum. Meth. A **441**, 175-182, 2000.

[10] S. Antipov, *et al.*, “IOTA (Integrable Optics Test Accelerator): Facility and Experimental Beam Physics Program”, JINST **12**, no.03, T03002, 2017.

[11] A. Valishev, *et al.*, “First Results of the IOTA Ring Research at Fermilab”, in *Proc. IPAC’21*, Campinas, SP, Brazil, May 2021, pp. 19–24.

[12] G. Stancari, *et al.*, “Beam physics research with the IOTA electron lens”, JINST **16**, no.05, P05002, 2021.

[13] A. Burov, “Convective Instabilities of Bunched Beams with Space Charge”, Phys. Rev. Accel. Beams **22**, no.3, 034202, 2019.

[14] J. Bridges, *et al.*, “Fermilab Electron Cooling Experiment: Design Report”, FERMILAB-DESIGN-1978-01, 1978. `https://lss.fnal.gov/archive/design/fermilab-design-1978-01.pdf`

[15] V. V. Parkhomchuk, “New insights in the theory of electron cooling”, Nucl. Instrum. Meth. A **441**, 9-17, 2000.

[16] D. Perini, A. Kolhemainen, A. Rossi, S. Sadovich and G. Stancari, “Design of high-performance guns for the HL-LHC HEL”, JINST **16**, no.03, T03010, 2021.

[17] G. Tranquille *et al.*, “Commissioning the ELENA Beam Diagnostics Systems at CERN”, in *Proc. 9th Int. Particle Accelerator Conf. (IPAC’18)*, Vancouver, Canada, Apr.-May 2018, pp. 2043–2046.

[18] H. Zhang, S. V. Benson, M. W. Bruker, and Y. Zhang, “JSPEC - A Simulation Program for IBS and Electron Cooling”, in *Proc. 12th Int. Particle Accelerator Conf. (IPAC’21)*, Campinas, Brazil, May 2021, pp. 49–52.

[19] A. Shishlo, S. Cousineau, J. Holmes, T. Gorlov, “The Particle Accelerator Simulation Code PyORBIT”, Procedia Computer Science, **51**, 2015, pp. 1272–1281.

[20] M. Titze, “Space Charge Modeling at the Integer Resonance for the CERN PS and SPS”, PhD thesis, Humboldt-Universität zu Berlin, Germany, 2020. `https://doi.org/10.18452/21423`

[21] F. Schmidt *et al.*, “Code Bench-Marking for Long-Term Tracking and Adaptive Algorithms”, in *Proc. 57th ICFA Advanced Beam Dynamics Workshop on High-Intensity and High-Brightness Hadron Beams (HB’16)*, Malmö, Sweden, Jul. 2016, pp. 357–361.

ISBN: 978-3-95450-243-1 ISSN: 2226-0374 doi:10.18429/JACoW-COOL2021-S302

RECOMMISSIONING OF THE CERN AD STOCHASTIC COOLING SYSTEM IN 2021 AFTER LONG SHUTDOWN 2

W. Höfle*, J. C. Oliveira, C. Carli, F. Caspers, B. Dupuy, D. Gamba,
R. Louwerse, L. Ponce, V. R. Myklebust, S. F. Rey, L. Thorndahl
CERN, Geneva, Switzerland

Abstract

The power amplifier system of the Stochastic Cooling System of the Anti-proton Decelerator (AD) at CERN, installed on top of the shielding blocks of the AD ring, was completely dismantled during the long shutdown 2 (LS2) at the end of the 2018 run in order to gain access to the accelerator for magnet consolidation. At start-up, this required finding and verifying the correct electrical delays for all 48 power amplifiers feeding the two kickers, by means of beam transfer functions for the two cooling plateaus at 3.57 GeV/c and 2 GeV/c. We describe the methods used for the setting up and the results of the optimization for the cooling in all three planes, longitudinal, horizontal and vertical. An experimental set-up has been put into operation for automatic monitoring and correction of the notch position of the longitudinal cooling at 3.57 GeV/c with optical delay lines. We also comment on the lessons learnt during the recommissioning including the repair work for a vacuum leak in the water cooling circuits of the kicker following bake-out and the verification of the internal loads by RF reflectometry.

INTRODUCTION

In the CERN Anti-proton Decelerator (AD) anti-protons are routinely decelerated since 1999 and distributed to experiments located in the same hall as the AD machine [1]. The AD machine itself is covered for radiation shielding purposes by concrete blocks leaving only limited space for access to equipment inside the ring. In case a bulky element in the ring needs to be shifted or exchanged concrete blocks covering the AD ring have to be removed so that the equipment can be accessed by the overhead crane. The CERN Long Shutdown 2 (LS2) from 2019 to 2020 saw a number of interventions for consolidation in AD and for connection of beam transfer lines between ELENA and the newly installed experiments. Notably the change of a magnet in between the two kicker tanks of the stochastic cooling system and the installation of the extraction line from ELENA (LNE00) necessitated the temporary dismantling of the stochastic cooling power amplifier system.

RECAP OF STOCHASTIC COOLING PICK-UPS AND KICKERS

The stochastic cooling system in AD comprises four elements in the ring: horizontal pick-up UHM 3107 and horizontal kicker KHM 0307, and vertical pick-up UVM 3207 with vertical kicker KVM 0407 [2]. The longitudinal cooling is using the same pick-ups and kickers in their common mode combining both signals from the horizontal and vertical pick-ups and splitting on the back-end the signal to feed both the horizontal and vertical kickers.

The basic element in these pick-ups and kickers is a rectangular short electrode of a length of 33 mm (in beam direction) and width of 46 mm. A total of 48 of these small electrodes are lined up on a rail with a gap of 10.85 mm to form what is called a “super-electrode” with a total active length of 2093.95 mm. The individual electrodes are grouped in 12 sets of four electrodes (Figure 1). For the kicker, each set is fed by a single 100 W power amplifier connected to a dedicated RF vacuum feedthrough on the tank.

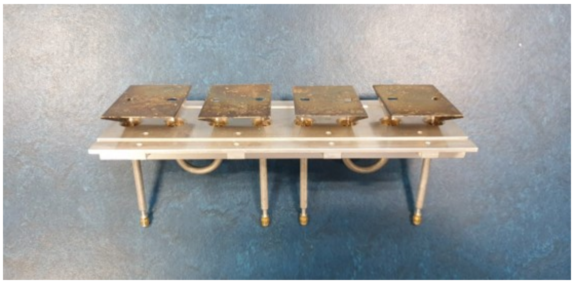

Figure 1: Set of four electrodes (length of support 175.4 mm) powered by a single amplifier (see text).

Within the set of four electrodes the power is distributed through a 2:1 splitter of Wilkenson type, but without matching resistor, mounted on the rail inside the vacuum tank. Power is then applied to two pairs of adjacent electrodes connected in series and proper terminations ensure that the lack of resistor in the power splitter does not result in adverse reflections. Electrical delays match the time of flight to give a maximum of the shut impedance at the beam momentum the structure was originally optimized for (3.57 GeV/c). Power is dissipated in 12 RF loads mounted on the side of the rail opposing the beam. Damping of higher order and propagating modes in the structure is achieved by ferrite tiles attached to two rails in the plane perpendicular to the electrodes.

The rails supporting the electrodes can be moved, however this movement is no longer used for the case of the kickers since LS1 (2014) and the mechanism has been blocked in the position giving the maximum acceptance for the beam. In addition to reducing the operational complexity, the suppression of the kicker movement also renders the performance less sensitive to beam position as the region of homogeneous field is larger with jaws open. Additionally, final smaller

---

* Wolfgang.Hofle@cern.ch

emittances were achieved in the past during routine operation with the jaws of the kicker kept fully open. These advantages outweigh the faster cooling times that would be possible with moving jaws and perfect adjustments of orbit. Sufficient power is available and the cycle length is designed to allow for the somewhat slower cooling times with the open jaws.

For the pick-up the movement is still used, closing the electrodes to increase sensitivity as the beam is transversely cooled at 3.57 GeV/c, and electrodes are closed for the cooling at 2 GeV/c. Water cooling has been originally only applied to the electrodes supporting the RF loads. However, when the equipment originating from the CERN AC machine was recommissioned as part of the AD machine in 1999 water cooling got added to the rails supporting the ferrite tiles, presumably related to vacuum specifications that called for an improvement that could be compromised by outgasing of the ferrites. Therefore the presently installed kicker tanks each feature four water cooling circuits two of which do not form part of the original construction documentation from the 1980's.

One of the cooling circuits in the horizontal kicker tank developed a leak during bake-out in the early years of operation of the AD in 2001. It was at the time in-situ repaired by injecting a resin (araldite) into the circuit. Twenty years later in 2021 a similar leak developed on the same horizontal tank on the cooling circuit of the opposing electrode following the bake-out needed at the end of LS2. The leak could again be repaired in spring 2021 using the same procedure as 20 years ago. This event of 2021 demonstrates the fragility of the system in case a future bake out is required for one of the kicker tanks. It also motivates, combined with a lack of a spare, the launch of a study to construct full spares of improved design. Apart from mechanical improvements the study can also review and explore the electromagnetic and RF design. In particular in view of today's usage of the cooling system on a second plateau at a beam momentum of 2.0 GeV/c, for which the structure was originally not optimised, improvements might be possible. Consolidation of the power amplifier system will need to wait until the results of the study show which path for consolidation should be taken. Alternative paths could leverage on developments of kickers for similar systems under study or construction for FAIR at GSI in Germany [3], NICA at JINR in Dubna, Russia and HIAF in China [4].

For the pick-ups, the signals of all individual electrodes of a super-electrode are combined within the vacuum tank. The required termination resistors of the combiners inside the pick-up are cooled by conduction using gaseous He from a cryo pump. Instrumentation inside the tank is insufficient to precisely determine the relevant equivalent noise temperature to use in a simulation of the cooling process. Outside the pick-up tank a set of two low noise amplifiers in series per electrode amplify the signal before it is combined in a hybrid to yield the transverse and longitudinal signal for beam cooling.

The homogeneous region of the field in the center is limited to a small area for both pick-up and kicker. The limited possibilities of adjusting for a displaced orbit, and for ensuring in the system a perfect symmetry between the two sides of both pick-up and kicker electrodes, represent an operational challenge to keep high cooling efficiency. Increasing the means to compensate for these effects electronically, represents an option for future consolidation of the equipment.

Layout and Optics for Stochastic Cooling at 2 GeV/c and 3.57 GeV/c

The two pairs of pick-up and and kicker are installed in locations opposing each other in the ring. For a ring circumference of 182.43 m the beam orbit length between pick-up to kicker and kicker to pick-up amounts to ~ 91.22 m in length. For the two cooling plateaus (2 GeV/c and 3.57 GeV/c) the beam β equals 0.90532 and 0.96724, respectively, giving time of flights of 336 ns and 314 ns. The time of flight difference of ~ 22 ns must be properly compensated when switching between the two plateaus. Implementation of the switching is by means of RF relays controlled by a PLC system and with the total delay difference split into several parts located along the signal chain. Table 1 shows the values for the transverse tune and phase advances from pick-up to kicker. Phase advances deviate by less than 20° from the optimum value for transverse cooling. In an open loop beam transfer measurement this deviation will be visible in a Nyquist plot as a rotation of the circles corresponding to the lower and upper betatron side bands in the opposite sense [5]. During setting-up of the system this can be discriminated from an error of the delay in the system which will rotate these circles in the Nyquist plot in the same orientation sense. While the delay can be easily adjusted remotely in the system, no means to adjust for the phase advance are presently used. In the past, a comb filter was used to make an adjustment possible. This filter used a resonant line. However, such a filter achieves the phase advance adjustment by adding to the directly transmitted signal a delayed signal that will increase the undesirable mixing from pick-up to kicker.

Table 1: Optics Parameters Transverse Cooling in AD

horizontal tune Q_H	5.385
Phase advance from H pickup to H kicker	256°
vertical tune Q_V	5.369
Phase advance from V pickup to V kicker	283°

Acceptance and Initial Conditions for Stochastic Cooling at 3.57 GeV/c

The longitudinal acceptance of the AD machine is quoted to be ±3 % in relative momentum $\Delta p/p$ corresponding to ±111 MeV in energy with an almost flat distribution used in a preliminary simulation of the bunch rotation [6] in line with previous experience [7]. In the same preliminary study a bunch length of 35 ns was used (2σ, parabolic distribution) yielding after rotation an energy spread of 16.86 MeV rms with no particles outside ±45 MeV for an optimised voltage program of the 10 MHz bunch rotation system respecting the limits of this system. Studies are needed to confirm the previously quoted acceptance of the stochastic cooling system in the range of ±0.5 % to ±1.0 % in $\Delta p/p$. In principle these parameters are experimentally accessible by comparing the time evolution of Schottky spectra and losses in different combinations of machine conditions with bunch rotation "off", "on" and stochastic cooling "off" and "on". Future studies are expected to be made easier by an improved Schottky diagnostics system. The procedure to align the two bunch rotation cavities in phase with respect to each other and the incoming beam is outlined in [8] and an important pre-requisite for efficient stochastic cooling.

PREPARATIONS FOR 2021 RUN AND SHUTDOWN WORK

Power Amplifiers

Power amplifiers had the usual maintenance during the long shutdown 2 and reference measurements saved for each re-installed amplifier. These 100 W amplifiers feature 40-41 dB gain at a mean delay of 10.5 ns in the frequency range of 600 MHz to 1.8 GHz (-3dB). The variation of phase from the mean delay is very flat in the pass band (±5°). This and the smooth role-off of gain at the lower and upper limits of the pass band is essential for efficient cooling. Any signal fed back at the edges of the band and out-of-band with the wrong phase will counteract cooling and lead to hidden heating. During operation in 2021 several amplifiers showed repeated issues and needed to be disabled. When possible, pairs of amplifiers feeding opposing parts of the structure are disabled to keep the kicks as homogeneous as possible. With the recovering of more spare amplifiers it is expected to start 2022 operation with all 48 amplifiers fully operational. Additional interlocks have been added to protect against the case of compromised water cooling for both the final 100 W amplifiers and their drivers.

Kickers

During the dismantling of the installation at the start of LS2 in 2018 all RF lines connecting amplifiers to the kicker tanks as well as the matching of the loads in the kicker tank have been checked by RF time domain reflectometry. Figure 2 shows as an example a typical measurement in-situ on one of the lines with the end reflection of -17.7 dB representing the matching of the load. A faint DC current is used to detect the presence of the loads and interlock the RF power. The circulator which protects the amplifier from reflected power was removed for these measurements. Visible in the measurement are also imperfections on the line by the discs supporting the inner conductor and reflections from joints and connectors. All reflections are below -25 dB. A number of bad contacts with higher reflection were identified and corrected as part of the program during LS2.

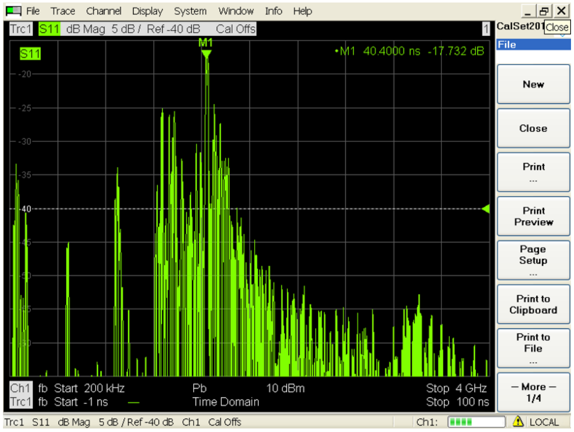

Ch1 fb Start 200 kHz Pb 10 dBm Stop 4 GHz
Trc1 fb Start -1 ns Time Domain Stop 100 ns
Trc1 S11 dB Mag 5 dB / Ref -40 dB Ch1 Cal Offs Ch1: LOCAL

Figure 2: RF reflectometry on an RF line connecting the power amplifier to the kicker tank.

Controls

Controls is provided by a PLC system that was also upgraded to a more modern version during LS2. It will allow for the future to add more remote control functionality. This system needed commissioning of all its newly wired hardware, and the different layers of the control system in parallel to RF measurements and commissioning.

Optical Delay Notch filter and Automizing of the Hardware Transfer Function (HTF) Measurement

The optical delay line notch filter had been tested successfully pre-LS2 [9] and was recommissioned with an add on to monitor and adjust its transfer function automatically. In segments of the AD cycle without beam a network analyzer sweeps in frequency to verify the transfer function of the longitudinal branch, checking the position of notches and applies a correction if a deviation is noticed by the system. Once commissioned at 3.57 GeV/c the optical notch became the operational system and provided excellent stability over the year. It is now planned to extend the system to 2 GeV/c and to evolve the transfer function measurements towards also automatically measuring beam transfer functions.

Figure 3 as an example shows how over a period of ~four weeks the system kept the notch frequency of the 1000th revolution harmonic in the longitudinal cooling branch at 3.57 GeV/c within 2.5 kHz of the target frequency of 1.589411 GHz. The variation of programmed delay required to keep the stability in this one month period was 10 ps approximately and the notch depth remained better than -30 dB on average.

START-UP WITH BEAM

Following verification of all hardware transfer functions the beam time required for bringing back the system in operation was spread over three weeks in Summer 2021. The principle challenge was to find back the correct settings for the delay, matching time of flight between pick-up and kicker. This can done by measuring beam transfer functions

ISBN: 978-3-95450-243-1 ISSN: 2226-0374 doi:10.18429/JACoW-COOL2021-S302

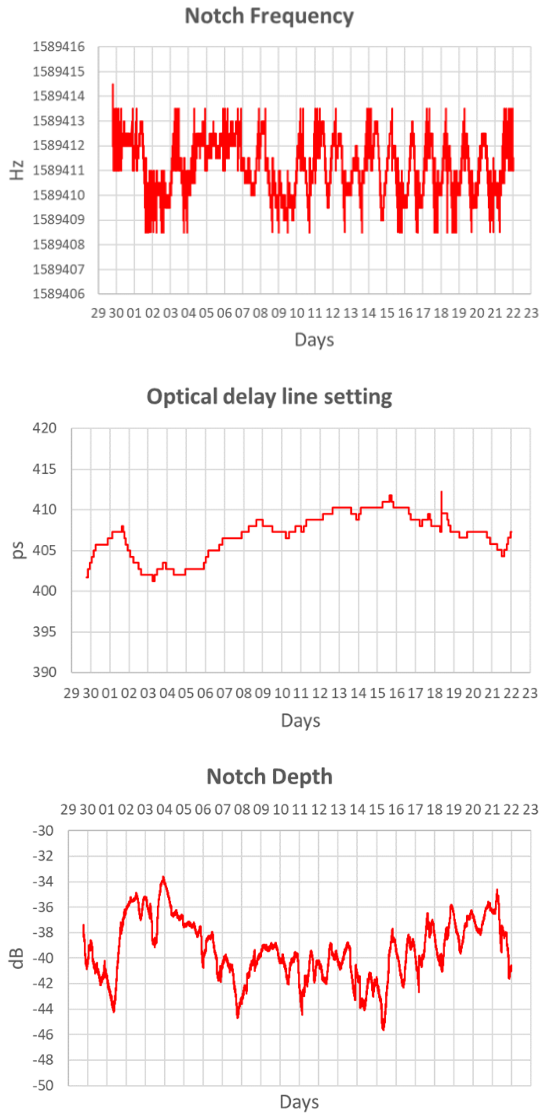

Figure 3: Notch frequency at 1000th harmonic, notch depth and programmed delay to keep stability over a period of ~four weeks from 29.09.2021 to 23.10.2021.

in multiple narrow bands each covering a few revolution harmonics. In order to get clean measurements additional low-noise pre-amplifiers were used at the network analyzer input. The cooling loops can be remotely opened to do the measurement following a calibration of the signal cables from the AD control room to the installation. The amplitude response over the frequency range of interest shows that the overall system has gain between 900 MHz and 1.8 GHz at 3.57 GeV/c with -3 dB points at approximately 1.1 GHz and 1.5 GHz. The complex response can be displayed as Nyquist plot. Here the relevant circles must be oriented towards the negative real axis for stability of the closed loop that also corresponds to optimum damping [5].

The measurements in the longitudinal plane are carried out with the long line of the notch filter disabled and only the short direct signal path left in place. Figure 4 shows an example of the plots used to adjust the delay in the horizontal plane. The top plot shows the amplitude response with significant contributions at the revolution harmonics in addition to the response at the betatron frequencies. A frame of 5 MHz width is shown covering four revolution harmonics with six betatron sidebands. The unwanted signal at the revolution harmonics is due to the imperfect cancellation in the hybrid of the orbit component and its excitation by asymmetries. Improvements are possible by ensuring that only transverse motion is excited and by making the hardware adjustable to achieve a better suppression of the orbit. The beam orbit itself must be kept within the homogeneous field region and should ideally be physically centered in the structures both of the pick-ups and kickers. The Nyquist plot shows the correct orientation of circles of the betatron side bands. For the case that the undesired longitudinal response has a wrong orientation, there will be a contribution that heats the beam longitudinally. This is a general observation that in the sequence of setting-up first the longitudinal system must be commissioned as it is needed to counteract the longitudinal heating introduced by the transverse systems.

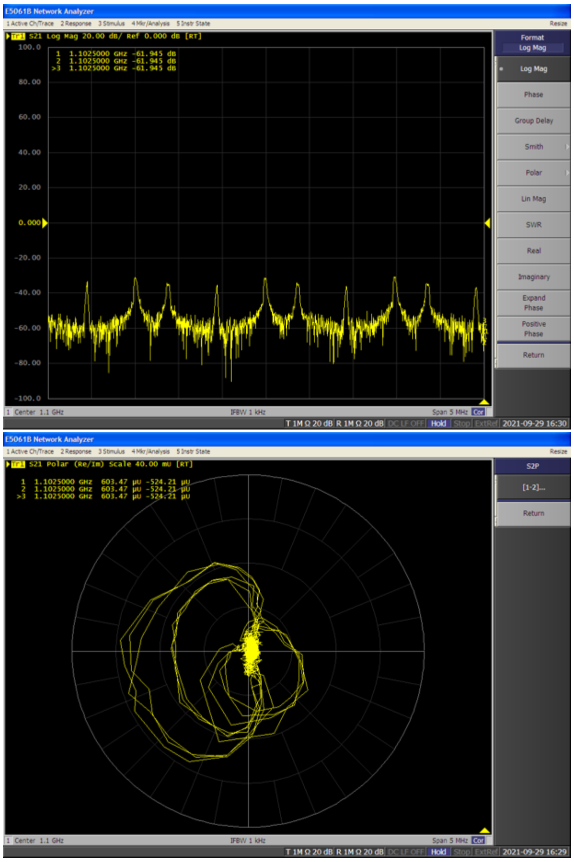
```
Tr1 S21 Log Mag 20.00 dB/ Ref 0.000 dB [RT]
 1  1.1025000 GHz -61.945 dB
 2  1.1025000 GHz -61.945 dB
>3  1.1025000 GHz -61.945 dB
```

```
Tr1 S21 Polar (Re/Im) Scale 40.00 mU [RT]
 1  1.1025000 GHz  603.47 µU -524.21 µU
 2  1.1025000 GHz  603.47 µU -524.21 µU
>3  1.1025000 GHz  603.47 µU -524.21 µU
```

Figure 4: Beam transfer function in open loop, horizontal system at 3.57 GeV/c at 1.1 GHz.

PERFORMANCE WITH BEAM

Longitudinal Plane

Figure 5 shows the longitudinal cooling achieved at 3.57 GeV/c on the left side and 2 GeV/c on the right side. Cooling in both cases was re-established and permitted deceleration of the beam to the next plateau. The good results at 3.57 GeV/c and the stability obtained with the described HTF monitoring and adjustment justifies to introduce this technology also to the cooling at 2 GeV/c as soon as the hardware will be ready.

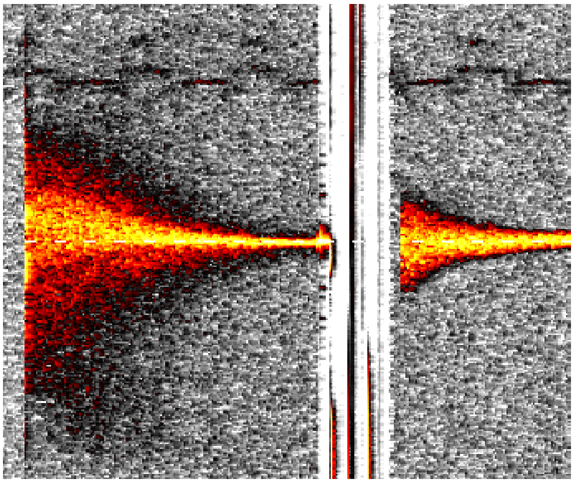

Figure 5: Stochastic Cooling at 3.57 GeV/c (left) and 2 GeV/c (right).

Transverse Cooling

Transverse Cooling is somewhat more demanding to set-up as Schottky diagnostics is not available in AD for the transverse plane. The emittances before and after cooling can be measured by a scraper system to confirm by how much the emittances are reduced by the cooling. Without transverse cooling losses are also visible during deceleration and can serve as an observable for optimization.

Following recommissioning, cooling at 3.57 GeV/c in the horizontal plane was re-established faster than at 2 GeV/c with ~20-fold reduction in emittances from 230π mm mrad to 10π mm mrad (H-plane) and 12π mm mrad (V-plane). At 2 GeV/c the 2021 experience is that the system performs less well than before LS2 with emittances reduced in the H-plane from 18.5π mm mrad to 12.6π mm mrad and in the V-plane from 28.9π mm mrad to 15.8π mm mrad. These post-LS2 values cannot be readily be compared with pre-LS2 values due to changes in the scraper system and the analysis software used. Further studies are required to confirm the performance and to find the handles to improve in particular the cooling at 2 GeV/c.

Transmission

Figure 6 shows the re-established AD cycle with the first two plateaus with stochastic cooling and the second two plateaus at 300 MeV/c and 100 MeV/c where electron cooling is used [10]. Losses remain prominent on the 3.57 GeV/c where the handover between bunch rotation system and stochastic cooling system deserves more scrutiny. Losses during re-capture and deceleration are very small and thanks also due to the excellent performance of the new digital LLRF system [11].

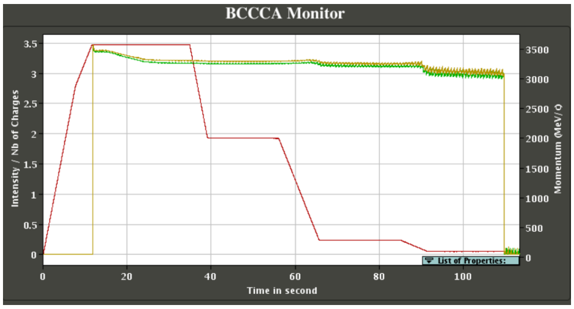

Figure 6: AD cycle with good transmission after LS2.

CONCLUSION

The stochastic cooling power system of AD was completely dismantled during the CERN long shutdown 2 (LS2) and required a substantial effort to recover an acceptable performance in 2021. A vacuum leak on the horizontal tank water cooling circuit was successfully repaired. The start-up with beam in Summer 2021 took longer than expected with settings for the delays that had to recovered from scratch without a well established procedure from past years. There remains margin to improve the performance of the transverse cooling at 2 GeV/c. The experience gained during the start-up will guide studies in the following years to better characterize the system and identify areas that need further improvement to boost performance in future years.

ACKNOWLEDGEMENT

The authors would like to thank their colleagues from SY-RF, BE-OP, TE-VSC, TE-MSC, EN-MME and EN-CV who have helped during the recommissioning of the system and the necessary repair and maintenance work and who have given advice during LS2.

REFERENCES

[1] P. Belochitskii *et al.*, “Commissioning and First Operation of the Antiproton Decelerator AD”, *in proc. PAC’01*, Chicago, Ill., USA, June 2001, pp. 580–584.

[2] F. Caspers and C. Carli, “Stochastic Cooling at the CERN Antiproton Decelerator”, *in proc. EPAC2000*, Vienna, Austria, 2000, pp. 2014–2016.

[3] C. Dimopoulou, “Stochastic Cooling System for the Collector Ring at FAIR”, *in proc. of COOL’21*, Novosibirsk, November 2021, paper S301, these conference.

[4] G. Zhu *et al.*, “Stochastic Cooling Pickup/Kicker Developments for the High-precision Spectrometer Ring in the HIAF Project at IMP”, *IEEE Trans. Nucl. Sci.*, Vol. 68, No. 1, January 2021, pp. 9–20.

[5] H. Stockhorst, T. Katayama, R. Maier, "Beam cooling at COSY and HESR, Part 1 Theory", *Schlüsseltechnologien*, Volume 120, Forschungszentrum Jülich, Jülich,2016. https://juser.fz-juelich.de/record/807739

[6] S. Albright, *private communication*, CERN, Geneva, 2021.

[7] M. E. Angoletta et al., "Experience with antiproton stacking at injection energy in CERN's AD, CERN-ACC-Note-2019-0025, CERN, Geneva, 2019.

[8] S. Albright, "A Method for Aligning the Phases of C10 Cavities in the AD", CERN-ACC-NOTE-2021-0026, CERN, Geneva, 2021.

[9] F. Caspers *et al.*, "First Operation for Stochastic Cooling of P-Bars in the CERN AD using Optical Delay Notch Filter and Plans for 2021 Operation", 12th Workshop on Beam cooling and Related Topics (*COOL'19)*, Novosibirsk, Sep.2019 doi:10.18429/JACoW-COOL2019-MOY01

[10] D. Gamba *et al.*, "AD/ELENA electron cooling experience during and after CERNs Long Shutdown (LS2)", *in proc. of COOL'21*, Novosibirsk, November, 2021, paper S503, these conference.

[11] M. E. Angoletta *et al.*, "A New Digital Low-Level RF and Longitudinal Diagnostic System for CERN's AD", *in proc. of IPAC'19*, Melbourne, Australia, 2019, pp. 3966–3969. doi:10.18429/JACoW-IPAC2019-THPRB070

ELECTRON COOLER OF THE NICA BOOSTER AND ITS APPLICATIONS

S.A. Melnikov†, I.N. Meshkov, E.V. Ahmanova, A. A. Baldin, A.V. Butenko, I. V. Gorelyshev, A.G. Kobets, D. S. Korovkin, O.S. Orlov, K.G. Osipov, A.V. Philippov, S.V. Semenov, A.S. Sergeev, A.A. Sidorin, A.O. Sidorin, E.M Syresin,
Joint Institute for Nuclear Research, Dubna, Russia

Abstract

The report presents the results obtained during the commissioning the Electron Cooling System (ECS) of the Booster, the first in the chain of three synchrotrons of the NICA accelerator complex. The work was performed with a circulating ion beams $^{4}He^{1+}$ and $^{56}Fe^{14+}$ at ion injection energy of 3.2 MeV/u. In the first experiment (December 2020) with a circulating $^{4}He^{1+}$ ion beam, the effect of reducing the lifetime of the circulating ions was observed when the velocities of the cooling electrons and the cooled ions coincide. In second experiment (September 2021) the effect of electron cooling of $^{56}Fe^{14+}$ ion beam was registered both for longitudinal and transverse degrees of freedom using Schottky noise spectrometer and ionization profilometer.

INTRODUCTION

The main tasks of the Booster synchrotron of heavy ions are the accumulation of gold ions or other low-charged heavy ions and their acceleration to the maximum energy 578 MeV/u for gold ions, which is sufficient for their subsequent stripping to the state of bare nuclei. The application of electron cooling in a Booster at ion energy up to 65 MeV/u makes it possible to significantly reduce the 6D emittance of the beam.

NICA BOOSTER ELECTRON COOLING SYSTEM (ECS)

The Booster ECS (Fig. 1) was constructed according to the classical scheme proposed and implemented in 1970 in the Institute of Nuclear Physics (Novosibirsk) [1]. Its present version is significantly developed by the team of V. V. Parkhomchuk in the same Institute named after the founder academician G.I.Budker. In electron cooling set-up, an electron beam passes from the cathode of the electron gun to the collector in a uniform longitudinal magnetic field. In the ECS, the homogeneity of the magnetic field of this solenoid is made at the level of $3{\cdot}10^{-5}$ (straightness of the magnetic field line) that provides the design value of the cooling time. The energy of the ECS electrons variates in this range from 1.0 to 50.0 keV. The main Booster ECS parameters are shown in the Table 1.

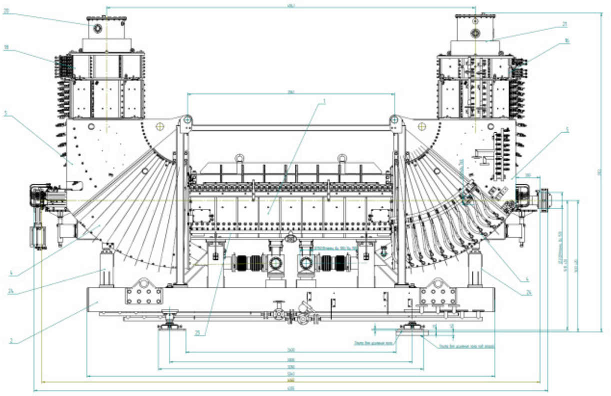

Figure 1: The Booster ECS scheme.

Table 1: The main Booster Electron Cooling System Parameters

Parameter	Value
Electron energy E, keV	≤ 1
Accuracy of energy adjustment and its stability, ΔE/E	$\leq 1{\cdot}10^{-5}$
Beam current stability, ΔI/I	$\leq 1{\cdot}10^{-4}$
Electron beam loss current, δI/I	$\leq 3{\cdot}10^{-5}$
The strength of the ECS longitudinal magnetic field, kGs	1 – 2
Permissible inhomogeneity of the longitudinal magnetic field in the cooling area, ΔB/B	≤ 3·10-5 on the length 15 cm
Transverse temperature of electrons in the cooling section (in the particle system), eV	≤ 0.3
Correction of the ion orbit at the input and output of ECS	offset, mm ≤ 1,0 angular deviation, mrad ≤ 1,0

FIRST ION ELECTRON COOLING EXPERIMENT

During the first Booster session in December 2020, an experiment was conducted to commission the ECS with a circulating $^{4}He^{1+}$ helium ion beam with an energy of 3.2 MeV/u (injection energy into the Booster) (Table 2). In this experiment the only diagnostic devices that allowed observing the cooling effect were used: a parametric current transformer (PCT) measuring ion beam current and the A. A. Baldin ionization profilometer [2], that was operated in summing mode the counting rate of all the MCP channels

---

†smelnikov@jinr.ru

registering the vertical distribution of the beam density (relative counts – RC), and the time dependence RC(t) was measured. Then the results were summed over several injection cycles ⟨RC(t)⟩ (Fig. 2).

Table 2: First Ion Electron Cooling Experiment Parameters

Parameter	Value
Ion type	$^4He^{1+}$
Ion energy, MeV/u	3.2
Electron energy, keV	1.73 – 1.8
Electron beam current, A	0.1 – 0.2
Electron beam diameter, mm	28

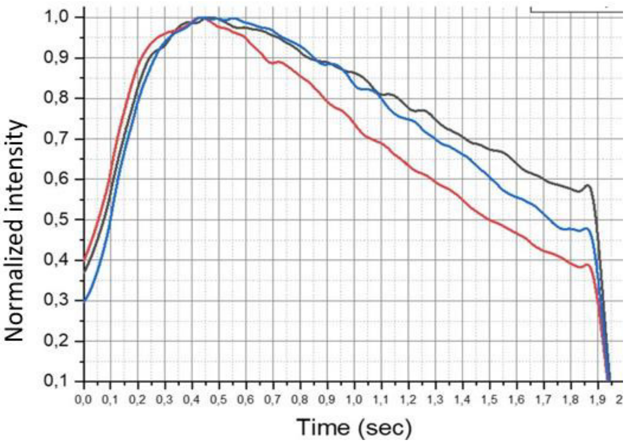

Figure 2: Normalized intensity for different electron energy. Black curve – 1.82 keV, blue curve – 1.72 keV, red curve – 1.76 keV.

As can be seen from figure 2, the strong decrease in the lifetime of the ion beam occurs at the energy 1.76 keV, which is in good agreement with the theoretical value. The optimal (theoretical) value of the electron energy is equal to $E_e = \frac{m_e}{m_n} E_{ion}$. For E_{ion}=3.2 MeV it gives E_e=1.754 keV, what is different from 1.76 keV by the ≈5.7 V, or 0.3%.

SECOND ION ELECTRON COOLING EXPERIMENT

During the second run of the Booster in September 2021, an experiment was conducted to electron cooling of iron ion $^{56}Fe^{14+}$ beam circulating at injection energy of 3.2 MeV/u (Table 3). A Schottky spectrometer was used as the device detecting beam momentum spread, as well as a horizontal and vertical profilometers used during first experiment.

Table 3: Second Ion Electron Cooling Experiment Parameters

Parameter	Value
Ion type	$^{56}Fe^{14+}$
Ion energy, MeV/u	3.2
Electron energy, keV	1.73 – 1.93
Electron beam current, A	0.02 – 0.13
Electron beam diameter, mm	28

Unfortunately, at high intensities of the ion beam the channels of the profilometer were overloaded and the signal could not be received from it. On the other hand, at low intensities the signal from the Schottky spectrometer was too weak. Also, it is possible to register the signal from the pickup stations in the Electron Cooling System about the position of the ion beam only when the RF is turned on. The cooling itself took place on a continuous beam. Therefore, the experiment was carried out as follows: the ion beam was injected at maximum intensity when the RF was turned on, and the beams were exposed in parallel and as close as possible to each other, after this the RF was turned off and the signal was registered from the Schottky spectrometer. Then the intensity was lowered, and the transverse sizes of the beam were measured from a profilometer.

Longitudinal Cooling Measurements

Spectrum measurements were carried out using a Schottky spectrometer at the 4th harmonic of the revolution frequency. The frames received from the detector were digitized and linearized (Fig. 3) for further processing.

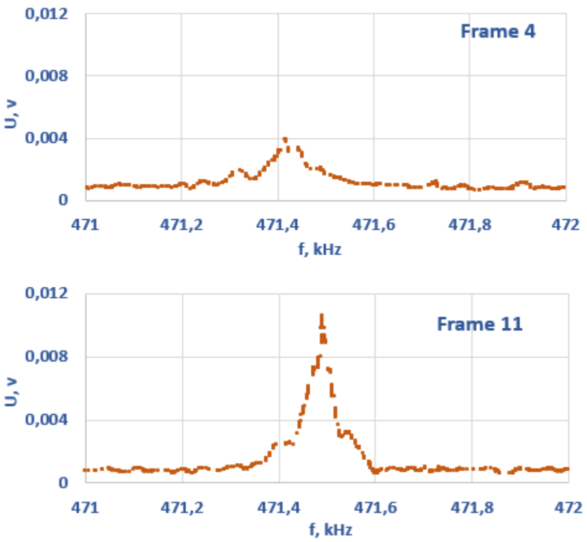

Figure 3: Schottky spectrometer signal. Frame 4 shows the signal at a time of 0.6 sec from the beginning of injection, frame 11 – 2 sec from the beginning of injection.

As can be seen from Fig. 3 and Fig. 4 the frequency of spectrum maximum during one injection and circulation cycle is changing and increasing with time, which indicates the compression of the beam orbit, which will also be shown on the data from the ionization profilometer.

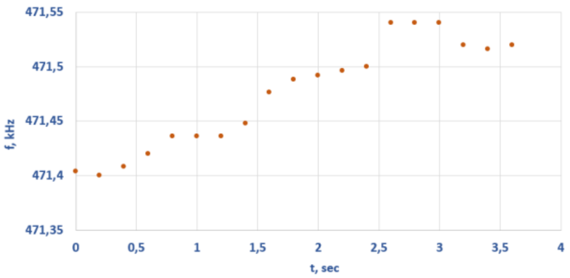

Figure 4: Spectrum maximum versus time.

For the resulting set of frames, the full width of the signal at half its magnitude was measured, after that the values were converted to the values of the momentum spread (Fig. 5).

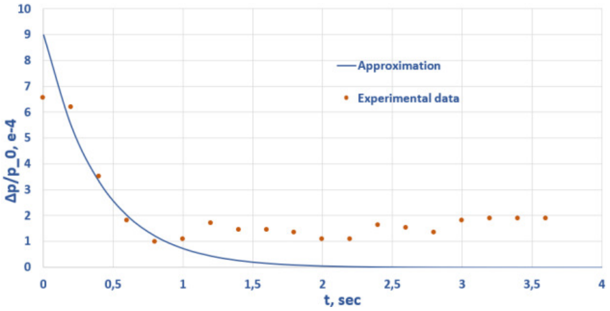

Figure 5: Momentum spread versus time.

Here, the dots show experimental data that were approximated by an exponential function, from which the characteristic cooling time of the ion beam momentum spread rms value, equal to 200 milliseconds, was obtained.

Transversal Cooling Measurements

After receiving the signal from the Schottky spectrometer, the intensity of the ion beam was reduced, which made it possible to receive a signal from the ionization profilometer. As can be seen from Fig. 6, initial transvers dimensions of the ion beam (one sigma) with the electron beam turned off equal to 9 mm and 10.5 mm for horizontal and vertical degrees of freedom, respectively. In addition, it is important to note that in the horizontal direction the ion beam is strongly shifted to the outer edge of the beam tube.

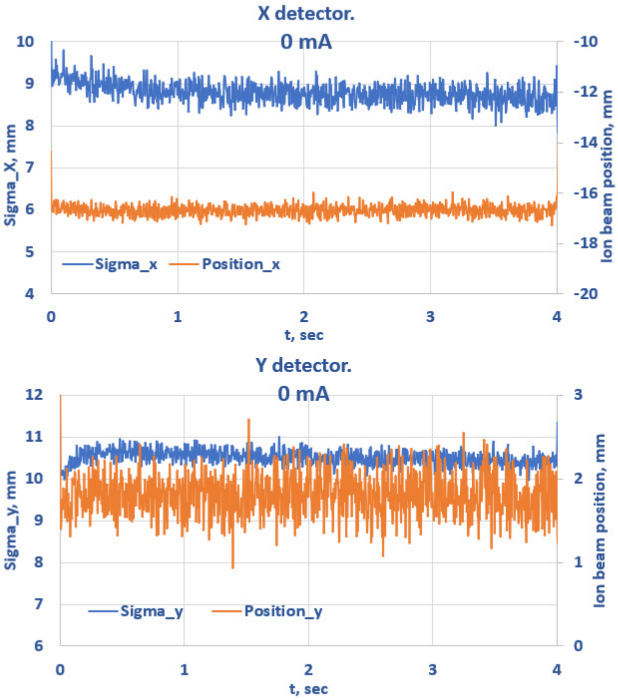
X detector.
0 mA

Y detector.
0 mA

Figure 6: Ion beam transvers dimensions (blue curve) and ion beam axis coordinates (orange curve) in the profilometer with the electron beam turned off.

At first, the electron beam energy values were set close to the optimal theoretical value of 1.75 keV at an electron current of 46 mA (Fig. 7).

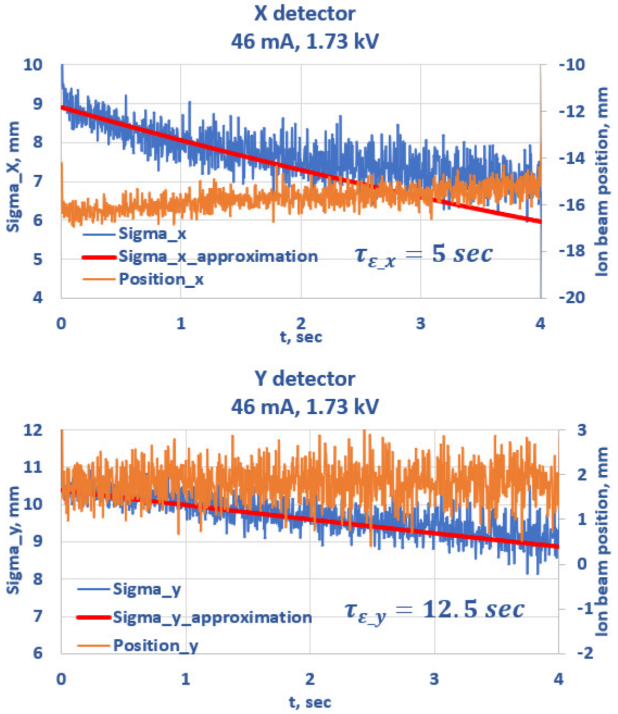
X detector
46 mA, 1.73 kV

Y detector
46 mA, 1.73 kV

Figure 7: Ion beam transvers dimensions (blue curve) and ion beam axis coordinates (orange curve) in the profilometer with the electron beam current 46 mA and energy 1.73 keV.

According to the Fig 7, it can be noticed that the cooling time is very long both horizontally and vertically (5 sec and 12.5 sec respectively). This was because the fact that the beams were not aligned, and they were separated from each other by some distance, and, accordingly, there was a sagging of the electron beam potential along the radius (Fig. 8).

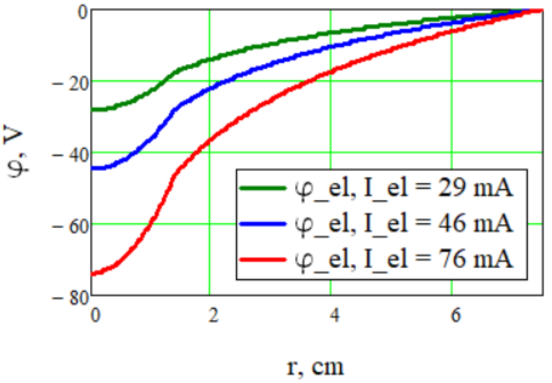

Figure 8: Electron beam potential sagging along the radius (electron beam radius equal to 1.4 cm) for different currents.

So long as RF was turned off and it was not possible to correct the orbit of the ion beam in the cooling section, it was decided to adjust the energy of the electron beam. The main problem here was that the potential change at the cathode is possible only in steps of 10 volts, which is a very large value for an energy of 3.2 MeV/u. Therefore, in addition to changing the cathode potential, the current also was changed.

The best results for a current of 46 mA were obtained at an energy of 1.83 keV (Fig. 9) – cooling time for horizontal degree of freedom varies from 2 to 4 sec and for vertical, equal to 5 sec, thus the difference between experimental and theoretical values amounted to 80 volts.

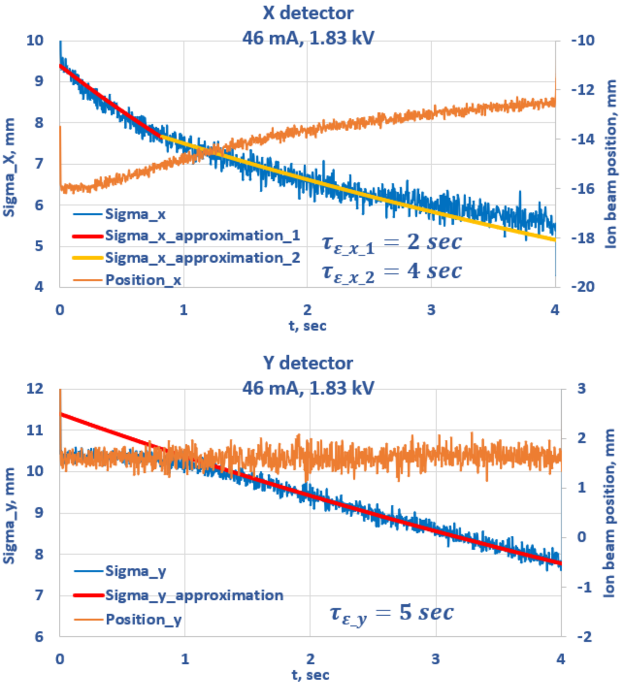

Figure 9: Ion beam transvers dimensions (blue curve) and ion beam axis coordinates (orange curve) in the profilometer with the electron beam current 46 mA and energy 1.83 keV.

This energy difference is approximately preserved at other electron beam currents. The best cooling times obtained for other values of the electron beam are shown in the Table 4.

Table 4: Transversal Cooling Times for Different Values of Electron Beam

I, mA	W, keV	τx, sec	τy, sec
29	1.81	4	14
46	1.83	2	5
76	1.86	3	4

Hence, it can be concluded that the electron and ion beams axes were far enough apart from each other, therefore the ion beam moved under action of electron cooling force.

DEVELOPMENT OF THE PARKHOMCHUK FORMULA

Due to the strong discrepancy between the theoretical and optimal experimental energy of the electron beam, it was decided to add to the classical Parkhomchuk formula for the friction force dependence on:

- sagging of the electron beam potential resulting in increase of the difference of electron and ion velocities, which significantly exceeds the velocity spread due to flattened distribution;
- effect of the drift velocity in the crossed longitudinal magnetic field and electric field of the electron beam

$$v_d(I_{el},\,r) = \gamma \cdot c \frac{E_{el}(I_{el},r)_{\left[\frac{V}{cm}\right]}}{300 \cdot B_{[G]}}. \tag{1}$$

Considering these corrections, the total transverse and longitudinal velocities are now determined by the expressions

$$V_{x,y}(I_{el},r) = \\ = \sqrt{V^2_{Ion_{x,y}} + \Delta^2_{el_{x,y}} + \frac{v_d(I_{el},\,r)^2}{2} + (\gamma V_0 \vartheta_B)^2} \\ V_s\left(\frac{dp}{p}, I_{el}, r\right) = \sqrt{V^2_{Ion_s}\left(\frac{dp}{p}\right) + \Delta v^2_{el_s}(I_{el},\,r)}, \tag{2}$$

where Δv_{el_s} – difference between the longitudinal velocities of the ions and the electrons, determined by the expression

$$\Delta v_{el_s} = \left(\sqrt{2\frac{U_{cath} - U(I_{el},r)}{m_{el}}} - \beta_{ion}\right)c. \tag{3}$$

Expression under the root is the longitudinal electron velocity, which depends on the voltage at the cathode and on the potential sagging along the electron beam radius. The friction force can now be written as follows

$$F_{x,y}\left(\frac{dp}{p}, I_{el}, r\right) = q_{el} V_{Ion_{x,y}} \cdot \Big[(V_x(I_{el},r) + \\ \gamma V_0 \vartheta_B)^2 + \left(V_y(I_{el},r) + \gamma V_0 \vartheta_B\right)^2 + \\ V_s\left(\frac{dp}{p}, I_{el}, r\right)^2\Big]^{-\frac{3}{2}} \cdot \ln\left(1 + \frac{\rho_{\max\left(\frac{dp}{p}, I_{el}, r\right)}}{\rho_L + \rho_{\min\left(\frac{dp}{p}, I_{el}, r\right)}}\right). \tag{4}$$

Then the formulas for the cooling decrement and the corresponding emittance cooling time will take the form

$$D_{x,y}\left(\frac{dp}{p}, I_{el}, r\right) = \frac{F_{x,y}\left(\frac{dp}{p}, I_{el}, r\right) \cdot c^2}{AmV_{Ion_{x,y}}}; \tag{5}$$

$$\tau_{emit_{x,y}} = \frac{1}{2}\frac{\gamma}{\eta} D_{x,y}\left(\frac{dp}{p}, I_{el}, r\right)^{-1}. \tag{6}$$

Since the electron beam is magnetized, the collision of an electron with an ion can be considered as an absolutely elastic collision. For this reason, the transverse temperature of the electrons was chosen to be zero.

With an increasing in the electron current, a competition of micro and macro interactions can be observed:

- increasing in the sagging potential, which leads to an increase in the difference in the longitudinal velocities of ions and electrons, as a result decreasing of the friction force (Fig. 10).
- increasing in the electron density, which leads to an increase in the friction force (Fig. 11).

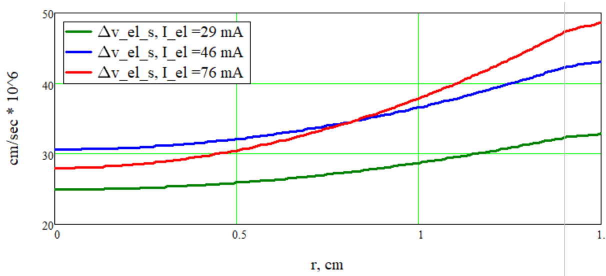

Figure 10: The difference between the longitudinal velocity of electrons and ions vs radial coordinate.

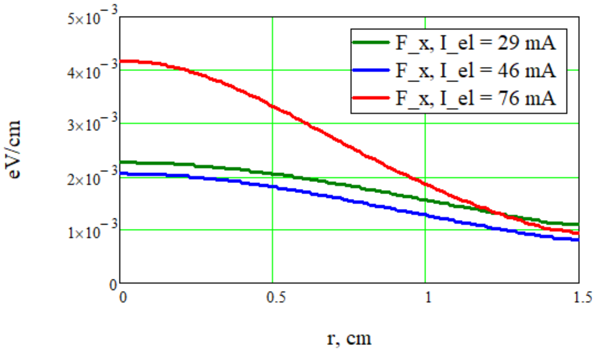

Figure 11: Horizontal friction force vs radial coordinate for dp/p=6e-4.

As the electron current increases, the influence of the space charge increases as well, and the cooling time increases first (Fig. 12, green and blue curves). But with a further increase of the current, the influence of the friction force growth begins to prevail over the influence of the longitudinal velocity spread. Therefore, cooling time decreases significantly (blue and red curves).

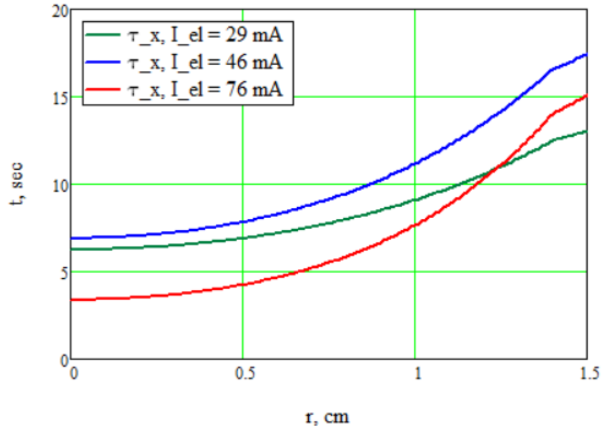

Figure 12: Horizontal emittance cooling time vs radial coordinate for dp/p = 6e-4.

CONCLISIONS

Electron cooling of heavy ions at injection energy (3.2 MeV/u) is of practical interest, because it makes it possible to use multi-turn or multiple injection. The peculiarity of low energy electron cooling is strongly influenced by the space charge of the electron beam. In this case well known Parkhomchuk formula needs appropriate correction.

REFERENCES

[1] V.I.Kudelainen, I. N. Meshkov, and R.A.Salimov., “Commissioning of the set-up for electron cooling experiment”, Preprint of G.I.Budker INP, Novosibirsk, USSR, vol. 72-70, 1970.

[2] A. A. Baldin *et al.*, “Non-destructive diagnostics of accelerated ion beam with MCP-based detectors at the NICA accelerator complex. Experimental results and prospects”, in *Proc. 27th Russian Particle Accelerator Conf. (RuPAC’21)*, Alushta, Russia, Sep. 2021, paper WED05.

13th Workshop on Beam Cooling and Related Topics COOL2021, Novosibirsk, Russia JACoW Publishing
ISBN: 978-3-95450-243-1 ISSN: 2226-0374 doi:10.18429/JACoW-COOL2021-S501

SCALABLE HV-MODULES FOR A MAGNETIZED RELATIVISTIC ELECTRON COOLER

K. Aulenbacher*,[1], J Dietrich, W. Klag,
Helmholtz Institut Mainz, Germany
[1] also at GSI Helmholtzzentrum für Schwerionenforschung, Darmstadt, Germany

Abstract

At HIM in Mainz the test setup for the magnetized relativistic cooler is progressing. The first 600 kV module at 1:1 scale for the HESR-cooler has been installed in its pressure tank. Our goal is to show the scalability of the approach aiming at stacking 13 modules in the final version at HESR. Plans for the near future are reported. Ideas for converting the prototype into an experimental facility are presented.

INTRODUCTION

Research at Helmholtz Institute Mainz (HIM) is aiming to resolve technical challenges that are related to high energy electron cooling, in particular connected to a possible relativistic magnetized electron cooler for the High Energy Storage Ring HESR at FAIR. An electron kinetic energy of almost 8 MeV would be required, which exceeds the voltage of the Jülich cooler [1] considerably, which is currently the cooler with the largest voltage and magnetized beam. In cooperation with BINP we have proposed a modular concept based on high voltage platforms, each delivering a potential of 600 kV. The floating electric power is provided by 5 kW turbo-generators which supply the solenoids and auxiliary devices such as electron source, collector or vacuum pumps. A first module was built by BINP and delivered to Mainz in 2018 [2]. These modules are intended to be 1:1 scale size prototypes for the HESR-cooler. A second module is currently under production at BINP and could be delivered during the first half of 2022.

During the last almost two years, our work was seriously hampered by the COVID-19 pandemic because of extended lockdowns. Nevertheless, some progress was achieved which we report in the next paragraph, including a description of the new pressure vessel and an improved concept for closed cycle operation of the turbo-generators. The main purpose of the ongoing work is to demonstrate the reliability of the power generation approach and the scalability of the stages.

HV TANK

The existing module was tested with turbine-based power generation. During these tests, high voltage (HV) was limited because of the absence of a pressure tank. This tank was ordered in 2019 and delivery took place in spring 21. The tank consists of three parts (see Fig. 1 and Fig. 2).

Figure 1: Lower part of HV tank at HIM with first platform installed. Inner diameter of tank is 4 meter.

In the bottom of the lower part, the feedthroughs for the gas supplies and for outgoing/ingoing beam are located. A manhole will allow maintenance once the device is fully assembled. Additional ports for filling with insulating gas are foreseen, the vessel is designed for a pressure of 10 bar and has been subject to the usual safety tests by the authorities. The gas filling is planned with nitrogen, the same gas will be used to drive the turbines. About 6 bar pressure of the insulating gas is sufficient to operate with two platforms at an acceleration voltage of 1.2 MV [2]. First HV tests under pressure are foreseen in 2022.

Figure 2: “Big-Blue-Bubble” HV tank with still open flanges.

---

* aulenbac@uni-mainz.de

ISBN: 978-3-95450-243-1 ISSN: 2226-0374 doi:10.18429/JACoW-COOL2021-S501

GAS FLOW FOR TURBINE DRIVE

The turbines shall be driven with nitrogen under ~3 bar inlet pressure which is generated by a single stage screw compressor. This already existing compressor is powerful enough to drive two turbines with 5 kW output power. Nitrogen will be used in a closed circuit. This requires a careful analysis of the operational parameters. In a cooperation with Prof. Wirsum from the institute of turbomachines at RWTH Aachen [3] it was shown that a stable operation can be expected if additional measures are taken. The main task is to install an additional regulation valve (outside the tank) into the high pressure line leading to the turbine. In addition, minor modifications of the existing circuit will take place, for instance increasing an already existing gas buffer tank by about 1 m^3. These modifications are currently under way. Tests of the turbine circuit are foreseen within the first half of 2022. The design of the hydrodynamic system for multi-turbine operation is ongoing. This will take into account load variations and behaviour under a fast shutdown.

DUAL-PLATFORM EXPERIMENT

After the second platform is delivered, a test of the scalability of the platform concept is mandatory. Practical experience with the gas-distribution system and the heat exchangers inside the HV-tank has to be gained. Demonstration of the HV-capabilities of the turbine driven approach is the most important point, including the hitherto more or less untested gas-flow under high electrical fields and voltages. Measurement of voltage-stability is planned, probably requiring to install an electron source and a spectrometer magnet external to the tank. This can be achieved in conjunction with the attempts for experiments mentioned in the next section. These experiments will extend over long a timespan. However, since the availability of HESR is still several years ahead, the period seems sufficient to come to conclusive result.

APPLICATIONS FOR EXPERIMENTS

With 1.2 MV the HESR-prototype does not deliver a very high energy, even if compared to existing DC-accelerators. However, the prototype with its “Big Blue Bubble” pressure tank (Fig. 2) has some distinct features which may become attractive for applied or even fundamental research. First there is the availability of sufficient electrical floating power on different levels of potential. This in conjunction with a good thermal management, because of the cooling down of the exhaust gas of the turbines [2]. Second, the space available on the HV-platforms is considerable and allows installing even bulky devices. We have plans to use this space for the installation of a photosource which has considerable space requirements that can be fulfilled here. The application is to generate short pulses of several ampere peak current with low duty cycle, i.e. small average current of less than 1 μA. These pulses can be guided to a tungsten target where short flashes of X-rays will be produced. Since the beam spots on the target can be made small, high peak brightness pulsed X-rays can be produced. Special collimators will allow producing a modulated radiation field in space. The apparatus will serve as a test stage for new types of dosimetry which are required for new approaches in radiation therapy such as “flash therapy” and “microbeam radiation therapy” [4].

Another application in fundamental research could be to build an electrostatic storage ring of the “figure of eight type” which employs two kinetic energies during one turn. Such a device was recently suggested to measure the hitherto not observed electric dipole moments of electrons [5] and would use polarized electrons with 200 and 600 keV energy. The space requirements of such a device can be met in our set-up.

ACKNOWLEDGEMENTS

We thank V. V. Parkhomchuk and his team from BINP for important advice and for the fabrication of the hardware.

REFERENCES

[1] V.B. Reva *et al.*, “Experimental observation of longitudinal electron cooling of DC and bunched proton beam at 2425 MeV/c at COSY”, in *Proc. 10th Workshop on Beam Cooling and Related Topics (COOL'15),* Newport News, VA, USA, Sep.-Oct. 2015, paper MOXAUD02, pp. 10-14.

[2] K. Aulenbacher et al., “Status of the turbine-driven HV-generator for a relativistic electron cooler”, in *Proc. 12th Workshop on Beam Cooling and Related Topics (COOL'19)*, Novosibirsk, Russia, Sep. 2019, pp. 11-13. doi:10.18429/JACoW-COOL2019-MOY02

[3] R. Wirsum, “Konzeptpapier–potentialfreie stromversorgung mit turbogenerator“, Mainz, 2021, unpublished.

[4] J. Winter *et al.,* “Clinical microbeam radiation therapy with a compact source: specifications of the line-focus X-ray tube”, *Phys. & imaging in rad. Oncology,* 14, 74, 2020. https://doi.org/10.1016/j.phro.2020.05.010

[5] R. Suleiman *et al.* “On possibilities of high precision experiments in fundamental physics in storage rings of low energy polarized electron beams” https://arxiv.org/abs/2105.11575

13th Workshop on Beam Cooling and Related Topics COOL2021, Novosibirsk, Russia JACoW Publishing
ISBN: 978-3-95450-243-1 ISSN: 2226-0374 doi:10.18429/JACoW-COOL2021-S502

OBSERVATION OF BEAM INDUCED FLUORESCENCE (BIF) AT THE ELECTRON COOLER TEST BENCH AT HELMHOLTZ-INSTITUT MAINZ (HIM)*

T. Beiser†[1], K. Aulenbacher[1], J. Dietrich,
Helmholtz-Institut Mainz, Mainz, Germany and
GSI Helmholtzzentrum für Schwerionenforschung, Darmstadt, Germany
[1]also at Johannes Gutenberg-Universität, Mainz, Germany

Abstract

Further wavelength-resolved studies of the beam-induced fluorescence have been made at the electron cooler test bench at Helmholtz-Institut Mainz (HIM). As a new feature a low-noise, cooled sCMOS-camera was utilized. Beam current dependence of the fluorescence has been recorded. Data evaluation is imminent and options for further experiments will be discussed.

ELECTRON COOLER TEST BENCH AT HIM

An electron cooler test bench including components from TSL (Uppsala) and BINP (Novosibirsk) is operated at Helmholtz-Institut Mainz (HIM) with $U_{\text{Source}} = 18\,\text{kV}$, $U_{\text{Collector}} = 3\,\text{kV}$ and $I = 0.55\,\text{A}$ (Fig. 1). The beam pipe vacuum meets UHV conditions, i.e. in this case $p \approx 3 \times 10^{-10}$ mbar when the electron beam is switched on. A detailed description of our apparatus and efficiency measurements of its energy-recovering-setup can be found in [1]. An upgrade to the electron source, made to suppress penning discharges around the Pierce electrode for solenoid fields that are strong enough to allow higher extraction voltages ($U_{\text{Source}} \approx 30\,\text{kV}$) and therefore beam currents ($I \approx 1$ A), is described in [2].

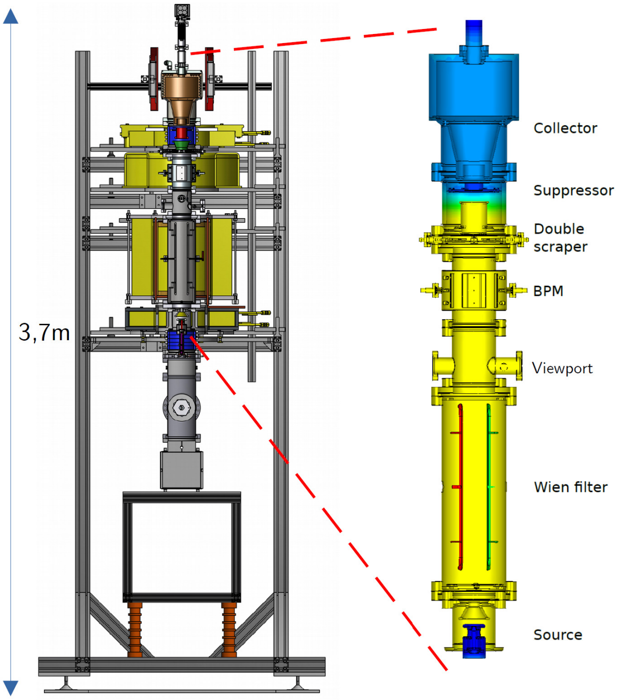

Figure 1: Schematic sketch of the electron cooler test bench at HIM.

PHOTON MEASUREMENTS

Early Measurements

During early photon measurements with an optical setup a signal was found at the location of the electron beam. The setup consisted of a photomultiplier tube (PMT), a slit and lens, both motorized and a set of optical bandpass filters (center wavelengths $\lambda = 400 - 650\,\text{nm}$ in $\Delta\lambda = 50\,\text{nm}$ steps and a FWHM of $\lambda_{width} = 50\,\text{nm}$) A significant infrared background caused by the thermionic cathode ($T \approx 1000 - 1100°C$) was detected for wavelengths above $\lambda = 550\,\text{nm}$, but could be reduced by blackening (coating with a thin carbon layer) the inside of the beam pipe at the location of the utilized viewport.

New Measurements

Due to the 180 min duration of one measurement of the signal and its corresponding background (i.e. a measurement with the electron beam turned off) digital cameras suitable for extremely low light conditions / single photon counting were considered. Scientific complementary metal-oxide-semiconductor (sCMOS) and electron-multiplying charge-coupled-device (emCCD) image sensors were tested at the electron cooler test bench. The peak quantum-efficiencies of such devices are $QE_{sCMOS} \approx 80 - 90\%$ and $QE_{emCCD} \approx 95\%$ (PMT: $QE_{PMT} \approx 35\%$). The emCCD is more fragile and its gain register can degrade over time. After taking the dark current, the readout noise, the robustness and versatility of the chip and the price into account, the sCMOS variant was chosen. The acquired camera and the used lens were then tested to optimize the position in front of the viewport with suitable aperture settings, considering its depth-of-field and to allow size comparisons for the measurements of the observed BIF, one of which can be seen in Fig. 2. It was taken over a timespan of $t_{exposure} = 30\,\text{s}$ with a bandpass filter ($\lambda_{CWL} = 450\,\text{nm}$, $\lambda_{width} = 50\,\text{nm}$). The simulated

---

* Work supported by BMBF Verbundforschung 05P18UMRB1

† thbeiser@uni-mainz.de

ISBN: 978-3-95450-243-1 ISSN: 2226-0374 doi:10.18429/JACoW-COOL2021-S502

electron beam-width at the location of the viewport is on the same scale as the observed signal (Fig. 2).

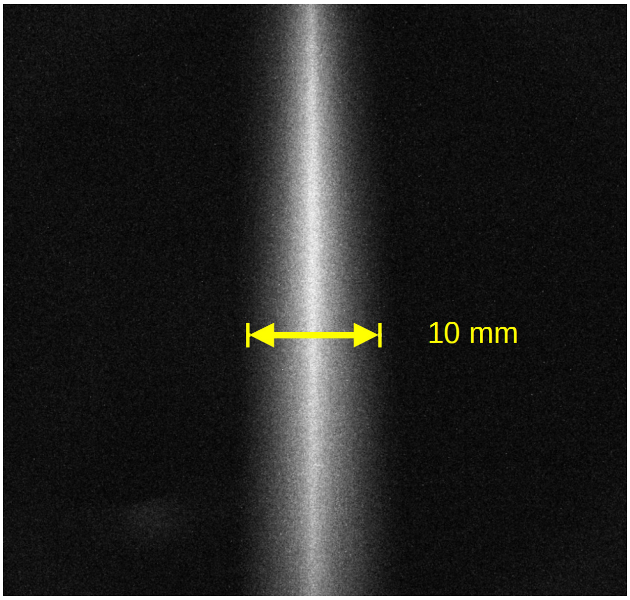

Figure 2: sCMOS measurement of signal ($t_{exposure} = 30\,\mathrm{s}$) with a bandpass filter ($\lambda_{CWL} = 450\,\mathrm{nm}$).

Figure 3 shows the profile of the BIF signal (Fig. 2) measured with different bandpass filters ($\lambda_{width} = 50\,\mathrm{nm}$) and averaged over approximately 800 pixel (px) rows. The distribution of the photons over different wavelength regions might point to fluorescence lines of the residual gas. At $\lambda_{CWL} = 600\,\mathrm{nm}$ the signal-to-background ratio decreases as expected and encourages to concentrate on the wavelength region of 400 – 550 nm for non-wavelength-dependend measurements, which was achieved with a further bandpass filter ($\lambda = 400 - 550\,\mathrm{nm}$).

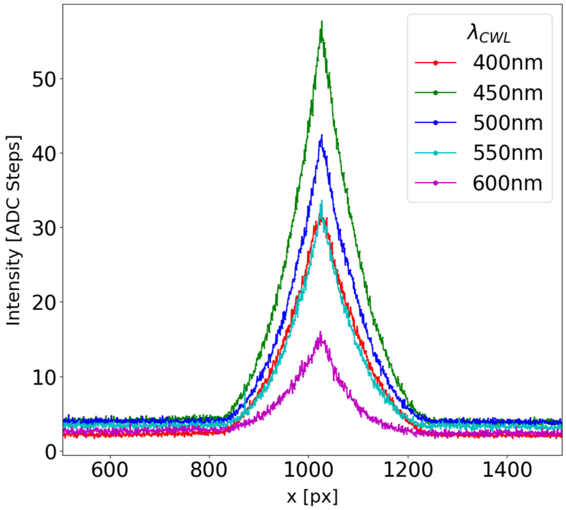

Figure 3: Signal for different bandpass filters with $\lambda_{width} = 50\,\mathrm{nm}$; $400px \approx 10mm$; Intensity in voltage steps of the cameras analog-to-digital-converter (ADC Steps).

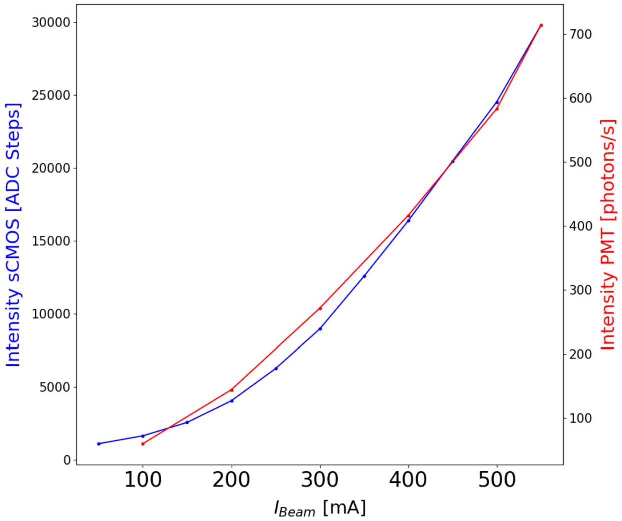

Figure 4: BIF signal for different beam currents measured with sCMOS and PMT.

For rising beam currents the BIF signal increases overproportionally and confirms older PMT measurements (Fig. 4).

If the electron beam current of the test bench is set to $I_{Beam} = 550\,\mathrm{mA}$ and a series of $\Delta t = 30\,\mathrm{s}$ measurements is started at the time when the electron beam is switched on, the corresponding increase in signal intensity (normalized for pressure rise) suggests an accumulation period of $3 - 4\,\mathrm{min}$ (Fig. 5).

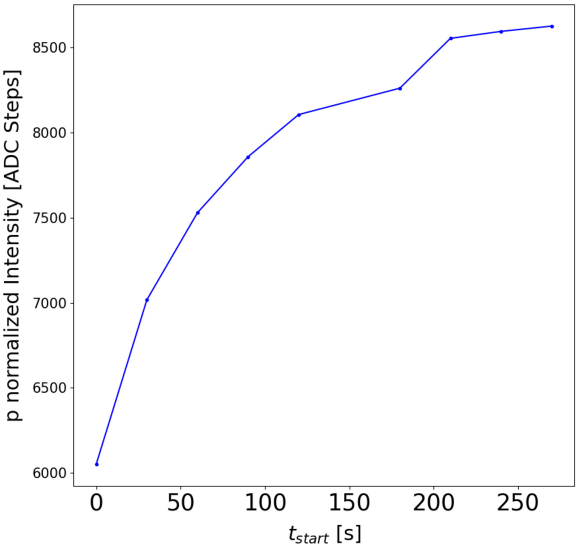

Figure 5: Pressure normalized BIF signal after electron beam switch-on.

PRELIMINARY INTERPRETATION

The residual gas of a baked out UHV system mostly consists of hydrogen. The fact that the BIF signal is observed at the location of the electron beam and the measured electron induced fluorescence spectrum of the H_2 molecule by Danko *et al.* [3] suggests the conclusion, that H_2^+-ions trapped in the electron beams potential are the cause for the beam induced fluorescence. The distribution of the fluorescence lines of the Balmer series and the Fulcher system might explain the different photon intensities seen in Fig. 3. Shemyakin *et al.* also assume H_2^+-ion accumulation as the reason for certain measurements concerning electron cooling at the recycler electron cooler at Fermilab [4]. Furthermore, there might be ion trapping along the electron beam axis caused by a local minimum of the test benches solenoid field around the location of the viewport.

CONCLUSION

A new iteration of imaging technology (sCMOS) was shown to be a viable tool for measurements in low light environments and photon counting. An additional way to locate the center of the electron beam inside the test bench, other than the commonly used beam position monitor (BPM) was found. These two methods might be used to validate each other. A distribution of ions that cause space charge compensation in an electron cooler beam could have an influence on cooling power. The next step would be a spectral analysis of the beam induced fluorescence, which is already prepared. Simulations for solenoid currents of the test bench that should remove the local field minimum are completed and will be implemented soon. Following the experiments done by Shemyakin *et al.* [4], attempts to clear the trapped ions through repeated electron beam interruptions will be made after the solenoid field modifications.

REFERENCES

[1] M.W. Bruker *et al.*, “Secondary electron measurements at the HIM electron cooler test set-up”, *Nuclear Inst. and Methods in Physics Research*, A 872 (2017), pp.169–173.

[2] T.Beiser *et al.*, “Preliminary studies of beam-induced fluorescence and status of the beam-current upgrade of the electron-cooler test-bench at HIM”, *Proc. 12th International Workshop COOL’19*, Novosibirsk, Russia, Sep. 2019, paper TUPS04, pp. 83-85, doi:10.18429/JACoW-COOL2019-TUPS04

[3] M.Danko *et al.*, “Electron induced fluorescence of the H_2 molecule - Balmer lines and Fulcher system”, *Plasma Sources Sci. Technol.*, 25 (2016) 065007.

[4] A.Shemyakin *et al.*, “Effect of secondary ions on the electron beam optics in the Recycler electron cooler”, *Proceedings of IPAC’10*, Kyoto, Japan, May 2010, paper MOPD075, pp. 867-869.

ISBN: 978-3-95450-243-1 ISSN: 2226-0374 doi:10.18429/JACoW-COOL2021-S503

AD/ELENA ELECTRON COOLING EXPERIENCE DURING AND AFTER CERN LONG SHUTDOWN (LS2)

D. Gamba*, L. Bojtar, C. Carli, B. Dupuy, A. Frassier, L. V. Joergensen, L. Ponce, G. Tranquille,
CERN, 1211 Geneva, Switzerland

Abstract

Electron cooling is a key ingredient of the Antimatter Factory at CERN, now composed of the AD and ELENA rings, both featuring an electron cooler. After the successful commissioning of the ELENA ring and electron cooling with antiprotons in 2018, the facility was shutdown for the CERN long shutdown (LS2). In the meantime, ELENA has been operating with H⁻ ions generated from a local source and electron cooling of these H⁻ was demonstrated. The facility has restarted with antiproton operation during summer 2021, and it is now delivering 100 keV production beams through newly installed electro-static extraction lines to all the experiments for the very first time. We will give an overview of the experience gained and difficulties encountered during the restart of the AD and ELENA electron coolers. The experience with electron cooling of H⁻ beam in ELENA and the comparison with antiproton cooling will also be presented.

INTRODUCTION

The Antimatter Factory at CERN is a unique facility that provides antiproton beams to several experiments [1]. The facility, originally composed only by the Antiproton Decelerator (AD) [2], was complemented with the Extremely Low ENergy Antiproton (ELENA) ring [3] which was successfully commissioned in 2018 [4]. The AD provides about 3×10^7 antiprotons in a single bunch at 5.3 MeV kinetic energy approximately every two minutes. The ELENA ring allows to further decelerate the antiprotons down to 100 keV kinetic energy and produces 4 bunches of about 5×10^6 antiprotons per bunch, which are distributed to up to 4 experiments at the same time. The cycle length of ELENA, of about 15 seconds, falls in the shadow of the next AD cycle.

Stochastic cooling (in AD) and electron cooling (both in AD and ELENA) are used on several plateaus placed at injection (in AD), during the deceleration process, and before extraction in order to counteract the adiabatic emittance increase as well as possible heating effects.

Till the end of 2018, GBAR [5] was the only experiment connected to ELENA. During CERN Long Shutdown 2 (LS2), all AD experiments were connected to ELENA with the installation of electrostatic transfer lines. Despite the unavailability of antiprotons during LS2, the ELENA ring could still be operated with beams from of a local H⁻/p source [6,7]. This allowed for progressing in the optimisation of beam performance in the ELENA ring, including e-cooling, as well as to commission the transfer line beam transport well before the arrival of the first antiproton beam after LS2.

The first proton beam for pbar production after LS2 was delivered at the end of June 2021. In the following weeks the AD operation was restored, including the setup of AD stochastic cooling [8] and electron cooling. The first pbar beam was delivered to ELENA mid August 2021 and 100 keV antiproton beams were available for users starting on August 23$^{\text{rd}}$, as scheduled. During this short time, only minor adjustments of the previously prepared H⁻ cycle were necessary to decelerate and cool pbars, demonstrating that H⁻ beams can be used for optics and cooling studies in ELENA without the need of pbars.

In the following sections, the achieved beam performance of the facility will be outlined followed by observations of e-cooling related aspects during the restart in 2021.

BEAM PERFORMANCE IN 2021

During the run, further optimisation of both AD and ELENA cycles allowed to improve the overall performance of the facility. By construction, the characteristics of the beam delivered to experiments are defined by the e-cooling performance and heating effects (like Intra-Beam Scattering (IBS)) on the extraction plateau of ELENA, while the final intensity is driven by the efficiency of antiproton production and collection (in AD), and deceleration. For this, stochastic and electron cooling play a key role to at least counteract the adiabatic increase of the beam transverse and longitudinal emittances. The final AD and ELENA cycle deceleration efficiency are presented in Fig. 1 and Fig. 2, respectively. In AD the beam intensity is measured by a Cryogenic Current Comparator (CCC) [9], which allows to measure the beam current also while the beam is unbunched, while in ELENA the beam intensity is estimated by the Low Level Radio Frequency (LLRF) system which only works when the beam is bunched and does not take into account for longitudinal

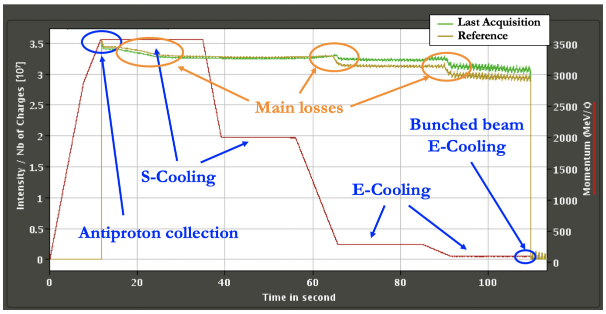

Figure 1: Beam intensity (in units of 10^7 charges) along a typical AD cycle. The main observations are highlighted.

---

[*] davide.gamba@cern.ch

distribution variations and therefore has a lower accuracy than the AD CCC.

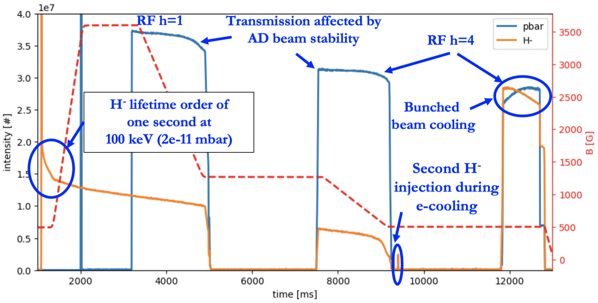

Figure 2: H$^-$ (orange) and pbar (blue) beam intensity along a typical ELENA cycle (dashed red). The main observations are highlighted.

During the 2021 run it was not possible to re-establish the same pbar production and/or AD injection efficiency that was achieved in 2018, which was as high as 5e7 pbars injected, while the final AD deceleration efficiency of about 85% is close or better than what was achieved in the past. In AD, the main losses appear on the injection plateau, likely due to the limited longitudinal acceptance of the stochastic cooling system, and during the 2 GeV/c to 300 MeV/c, and 300 MeV/c to 100 MeV/c ramps, likely due to poor cooling performance on the tails of the beam distribution. In ELENA, the achieved transmission was of the order of 80%, which is much higher than the 60% from the design [3] and the 50% achieved in 2018 [4].

The typical distribution of single bunch intensities over 7 days of operation is shown in Fig. 3. In this case, the bunch intensity is measured by two beam current transformers [3] installed on the two extraction lines, named LNE50 and LNE00. GBAR is presently the only experiment in the LNE50 line. The discrepancy in the average beam intensity between GBAR and the other experiments is due to the presence of a partially-intercepting beam profile monitor upstream the intensity monitor but also due to systematic calibration and measurement issues on the two LNE50 and LNE00 pickups, which are being investigated.

Other main beam characteristics at ELENA extraction are summarised in Table 1 together with design values.

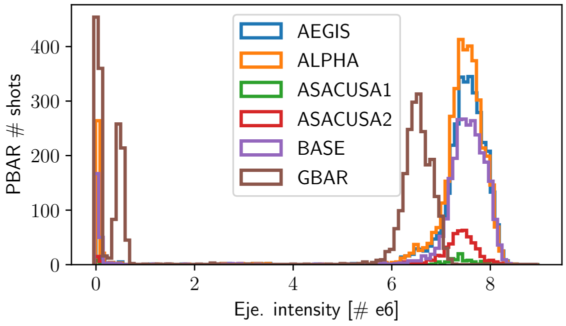

Figure 3: Typical distribution of ELENA extracted bunch intensities per experiment over one week of operation.

Table 1: Design [3] and estimated beam parameters at ELENA extraction at the end of 2021 run for the pbar cycle.

Parameter	Design	Obtained
Q_x/Q_y	$\approx 2.3/\approx 1.3^a$	2.38/1.39
Cycle duration [s]	20	<15
Injected intensity [pbars]	3e7	≈3e7
Efficiency [%]	60	≈80
Extracted bunches [#]	4	4
Bunch population [pbars]	4.5e6	≈7e6
$\Delta p/p_0$	5e-4	≈4.5e-4
Bunch length (rms) [ns]	75	<75
ϵ_{phys} x/y [μm]	1.2/0.75	≈2/≈2

[a] With sufficient tuning range to choose working point in vicinity.

E-COOLERS AND INSTRUMENTATION

The main parameters of the AD and ELENA e-coolers are summarised in Table 2.

The AD e-cooler is the oldest built at CERN: it was used in the Initial Cooling Experiment (ICE) in 1977-80, then used in LEAR (1982-97) and finally moved to the AD where is being used since 1999. Due to the critical spare parts situation, a new e-cooler for AD is being designed [10]. During LS2, it was planned to already replace the present electron collector with one compatible with the new e-cooler design. Unfortunately, the pandemic situation, and high-voltage issues discovered during testing of the first prototype did not allow to perform this exchange. This would have been the occasion to also replace the thermionic cathode in the electron gun, which is now being operated for several years. However, the unavailability of the new collector and the overall good performance of the present cathode did not justify to break the vacuum, which is always considered to be a risky operation for the long baking time needed to recover good vacuum (typically of the order of 10^{-11} mbar).

The ELENA e-cooler [11–13] was commissioned in 2018 [14], and did not require any special modification. Therefore, no modifications nor major maintenance was done in either AD and ELENA e-cooler during LS2.

The key instrument for the setup and optimisation of cooling is the longitudinal Schottky system. In AD this is realised by looking at the second (300 MeV/c) or eighth (100 MeV/c)

Table 2: AD and ELENA E-Cooler Main Parameters

Parameter	AD		ELENA	
Ion p [MeV/c]	300	100	35	13.7
Ion E_k [MeV]	46.8	5.3	0.635	0.1
e$^-$ E_k [keV]	25.5	2.9	0.355	0.055
β_{rel}	0.305	0.106	0.037	0.015
I_{e^-} [mA]	2.5e3	100	5	1
Cooler L [m]	1.5		1	
Ring L [m]	182.43		30.41	
Gun B [G]	590		up to 1000	
Drift B [G]	590		100	
e$^-$ beam r [mm]	25		8 to 25	

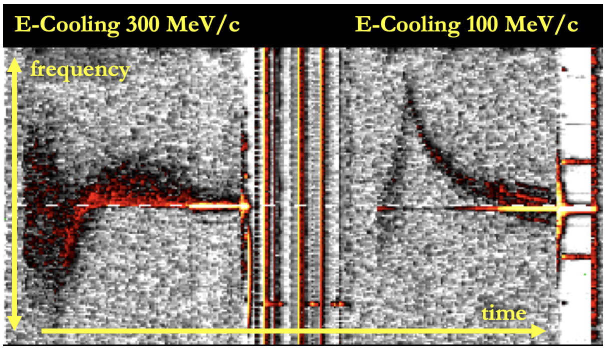

Figure 4: Example of AD longitudinal Schottky measurement along the two e-cooling plateaus.

revolution harmonic on the signal generated by the ring longitudinal pickup [15]. The signal is downmixed to 50 kHz central frequency at each cooling plateau, allowing for observing the Schottky all along the cycle and in real time on a simple spectrum analyser and by simple digital signal processing as shown in the example waterfall acquisition in Fig. 4. The ELENA longitudinal pickup [16] turned out to have a lower Signal-to-Noise Ratio (SNR) than expected. Instead, the Schottky signal could be easily seen by using a single ELENA Beam Position Monitor (BPM) [17] sum signal or by merging the signal of several pickup which allowed to further gain in SNR [18].

The transverse beam profiles are measured by scrapers [19, 20], which are devices that measure the secondary emission of a moving blade progressively entering the beam pipe. Due to the destructive nature of those devices, and the very low repetition rate of the machine, those devices cannot be easily used for measuring the time-evolution of the cooling process. On the other hand, they allow for estimating the transverse cooling performance and therefore guide the cooling optimisation by comparing the transverse profile measured before cooling with profiles measured at subsequent shots with cooling, as shown in the following section.

Semi-intercepting micro-wire monitors (also called SEM) [21] are also installed in the AD-to-ELENA and ELENA-extraction transfer lines. Only about 10% of the beam intensity is lost per crossing. This allowed to develop a multi-profile Twiss measurement to characterise the extracted beam, as shown for example in Fig. 5. Profile monitors in the AD-to-ELENA transfer also allowed for AD e-cooling optimisation at 100 MeV/c without the need of scraper measurements. They also allowed for tracing back poor shot-to-shot ELENA injection efficiency to a poor current regulation of the AD extraction septa.

The e^- beam position in the e-cooler drift section could be measured by the thereby installed BPMs after imprinting an e^- intensity modulation. The modulation was generated by installing a coupling transformer on the cable supplying the e^- gun grid electrode voltage, as shown in Fig. 6. The frequency of the modulation was generated by the BPM acquisition system locked to the beam revolution frequency and for a user-selectable harmonic. This allowed to measure the e^- orbit on the very same pbar BPM acquisition system without the need of dedicated system. Following first promising experiments in ELENA in 2019, this technique was deployed on all CERN e-coolers during LS2, and this allowed to quickly establish cooling by carefully matching the ion and e^- orbits.

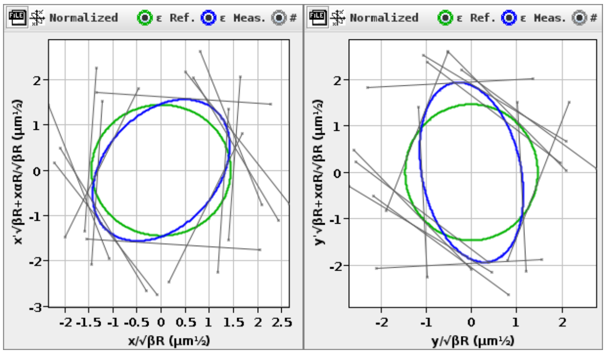

Figure 5: Horizontal (left) and Vertical (right) transverse Twiss measurement (blue) and nominal (green) presented in normalised phase space. Gray lines correspond to beam sizes measured by several SEM along the LNE00 transfer line.

E-COOLING OBSERVATIONS

E-cooling setup and adjustment in AD was reported in the past as a lengthy process, especially at 300 MeV/c where the nearby orbit corrector strength is limited [22]. Thanks to the e^- orbit measurement deployed during LS2, it was possible to start from reducing the orbit corrector strength, and then add the minimum strength necessary to match the e^- and pbar orbits within a few mm. With subsequent adjustments of the e^- energy by looking at the longitudinal Schottky spectra evolution, it was then rather fast to establish first longitudinal cooling. Transverse cooling was then optimised mainly by scanning the pbar angle in the e-cooler in steps of the order of 0.1 mrad and by continuously looking at scraper data or, only at 100 MeV/c, by looking at the transverse beam profile measured by a SEM in the AD-to-ELENA transfer line.

A typical Schottky waterfall after optimisation of the 300 MeV/c cooling is shown in Fig. 7. The total length of the cooling plateau is about 15 s, as also shown in Fig. 1. The initially wide frequency spread observed in the Schot-

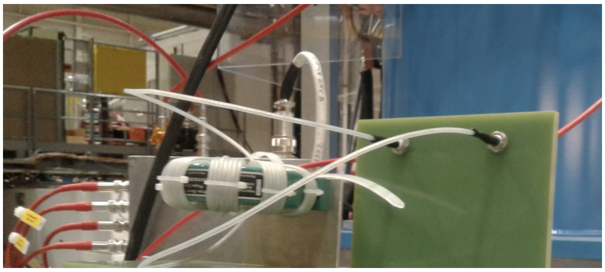

Figure 6: Coupling transformer installed on the high voltage cable powering the grid electrode at the ELENA e-cooler.

ISBN: 978-3-95450-243-1 ISSN: 2226-0374 doi:10.18429/JACoW-COOL2021-S503

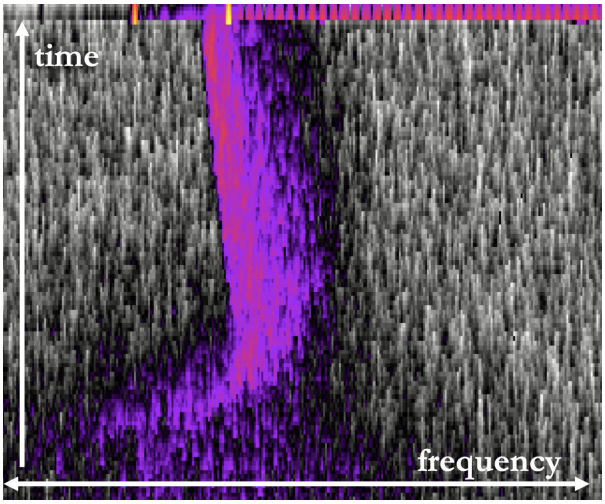

Figure 7: Schottky spectra ($h = 2$) evolution along the 15 s-long 300 MeV/c plateau.

tky is quickly reduced to about 10^{-4} rms, but then a tail on the high-frequency side of the spectrum develops and this is later cooled back. A sharp edge instead develops on the low-frequency side of the spectra, and remains as such but for a small drift in frequency along the plateau. Such a behaviour could be explained by the interplay of e^- space charge, and pbar longitudinal and transverse cooling, as shown in preliminary simulations presented in [23].

Transverse cooling at 300 MeV/c was confirmed by looking at the transverse beam profile measured with scraper without and with cooling on, see Fig. 8. Note that an ideal scraper measurement of a monochromatic Gaussian beam would look like a perfect half-Gaussian. Deformation with respect to this ideal situation can be due to non-Gaussian beam profile, or non-zero dispersion at the location of the scraper [24]. The not-cooled profiles measured in Fig. 8 seems to suggest a rather hollow beam distribution before cooling. On the other hand, inconsistencies have been seen in the data provided by the scraper control system, therefore investigation on the accuracy of such a measurement and possibly crosscheck with other methods should be envisaged before drawing any quantitative conclusion.

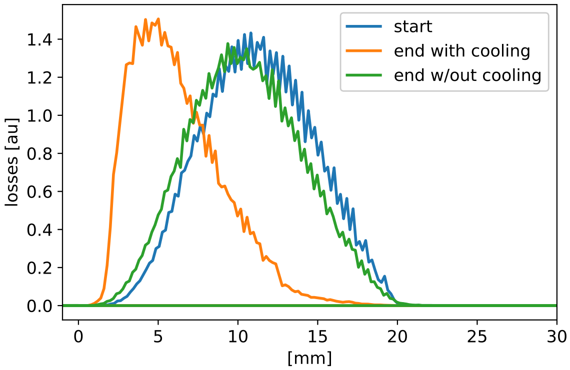

Figure 8: Pbar horizontal half-profile measured by the AD scraper at 300 MeV/c at the beginning (blue) and end (orange and green) with (orange) and without (green) cooling with coasting beam. The Twiss β function at the scraper is about 5 m and zero dispersion.

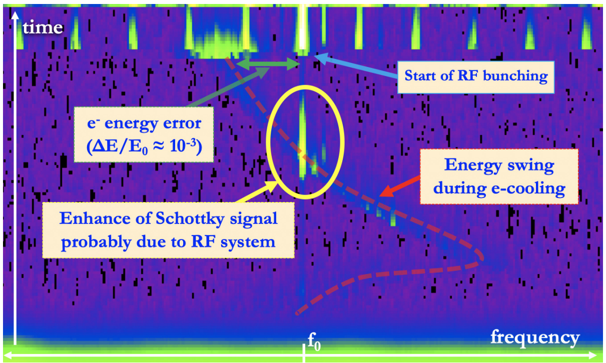

Figure 9: Schottky spectra ($h = 8$) evolution along the 15 s-long 100 MeV/c plateau.

Due to a tight commissioning schedule, it was found that bunched-beam cooling on the whole 100 MeV/c plateau was the faster way to deliver good beams to ELENA, and so allowing to start its commissioning. The nominal un-bunched beam cooling was then re-established during the physics run. Even then, bunched-beam cooling was kept for about 2.5 s before extraction in order to obtain low bunch length at extraction. Figure 9 shows the Schottky waterfall evolution on the 100 MeV/c plateau in this final configuration. Note that the central beam energy as seen by the Schottky spectra drifts toward about 10^{-3} higher relative frequency before being dragged back to lower frequencies. This beam energy swing was already observed in the past and no clear explanation is known, but it might still be due to the interplay between e^- space charge and cooling process. Simulation studies should be envisaged to clarify this observation. When the beam crosses the programmed RF frequency, the Schottky spectra in Fig. 9 looks enhanced. This is a new effect observed after LS2, and it is believed to be due to the not-full closure of the gap relay in the newly installed Finemet cavity [25] used for the beam deceleration. No sizeable perturbation of the cooling process were associated to this perturbation. Instead, a more serious perturbation on the cooling at 100 MeV/c was the shot-to-shot drift of the final beam energy after cooling, which could sensibly deviate from the central RF frequency, as also visible in Fig. 9, and which therefore had detrimental effect on the re-bunching, on the subsequent bunch-beam cooling, and finally on the overall beam transmission to ELENA. This perturbation was traced back to a sudden raise of the vacuum level in the e-cooler region from the nominal 10^{-11} mbar to up to about 10^{-9} mbar. Those variations were linked to vacuum activity in the stochastic cooling pickup and bunch-rotation cavities which are located in the nearby vacuum sectors. The beam energy could be re-adjusted by correcting the e^- acceleration voltage while nominal vacuum level was re-established. Fortunately, such an event were rare (once every few days on average) and of short duration (up to one hour), therefore the impact on the physics was limited.

The ELENA e-cooler was commissioned before the start of the pbar run using H$^-$. Despite previous observation of poor lifetime in LEAR [26,27], no clear sign of beam lifetime degradation due to interaction of H^- with the electron cooler e^- beam was observed. This observation is compatible with the expected low cross section for H$^-$ electron detachment for electron energies below a few eV [28] to be compared with typical e-cooler e^- temperature of less than 0.1 eV.

Due to the slightly different mass of pbar and H$^-$, the programmed momentum on the cooling plateaus for the H$^-$ cycle was increased by about 0.1% such as to obtain the same speed of H$^-$ and pbar beams on the plateaus, and therefore keep the same settings for the electron energy for both cycle types. Apart from this correction, no noticeable difference in cooling performance were seen between H$^-$ and pbar, except for lower equilibrium emittances for low intensity H$^-$ beams.

Figure 10 shows the Schottky spectra evolution as a function of time on the ELENA intermediate plateau at 35 MeV/c both with and without cooling on. In this case, the initial revolution frequency is mismatched with respect to e^- energy, therefore, with cooling, the beam is dragged in about 800 ms to the e^--defined energy. From this dragging one can estimate a rather constant dragging force of about 6 meV/m, which is compatible with expected force as simulated in RF-Track [29] assuming the cooling parameters from Table 2.

Figure 11 shows several vertical scraper measurement along the 35 MeV/c plateau. The V-shape structure that appear in the middle of the overall profile seen in Fig. 11 could be an indication of non-zero vertical dispersion at the scraper location, or rather an accuracy issue of the scraper which should be further investigated. Similar behaviour as in Figs.10 and 11 was seen also in the horizontal plane and at the lowest momentum plateau of 13.7 MeV/c. In both the longitudinal and transverse phase space one can notice that equilibrium is reached rather quickly, after about 1 s, suggesting that ELENA cycle lengths could potentially be shorter.

Figure 12 shows the extracted transverse emittances as a function of bunch intensity observed along a typical day of operation and estimated from the beam size measured at the first SEM in LNE50 line and assuming the design Twiss β_x/β_y = 7.7/1.3 m at that location. A clear dependence between intensity and emittance is visible. This could be a first indication of the space-charge driven limitations discussed in the ELENA design [3] and which should be further investigated in the next run.

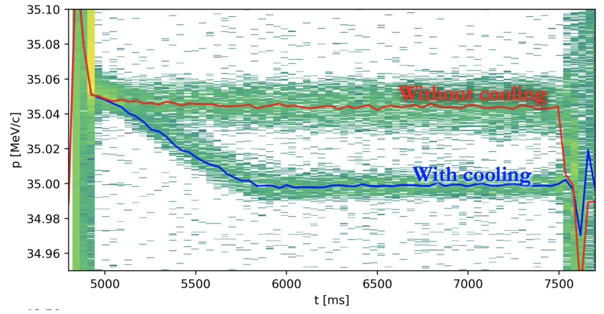

Figure 10: Comparison of Schottky spectra (h = 7) evolution at 35 MeV/c without (red) and with (blue) e-cooling on.

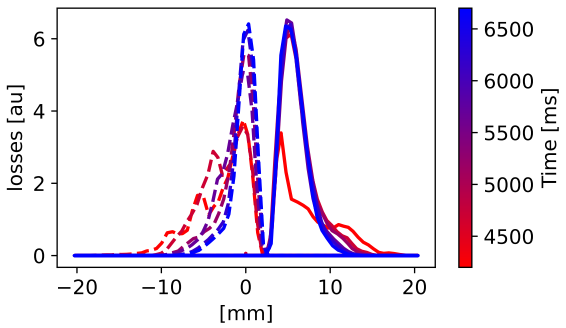

Figure 11: Vertical half-profile evolution (colour code) measured with scraper on the ELENA 35 MeV/c plateau with cooling. The scraper blade was intercepting the beam starting from negative (dashed) or positive (solid) position.

CONCLUSIONS

The AD and ELENA was successfully re-commissioned after LS2, and e-cooler performance comparable to pre-LS2 times were re-established. Schottky diagnostics was the preferred tool for e-cooling setup, despite of observations that are yet to be fully understood. Scraper measurements were found to be ambiguous at times. For the next run it is envisaged to re-establish the Ionisation Profile Monitor already installed in AD as an alternative and hopefully more effective way to measure the transverse emittance evolution along the cycle. The possibility of using H$^-$ for the setup and optimisation of e-cooling in ELENA allowed to minimise the time needed to re-commission ELENA with pbars. During the next run it is envisaged to study and possibly reduce the beam emittance at extraction in order to match the design values.

ACKNOWLEDGEMENTS

The success of the AD and ELENA commissioning were made possible only thanks to many groups and people who worked with dedication and perseverance despite the pandemic situation and the planned commissioning over the summer-holiday period.

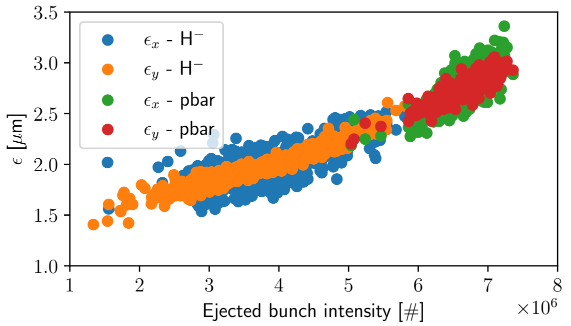

Figure 12: Transverse rms emittance estimate as a function of bunch intensity for H$^-$ and pbar extracted from ELENA.

ISBN: 978-3-95450-243-1 ISSN: 2226-0374 doi:10.18429/JACoW-COOL2021-S503

REFERENCES

[1] M. Hori and J. Walz, “Physics at CERN’s Antiproton Decelerator”, *Prog. Part. Nucl. Phys.*, vol. 72, pp. 206 - 253, Sep. 2013.

[2] B. Autin *et al.*, “The Antiproton Decelerator (AD), a Simplified Antiproton Source (Feasibility Study)”, CERN, Geneva, Switzerland, Rep. CERN-PS-95-36-AR, Nov. 1995.

[3] V. Chohan (ed.) *et al.*, “Extra Low ENergy Antiproton (ELENA) ring and its Transfer Lines: Design Report”, CERN, Geneva, Switzerland, Rep. CERN-2014-002, Jan. 2014.

[4] D. Gamba *et al.*, “ELENA Commissioning”, in *Proc. NA-PAC’19*, Lansing, MI, USA, Oct 2019, paper WEYBB1, pp. 626–631.

[5] P. Perez and Y. Sacquin, “The GBAR experiment: gravitational behaviour of antihydrogen at rest”, *Classical and Quantum Gravity*, vol. 29, pp. 184008, Aug. 2012.

[6] A. Megía-Macías, R. Gebel and B. Lefort, “The ion source for the commissioning of ELENA ring”, in *Proc. ICIS’2017*, Geneva , Switzerland, Oct. 2017, vol. 2011, no.1, p. 090014.

[7] D. Gamba *et al.*, “Operational experience with the ELENA ion source”, in *AIP Conf. Proc. NIBS 2020*, Online, Sep. 2020, vol. 2373, no.1, p. 040005.

[8] W. Höfle *et al.*, “Recommissioning of the CERN AD Stochastic Cooling System in 2021 after Long Shutdown 2”, *these proceedings*, Novosibirsk, Russia, Oct. 2021, Paper S302.

[9] M. Fernandes *et al.*, “Operation of a Cryogenic Current Comparator with Nanoampere Resolution for Continuous Beam Intensity Measurements in the Antiproton Decelerator at CERN”, in *Proc. IPAC’18*, Vancouver, Canada, May 2018, paper THPML044.

[10] G. Tranquille *et al.*, “A New Electron Cooler for the CERN Antiproton Decelerator (AD)”, *these proceedings*, Novosibirsk, Russia, Oct. 2021, Paper P2004.

[11] G. Tranquille *et al.*, “The ELENA Electron Cooler”, in *Proc. IPAC’16*, Busan, Korea, May 2016, paper TUPMR006.

[12] G. Tranquille *et al.*, “Design and Optimisation of the ELENA Electron Cooler Gun and Collector,” in *Proc. IPAC’16*, Busan, Korea, May 2016, paper THPMB048.

[13] G. Tranquille *et al.*, “The CERN-ELENA Electron Cooler Magnetic System”, in *Proc. IPAC’18*, Vancouver, Canada, Apr. 2018, paper TUPAF056.

[14] G. Tranquille and J. Cenede and S. Deschamps and A. Frassier and L.V. Jørgensen, “Commissioning the ELENA Electron Cooler”, in *Proc. COOL’19*, Novosibirsk, Russia, Nov. 2019, paper TUPS12.

[15] C. Gonzalez and F. Pedersen, "An ultra low noise AC beam transformer for deceleration and diagnostics of low intensity beams," in *Proc. PAC’99*, New York, NY, USA, Mar. 1999.

[16] J. Sanchez-Quesada, “ELENA Ring Longitudinal Pick-ups Commissioning Report”, CERN, Geneva, Switzerland, EDMS 1740107, Jan. 2017.

[17] O. Marqversen (ed.) *et al.*, “The Orbit Measurement System for the CERN Extra Low Energy Antiproton Ring”. in *Proc. IBIC’17*, Grand Rapids, Michigan, USA, Aug. 2017, paper TUPCF05.

[18] O. Marqversen and S. Jensen, "Schottky Signal from Distributed Orbit Pick-Ups," in *Proc. IBIC21*, Online, Online, Sep. 2021, paper WEPP04.

[19] P. Grandemange, “Preliminary simulation with Geant4 for the AD scraper renovation,” CERN, Geneva, Switzerland, Oct. 2016.

[20] J. R. Hunt, “Beam Quality Characterisation and the Optimisation of Next Generation Antimatter Facilities,” PhD Thesis, U. Liverpool, United Kingdom, 2019.

[21] M. Hori, “Photocathode Microwire Monitor for Nondestructive and Highly Sensitive Spatial Profile Measurements of Ultraviolet, X-Ray, and Charged Particle Beams”, *Rev. Sci. Instrum.*, vol. 76, no. 11, p. 113303, Nov. 2005.

[22] P. Belochitskii *et al.*, “Two years of AD operation: Experience and progress”, in *Proc. EPAC’02*, Paris, France, Jul. 2002, paper MOPLE081.

[23] A. Borucka and D. Gamba and A. Latina, “Comparison of available models of electron cooling and their implementations”, *these proceedings*, Novosibirsk, Russia, Oct. 2021, Paper P1005.

[24] J.R. Hunt *et al.*, “Emittance Measurements in Low Energy Ion Storage Rings,” *Nucl. Instr. Meth.*, vol. 896, pp. 139-151, Jul. 2018.

[25] M.E. Angoletta *et al.*, “A New Digital Low-Level RF and Longitudinal Diagnostic System for CERN’s AD”, in *Proc. IPAC’19*, Melbourne, Australia, May, 2019, paper THPRB070.

[26] M. Chanel *et al.*, “Measurements of H^- intra-beam stripping cross-section by observing a stored beam in LEAR”, CERN, Geneva, Switzerland, Feb. 1987, report CERN-PS-87-012-LEA.

[27] The LEAR Team, “Epluchage des H^- dans LEAR par le gas residuel, la lumière des jauges par un faisceau laser ou une lampe spot”, CERN, Geneva, Switzerland, 1987, report CERN/PS/LEA Note 87 (unpublished).

[28] B. Peart and D. S. Walton and K. T. Dolder, “Electron detachment from H^- ions by electron impact”, Journal of Physics B: Atomic and Molecular Physics, Oct. 1970, pp. 1346–1356.

[29] A. Latina, “RF-Track Reference Manual”, CERN, Geneva, Switzerland, 2021, `https://doi.org/10.5281/zenodo.4580369`.

ISBN: 978-3-95450-243-1 ISSN: 2226-0374 doi:10.18429/JACoW-COOL2021-S601

ELECTRON COOLING OF COLLIDING ION BEAMS IN RHIC: STATUS AND PERSPECTIVES*

A. V. Fedotov#, W. Fischer, X. Gu, D. Kayran, J. Kewisch,
M. Minty, V. Schoefer, S. Seletskiy, H. Zhao**
Brookhaven National Laboratory, Upton, NY 11973, U.S.A.

Abstract

Electron cooling of ion beams employing a high-energy approach with rf-accelerated electron bunches was recently implemented at BNL using the LEReC accelerator. Following the successful cooling commissioning in 2019, it was used to cool ion beams in both collider rings with ion beams in collision. The electron cooler LEReC successfully operated for the RHIC physics program in 2020 and 2021 and was essential in achieving the required luminosity goals. Apart from its use in RHIC operations, LEReC is used to study various aspects of electron cooling physics using short electron bunches. This report summarizes experience with electron cooling of colliding ion beams in RHIC, as well as ongoing studies.

INTRODUCTION

Electron cooling is a well-established technique for obtaining low-emittance ion beams [1]. In this method, the phase-space density of an ion beam is increased by means of dissipative forces – the dynamic friction on individual ions undergoing Coulomb collisions with electrons which have lower transverse and longitudinal temperatures.

Electron cooling of ion beams employing a high-energy approach with RF-accelerated electron bunches was recently successfully implemented at BNL [2-6]. Such a scheme of cooling with a bunched electron beam is a natural approach for the extension of electron cooling to high beam energies. As such, the successful demonstration of Low Energy RHIC electron Cooling (LEReC) serves as a prototype for future high-energy electron coolers, both in physics and technology.

The high-current high-brightness electron accelerator was commissioned in 2018 with all required electron beam parameters achieved [3]. During the 2019 RHIC run with Au ions, electron cooling was commissioned for 3.85 GeV/nucleon total energy gold beams using electrons with a kinetic energy of 1.6 MeV and then for 4.6 GeV/nucleon gold beams using 2 MeV electrons. At the same time, the first electron cooling of hadron beams in collisions was also successfully demonstrated [2]. Electron cooling of colliding gold beams became fully operational during the 2020 RHIC physics run. It successfully operated in 2020 and 2021 for the RHIC Beam Energy Scan II physics program in search of a QCD critical point on the phase diagram and was essential in achieving the required luminosity goals [7].

THE LEReC ACCELERATOR

LEReC is based on state-of-the-art accelerator physics and technology: reproducibly high quantum efficiency photocathodes with a sophisticated delivery system which can hold up to 12 cathodes simultaneously (specifically designed to support long-term operation with up to one cathode exchange per day); a high-power laser beam with laser shaping and stabilization; a high-voltage high-current DC gun; RF gymnastics using several RF cavities; instrumentation, controls and a machine protection system (see, for example, Ref. [3] and references therein).

Electron bunches are generated by illuminating a multialkali photocathode, inserted into a DC gun with an operating voltage around 400 kV. The 704 MHz fiber laser produces bunch trains with individual electron bunches of about 40 ps full length at 9 MHz bunch train frequency, which matches the repetition rate of ion bunches in RHIC. For RHIC operations, 30-36 electron bunches per bunch train were used.

Once electron bunches of the desired quality are generated from the gun, they are further accelerated to the required energy by the 704 MHz SRF booster cavity, transported to the first cooling section in the Yellow RHIC ring, used to cool the ions in that ring, turned around using a 180-degree dipole magnet, used to cool ions in the Blue RHIC ring and transported to the high-power beam dump. Figure 1 shows layout of the LEReC accelerator.

To prevent degradation of energy spread due to the longitudinal space charge forces, electron bunches are ballistically stretched after slightly off-crest acceleration in the booster cavity to produce an energy chirp (the correlation between particle position within the bunch and its energy).

A series of normal conducting RF cavities are used to reduce the energy spread within electron bunches to the required level. A warm 2.1 GHz cavity (3rd harmonic of the 704 MHz) is used to remove the non-linear energy spread introduced by the RF curvature. For operation with longer electron bunches in 2021, an additional 1.4 GHz cavity (2nd harmonic of the 704 MHz) was successfully employed. After the bunches are stretched, another 704 MHz warm RF cavity is used to remove the energy chirp. An additional 9 MHz warm RF cavity is employed to remove bunch-by-bunch energy variations within the bunch train (macrobunch) caused by beam loading in the RF cavities.

---

* Work supported by the US Department of Energy under contract No. DE-AC02-98CH10886.
# fedotov@bnl.gov;
**presently at IMP, Lanzhou, China

ISBN: 978-3-95450-243-1 ISSN: 2226-0374 doi:10.18429/JACoW-COOL2021-S601

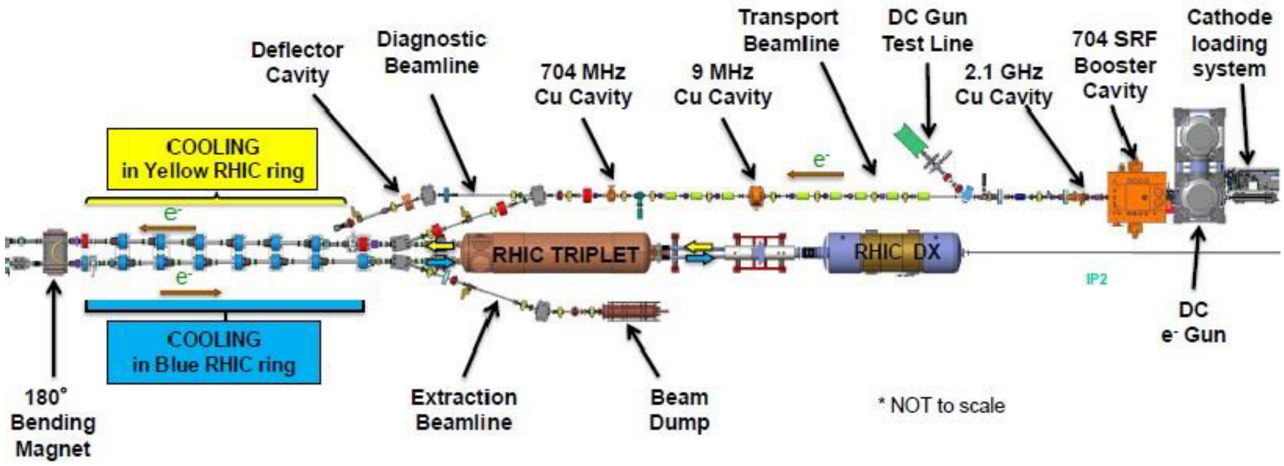

Figure 1: Layout of the LEReC accelerator.

SPECIAL DESIGN FEATURES

Unlike in any previous coolers, the LEReC cathode is not immersed in a magnetic field and no continuous magnetic field with precise solenoids is required in the cooling regions. This significantly simplifies the technical design. However, the requirements for the electron beam quality become more demanding since one needs to have tight control of the transverse electron velocities.

The space-charge beam dynamics during the acceleration of the bunches inside the gun determines the temperature of the electron beam, which is very different from the electron beam temperatures typically obtained during electrostatic acceleration of dc beams in standard coolers. For LEReC, a CsK_2Sb photocathode and laser pulse shaping are used to generate "cold" electron beams with small longitudinal and transverse temperatures.

The low transverse angular spread for the electron beam was achieved by a proper design of the space-charge dominated beam transport and the engineering design of the cooling sections, shown in Fig. 2.

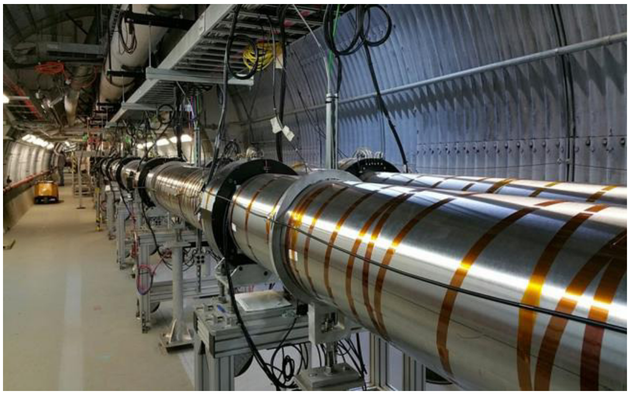

Figure 2: LEReC cooling sections in the Yellow and Blue RHIC Rings.

The required low energy spread in an electron bunch was obtained by producing a close to uniform longitudinal bunch profile using laser pulse stacking and rf gymnastics. Measurements made using a transverse mode deflecting cavity showed that a relative energy spread of less than $2x10^{-4}$ corresponding to an absolute energy spread of 400 eV was achieved for the 2 MeV electron beam.

In the LEReC approach an individual electron bunch occupies only a small portion of the ion bunch and only selected ions experience the friction force during a passage through the cooling section. However, as a result of the synchrotron motion of ions, on successive passages all ions experience interactions with electrons and are cooled with characteristic times larger than the synchrotron period.

One more innovation is that the electron beam, after cooling ions in one RHIC ring, is used again to cool the ions in the other RHIC ring. This is also the first implementation of electron cooling for colliding ion beams. The latter is also of importance in the context of using electron cooling in future high-energy colliders.

ROADMAP TO COOLING IN A COLLIDER

The matching of electron and ion beam average longitudinal velocities was achieved by employing a well-calibrated 180-degree dipole spectrometer magnet between the two cooling sections and by observing losses caused by a radiative recombination of heavy ions with electrons [4]. Once the electron and ion beam velocities were matched, longitudinal cooling of Au ion beam was observed on April 5, 2019.

Shortly after the demonstration of cooling in the longitudinal plane, the electron-ion trajectories in the cooling sections were carefully matched transversely. This led to the first observation of transverse cooling, seen as a reduction of the transverse beam sizes.

After full 6-D cooling of the ion bunches was established in the Yellow RHIC ring, cooling of ions was also commissioned in the Blue RHIC ring, which was quickly followed by simultaneous cooling of ion bunches in both RHIC rings using the same electron beam.

Following the cooling demonstration of all ion bunches in both RHIC rings using the 9 MHz CW electron beam, the focus shifted next towards operational aspects of cooling in RHIC, thus commissioning first electron cooling in a collider.

Cooling was successfully commissioned at 3.85 and 4.6 GeV/nucleon ion beam energies using electrons with kinetic energies of 1.6 and 2 MeV, respectively. An example of cooled ion bunches in two RHIC rings undergoing collisions during normal physics operation is shown in Fig. 3. In the absence of cooling both the transverse and longitudinal beam sizes are increasing due to a diffusion process called intrabeam scattering.

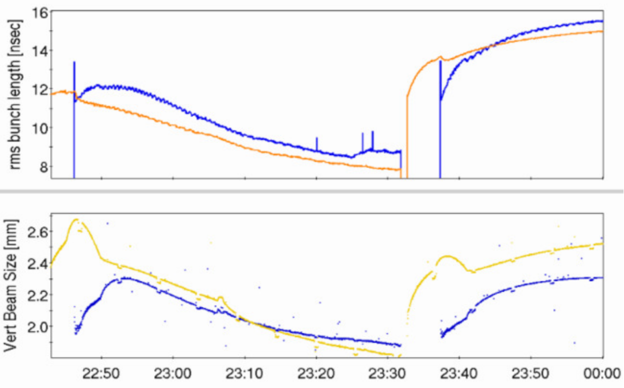

Figure 3: RHIC physics stores with Au ions at 4.6 GeV/nucleon using 2 MeV electrons. First store: with cooling, second store: without cooling. Top plot – rms bunch length of ion bunches in the Yellow and Blue RHIC rings; Bottom plot - rms vertical size of ion bunches.

OPERATIONAL EXPERIENCE

During the 2020 RHIC physics run electron cooling became fully operational; stable 24/7 running of high-current electron accelerator and robust cooling was provided over many months. Reliable long-term operation was ensured by implementation of laser position feedbacks [8, 9], intensity feedback, energy feedback, automatic cooling section orbit correction and orbit feedback. Robust cathode production and a transporter system (holding up to 12 cathodes) were fully operational, and delivered high quality cathodes [10]. The initial cathode quantum efficiency was routinely around 8% with a lifetime of about 10 days (determined by the gun vacuum pressure). This allowed for stable long-term operation with only a short access to the RHIC tunnel (on scheduled maintenance days) once every few weeks to exchange cathodes.

The electron current, which was selected based on optimization between cooling and effects on luminosity, was 15-20 mA (for operation with Au at 4.6 GeV/nucleon in 2020) and 8-20 mA (for operation with Au at 3.85 GeV/nucleon in 2021). Typical electron beam emittances used in operations were < 2 µm (rms, normalized) and the relative rms energy spread of electron bunches $< 4\times10^{-4}$. Matching of average longitudinal velocities between electrons and ions was maintained at $< 1\times10^{-4}$ (using longitudinal cooling process), with energy regulation at the 1×10^{-4} level. The cooling performance during typical physics stores at 4.6 GeV/nucleon is shown in Fig. 4.

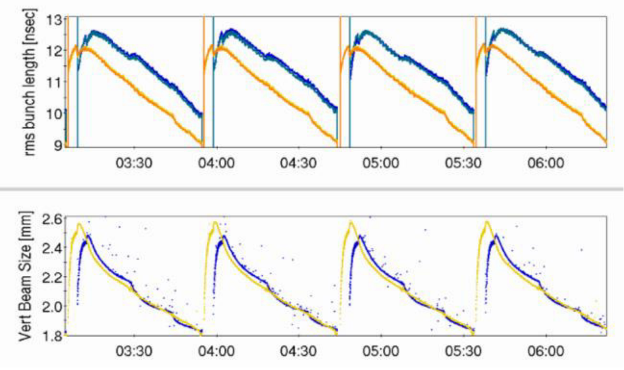

Figure 4: RHIC physics stores with Au ions at 4.6 GeV/nucleon using 2 MeV electrons. Top plot – rms bunch length of ion bunches in the Yellow and Blue RHIC rings; Bottom plot - rms vertical size of ion bunches.

The positive effect of cooling on the event rate, illustrated in Fig. 5 (typical physics stores from the 2020 physics run with Au ions at 4.6 GeV/nucleon), is a part of multi-parametric optimization of RHIC operations. Among other aspects, this includes the fine-tuning of the RHIC rings working point, the lengthened cooled stores due to a slower decay in the event rate, an ability to perform a beta-squeeze of the cooled stores (in the shown example it takes place at 900 s into the cooled store), and a reduced detector background due to the longitudinal cooling eliminating the ion debunching. For details of RHIC operation with cooling see Ref. [7].

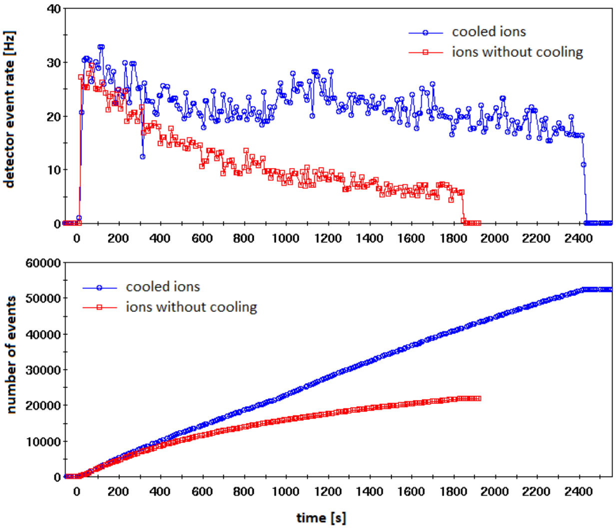

Figure 5: RHIC STAR detector event rate (top plot) and number of accumulated events per physics store (bottom plot) for cooled (blue line) and not cooled (red line) stores.

Cooling performance in 2021, during typical physics stores with Au ions at 3.85 GeV/nucleon, is shown in Figure 6. The jumps in the bunch length during physics stores reflect an additional RF manipulation for ion beams during the beta-squeeze to alleviate space-charge effects.

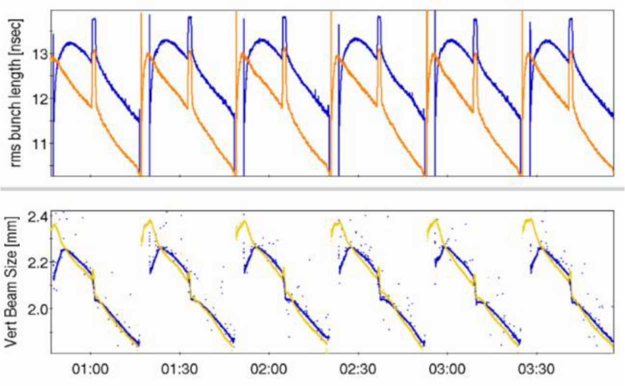

Figure 6: RHIC physics stores with Au ions at 3.85 GeV/nucleon using 1.6 MeV electrons. Top plot – rms bunch length of ion bunches in the Yellow and Blue RHIC rings; Bottom plot - rms vertical size of ion bunches.

LUMINOSITY OPTIMIZATION WITH COOLING AND CHALLENGES

Application of electron cooling directly at the collision energy of the hadron beams brings several challenges and requires special optimizations. For example, control of the ion beam distribution under cooling to not overcool the beam core and control of the ion bunch peak current, especially when ion beam space charge is significant. The interplay of ion beam space-charge and beam-beam effects requires finding the best collider settings, including working point on the tune diagram, which then has to be reconciled with the presence of the electron beam. The dominant effect for collider performance becomes luminosity lifetime in the presence of the electron beam. The final optimization of cooling has to be performed during operational conditions for physics, optimizing various effects with a goal to maximize the integrated luminosity, rather than maximizing the cooling process by itself.

During physics operation in 2020 and 2021 electron cooling effectively counteracted emittance and bunch length growth due to the intrabeam scattering. In addition, the electron beam angles in the cooling section were optimized to provide transverse cooling thus reducing the ion beam sizes. Once the transverse beam sizes were cooled to small values, the dynamic squeeze of ion beta-function at the collision point was established. Providing transverse cooling appeared to be more beneficial for collider operations compared to the longitudinal cooling, which led to higher peak currents of ions, affecting the ion beam's lifetime due to the space-charge effects of ion beams.

An increase of the ion bunch intensity allowed to boost the initial luminosity significantly. However, high ion beam intensities resulted in stronger focusing of the electrons, and resulted in reduced cooling during the initial part of the physics store.

Using many short electron bunches to cool a long ion bunch at such a low energy can lead to emittance growth of ions, which we called "heating". Several models were developed which predicted such emittance growth (see for example Ref. [11] and references therein) caused by the space-charge interactions with electron bunches. Subsequently, more models were developed to reconcile theory with observations. Systematic measurements of heating rates were reported in [12], while an exact mechanism behind the observed emittance growth is still being explored. During operation in 2021, the newly implemented 1.4 GHz RF cavity was successfully used to lengthen electron bunches which helped reducing the heating effect. It is important to note that this additional diffusion mechanism (heating) was counteracted by cooling and was not a limiting factor for collider operation with cooling. However, in addition to this heating mechanism, the presence of the electron beam affected the lifetime of the ions. The mechanism behind the latter effect is presently under study. The stronger the electron current the stronger the lifetime of the ions was impacted. As a result, an increase in the electron beam current, with resulting stronger longitudinal and transverse cooling, was not necessarily the best way to increase the luminosity. Scans of the electron beam current were regularly conducted, and, depending on the collider working point in the tune space and other settings, optimized electron current values were chosen to maximize the luminosity. For example, for a working point just below the ¼ tunes, the effect on ion beams lifetime was less pronounced allowing for a higher optimum electron current of around 20 mA. On the other hand, for a working point closer to 0.1, the effect on the ion beam lifetime from the electrons was stronger requiring a reduction of the electron current, at the expense of cooling performance.

In addition, with average velocities of the electrons and ions well matched, losses of the ions due to radiative recombination were noticeable. Suppression of losses on recombination in electron coolers without continuous longitudinal magnetic field was considered in the past [13]. However, such suppression was not implemented in LEReC since the predicted losses were relatively low. In operations, losses due to recombination were partially reduced by introducing a small velocity offset between electrons and ions.

Despite some challenges of cooling optimization for ion beams in collisions, cooling was beneficial for collider operations and helped to achieve the physics goals [7]. This experience with first application of electron cooling for colliding beams allows us to explore various effects and limitations. Some of these observations were already explored using computer simulations [14]. Dedicated study of other effects, found during operations, are presently underway, and the knowledge gained will be applicable to the design of high-energy coolers.

ONGOING COOLING STUDIES

Apart from its use in RHIC operations, LEReC offers a unique opportunity to study various aspects of electron cooling using short electron bunches, as well as effects relevant to the ion beam lifetime in a collider in the presence of electron cooling. The following dedicated studies started in 2021 using Accelerator Physics Experiments (APEX) program at RHIC: 1) emittance growth of ion beam due to interaction with electrons [12]; 2) coherent excitations and circular attractors in cooled ion bunches [15]; 3) recombination of ions due to interactions with electrons in the cooling section without continuous magnetic field; 4) cooling of ion bunches with electrons overlapping only small portion of an ion bunch; 5) dispersive cooling (redistribution of cooling decrements) to provide stronger transverse cooling at the expense of the longitudinal cooling; 6) effects of the presence of an electron beam on ion beam lifetime.

A detailed experimental exploration of the effects above is critical for a proper design of high-energy coolers, including those proposed for the Electron Ion Collider (EIC).

HIGH-ENERGY COOLING APPLICATIONS

A successful demonstration of cooling using LEReC approach allows us to consider similar technique for higher energies. This was done, for example, in a recent feasibility study of electron cooling applications for the EIC.

To obtain a small vertical emittance of protons, cooling can be performed at the relatively low proton energy of 24 GeV using 13 MeV electrons. The same electron accelerator can be used to cool protons at 41 GeV using 22 MeV electrons. A feasibility study of such an electron cooler is reported in [16].

Extending the LEReC approach to even higher electrons energy of 150 MeV, which is needed to cool protons at 275 GeV in the EIC, is not practical due to the high current requirement for such an electron accelerator. Instead, for a 150 MeV electron cooler, one can use electron storage ring approach. With such a ring-based electron cooler, electrons would cool protons, while the electron beam parameters required for cooling could be maintained via radiation damping provided by wigglers installed in one of the sections of an electron ring. A feasibility study of ring-based electron cooler, which employs non-magnetized cooling (similarly to LEReC) and uses the ions and electrons dispersion in the cooling section to redistribute cooling decrements, is reported in Ref. [17].

Ongoing experimental studies of various cooling effects using LEReC are aimed to assist with high-energy cooler designs described above.

SUMMARY

Electron cooling of ion beams employing a high-energy approach with RF-accelerated electron bunches was recently implemented at BNL. It was successfully used to cool ion beams in both collider rings with ion beams in collision during RHIC operation in 2020 and 2021. Robust and stable cooling was maintained over many months of collider operation.

LEReC operations for RHIC physics program concluded in 2021. The focus now is shifted towards studies of various aspects of cooling process using short electron bunches and high-current electron accelerator R&D.

ACKNOWLEDGMENTS

The LEReC operation was made possible by the strong support of BNL's Collider-Accelerator Department staff whose collective accomplishments are reported on here. For their round-the-clock support we gratefully acknowledge Z. Altinbas, D. Bruno, A. Drees, M. Gaowei, R. Hulsart, P. Inacker, J. Jamilkowski, C. Liu, M. Mapes, K. Mernick, C. Mi, R. Michnoff, T. Miller, L. Nguyen, M. Paniccia, J. Sandberg, F. Severino, L. Smart, A. Sukhanov, R. Than, P. Thieberger, J. Tuozzolo, E. Wang, A. Zaltsman, Z. Zhao as well as many LEReC system experts and the RHIC operators who maintained outstanding performance of LEReC accelerator during RHIC operations.

REFERENCES

[1] G. I. Budker, "An effective method of damping particle oscillations in proton and antiproton storage rings", *Soviet Atomic Energy*, vol. 22, pp. 438-440, May 1967. doi:10.1007/BF01175204

[2] A. Fedotov *et al.*, "Experimental demonstration of hadron beam cooling using radio-frequency accelerated electron bunches", *Phys. Rev. Lett.*, vol. 124, p. 084801, Feb. 2020. doi:10.1103/PhysRevLett.124.084801

[3] D. Kayran *et al.*, "High-brightness electron beams for linac-based bunched beam electron cooling", *Phys. Rev. Accel. Beams*, vol. 23, p. 021003, Feb. 2020. doi:10.1103/PhysRevAccelBeams.23.021003

[4] S. Seletskiy *et al.*, "Accurate setting of electron energy for demonstration of first hadron beam cooling with rf-accelerated electron bunches", *Phys. Rev. Accel. Beams*, vol. 22, p. 111004, Nov. 2019. doi:10.1103/PhysRevAccelBeams.22.111004

[5] X. Gu *et al.*, "Stable operation of a high-voltage high-current dc photoemission gun for the bunched beam electron cooler in RHIC", *Phys. Rev. Accel. Beams*, vol. 23, p. 013401, Jan. 2020. doi:10.1103/PhysRevAccelBeams.23.013401

[6] S. Seletskiy *et al.*, "Obtaining transverse cooling with non-magnetized electron beam", *Phys. Rev. Accel. Beams* vol. 23, p. 110101, Nov. 2020. doi:10.1103/PhysRevAccelBeams.23.110101

[7] C. Liu *et al.*, "RHIC Beam Energy Scan Operation with Electron Cooling in 2020", presented at IPAC'21, Campinas, Brazil, May 2021, paper MOPAB010, this conference.

[8] L. K. Nguyen *et al.*, "Active pointing stabilization techniques applied to the Low Energy RHIC Electron Cooling laser transport at BNL", in *Proc. North American Particle Accelerator Conf. (NAPAC'19)*, Lansing, MI, USA, Sep. 2019, pp. 938-941. doi:10.18429/JACoW-NAPAC2019-THYBA6

[9] L. K. Nguyen, "Pointing stabilization algorithms explored and implemented with the Low Energy RHIC Electron Cooling laser", presented at IPAC'21, Campinas, Brazil, May 2021, paper WEPAB290, this conference.

[10] M. Gaowei *et al.*, "Bi-alkali antimonide photocathodes for LEReC DC gun", in *Proc. 10th Int. Particle Accelerator Conf. (IPAC'19)*, Melbourne, Australia, May 2019, pp. 2154-2156. doi:10.18429/JACoW-IPAC2019-TUPTS101

[11] M. Blaskiewicz, “Emittance growth from modulated focusing in bunched beam cooling”, in *Proc. North American Particle Accelerator Conf. (NAPAC'16)*, Chicago, IL, USA, Oct. 2016, pp. 833-837. doi:10.18429/JACoW-NAPAC2016-WEA3IO0

[12] S. Seletskiy, A. Fedotov, D. Kayran, H. Zhao, “Emittance growth of ion beam caused by space-charge force of electron bunches”, presented at *64th ICFA workshop HB2021,* Fermilab, Batavia, IL, USA, Oct. 2021.

[13] A. Fedotov *et al.*, “Electron cooling in the presence of undulator fields”, in *Proc. 22nd Particle Accelerator Conf. (PAC'07)*, Albuquerque, NM, USA, Jun. 2007, pp. 3696-98. doi:10.18429/JACoW-PAC2007-THPAS092

[14] H. Zhao *et al.*, “Cooling simulations and experimental benchmarking for an rf-based electron cooler”, *Phys. Rev. Accel. Beams*, vol. 23, p. 074201, Jul. 2020. doi:10.1103/PhysRevAccelBeams.23.074201

[15] S. Seletskiy, A. Fedotov, D. Kayran, “Theory and observation of circular attractors in cooled ion bunches”, presented at *COOL21 workshop,* Novosibirsk, Russia, Nov. 2021.

[16] S. Benson, M. Bruker, A. Fedotov *et al.*, “Low-Energy Electron Cooling for the Electron Ion Collider”, BNL Tech Note, BNL-220686-2020-TECH, Dec. 2020.

[17] H. Zhao, J. Kewisch, M. Blaskiewicz, A. Fedotov, “Ring-based electron cooler for high-energy beam cooling ”, *Phys. Rev. Accel. Beams*, vol. 23, p. 074201, Jul. 2020. doi:10.1103/PhysRevAccelBeams.24.043501

ISBN: 978-3-95450-243-1 ISSN: 2226-0374 doi:10.18429/JACoW-COOL2021-S603

MAGNETIZED DYNAMIC FRICTION FORCE IN THE STRONG-FIELD, SHORT-INTERACTION-TIME LIMIT*

I.V. Pogorelov† and D.L. Bruhwiler, RadiaSoft LLC, Boulder, CO, USA

Abstract

Relativistic magnetized electron cooling is one of the techniques explored for achieving the ion beam luminosity requirements of the presently designed electron-ion collider (EIC) facility at Brookhaven National Lab. Because the cooling system will have to operate in previously untested parameter regimes, accurate computation of magnetized dynamic friction is required at the design stage in order to obtain reliable estimates of the cooling time. At energies of interest to the EIC cooling system design, the beam-frame interaction time in the cooler becomes short compared to the plasma period, and some assumptions applicable to the physics of cooling at lower energies become invalid in this high-energy setting. We present and discuss the results of first-principles modeling the magnetized dynamic friction force in the strong-field, short-interaction-time regime, as well as a parametric longitudinal friction force model that we developed starting with a reduced ion-electron interaction potential. The model parameters are related in a simple way to the interaction time and the ion charge. We compare our simulation results to the predictions of previously developed theoretical models.

REDUCED 1D ION-ELECTRON INTERACTION MODEL

We follow the general approach of Derbenev [1], wherein the total time-dependent E-field at the location of the ion $\vec{E}(\vec{r},\vec{v},t)$ is viewed as comprised of three contributions: (i) $\langle\vec{E}^0\rangle(\vec{r},t)$, the Coulomb field from the bulk charge of the electron distribution, (ii) $\langle\Delta\vec{E}\rangle(\vec{r},\vec{v},t)$, the dynamic friction force, the occurrence of which is due specifically to the modulation of the electron phase space distribution caused by the presence of the ion, and (iii) $\vec{E}^{fl}(\vec{r},\vec{v},t)$, statistical fluctuations due to irregularity of the electron distribution at the microscopic scale:

$$\vec{E}(\vec{r},\vec{v},t) = \langle\vec{E}^0\rangle(\vec{r},t) + \langle\Delta\vec{E}\rangle(\vec{r},\vec{v},t) + \vec{E}^{fl}(\vec{r},\vec{v},t). \quad (1)$$

The friction force is then calculated along the ion trajectory:

$$\vec{F}(\vec{r},\vec{v},t) = -Ze\ \langle\Delta\vec{E}\rangle(\vec{r},\vec{v},t)\Big|_{\vec{r}=\vec{r}(t),\dot{\vec{r}}=\vec{v}(t)}. \quad (2)$$

In practice, of interest is the dynamic friction force averaged over the time it takes the beams to traverse the cooler solenoid, which is what we compute in this paper. Furthermore, in this paper we limit discussion to the computation of the ensemble-averaged expectation value of the friction force for the ion moving longitudinally (along the magnetic field lines). We assume a constant and uniform magnetic field in the solenoid.

By short interaction time we mean interaction time T_{int} short compared to the beam-frame plasma period $T_{pl} = \sqrt{\pi/n_e r_e c^2}$, where n_e is the local, beam-frame electron number density (assumed constant over the spatial scales of interest) and $r_e = e^2/(4\pi\epsilon_0 m_e c^2)$ is the classical electron radius. In the beam frame, the interaction time is Lorentz-contracted by a factor of γ, and the plasma period is increased by a factor of $\gamma^{1/2}$ due to electron density dilation. Hence, high-energy conventional cooling systems, both magnetized and unmagnetized, that are designed to cool at $\gamma \sim 20-300$ will likely operate in the short-interaction-time regime. The model presented here assumes $T_{int} << T_{pl}$ and leaves out the Debye screening of the ion potential and the corresponding electron-electron interaction.

As a matter of convenience, we work in a reference frame where the ion remains at rest at the origin of the coordinate system during the interaction time in the cooler. In the beam frame, the dynamics are non-relativistic. The friction force is computed by adding up momentum kicks from binary ion-electron interactions, *subject to the background subtraction procedure* described below. In the limit of a strong magnetic field, to the leading order of canonical perturbation theory (with a small parameter proportional to $1/B$) the electron gyrocenters are confined to cylinders of constant radius equal to the electron's initial impact parameter D. Therefore, with the Larmor radius equal to zero in the limit of infinitely strong magnetic field, in our model the electron macroparticles move in an effective nonlinear $1D$ potential:

$$\ddot{z}(t) = -Zr_e c^2 \frac{z}{(z^2+D^2)^{3/2}}, \quad (3)$$

where Z is the ion charge number and the z axis is in the direction of the magnetic field in the solenoid.

The effective potential is a “soft” nonlinear potential, in the sense that the period of oscillations increases with amplitude and both oscillatory and unbounded orbits are possible. (The shortest possible oscillation period $T_{min} = 2\pi\sqrt{D^3/Zr_e c^2}$ for a given impact parameter D is realized in the limit of infinitely small amplitude.) Depending on the initial conditions, the electron trajectory can be classified as either unbounded, oscillatory, or technically oscillatory but with a period of oscillation that is larger (possibly, much larger) than the interaction time in the cooler. The net dynamic friction force on the ion is determined by contributions from these three orbit types and, due to the nonlinear nature of the interaction potential, it has to be evaluated numerically.

---

* Work supported by the U.S. Department of Energy, Office of Science, Office of Nuclear Physics under Award Number DE-SC0015212.

† ilya@radiasoft.net

A subtle point of critical importance in computing the friction force numerically is that, because the dynamic friction force is due to the perturbation of the electron distribution by the ion, it should be computed as the difference between (i) the Coulomb force on the ion from the electron macroparticles moving on the ion-perturbed orbits and (ii) the force from the electron macroparticles with identical initial conditions moving along the orbits not perturbed by the ion. This approach to numerical computation of the dynamic friction force has another important advantage: By virtue of the perturbed and unperturbed trajectories having the same initial conditions, one gains both the cancellation of the bulk background force and the suppression of the diffusive momentum kicks whose origin is in the discrete nature of the electron macroparticle distribution.

SIMULATION SETUP AND WORKFLOW

For simulations presented here, we worked in the parameter regime of [2], which is broadly relevant to high-energy cooling systems. We assume a locally constant beam-frame electron number density of $n_e = 4.2 \times 10^{15}\ m^{-3}$, corresponding to the expectation value of the distance to the nearest (to the ion) electron of $r_1 \approx 4.9 \times 10^{-6}\ m$. The beam-frame interaction time in the cooler is taken to be $T_{int} = 4. \times 10^{-10}$ s, or approximately $0.16 \times T_{pl}$. We considered two ion species: protons and fully-stripped gold ions ($Z = 79$). For simulations and the parametrized model presented here, we consider the case of the ion velocity parallel to the magnetic field lines, and compute the longitudinal component of the dynamic friction force.

The overall approach is to first compute the dynamic friction force on the ion from the cold electron gas, where, in the reference frame used in our simulations (*i. e.*, centered on the stationary ion), all electron macroparticles have the same initial velocity, equal in magnitude to the ion velocity in the beam frame. Once the friction force is known for the ion interacting with the cold electrons, the dynamic friction force acting on the ion from a gas of warm electrons can be computed by convolution,

$$F_{\parallel}^{(w)}(V_i) = \int_{-\infty}^{\infty} F_{\parallel}^{(c)}(V_i - v_e) f(v_e) dv_e, \tag{4}$$

with superscripts w and c indicating the force computed for the ion interacting with the warm and cold electron gas, respectively, and the (arbitrary) distribution density of electrons in the longitudinal velocity space denoted by $f(v_e)$. In what follows, we discuss the calculation of the drag force from the cold electron gas and the superscript c is omitted.

As mentioned, we track pairs of electron macroparticles, the two particles in the same pair having identical initial conditions. One electron in each pair moves in the effective potential of Eq. (3), while the other stays on the unperturbed trajectory. The contribution to the net friction force from each initial condition is then computed from the difference between the momentum kicks imparted to the ion by the two electrons in the same pair over the interaction time.

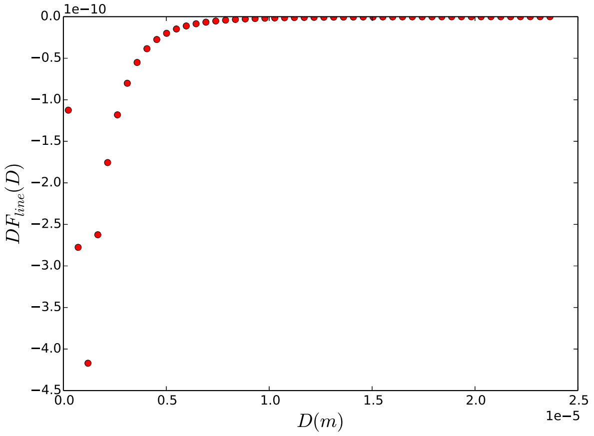

Figure 1: The unnormalized integrand of the r.h.s. of Eq. (5), showing the contribution to the total dynamic friction force from different impact parameters, for a proton with $V_{\parallel} = 1.5 \times 10^4$ m/s interacting with cold electrons.

We used a second-order, symplectic integrator to generate the results presented in this paper. Taking advantage of the axial symmetry of the configuration under study, we chose the initial conditions along the lines of constant impact parameter D parallel to the z axis (for multiple values of D). Given the assumption of a constant local density n_e and our interest in the (ensemble-average) expectation value of the friction force, the initial conditions were spaced uniformly in z. For a given value of the ion velocity, we first compute the contributions to the total force from all initial conditions with the same impact parameter, $F_{line}(D)$, and then integrate over the impact parameters to obtain the total friction force:

$$F_{\parallel}(V_i) = 2\pi n_e \int_0^{\infty} D F_{line}(D) dD\ . \tag{5}$$

Figure 1 shows the unnormalized integrand of the r.h.s. of Eq. (5) for the case of a proton moving at 1.5×10^4 m/s, illustrating two generally valid findings. The first one is that the contributions to the total friction force tend to zero as the impact parameter approaches zero. The second finding is that the large-impact-parameter tail of the integrand falls off approximately exponentially (as seen when plotting the logarithm of the integrand), and so the result for the total friction force is finite even when the integration over the impact parameter is carried out to infinity as the upper limit. (This also allows us to analytically estimate the contributions to the net friction force from impact parameters beyond the largest one that we use in simulations.) Thus, in the model described here, there are *no divergences at either small or large impact parameters* and, therefore, no need to introduce the maximum and minimum cut-off impact parameters and the Coulomb log in order to arrive at a finite value of the friction force.

To compute the longitudinal dynamic friction force as a function of the ion velocity, the procedure outlined in this section is repeated for different values of the ion velocity.

ISBN: 978-3-95450-243-1 ISSN: 2226-0374 doi:10.18429/JACoW-COOL2021-S603

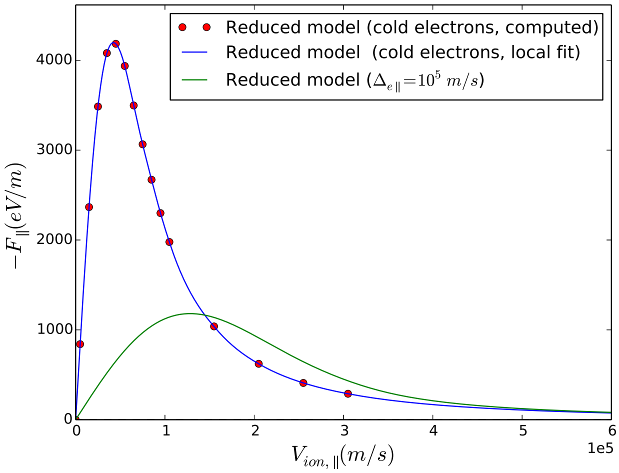

Figure 2: Longitudinal dynamic friction force as a function of the ion velocity, computed from first principles in the limit of infinitely strong B. Gold ion, zero transverse ion velocity component, cold (blue) and warm (green) electrons.

SIMULATION RESULTS

Figure 2 presents the results of computation of the longitudinal dynamic friction force for the gold ion ($Z = 79$). The beam-frame interaction time $T_{int} = 4.0 \times 10^{-10} s$. The interpolated cold-electrons result is shown in blue (the red dots are computed values), while the green line shows the result for a warm electron gas, assuming for this example a Maxwellian distribution in beam-frame $v_{e,\parallel}$ with the rms longitudinal velocity $\Delta_{e\parallel} = 1.0 \times 10^5 m/s$. The warm-electrons result was computed via the convolution procedure of Eq. (4). Because convolution with a Gaussian is, in effect, an application of a smoothing filter (a "moving average"), the maximum friction force in a warm electron gas is smaller than the peak dynamic friction force from interaction with cold electrons. For both cold and warm electrons, we find the expected linear dependence of the friction force on the ion velocity at small V, as well as a $1/V^2$ dependence at high velocity. The convergence of the "warm" and "cold" results at ion velocities much higher than the rms thermal electron velocity makes sense on qualitative grounds, as well.

Figure 3 shows the computed dynamic friction for protons in a cold gas of strongly magnetized electrons, for three values of the interaction time, namely T_{int}, $0.5 \times T_{int}$, and $0.25 \times T_{int}$. In addition to a linear dependence on the ion velocity at small V, we find a linear scaling of the friction force in the interaction time. However, the dependence on the interaction time disappears at high ion velocity.

In a study based on a combination of scaling and dimensional analysis and fitting the data, we found the following scaling and asymptotic behavior of the longitudinal friction force computed with our reduced binary interaction model. At low velocity, the friction force is well approximated by

$$F_{\parallel}(V_{\parallel}) \approx -2Zn_e m_e r_e c^2 T_{int} V_{\parallel} \quad (small\ V_{\parallel}), \qquad (6)$$

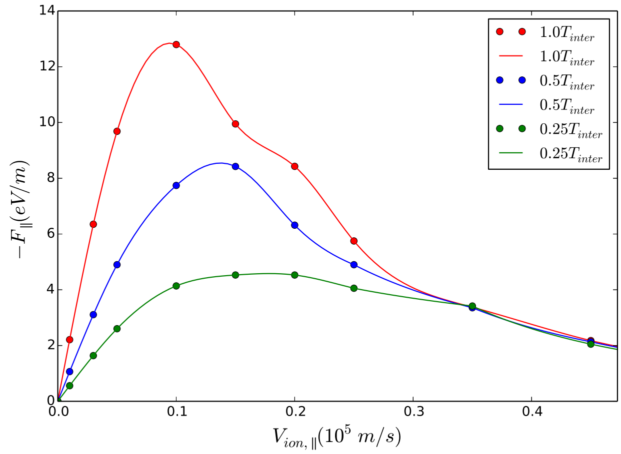

Figure 3: Longitudinal dynamic friction force as a function of the ion velocity, computed from first principles for three different values of the interaction time, in the limit of infinitely strong B. Protons, cold electrons, zero transverse ion velocity component.

with a linear dependence on the ion charge, velocity, and the interaction time. At high ion velocity, the results of the simulations are very well approximated by the expression

$$F_{\parallel}(V_{\parallel}) = -2\pi Z^2 n_e m_e (r_e c^2)^2 / V_{\parallel}^2 \quad (large\ V_{\parallel}). \qquad (7)$$

that shows a Z^2 dependence on the ion charge number, a $1/V^2$ dependence on the ion velocity, and no dependence on the interaction time. In addition, the peak friction force scales with the ion charge as $F_{\parallel}^{max} \propto Z^{4/3}$.

PARAMETRIZED MODEL

From our simulation results, we have constructed a simple parametrized model for the longitudinal interaction-time-averaged dynamic friction force on the ion, for the case of strongly-magnetized, longitudinally-cold electrons and short interaction time. In this regime the physical system is described by three independent parameters: the ion charge number Z, the local electron number density n_e, and the beam-frame interaction time in the cooler T_{int}. By construction of our simulation procedure, the friction depends linearly on n_e. Introducing two auxiliary parameters,

$$A = 2\pi Z^2 n_e m_e (r_e c^2)^2$$

and

$$\sigma \approx (\pi Z r_e c^2 / T_{int})^{1/3} ,$$

the longitudinal dynamic friction force is given by

$$F_{\parallel}(V) = -\frac{AV}{(\sigma^2 + V^2)^{3/2}} \quad . \qquad (8)$$

In addition to correctly capturing the qualitative behavior of $F_{\parallel}(V)$, this model reproduces the small- and large-ion velocity asymptotic results of Eqs. (6) and (7). Furthermore,

ISBN: 978-3-95450-243-1 ISSN: 2226-0374 doi:10.18429/JACoW-COOL2021-S603

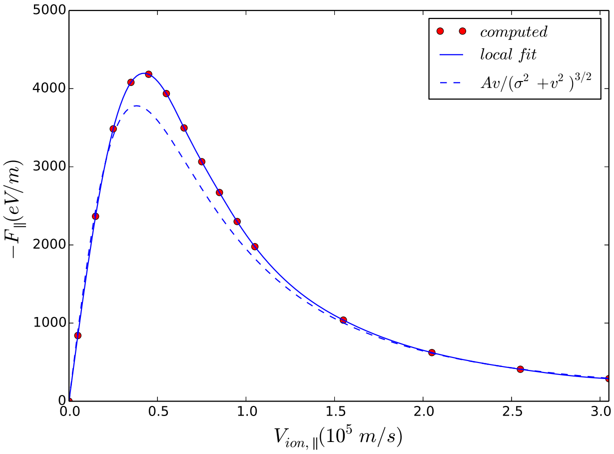

Figure 4: A two-parameter model for the longitudinal dynamic friction force as a function of the ion velocity, Eq. (8), compared with results of first-principles computation in the limit of infinitely strong B. Gold ion, cold electrons, zero transverse ion velocity component.

the model predicts the scaling of the peak friction force with the ion charge and the interaction time:

$$F_{\parallel}^{max} \propto Z^{4/3} T_{int}^{2/3} , \tag{9}$$

in agreement with empirically found $Z^{4/3}$ scaling mentioned in the previous section.

Figure 4 illustrates the agreement between the simulation results and our parametrized model for the case of $Z = 79$ (gold ion). The agreement is generally quite good, although the peak force is underestimated by $\sim 10 - 15\%$.

COMPARISONS WITH ANALYTIC AND SEMI-ANALYTIC MODELS

We compared the results of our first-principles simulations to the predictions of two theoretical models: an analytical expression for the longitudinal friction force in the strong-field limit, due to Derbenev and Skrinsky [1, 3], and the predictions of the semi-analytic model for the magnetized friction force, introduced by Parkhomchuk [4]. In both cases we took the transverse ion velocity to be zero so as to compare the results for the longitudinal magnetized friction force. For the Derbenev and Skrinsky (DS) model, we considered the large-velocity asymptotic limit (the ion velocity is much larger than the longitudinal thermal electron velocity), where their result for the longitudinal friction force simplifies to

$$F_{\parallel}(V_{\parallel}; V_{\perp} = 0) = -\frac{2\pi Z^2 n_e m_e (r_e c^2)^2}{V_{\parallel}^2} , \tag{10}$$

exhibiting a Z^2/V^2 scaling of the friction force, with no dependence on the interaction time and no Coulomb log term. (This is in agreement with [1] and corrects a factor of 2 misprint found in several publications.) For the Parkhomchuk model, we used the definition of the minimum cut-off impact parameter ρ_{min} that enters in the Coulomb log as in BETACOOL [5–7], *i.e.*, $\rho_{min} = Z r_e c^2/(V_{ion}^2 + V_{e,eff}^2)$, taking $V_{e,eff} = \Delta_{e\parallel}$, the rms electron thermal velocity. In the Parkhomchuk model, dependence on the magnetic field is via the Larmor gyration radius that enters in the calculation of the Coulomb logarithm, with the infinite-B limit well-defined (non-singular).

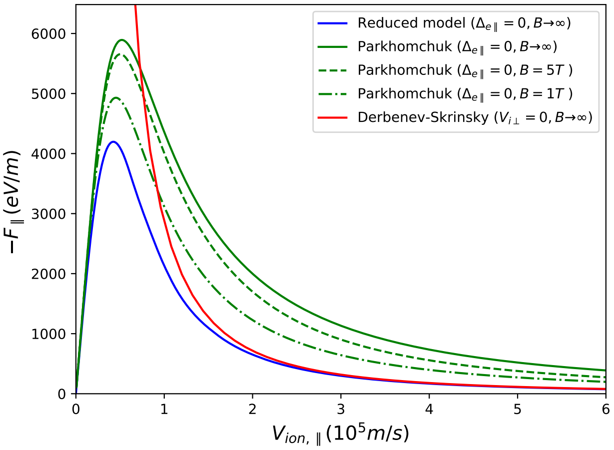

Figure 5: Comparison of the longitudinal dynamic friction force computed from first principles (with the reduced, strong-field model of Eq. (3)) with the predictions of the Parkhomchuk model and the strong-field, high-velocity limit of the Derbenev and Skrinsky model. Results shown are for Au^{+79} and cold electrons.

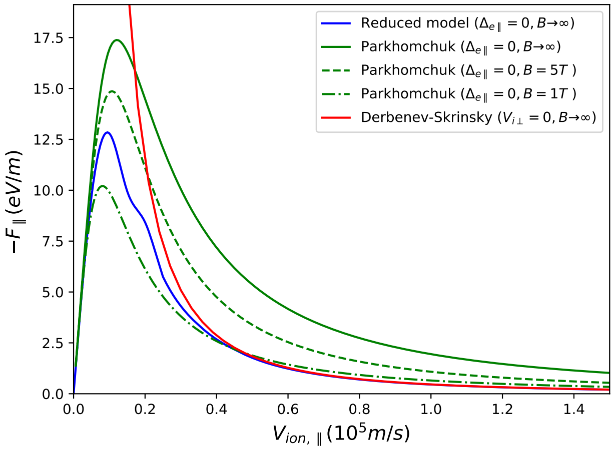

Figure 6: Same as Fig. 5 except the results shown are for protons and cold electrons.

For cold electrons, the results of comparison for the gold ion (Z=79) and protons are shown in Fig. 5 and Fig. 6. We find an essentially exact agreement with the large-velocity asymptotic of the DS model where the assumptions regarding system parameters are the same as those used in our simulations. It should be noted, however, that while Derbenev and Skrinsky consider a perturbative dielectric response of a plasma, our approach is based on a binary collision model.

ISBN: 978-3-95450-243-1 ISSN: 2226-0374 doi:10.18429/JACoW-COOL2021-S603

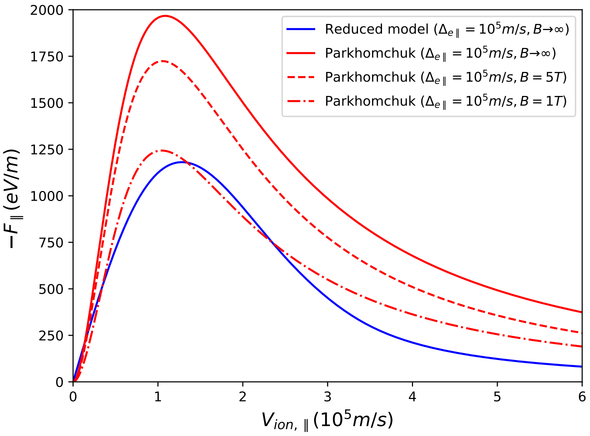

Figure 7: Comparison of the longitudinal dynamic friction force computed from first principles (with the model of Eq. (3)) with the predictions of the Parkhomchuk model with the definition of ρ_{min} as used in BETACOOL [7]. Results shown are for Au^{+79} and warm electrons ($\Delta_{e\parallel} = 1.0 \times 10^5$ m/s).

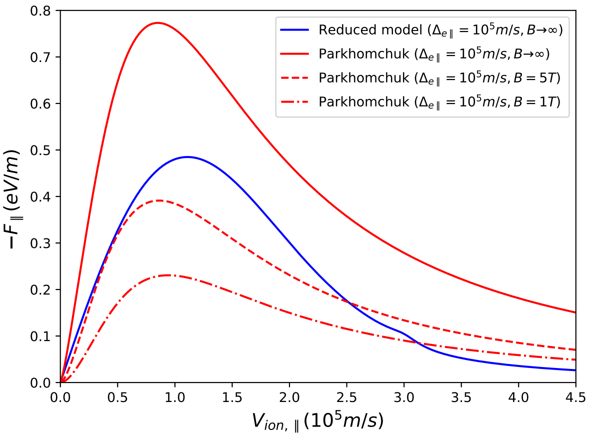

Figure 8: Same as Fig. 7, except the results shown are for protons.

Our longitudinal friction force results are consistently lower, for all ion velocities, than the predictions of the Parkhomchuk model in the strong-field limit. This is also the case for warm electrons, as illustrated in Figs. 7 and 8 for a "representative" choice of the rms electron thermal velocity spread $\Delta_{e\parallel} = 1.0 \times 10^5$ m/s. This may indicate a possible overestimation of the dynamic friction force in the Parkhomchuk model in this regime. By extrapolation, one may expect to find such overestimation for the finite values of B, as well.

DYNAMIC FRICTION FORCE FOR ANTIPROTONS

We applied the approach presented here to compute the longitudinal dynamic friction force acting on an antiproton ($Z = -1$) interacting with a cold, strongly magnetized electron gas, and compare the results to those presented above for protons, keeping system parameters other than the charge number the same. As shown in Fig. 9, our first-principles simulations with the reduced binary collision model yield a significantly stronger friction force for the case of the repulsive ion-electron interaction potential. Qualitatively, this can be traced to the different topology of electron orbits in the repulsive-interaction potential ($Z < 0$) compared to the case of $Z > 0$. For $Z < 0$, no oscillatory orbits are possible, only unbound orbits and orbits having at most one turn-around point (depending on the T_{int} and initial conditions). Most of the contribution to the ensemble-averaged net force for $Z < 0$ comes from strong, small-impact-parameter interactions, yet a finite result for the friction force is obtained when the statistics of the collisions is handled properly. This will be discussed in a separate publication.

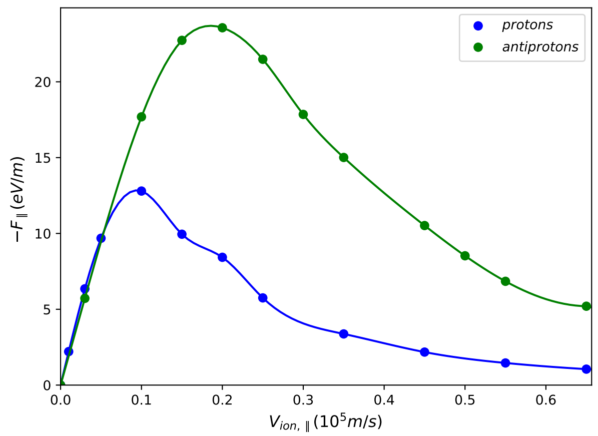

Figure 9: Longitudinal dynamic friction force for protons and antiprotons computed with a reduced ion-electron binary interaction model, assuming a cold, strongly magnetized electron gas.

STATISTICAL CONSIDERATIONS

In the work presented here, our objective is to compute the expectation value of the dynamic friction force on a single pass through the cooler. However, estimates of statistical pass-to-pass variations in the momentum kick received by the ion in the cooler are of clear practical interest. Our procedure for computing the friction force makes it possible to estimate, for a given T_{int}, Z, and ion velocity, the volume from which comes (say) 95% of the contribution to the total force on a single pass through the cooler. Assuming a constant n_e, we then know the number of *physical* electrons, N_{95} in this volume. For example, for $Z = 79$, $V_{ion} = 4.5 \times 10^4$ m/s (near the peak of $F(V)$), N_{95} is ~ 220; while for $Z = 1$, $V_{ion} = 1.0 \times 10^4$ m/s (near the peak of $F(V)$ for protons), N_{95} is ~ 20. (Clearly, not all of these electrons contribute to the net force equally.) A number as low as 20 indicates a need to look carefully at the statistical properties of diffusive kicks experienced by the ion in traversing the cooler. This will be addressed in greater detail elsewhere.

REFERENCES

[1] Ya.S. Derbenev, *Theory of electron cooling*, `https://arxiv.org/abs/1703.09735v2`

[2] A.V. Fedotov *et al.*, *Phys. Rev. ST Acc. Beams* **9**, *074401* 2006.

[3] Ya. Derbenev and A. Skrinsky, *Part. Accel.* **8**, *235,* 1978.

[4] V. Parkhomchuk, *Nucl. Instrum. Methods Phys. Res., Sect.* **A 441**, *9,* 2000.

[5] A.O. Sidorin *et al.*, *Nucl. Instrum. Methods Phys. Res., Sect.* **A 558**, *325,* 2006.

[6] A. O. Sidorin and A. V. Smirnov, *ICFA Beam Dynamics Newsletter* **65**, *127,* 2014.

[7] I. Meshkov, A. Sidorin, A.V. Smirnov, G.V. Trubnikov, and A. Fedotov, *BETACOOL Physics Guide*, `http://lepta.jinr.ru/betacool`

MUON IONIZATION COOLING EXPERIMENT: RESULTS AND PROSPECTS

D. Maletic[†], Institute of Physics Belgrade, University of Belgrade, Belgrade, Serbia
C. T. Rogers, Rutherford Appleton Laboratory, Didcot, United Kingdom
on behalf of the MICE collaboration

Abstract

A high-energy muon collider could be the most powerful and cost-effective collider approach in the multi-TeV regime, and a neutrino source based on decay of an intense muon beam would be ideal for measurement of neutrino oscillation parameters. Muon beams may be created through the decay of pions produced in the interaction of a proton beam with a target. The muons are subsequently accelerated and injected into a storage ring where they decay producing a beam of neutrinos, or collide with counter-rotating antimuons. Cooling of the muon beam would enable more muons to be accelerated resulting in a more intense neutrino source and higher collider luminosity. Ionization cooling is the novel technique by which it is proposed to cool the beam. The Muon Ionization Cooling Experiment collaboration has constructed a section of an ionization cooling cell and used it to provide the first demonstration of ionization cooling. Here the observation of ionization cooling is described. The cooling performance is studied for a variety of beam and magnetic field configurations. The outlook for an experiment to measure muon ionization cooling in all six phase-space dimensions as part of the demonstrator facility being considered by the interna-tional Muon Collider collaboration will also be discussed.

INTRODUCTION

Muons are considered excellent beam particles for a collider applications due to their unique properties. Entire muon energy, being fundamental particle, is available for production of secondary particles. The design of such Muon collider is strongly influenced by radiative effects. The large muon mass also offers an increased coupling to Higgs boson compared to electron. Muon colliders can thus employ rings of small circumference for acceleration and collisions, reducing facility footprints and construction and operating costs. Production of high quality muon beams is challenging. Muon beam production starts by sending the high power proton beam to the target, where pions are produced subsequently decaying into muons. This way muons emerge as a tertiary beam with a very large initial emittance and energy spread, which requires a significant beam cooling in order to be able to achieve a sufficient luminosity in the collider applications. Due to the shortness of the muon lifetime the only cooling technique fast enough to be applicable to the muon beams is ionization cooling [1–3]. In muon ionization cooling, muons are passed through energy-absorbing material where the transverse and longitudinal momentum is reduced, reducing the normalised beam emittance and cooling the beam. Multiple Coulomb scattering from atomic nuclei induces an increase in transverse momentum and heats the beam. By focussing the beam tightly onto the absorber and using materials having low atomic number the heating effect may be suppressed, resulting in overall cooling. The ionization cooling of muons has been demonstrated for the first time experimentally by Muon Ionization Cooling Experiment (MICE) at RAL [4].

EXPERIMENT

The Muon Ionization Cooling Experiment (MICE) was designed, most importantly, to demonstrate the ionization cooling principle and amplitude non-conservation. Other components of the MICE program were to demonstrate high acceptance and tight focussing solenoid lattice, then to demonstrate the integration of liquid hydrogen and lithium hydride absorbers, and also to precisely measure the absorber material properties (dE/dx and multiple scattering distributions) that determine the performance of ionization cooling. MICE was approved in 2003 at RAL. After an extended design, construction, installation, and commissioning process, MICE recorded a substantial dataset (3.5 × 10^8 events) in 2016-17 with one absorber and no RF cavities. MICE collaboration grouped over 100 scientists from 30 institutions in 10 countries.

A schematic of MICE is shown in Fig. 1. Pions arising from protons striking a target in the fringe of the ISIS synchrotron proton beam were guided to the cooling apparatus by quadrupoles, dipoles and a solenoid. Momentum of the resultant beam was selected by the dipoles. A variable thickness diffuser at the upstream end of the cooling channel served to scatter the beam enabling choice of incident emittance. The beam was passed into a solenoid focussing channel. Spectrometer Solenoid modules were placed upstream and downstream of a Focus Coil module within which the absorber was placed providing a tight focus in both transverse planes suitable for ionization cooling. Liquid hydrogen and lithium hydride absorbers were used. Particles passed through a pair of Time-of-Flight (TOF) detectors, which were used to estimate the particle velocity. Scintillating fibre trackers upstream and downstream of the experiment in fields of up to 4 T enabled characterisation of particles' position and momentum before and after passing through the cooling section. By comparing the momentum measured in the trackers and the velocity measured in the TOFs, the particle species was identified and pion and electron impurities rejected. Muons were passed through the experiment one-by-one and an ensemble of muons was accumulated. The experiment was modelled using Geant4-based simulation [5].

[†] maletic@ipb.ac.rs

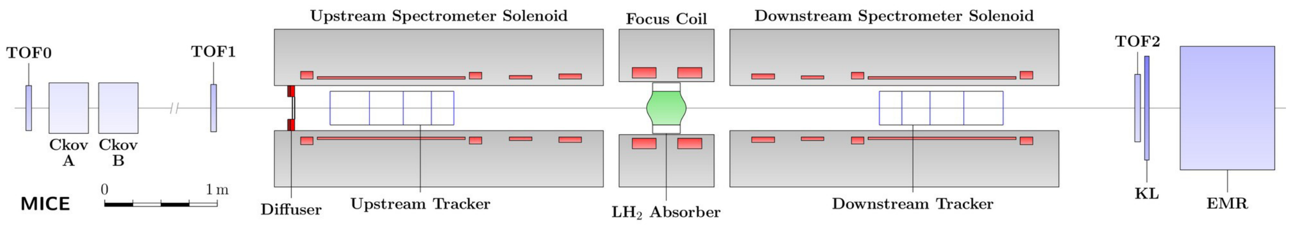

Figure 1: A schematic of MICE. Muons are incident from the left.

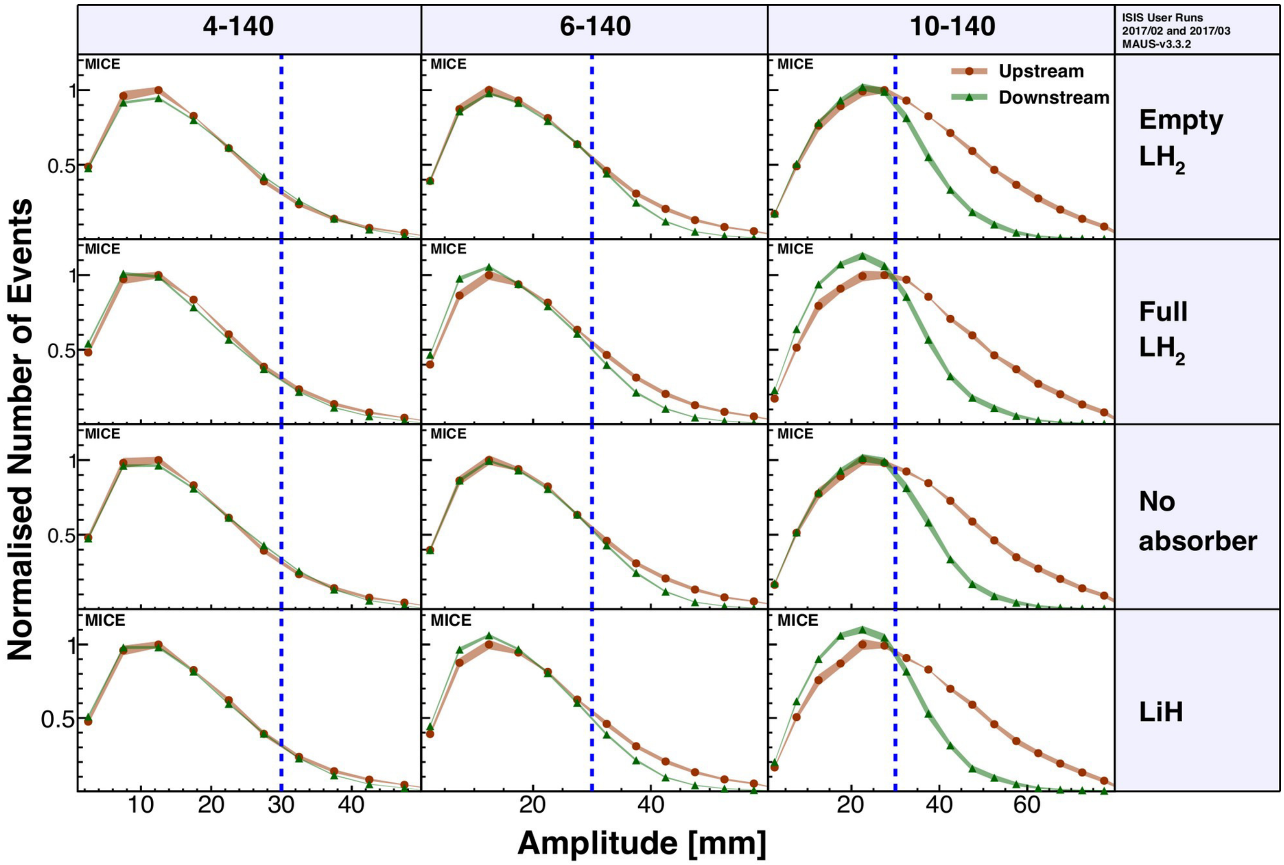

Figure 2: The amplitude distribution of the muon beam upstream and downstream of the absorber for a number of different configurations.

RESULTS

Transverse amplitude distributions were found by counting the number of muons sitting within hyper-ellipsoids of varying sizes in four dimensional phase space upstream and downstream. Enhancement in the number of particles at low amplitude when passing through the absorber was indicative of an increase in the number of muons in the beam core i.e. cooling. A decrease in the number of particles at high amplitude was indicative of either migration towards the beam core or scraping.

The amplitude distributions are shown in Fig. 2 [4]. Results are shown for beams having nominal momentum of 140 MeV/c and incident RMS emittances of 4, 6 and 10 mm (4-140, 6-140 and 10-140 respectively). Beam was passed through the liquid hydrogen vessel both in an empty (Empty LH2) and full (Full LH2) configuration. The beam was also passed through the experiment with No absorber and the lithium hydride (LiH) absorber. In the Empty LH2 and No absorber configuration, the core of the beam was observed to have the same number of particles both upstream and downstream of the absorber. The tail of the distribution was observed to be depleted above about 30 mm amplitude and this was attributed to beam scraping on the beam pipe leading to beam loss.

In the Full LH2 and LiH case, there was a significant enhancement in the number of muons downstream of the absorber in the beam core. This enhancement was the signal for cooling: the beam core density has increased. The ratios of the amplitude distributions are shown in Fig. 3 together with the simulated cooling performance. Where the number of muons has increased, the ratio is more than 1. Where the number of muons has decreased, the ratio is less than 1. A clear signal for the enhancement in core density is observed for settings where an absorber was installed. The simulated cooling performance shows good agreement with the measured data [5].

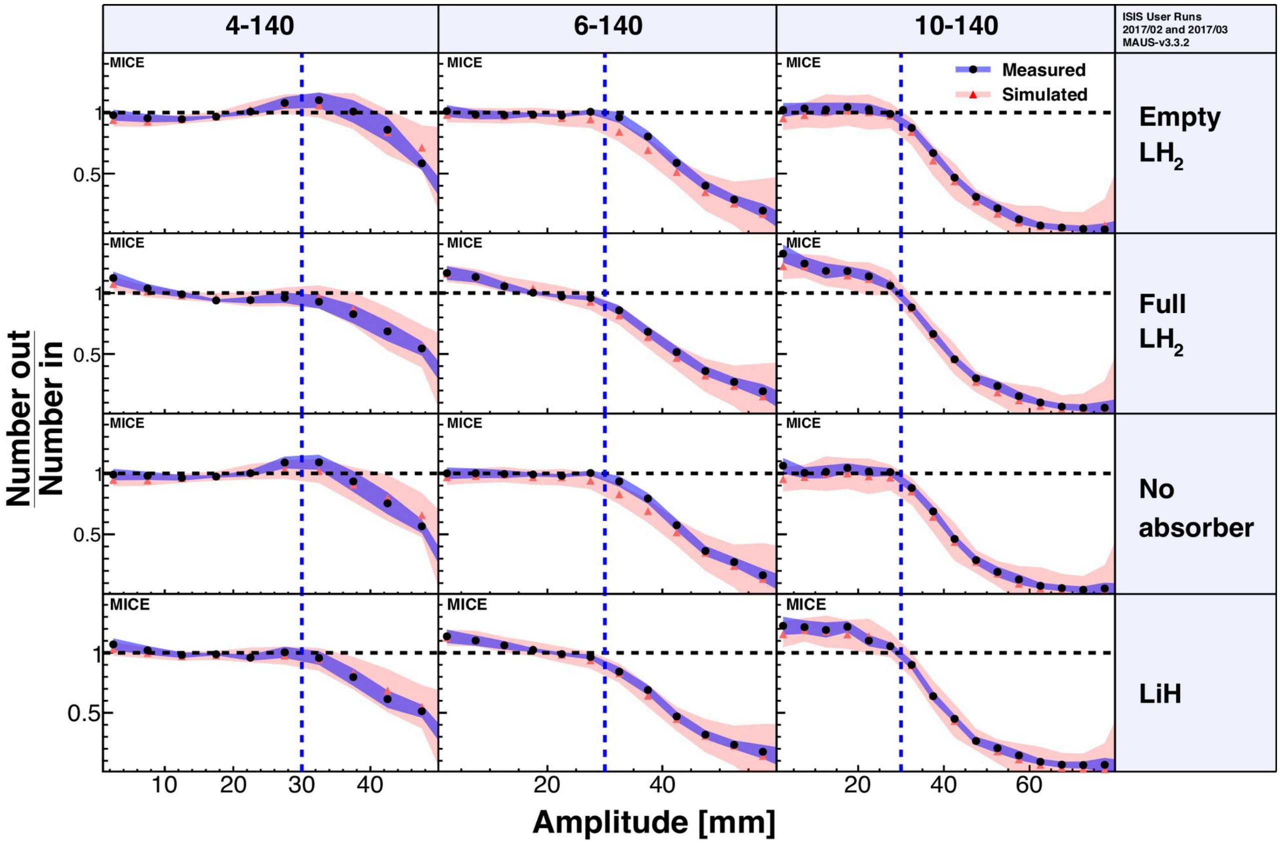

Figure 3: The ratio of downstream to upstream amplitudes. A ratio greater than 1 indicates an increase in particle density.

PROSPECTS AND CONCLUSIONS

The MICE Collaboration has recorded a substantial dataset with which to demonstrate muon ionization cooling and is well on its way to accomplishing its goals. Clear evidence of transverse ionization cooling has been presented. The analysis of MICE data continues.

Further settings are being explored having different momenta and different focussing properties. In particular, results including a lattice operating in solenoid mode and results showing RMS emittance are under study and are presented in [6] and [7]. Studies are in progress for a follow-up experiment. Designs are under study for lattices with enhanced cooling at lower emittances, including RF. In particular, by including a dipole in the lattice arrangement, a modest position-energy correlation may be introduced into the beam (dispersion). By passing the beam through an appropriately aligned wedge-shaped absorber, higher energy particles will experience greater energy loss leading to exchange of emittance from longitudinal to transverse. Together with the transverse cooling described here, so-called ‘6D’ cooling may be achieved. Studies of a muon source are underway. Using the proposed nuSTORM beam as a muon source is one particularly interesting proposal, described in [8]. The Muon Ionization Cooling Experiment has demonstrated conclusively the reduction of normalised emittance by ionization cooling. Analysis of data for a number of different beam conditions is ongoing. Design work to pursue a follow-up experiment is ongoing.

REFERENCES

[1] A. Skrinsky and V. Parkhomchuk, *Sov. J. Part. Nucl.* 12, 223, 1981.

[2] D. Neuffer, *Conf. Proc.* C 830811, 481, 1983.

[3] D. Neuffer, *Part. Accel.* 14, 75, 1983.

[4] M. Bogomilov, MICE collaboration, ”Demonstration of cooling by the Muon Ionization Cooling Experiment”, *Nature* 578, 53–59, 2020.

[5] C. T. Rogers, “Muon Ionization Cooling Experiment: Results & Prospects”, in *Proc. 12th Int. Particle Accelerator Conf. (IPAC'21)*, Campinas, Brazil, May 2021, pp. 4528-4530. `doi:10.18429/JACoW-IPAC2021-FRXB05`

[6] T. W. Lord, “Transverse Emittance Change and Canonical Angular Momentum Growth in MICE ‘Solenoid Mode’ with Muon Ionization Cooling”, in *Proc. 12th Int. Particle Accelerator Conf. (IPAC'21)*, Campinas, Brazil, May 2021, pp. 3289-3292. `doi:10.18429/JACoW-IPAC2021-WEPAB277`

[7] P. B. Jurj, “Normalized Transverse Emittance Reduction via Ionization Cooling in MICE ’Flip Mode’”, in *Proc. 12th Int. Particle Accelerator Conf. (IPAC'21)*, Campinas, Brazil, May 2021, pp. 474-477. `doi:10.18429/JACoW-IPAC2021-MOPAB134`

[8] C. T. Rogers, N. Gall, J.-B. Lagrange, and J. Pasternak, “nuSTORM Accelerator Challenges and Opportunities”, in *Proc. 12th Int. Particle Accelerator Conf. (IPAC'21)*, Campinas, Brazil, May 2021, pp. 4104-4106. `doi:10.18429/JACoW-IPAC2021-THPAB175`

PLASMA LENS IN PARAMETRIC RESONANCE IONIZATION COOLING

K. Yonehara, Fermi National Accelerator Laboratory, Batavia, IL, USA

Abstract

The article presents a concept of a plasma lens which will be generated in a dense hydrogen gas filled RF cavity. The plasma lens will be formed by beam-gas-plasma interactions. An exceptionally strong transverse magnetic and longitudinal RF electric focusing fields will appear in a short length. We consider that it will be integrated into a parametric-resonance muon ionization cooling channel as a strong momentum kicker to mitigate an issue of a large amplitude-dependent time of flight for a large angular distribution.

INTRODUCTION

A multi-TeV muon collider is a highly demanded machine for studying the Beyond Standard Model (BSM). Table 1 shows a step-approaching COM energy and luminosity of muon collider parameter proposed by the high energy physics theory and accelerator groups [1]. It should be noted that a 14-TeV machine is designed as a site-filler at the Fermilab campus. Besides, a 14 TeV μ+-μ- COM energy is equivalent to a 100 TeV pp collider.

Table 1: Muon Collider Parameter

Parameter (unit)	**3 TeV**	**10 TeV**	**14 TeV**
Lumi. L (10^{34} cm^{-2}s^{-1})	1.8	20	40
Num. of μs N_μ (10^{12})	2.2	1.8	1.8
Beam rep. rate (Hz)	5	5	5
μ beam power (MW)	5.3	14.4	20
B. field in coll. ring (T)	7	10.5	10.5
N. L. Emit. ε_L (MeV m)	7.5	7.5	7.5
E. spread (rms) ΔE/E (%)	0.1	0.1	0.1
N. T. Emit. ε_t (μm)	25	25	25
Beam size (rms) (mm)	3.0	0.9	0.63

To reach the desired luminosity, the muon beam size must be a sub-mm scale at a collision point. However, an initial size of the created muon beam is a foot-scale after the charged pions decaying. Ionization cooling is a promising technique to shrink a foot-size muon beam into a sub-mm. A timescale of the cooling should be an order of the average muon lifetime, $\gamma\tau_\mu$. A muon beam is incident into an ionization material and loses a kinetic energy due to ionizing the material. The beam lost energy is compensated by an RF accelerating field. As a result, the beam size continuously shrinks with repeating the process. However, nuclei in the material heat the muon beam via the multiple scattering. To mitigate the beam heating, a low-z element, like Hydrogen, Lithium or Beryllium are used as a cooling material and a beam window. Conventionally, a strong magnetic field is applied in a cooling channel to focus the beam at the material. The beam angular spread and therefore the beam emittance are reduced by ionization cooling. Therefore, to achieve a sub-mm-scale beam size, it requires a 50-Tesla focusing solenoid magnet in the final stage of cooling. Besides the muon beam is decelerated from 120-170 MeV to as an order of 10 MeV in the final cooling stage for applying a strong focusing force. Increasing transmission efficiency of muon beam in a high field solenoid cooling channel is challenging.

Significant progress has been made on a possible solution of the final cooling problem called Parametric-resonance Ionization Cooling [2-4]. Instead of focusing the beam by a strong focusing magnet, it uses a parametric resonant process to generate beam waist points. The beam phase space not evolutes on an elliptical trajectory (left-hand side plot in Fig. 1), but diverges on a hyperbolic function (right-hand side plot in Fig. 1). The main challenge of this solution is prevention of the beam smear at the focal points due to a large phase-space volume of even a pre-cooled muon beam. This can be done by compensating beam aberrations at the focal points or linearizing the beam dynamics between the focal points. The plasma focusing technique described in this article provides much stronger focusing magnetic fields than can be provided by conventional superconducting magnets and is also naturally compatible with and simplifies the complexity of the parametric-resonance ionization cooling approach by making the beam size smaller and therefore reducing the aberrations. The Parametric resonance Ionization Cooling scheme is described in the first half of the article. The plasma lens is presented in the second half of the article.

PARAMETRIC-RESONANCE IONIZATION COOLING CONCEPT

The limit on the minimum achievable emittances in muon ionization cooling comes from the equilibrium between the cooling process and multiple Coulomb scattering in the absorber material. The concept of Parametric-resonance Ionization Cooling (PIC) is to push this limit by an order of magnitude in each transverse dimension by focusing the muon beam very strongly in both planes at thin absorber plates. This creates a large angular spread of the beam at the absorber locations, which is then cooled to its equilibrium value resulting in greatly reduced transverse emittances. Achieving adequately strong focusing using conventional magnetic optics would require unrealistically strong magnetic fields. Instead, PIC relies on a resonant process to provide the necessary focusing. A half-integer parametric resonance is induced in a cooling channel, causing focusing of the beam with the period of the channel's free oscillations.

The resonant perturbation changes the particles' phase-space trajectories at periodic locations along the channel from their normal elliptical shapes to hyperbolic ones as shown in Fig. 1. Thus, at certain periodic focal positions, the beam becomes progressively narrower in x and wider in x' as it passes down the channel. Without damping, the beam dynamics are not stable because the beam envelope grows with every period as illustrated in Fig. 2. Placing energy absorbers at the focal points stabilizes the beam motion by limiting the beam's angular divergence at those points through the usual ionization cooling mechanism. These dynamics then result in a strong reduction of the beam spot size at the absorber locations leading to transverse beam emittances that are an order of magnitude smaller than without the resonance. The longitudinal emittance is maintained constant against energy struggling by emittance exchange occurring due to dispersion or its slope at the locations of wedge or flat absorbers.

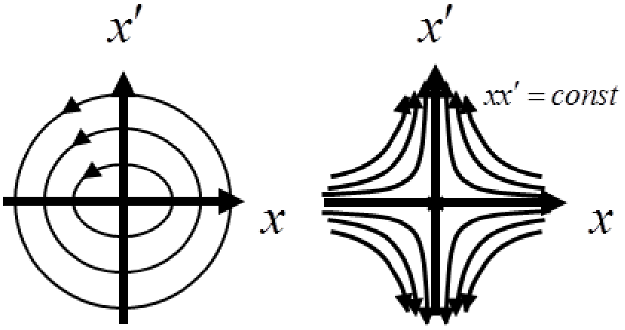

Figure 1: Parametric-resonance Ionization Cooling.

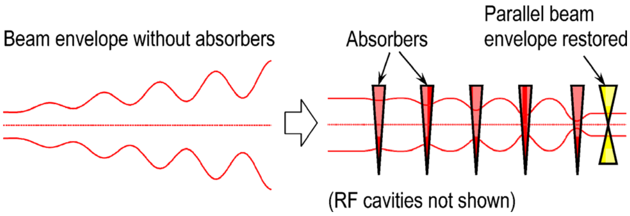

Figure 2: Stabilizing effect of ionization cooling energy absorbers in a channel with a half-integer resonance.

The normalized equilibrium transverse emittance achievable in PIC is given by [5]

$$\varepsilon_{\perp}^{n} = \frac{\sqrt{3}}{4\beta}(Z+1)\frac{m_e}{m_\mu}w\,,$$

where $\beta = v/c$ is the relativistic factor, Z is the absorber material's atomic number, m_e and m_μ are the electron and muon masses, respectively, and w is the average absorber thickness in the beam direction. The equilibrium beam size σ_a and angular spread θ_a at the absorber and the equilibrium momentum spread $\Delta p/p$ are given by [5]

$$\sigma_a^2 = \frac{1}{8}\frac{(Z+1)}{\gamma\beta^2}\frac{m_e}{m_\mu}w^2\,,$$

$$\theta_a^2 = \frac{3}{2}\frac{(Z+1)}{\gamma\beta^2}\frac{m_e}{m_\mu}\,,$$

$$\left(\frac{\Delta p}{p}\right)^2 = \frac{3}{8}\frac{(\gamma^2+1)}{\gamma\beta^2}\frac{m_e}{m_\mu}\frac{1}{\log}$$

where γ is the muon relativistic energy factor and log is the Coulomb logarithm of ionization energy loss for fast particles. The expected PIC parameters following from the equations above for a 250 MeV/c muon beam are summarized in Table 2. Note that the absorbers are thicker at the beginning of the channel in order to produce a higher cooling rate of an initially large-emittance beam. As the beam cools propagating down the channel, the absorber thickness is gradually reduced in order to reach the minimum practical transverse emittance. Since the cooling rate gets lower for thinner absorbers, the minimum practical absorber thickness is determined by the practically acceptable beam loss due to muon decay.

Table 2: Expected PIC Parameters

Parameter with unit	**Initial**	**Final**
Beam momentum, p MeV/c	250	250
Num. of particles per bunch, N_b 10^{10}	1	1
Be (z = 4) absorber thickness, w mm	20	2
Nor. Tran. Emit. (rms), $\varepsilon_x = \varepsilon_y$ µm	230	23
Beam size at abs., $\sigma_a = \sigma_x = \sigma_y$ mm	0.7	0.1
Ang. spr. at abs., $\theta_a = \theta_x = \theta_y$ mrad	130	130
Momentum spread (rms), $\Delta p/p$ %	2	2
Bunch length (rms), σ_z mm	10	10

A PIC cooling channel can be implemented using alternating transverse focusing. To provide focusing of the beam in both horizontal and vertical planes simultaneously, the horizontal oscillation period λ_x must be equal to or be a low-integer multiple of the vertical oscillation period λ_y. Emittance exchange also requires λ_x and λ_y to be low integer multiples of the dispersion period λ_D. Thus, a cooling channel with alternating focusing optics must have correlated values of λ_x, λ_y and λ_D:

$$\lambda_x = n\lambda_y = m\lambda_D\,,$$

where n and m are integers. An optics example satisfying the above equation with $\lambda_x = 2\lambda_y = 4\lambda_D$ is illustrated in Fig. 3. The correlated optics design allows one to excite parametric resonances independently in the two planes using periodically placed quadrupoles.

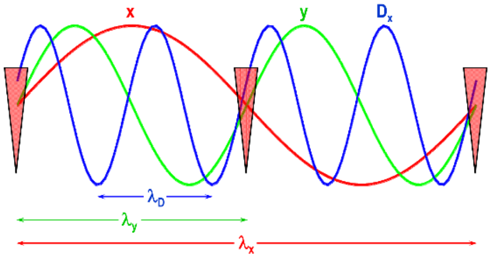

Figure 3: Particle's horizontal x and vertical y betatron trajectories and horizontal dispersion D_x for the $\lambda_x = 2\lambda_y = 4\lambda_D$ case of correlated optics.

There have been several correlated-optics designs of PIC cooling channels with increasingly improved performance:

1. Epicyclic channel consisting of lumped elements [2],
2. Epicyclic channel design using continuous fields [2],
3. Twin helix channel design using continuous fields [2, 3,4],

ISBN: 978-3-95450-243-1 ISSN: 2226-0374 doi:10.18429/JACoW-COOL2021-S702

4. Skew parametric-resonance ionization cooling channel [2,3].

Cooling in a PIC channel was successfully demonstrated with stochastic effects ignored. For example, Fig. 4 shows evolution of the three 2D emittances along a twin-helix channel where the correlated optics conditions have been tuned and parametric resonances have been excited in both transverse planes at appropriate growth rates.

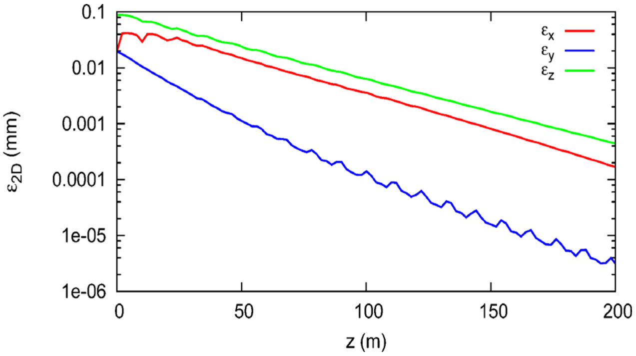

Figure 4: Evolution of the horizontal ε_x, vertical ε_y, and longitudinal ε_z 2D emittances along a twin-helix channel ignoring stochastic effects.

To proceed to cooling simulations including stochastic effects, compensation of beam aberrations is required. This was verified by running a first-order simulation with stochastic effects included. Aberrations from one absorber to another must be compensated to a degree where they are small compared to the beam size at the absorber. Since the equilibrium angular spread is on the order of a hundred milliradians, the angle-dependent aberrations must be precisely compensated over the angular range of a few hundred milliradians. This is perhaps the most challenging aspect of the PIC channel design.

Alternating transverse focusing allows one to use multipole fields to correct aberrations. However, multipole fields in combination with correlated optics introduce another serious problem, namely, non-linear resonances causing loss of dynamical stability. For example, multiple octupole families are needed in a cooling channel to compensate spherical aberrations. However, with our choice of betatron tunes of $\nu_x = 0.25$ and $\nu_y = 0.5$, any octupole periodicity m causes resonances in both planes. Dispersion further complicates the resonance structure. Selecting different betatron tunes does not help; as long as the betatron periods are integer multiples of the channel period as required for the correlated optics, multipole fields will tend to cause non-linear resonances. This makes it difficult to find a set of multipoles sufficient for aberration compensation that does not cause beam instabilities.

The Skew PIC concept was developed to overcome this issue. Skew PIC introduces coupling into a cooling channel in such a way that the periodic focusing is preserved, but the canonical betatron tunes are shifted from the resonant values that caused issues in the PIC channel. The beam is azimuthally rotated between consecutive focal points due to coupling, and this moves the betatron motion away from nonlinear resonances. This reduces the dimensionality of the aberration compensation problem to just the radial dimension, therefore reducing the number of required compensating multipoles. In addition, coupling equates the parametric resonance rates in the two transverse dimensions, thus requiring only one resonance harmonic, and equipartitions the cooling decrements in the two transverse dimensions.

A skew PIC channel still requires a large dynamic aperture to accommodate the large beam angular spread at the focal points, or equivalently large beam size between the focal points. A significant progress has been made on dynamic aperture optimization of the skew PIC channel using higher-order multipoles. It has been demonstrated [6] that an optimized channel with realistic magnetic fields can accommodate a beam with an angular divergence of 120 mrad at the focal points and a momentum spread of 1%. No particles were lost after tracking through 300 channel periods. However, this angular acceptance is still about a factor of two too small given the equilibrium rms angular spread of about 130 mrad at absorbers.

A short 3-dimensional momentum kicker is considered in the skew PIC which can mitigate the amplitude-dependent time of flight for a large angular spread beam. A dense hydrogen gas filled RF cavity will be the solution for this problem because the cavity can excite extremely high RF gradients (> 40 MV/m) in a strong magnetic field and the plasma lens is formed in the gas volume and induce a high magnetic field gradient (> 300 T/m) in a mm-scale volume. The plasma lens is discussed in the next section.

PLASMA DYNAMICS TO FORM PLASMA LENS IN GAS-FILLED RF CAVITY

The proposed plasma lens in a gas-filled RF cavity is induced in a dense hydrogen gas due to beam-gas-plasma interactions. Figure 5 shows a diagram of the interactions in the cavity. As the first step, a muon beam incident into the cavity ionizes hydrogen molecule (beam-gas interactions in Fig. 5). Because the gas density is an order of 10^{21} cm^{-3}, the number of electron-ion pairs in the gas by ionization is an order of 1,000/cm per muon. In the next step, because the gas density is so high, ionized electrons are quickly thermalized (gas-plasma interactions). The estimated mean thermalization time is $\tau_{therm} \sim 1/\zeta_e \cdot \nu_e$ = 1-20 ps [7] where ζ_e is an energy damping ratio (typically 0.1 to 0.005) and ν_e is a mean collision frequency of electrons in hydrogen gas (typically 10^{13} Hz). When the plasma reaches to an equilibrium condition, a mean electron velocity becomes a drift velocity v_d in τ_{therm} (gas-plasma interactions). v_d was measured in the past as a function of E_{rf}/p_{gas}, where E_{rf} is a peak RF field gradient and p_{gas} is a gas pressure at STP. The range of measured E_{rf}/p_{gas} is for ionization cooling. v_d is typically an order of 10^6 cm/s in the cavity [8,9].

A beam-induced gas plasma is polarized by an electric field due to the space charge of beam (beam-plasma interactions). The space charge is neutralized by the polarization. A time constant of the space charge neutralization is given $\tau_{SCN} \sim \frac{r_b}{2(n_p/n_b)v_d}$, where r_b is an RMS beam spot size, and n_p/n_b (typically 1,000) is the ratio of the plasma and the beam, respectively [7]. The estimated time is $\tau_{SCN} \sim$ 50 ps at r_b = 1 mm. It should be noted that the space charge neutralization time is simulated in WARP, which is $\tau_{SCN} \sim$ 15 ps. The beam bunch length is 50-200 ps. It will suggest that the space charge is neutralized during beam passing in the gas-filled cavity. It should also be noted that the space charge neutralization occurs with both signs by polarizing plasma.

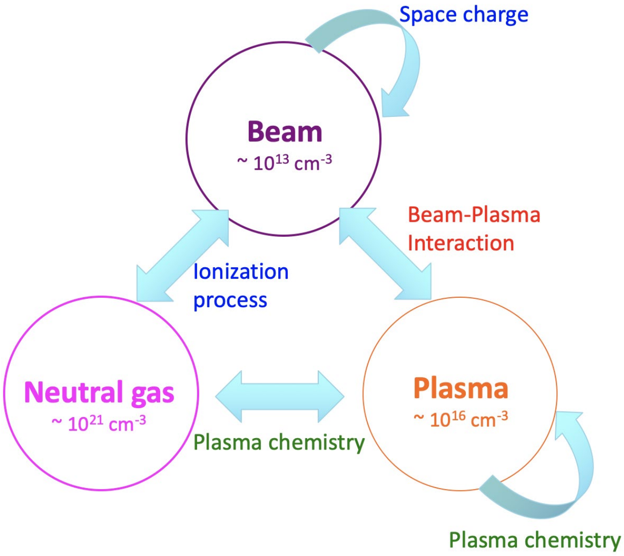

Figure 5: Diagram of beam-gas-plasma interactions.

Because the space charge is neutralized while the axial magnetic field still remains in the beam volume, the magnetic field focuses the beam. Figure 6 shows the estimated azimuthal magnetic fields with r_b = 2 mm (blue) and 1 mm (orange) [7]. The bunch length is 10 mm and the number of particles is 10^{12} per bunch. The magnetic field gradient is 87 (blue) and 326 (orange) T/m, respectively. This field will be used for focusing beam in the transverse direction.

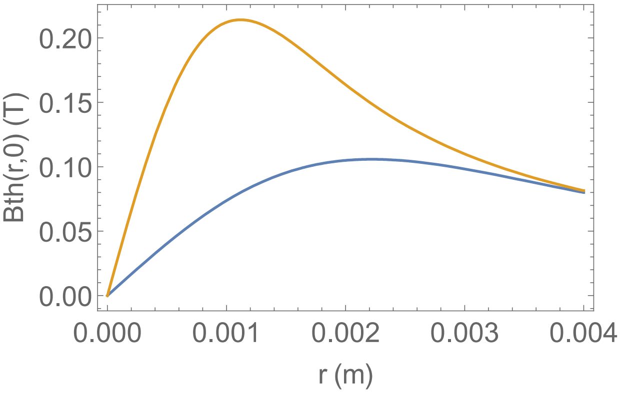

Figure 6: Estimated magnetic field induced by muon beam.

Figure 7 shows a preliminary simulation result of a plasma lens [7]. On the left-hand plot, there is no hydrogen gas in the beam volume. The size of muon beam, especially a tail grows due to a space charge. On the other hand, on the right-hand plot, a muon beam interacts with hydrogen gas and creates an electron-ion pair. For simplicity, the beam does not lose its kinetic energy by ionization, instead, the beam energy is immediately restored in simulation. There is no RF field so that there is no longitudinal focusing. Nevertheless, the beam size is shrunken, especially a tail due to the plasma lens effect.

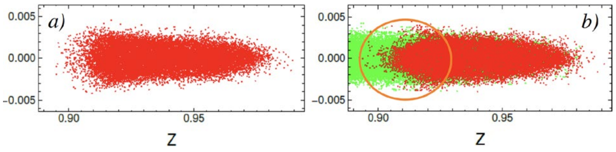

Figure 7: Preliminary simulation result of plasma lens. A red point is muon, a green point is electron. a). No hydrogen gas in the beam volume, while b) with hydrogen gas. The beam is focused at the tail (orange circle) due to the plasma lens.

As the last discussion, the maximum available RF gradient in the gas filled RF test cell is presented. Figure 8 shows the observed RF gradient as a function of the hydrogen gas density [10]. One conclusive result is that gas can greatly suppress the electric breakdown even an extremely high RF gradient is excited in the cavity in a strong magnetic field. The gas-filled RF can excite 40 MV/m or higher field gradients when the gas density > 0.0045 g/cm^3. The experiment validates a simple model. A dense gas increases an electrical resistance between two electrodes and suppresses the dark current flow. It suggests that the gas-filled RF cavity functions under strong magnetic fields and severe radiation environments. Also, we observed that no conditioning is needed in the gas-filled RF test cell. The breakdown probability is independent of surface condition of the electrodes. It may suggest that the gas-filled RF cavity removes the resonant frequency dependence on the maximum available field gradient expressed by Kilpatrick's limit. Further investigations are needed.

It should also be noted that the plasma density of the RF electric breakdown was measured in the gas-filled RF test cell. It is an order of 10^{19} cm^3. The value is three orders of magnitude lower than the beam-induced plasma density. It suggests that the beam-induced plasma does not induce the breakdown in the cavity. It is also experimentally validated. Instead, the beam-induced plasma consumes the RF power in the cavity. It is a considerable issue to design the cooling channel with the gas-filled RF cavity. Further investigations are needed.

Because the gas-filled RF cavity can excite extremely high RF gradients, the length of gas-filled RF cavity can be very short, a few mm. Besides, the focusing field gradient of the plasma lens can be > 360 T/m. It will be an ideal momentum kicker, $F \cdot \delta t = \delta p$ in the transverse direction by using the plasma lens and in the longitudinal direction by the high RF gradient. Further analysis is needed to apply the plasma lens in PIC. Possible study is given in the following list:

ISBN: 978-3-95450-243-1 ISSN: 2226-0374 doi:10.18429/JACoW-COOL2021-S702

- Validate the concept of plasma lens in numerical simulation. We need a numerical simulation to study beam-gas-plasma interactions.
- Manipulate the plasma lens parameter. Plasma density, temperature, electron drift velocity, etc can be controlled by adjusting E_{rf}/p_{gas} , and applying plasma chemistry. For example, a small electronegative dopant immediately reduces the electron plasma density and plasma temperature. Those were experimentally demonstrated in the gas-filled RF test cell. A new experiment is needed to measure the fast plasma signal.
- Optimize the plasma lens parameter and RF field gradient for PIC. Because the plasma lens is formed by the beam itself, the field gradient may not be linear. It may require correction fields to maximize the cooling performance. Those studies can be made in numerical simulations.

We have developed a parallel processing plasma simulation code, SPACE for the simulation study [11]

.

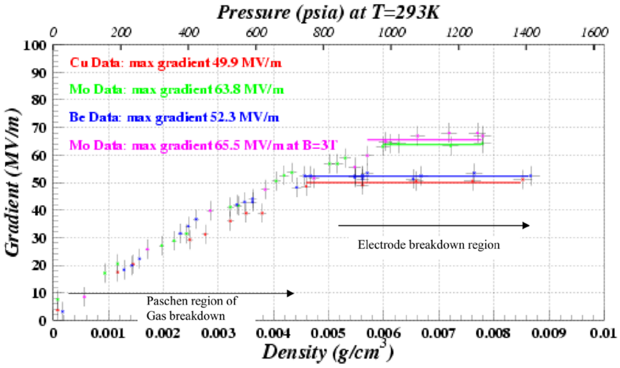

Figure 8: Measured maximum available RF gradient in the gas-filled RF test cell.

CONCLUSION

We propose a parametric resonance ionization cooling for the final muon ionization cooling channel. We found that solving the amplitude-dependent time of flight for a large angular spread beam is the key to make PIC for the real cooling channel. To mitigate the issue, we propose to integrate the plasma lens which is formed in the hydrogen gas-filled RF cavity. The design is still conceptual.

REFERENCES

[1] D. Schulte, "Roadmap Process of the Muon Beam Panel", presented in NuFACT 2021. `https://indico.cern.ch/event/855372/contributions/4456520/attachments/2303915/3919320/neutrino.pdf`

[2] Y. Derbenev and R.P. Johnson, "Ionization cooling using a parametric resonance", Proceedings of 2005 Particle Accelerator Conference, Knoxville, Tennessee, `https://accelconf.web.cern.ch/p05/PAPERS/TPPP014.PDF`

[3] Ya.S. Derbenev *et al.,* "Parametric-resonance Ionization Cooling of Muon Beams", `arXiv:1205.3476`

[4] J.A. Maloney, "Parametric-resonance ionization cooling for muon beams in the twin helix channel", NIU Thesis, `https://www.niu.edu/beam-physics-code/_pdf/_theses_dissertations/Maloney%20dissertation.pdf`

[5] K.B. Beard *et al.,* "Simulations of parametric resonance ionization cooling of muon beams", in Proc. PAC'05, Knoxville, TN, TPPP013, p. 1321. `https://accelconf.web.cern.ch/p05/PAPERS/TPPP013.PDF`

[6] A. Sy *et al.,* "Muon tracking studies in a skew parametric resonance ionization cooling channel", in Proc. IPAC'12, WEPJE015, p. 2705. `http://accelconf.web.cern.ch/IPAC2015/papers/wepje015.pdf`

[7] M. Chung and A. Tollestrup, unpublished.

[8] M. Chung *et al.,* "Pressurized H2 rf Cavities in Ionizing Beams and Magnetic Fields", *Phys. Rev. Lett.* 111, p. 184802, 2013.

[9] B. Freemire *et al.*, "Pressurized RF Cavities in Ionizing Beams", *Phys. Rev.* AB. 19, 062004, 2016.

[10]P. Hanlet *et al.,* "High Pressure RF cavities in magnetic fields", in proceedings of EPAC'06, Edinburgh, U.K., June 2006, paper TUPCH147,.

[11]K. Yu *et al.,* "Simulation of beam-induced plasma in gas-filled rf cavities", *Phys. Rev.* AB. 20, 032002, 2017.

ISBN: 978-3-95450-243-1 ISSN: 2226-0374 doi:10.18429/JACoW-COOL2021-S803

WIGGLER ENHANCED PLASMA AMPLIFIER FOR COHERENT ELECTRON COOLING*

G. Stupakov†, SLAC National Accelerator Laboratory, Menlo Park, CA, USA
A. Zholents, Argonne National Laboratory, Argonne, IL, USA

Abstract

Coherent electron cooling [1] using a plasma-cascade amplifier (PCA) [2] can provide much faster cooling rates of hadrons than the conventional microwave stochastic cooling due to an extremely wide bandwidth of a pickup modulator, a kicker, and the amplifier. A PCA creates unstable plasma oscillations using modulation of the plasma frequency by varying the transverse beam size along the beam line with strong field solenoids. In this work we propose an alternative approach to the problem: the plasma frequency is modulated in a sequence of wiggler magnets separated by drifts or chicanes. This approach has the promise of obtaining a compact amplifier due to a more efficient modulation of the plasma frequency, although it requires separation of the hadron and electron orbits in the amplifier region to synchronize their time of flight through the cooling system.

INTRODUCTION

Coherent electron cooling [1] (CEC) can provide much faster cooling rates of hadrons than the conventional microwave stochastic cooling due to a wide bandwidth of the pickup modulator, the kicker, and the amplifier. While the original idea of coherent cooling relied on a free electron laser as an amplifier, which has a relatively narrow bandwidth [3], a later development of the idea involved a broadband amplifier based on the microbunching instability [4–6]. This approach is known under the acronym of MBEC (microbunched electron cooling). More recently, in Ref. [2], the idea of a plasma cascade amplifier (PCA) was proposed that conceptually has an even broader bandwidth than MBEC. The PCA creates unstable plasma oscillations using modulation of the plasma frequency by varying the transverse beam size along the beam line with strong-field solenoids. Unfortunately, the PCA length with several amplification sections can become prohibitively long because the plasma wavelength increases with the Lorentz gamma factor as $\gamma^{3/2}$. In this work we propose an alternative approach to the problem: the plasma frequency is modulated in a sequence of wiggler magnets separated by drifts or small chicanes. We refer to this scheme as the *wiggler enhanced plasma amplifier*, or WEPA. This approach has the promise of obtaining a compact amplifier due to a more efficient modulation of the plasma frequency.

PLASMA OSCILLATIONS IN A RELATIVISTIC BEAM

We begin with a derivation of the frequency of plasma oscillations when a relativistic beam propagates inside a wiggler or in a drift. In our derivation, we neglect the particle energy spread assuming a cold beam. Our interest here is in short-wavelength plasma perturbations (with wavelength in the micron range, or even shorter) so we can treat the beam in local approximation assuming that its linear density n_0 is constant and neglecting its dependence on the longitudinal coordinate z. We consider the linear density perturbation $\Delta n(s,z)$ and the relative energy perturbation $\Delta\eta(s,z) = \Delta E(s,z)/E_0$, where z is the longitudinal coordinate in the beam relative to a reference particle, and s is the path length along the beam line. These quantities are Fourier transformed over the coordinate z: $\Delta\hat{n}_k(s) = \int_{-\infty}^{\infty} \Delta n(s,z)e^{-ikz}dz$ and $\Delta\hat{\eta}_k(s) = \int_{-\infty}^{\infty} \Delta\eta(s,z)e^{-ikz}dz$.

In a drift, we have the linearized continuity equation for cold plasma,

$$\frac{\partial \Delta n(s,z)}{\partial s} + \frac{1}{\gamma^2}\frac{\partial}{\partial z} n_0 \Delta\eta(s,z) = 0. \tag{1}$$

Applying the Fourier transform to this equation yields

$$\frac{d\delta\hat{n}_k}{ds} = -\frac{ikl}{\gamma^2} n_0 \Delta\hat{\eta}_k. \tag{2}$$

In a wiggler, particles move along the s coordinate with a smaller longitudinal velocity corresponding to the *longitudinal* gamma factor

$$\gamma_z = \frac{1}{\sqrt{1 - v_z^2/c^2}} = \frac{\gamma}{\sqrt{1 + K^2/2}}, \tag{3}$$

where $K = eB\lambda_w/2\pi mc^2$ is the wiggler parameter with B the amplitude magnetic field in the wiggler and λ_w the wiggler period. Here we assume a plane wiggler. Correspondingly, in a wiggler, we replace γ^2 by γ_z^2 in the continuity equation Eq. (2),

$$\frac{d\Delta\hat{n}_k}{ds} = -ik\frac{1}{\gamma_z^2} n_0 \Delta\hat{\eta}_k. \tag{4}$$

The equation for $\Delta\hat{\eta}_k$ describes the energy exchange between the particles due to the Coulomb interaction. Here we will accept the model of Ref. [5] in which the interaction between the particles of the beam is replaced by the Coulomb interaction of charged disks (or slices of the beam) with a Gaussian surface charge distribution. Then the equation for

---

* This work supported by the Director, Office of Science, Office of Basic Energy Sciences, of the U.S. Department of Energy under Contracts No. DE-AC02-06CH11357 and DE-AC02-76SF00515.

† stupakov@slac.stanford.edu

$\Delta\hat{\eta}_k$ can be recovered from Eqs. (54) and (55) of Ref. [5],

$$\frac{d\Delta\hat{\eta}_k}{ds} = \zeta(k)\Delta\hat{n}_k, \tag{5}$$

with

$$\zeta(k) = -\frac{2ir_e}{\gamma\gamma_z\sigma_\perp} H\left(\frac{k\sigma_\perp}{\gamma_z}\right), \tag{6}$$

where r_e is the classical electron radius, $\sigma_\perp$ is the rms size of the plasma in the wiggler (we assume an axisymmetric beam), and the function H is defined in Ref. [5]. Equation (6) is written for the wiggler; in free space one has to replace γ_z by γ. Combining Eqs. (4) and (5) we obtain

$$\frac{d^2\Delta\hat{n}_k}{ds^2} = -c^{-2}\omega_p^2(k)\Delta\hat{n}_k, \tag{7}$$

in which the plasma frequency ω_p is defined by

$$\omega_p(k) = \sqrt{\frac{r_e n_0 c^2}{\sigma_\perp^2\gamma\gamma_z^2}} F(\kappa_p), \tag{8}$$

where $F(\kappa_p) = \sqrt{2\kappa_p H(\kappa_p)}$ with $\kappa_p = k\sigma_\perp/\gamma_z$. The plot of the function F is shown in Fig. 1; for large values of its argument F tends to 1.

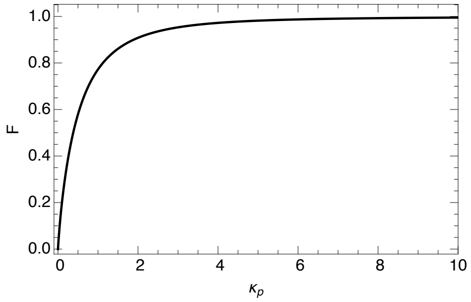

Figure 1: Plot of function $F(\kappa_p)$.

To illustrate the typical numerical values, for the electron beam with the peak current $I_e = 100$ A, $\sigma_\perp = 100\ \mu$m, and $\gamma_z = \gamma = 300$, the plasma period measured in units of length is $\lambda_p = 2\pi c/\omega_p \approx 45$ m, for $2\pi/k < 10\ \mu$m (in this region the function F is approximately equal to 1).

PERIODIC SYSTEM OF WIGGLERS AND DRIFTS

We now consider a periodic sequence of wigglers separated by drift sections. One cell of such a system of length $2L = l_w + l_d$ is shown in Fig 2. Our goal here is to calculate how an initial density perturbation $\Delta\hat{n}_k$ is amplified after the passage through the cell. For this, one has to consider the evolution of the column vector $(\Delta\hat{n}_k, \Delta\hat{\eta}_k)^T$. Noting that from Eq. (4) it follows that $\Delta\hat{\eta}_k \propto \gamma_z^2 d\Delta\hat{n}_k/ds$, it is more convenient to track the evolution of the vector

$$\left(\Delta\hat{n}_k, \frac{\gamma_z^2}{\gamma^2}\frac{d\Delta\hat{n}_k}{ds}\right)^T, \tag{9}$$

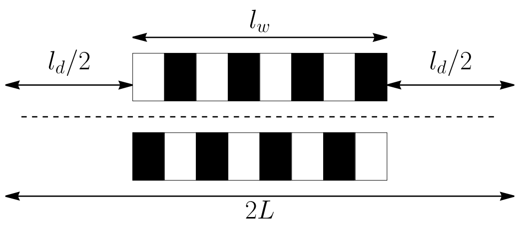

Figure 2: One cell of a periodic system of wigglers and drifts. The wiggler length is l_w and the drift length is l_d; the total cell length is $2L$.

where inside the wiggler γ_z is given by Eq. (3), and in the drift $\gamma_z = \gamma$.

Inside the wiggler the plasma frequency is constant, and using Eq. (7) it easy to find that the transformation of the vector in Eq. (9) over length s is given by the matrix

$$M_w(s, \omega_p) = \begin{pmatrix} \cos(\omega_p s/c) & \frac{\gamma^2 c}{\gamma_z^2\omega_p}\sin(\omega_p s/c) \\ -\frac{\gamma_z^2\omega_p}{\gamma^2 c}\sin(\omega_p s/c) & \cos(\omega_p s/c) \end{pmatrix}. \tag{10}$$

The same matrix can be used in the drift if we set $\gamma_z = \gamma$ in Eqs. (10) and (8). However, to simplify our analysis we assume that the plasma frequency in the drift is so small compared with the plasma frequency in the wiggler that it can be neglected. The matrix M in this case can be obtained from Eq. (10) as the limit $\omega_p \to 0$, which gives

$$M_d(s) = \begin{pmatrix} 1 & s \\ 0 & 1 \end{pmatrix}. \tag{11}$$

The matrix for the cell shown in Fig. 2 is then given by

$$M_{\text{cell}} = M_d(gL) \cdot M_w(2(1-g)L, \omega_p) \cdot M_d(gL), \tag{12}$$

where $g = l_d/2L$ is the fraction of the length occupied by the drifts.

GAIN IN THE WEPA AMPLIFIER

Let G be an eigenvalue of the one-cell matrix

$$M_{\text{cell}} - GI = 0, \tag{13}$$

where I is the unit 2×2 matrix. Because M_{cell} is symplectic, it has two eigenvalues of G with either $|G| = 1$, or one of the eigenvalues has $|G| > 1$. We define the *gain* $|G|$ in one cell as the maximum value of the two eigenvalues, $|G| \geq 1$.

In our analysis we will use the undulator parameter $K = 2$ that corresponds to $\gamma_z/\gamma = 0.58$. Figure 3 shows the plot of the gain as a function of the parameter g and the ratio of the half cell length L to the plasma period $\lambda_p = 2\pi c/\omega_p$ inside the wiggler. As we see from this plot, higher values of $|G|$ are attained for larger values of g. We choose $g = 0.9$ for further analysis, which means that the wiggler occupies 10% of the length of the cell. In order to obtain the gain factor as a function of the wavenumber k, we need to specify the

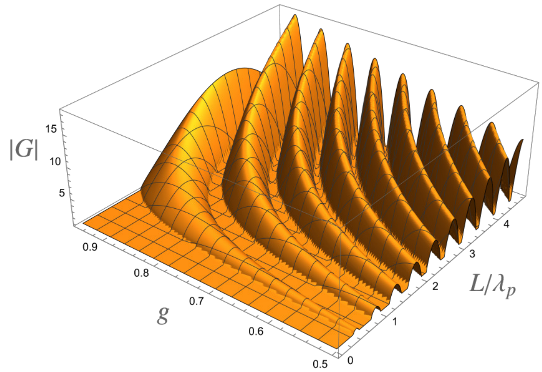

Figure 3: Gain for one cell as a function of g and $L_{/}\lambda_p$.

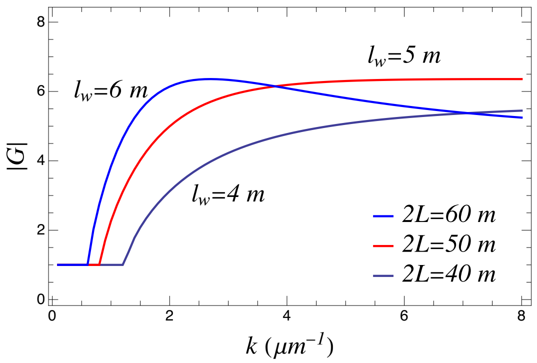

Figure 4: Gain per one cell for several values of l_w. Since we assume that l_w is equal to 0.1 of the cell length, the total length of the cell is ten times larger than l_w (indicated in the figure).

beam parameter for which we choose the values $I_e = 150$ A and $\sigma_\perp = 70$ μm. The gain profiles for several values of the length of the wiggler l_w are shown in Fig. 4. Note that formally, in the model of a cold beam, for these three cases the gain remains constant (non zero) when $k \to \infty$. If we choose $l_w = 5$ m as a reference case, then we see that at large values of k the gain function is approximately equal to 6. With four such cells the amplification factor will be $6^4 \approx 1300$, which is a large enough number to make it promising for use in a CEC cooling system.

Wigglers (and chicanes, see below) slow down the electrons, which should be carefully synchronized with hadrons in the modulator and the kicker of the cooling system. This means that the hadrons' path in the cooler should be modified (relative to the straight beam line) such that their time of flight between the modulator and the kicker is equal to that of the electrons.

SHORT CELLS WITH CHICANES

Unfortunately, the cell length of ∼ 50 m in the system considered in the previous section is relatively large. We can considerably shorten it if we notice that the drift matrix, Eq. (11), is physically equivalent to the transport matrix element R_{56} equal to its ballistic value, $R_{56} = l_d/\gamma^2$. This element converts the energy perturbation $\Delta\hat{\eta}_k$ in the plasma oscillation into a density perturbation $\Delta\hat{n}_k$. For $l_d = 45$ m and $\gamma = 300$, we find $R_{56} = 0.52$ mm. Such a value of R_{56} can be easily provided by a weak chicane (of length ∼ 1 m), which would drastically shorten the length of the WEPA amplification cell. Two cells of such a modified WEPA amplifier are shown in Fig. 5.

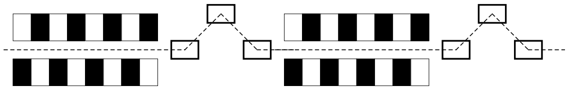

Figure 5: Two cells of a WEPA amplifier in which drifts are replaced by small chicanes.

EFFECTS OF BEAM ENERGY SPREAD AND CSR WAKE FIELDS

In our previous analysis we ignored the energy spread in the beam. A finite energy spread leads to Landau damping of plasma oscillation with very short wavelengths. This effect can also be explained as smearing of the density perturbations in a drift or a chicane due to the fact that particles with different energies are shifted in the longitudinal direction of the beam in proportion to $R_{56}\eta$. The suppression of the amplitude of the plasma oscillations is given by the factor [7]

$$\exp\left[-\frac{1}{2}k^2 R_{56}^2 \sigma_\eta^2\right], \tag{14}$$

where σ_η is the rms relative energy spread in the beam. As an example, let us take $\sigma_\eta = 2 \times 10^{-4}$ and $R_{56} = 0.5$ mm. With these parameters, the suppression of the amplification becomes noticeable at $k \sim \sqrt{2}/R_{56}\sigma_\eta \approx 13.5$ μm^{-1} (this corresponds to the frequency 640 THz).

Another effect that was ignored in our analysis is the coherent synchrotron radiation (CSR) wake field inside the wigglers. This wake field becomes more important in wigglers with a large value of K and hence a stronger magnetic field. Adding to space charge forces, this wake field will modify the property of the plasma oscillations. In the limit when this wake field dominates the space charge, it might lead to a different kind of instability as studied in Refs. [8,9].

SUMMARY

In this paper we extended the PCA concept for the case when the variation of the plasma frequency in the beam is achieved with the help of wiggler magnets. A periodic variation of this frequency leads to the parametric instability of plasma oscillations in the beam and can be used as an amplifier for the coherent cooling of hadrons beams. This system has an excellent frequency bandwidth that can be considerably larger than that of MBEC. We plan to include the CSR effects in future analysis of the WEPA cooling system.

ACKNOWLEDGEMENTS

The authors thank members of M. Blaskiewicz's group for useful discussions of this work.

REFERENCES

[1] V. N. Litvinenko and Ya. S. Derbenev, "Coherent electron cooling", *Phys. Rev. Lett.*, vol. 102. p. 114801, 2009.

[2] V. N. Litvinenko *e*t al., "Plasma-cascade instability", *Phys. Rev. Accel. Beams*, vol 24, p. 014402, Jan 2021.

[3] G. Stupakov and M. S. Zolotorev, "Comment on "coherent electron cooling"", *Phys. Rev. Lett.*, vol 110, p. 269503, Jun 2013; V. N. Litvinenko and Ya. S. Derbenev, "Litvinenko and Derbenev Reply", *Phys. Rev. Lett.*, vol. 110, p. 269504, Jun 2013.

[4] D. Ratner, "Microbunched electron cooling for high-energy hadron beams", *Phys. Rev. Lett.*, vol 111, p. 084802, Aug 2013.

[5] G. Stupakov, "Cooling rate for microbunched electron cooling without amplification", *Phys. Rev. Accel. Beams*, vol 21, p. 114402, Nov 2018.

[6] G. Stupakov and P. Baxevanis, "Microbunched electron cooling with amplification cascades", *Phys. Rev. Accel. Beams*, vol. 22, p. 034401, Mar 2019.

[7] E.L. Saldin, E.A. Schneidmiller, and M.V. Yurkov, "Klystron instability of a relativistic electron beam in a bunch compressor", *Nucl. Instrum. Methods Phys. Res., Sect. A*, vol. 490, no. 1, p. 1, 2002.

[8] G. Stupakov and S. Heifets, "Beam instability and microbunching due to coherent synchrotron radiation", *Phys. Rev. ST Accel. Beams*, vol. 5, p. 054402, 2002.

[9] S. Heifets, G. Stupakov, and S. Krinsky, "Coherent synchrotron radiation instability in a bunch compressor", *Phys. Rev. ST Accel. Beams*, vol. 5, p. 064401, 2002.

SIMULATION OF HIGH ENERGY PROTON BEAM COOLING IN EICC[*]

F. Ma[†1], J. Li, X. M. Ma, L. J. Mao, X. P. Sha, M. T. Tang, J. C. Yang, X. D. Yang, H. Zhao,
H. W. Zhao, Institute of Modern Physics, Chinese Academy of Sciences, 730000 Lanzhou, China
[1]Also at University of Chinese Academy of Sciences, 100049 Beijing, China

Abstract

The hadron beam cooling plays an important role in the future e-i collider machines to achieve various physical goals. In EicC, two-stage beam cooling scheme is proposed to maintain the luminosity during the long time collision. First, a traditional electron cooler will be used to pre-cool the low energy proton beam in the BRing. Then, an ERL-based electron cooler will be applied at the pRing to cool the proton beam at high energy. The main purpose of cooling is to counteract the emittance growth due to the IBS. In this paper, we focus on the high energy beam cooling and present some simulation studies on how the cooling rate will be affected by the electron bunch size, magnetic field, and ring parameters in the cooling section, which would be helpful for the cooler design.

INTRODUCTION

EicC is proposed to study of hadron structure and the strong interaction and to carry out the frontier research on both nuclear and particle physics [1]. It will be constructed based on the High Intensity heavy ion Accelerator Facility (HIAF) with an additional newly constructed electron ring and a proton ring. The proposed collider will provide highly polarized electrons (with the polarization ~80%) and protons (with the polarization ~70%) with the variable center of mass energies from 15 to 20 GeV and the luminosity of $(2-4)\times 10^{33}\ cm^{-2}s^{-1}$. The ion accelerator complex of the EicC accelerator facility mainly consists of a polarized ion source, the iLinac, the booster ring BRing, and the collider ring pRing with proton beam energy up to 19.08 GeV, and the electron accelerator complex is composed of an electron injector and an electron collider ring eRing. There are two identical interaction regions in the EicC accelerator design, as shown in Fig. 1.

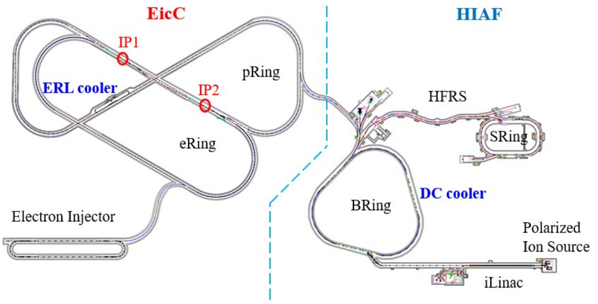

Figure 1: General layout of the EicC accelerator complex.

To achieve the high luminosity and long collision lifetime, beam cooling is required to counteract the emittance growth caused by IBS. In the past decades, electron cooling has become one of the most effective and well-developed methods. Based on ref. [2], the cooling rate will be significantly weakened at high energy, as described by Eq. (1).

$$\frac{1}{\tau_{cool}} \propto \frac{Z^2}{A}\frac{n_e L_c}{\beta^4\gamma^5\theta_{rel}^3} \qquad (1)$$

Considering this effect, the EicC will adopt a two-stage electron cooling scheme to improve the cooling efficiency. In the first cooling stage, an electron cooler, based on conventional electrostatic high voltage acceleration, will be installed in the BRing to reduce the transverse emittance and the momentum spread of the medium-energy ion beams. In the second cooling stage, a high energy electron cooler, based on ERL, will be installed in the pRing to compensate the IBS effect and maintain the emittance of the ion beam during the collisions, which can ensure high luminosity and long collision life required by the scientific goals. Due to reduced emittance after the low-energy cooling in the first stage, the cooling time for the high-energy beam can also be largely reduced, leading to a shortened total cooling time and enhanced cooling efficiency.

STUDIES ON BUNCHED BEAM COOLING IN PRING

In order to calculate the bunched beam cooling parameters efficiently and accurately, a flexible multiparticle tracking code is developed based on BETACOOL physics guide [3] and JSPEC code [4]. The magnetized friction force is calculated through the semi-empirical formula by V. Parkhomchuk [5] and the Martini model [6] is chosen for IBS calculation in this code. It has been benchmarked with BETACOOL program and they agree very well. In the following, we will give some simulation results and select the optimal parameters to achieve a high cooling rate. All the simulation input parameters are shown in Table 1.

IBS Effect During the Collision

Because of the long collision time, the emittance growth during the collision must be considered which have a great effect on the luminosity. Here we only considered the IBS effect, as shown in Fig. 2, beam emittance in three dimensions are all increased, which significantly affect the luminosity. Especially for the horizontal emittance growth rate, it will grow from 0.3 um to 0.7 um in three hours and the growth rate is about $2.3\times 10^{-4}\ s^{-1}$. The luminosity will decrease to $1.4\times 10^{33}\ cm^{-2}s^{-1}$ within three hours. To obtain a great

---

[*] This work was supported by the National Key R&D Program of China, Grant No.2019YFA0405400.

[†] mafu121@impcas.ac.cn

ISBN: 978-3-95450-243-1 ISSN: 2226-0374 doi:10.18429/JACoW-COOL2021-P1001

luminosity lifetime, the horizontal cooling rate must not be less than $2.3 \times 10^{-4}\ s^{-1}$.

Table 1: Simulation Parameters of Bunched Beam Cooling in pRing.

Parameters	Value
Particle type	proton
Kinetic energy	19.08 GeV
Number of particles per bunch	1.25×10^{11}
rms emittance x/y	0.3/0.18 π mm mrad
rms momentum spread	0.002
rms bunch length	4 cm
Number of electrons per bunch	2.5×10^{10}
Electron beam size (σx/σy/σs)	3/3/40 mm
Electron beam normalized rms emittance	2.5 π mm mrad
Electron beam rms momentum spread	0.0005
Length of cooling section	50 m
Longitudinal magnetic field in the cooling section	1.5 T
Parallelism of magnetic field	1.0×10^{-4}
Betatron function in the cooling section	30 m
Dispersion function in the cooling section (horizontal)	2 m

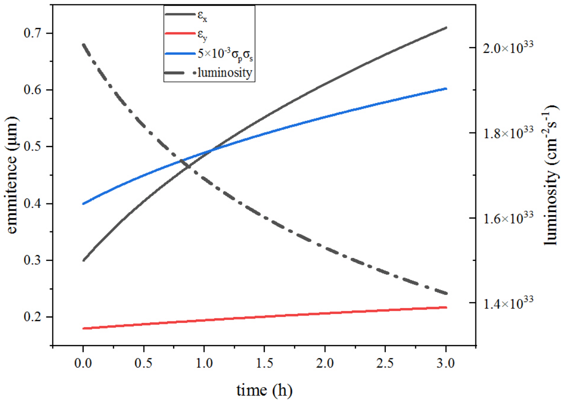

Figure 2: Evolution of ion beam emittance and luminosity during the collision.

Proper Electron Bunch Size

In the current baseline of the cooling of EicC, the ERL-based electron cooler provides a bunched electron beam with the charge of 4 nC and the energy of 10.4 MeV. Both the volume of the electron bunch and the local electron beam density affect the cooling rate, and they are contradictory. The larger the volume, the more ions are covered by the electron bunch and get cooled. However, the larger the volume, the lower the local electron density as the total charge per bunch is limited. Assume the electron bunch has round Gaussian distribution, transverse cooling rates are calculated for electron bunches with different radius and lengths while keeping electron beam emittance constant, as shown in Fig. 3. The parameters used in the calculation are list in Table 1. When the rms electron bunch length σ_{se} increases from 0.1 to 1.5 rms ion bunch length σ_s, the cooling rate increases until $\sigma_{se} = 0.75\sigma_s$, from where the cooling rate starts to decrease. For the electron bunch size, the turning point of the cooling rate is at $\sigma_{xe} = 0.45\sigma_x$. This is as expected since the bunch volume and the local electron density is competing. The volume dominates at the beginning and the cooling rate increases when more ions are enclosed by the electron bunch. Then the local electron density dominates when the volume is large enough. Another reason is that when local density is very large, the plasma oscillating frequency plays an important role on the collision parameters of cooling force formula. The change of longitudinal cooling rate is the same. According to the calculation, the highest cooling rate is achieved when the electron bunch is a little smaller than the ion bunch. And the cooling effect is distributed to the whole ion bunch via the transverse betatron oscillation and the longitudinal synchrotron oscillation.

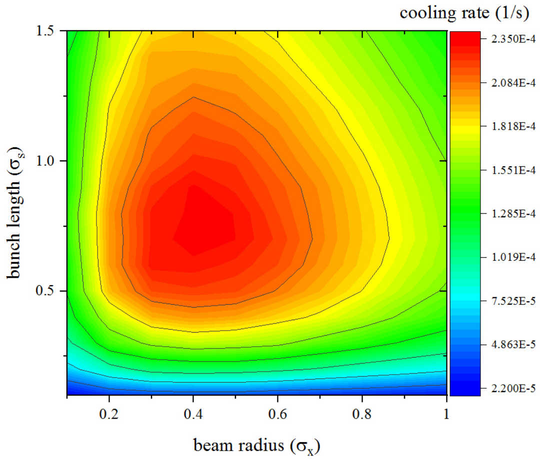

Figure 3: Transverse cooling rate for various electron bunch sizes.

Magnetic Field Parameters in the Cooling Section

The magnetic field strength and the parallelism of the magnetic field in the cooling section also have a great influence on the cooling rate in the magnetized electron cooling system. As shown in Fig. 4. The left one presents the transverse cooling rate as a function of the magnetic field strength in the cooling section, and the right one shows the transverse cooling rate change with different parallelism of the magnetic field. In the case of other fixed parameters, the cooling rate increases with the magnetic field strength and decreases with the increasing parallelism of the magnetic field in the cooling section. For the cooling in pRing, the magnetic field strength will be selected as 1.5 T and the parallelism of the magnetic field must be less than 1×10^{-4}.

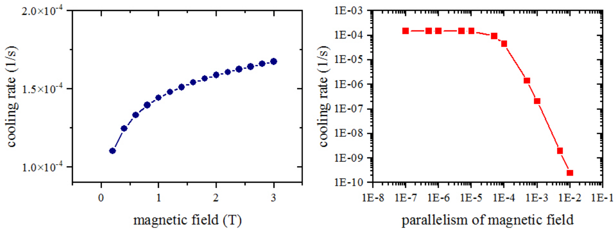

Figure 4: The transverse cooling rate as a function of the magnetic field strength (left) and the parallelism of the magnetic field (right) in the cooling section.

Lattice Function in the Cooling Section

Figure 5 gives the dependence of cooling rate on the transverse betatron function in the cooling section. We chose the same bunch size of the electron beam with the ion beam all the time in these calculations. One can see that the transverse cooling rate is increasing with a larger betatron function, however longitudinal is the opposite. The highest cooling rate in the transverse is achieved when the betatron function is equal to about 80 m. In the presence of dispersion, the horizontal cooling rate is enhanced with the expense of longitudinal cooling rate due to the coupling. And the vertical cooling rate decreases all the time because of the change of the ion beam size. The maximum horizontal cooling rate is achieved when the dispersion function reaches to 6 m, which is a little different from the theoretical results 2 m in the article [7]. The reason is the nonlinear terms of the cooling force depend on the large velocity spread of the ion beam. Based on the calculation, a small betatron function with dispersion in the cooling section is better to balance the cooling rate and compensate for the IBS effect in all dimensions.

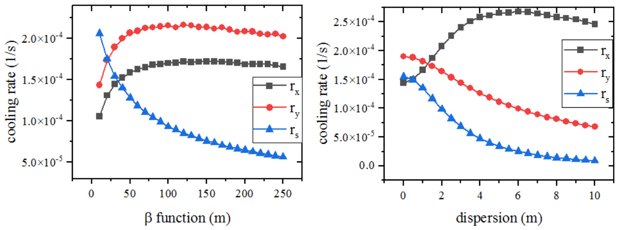

Figure 5: The cooling rate as a function of the betatron function (left) and the dispersion function (right) in the cooling section.

SIMULATION OF THE COOLING PROCESS IN PRING

By optimizing the above parameters, the proton beam cooling process in pRing is simulated. The electron bunch size is chosen as the same as ion beam to avoid the possible strong space charge effect of small electron bunch size. Due to the larger IBS growth rate in horizontal than both vertical and longitudinal, a dispersive electron cooling is chosen. By applying the dispersion on the proton beam in the cooling section with $D_x = 2$ m, $\beta_{x/y} = 30$ m, and introducing transverse coupling with 55% to transfer the IBS effect from the horizontal direction to the vertical direction, the proton beam can be cooled more effectively in all three dimensions. As shown in Fig. 6, the proton beam emittance is essentially unchanged within one hour with cooling, and the luminosity stays above 2×10^{33} $cm^{-2}s^{-1}$, which is close to the requirement in EicC.

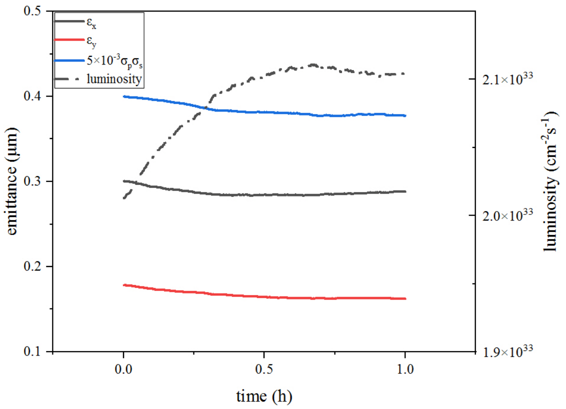

Figure 6: The evolution of the ion beam emittance and luminosity with cooling during the collision.

SUMMARY

The high energy bunched beam cooler of the two-stage electron cooling scheme for EicC is challenging, but possible. Based on the simulation results, the largest cooling rate can be achieved when the 4 nC charged electron bunch size is smaller than the ion bunch. The magnetic field strength of 1.5 T and 1.0×10^{-4} parallelism of the magnetic field is chosen based on the cooling requirement and technical risk. A dispersive beam cooling is suggested to suppress the large emittance growth by the IBS effect in the horizontal plane. The optimal ring parameters of betatron function and dispersion function are selected as 30 m and 2 m respectively in the cooling section. However, there are still many parameters to be optimized and many technical problems to be solved, especially for the stable operation of the ERL with 4 nC charge per bunch. The optical design is also an important work to optimize the IBS effect in the horizontal plane. The way to complete the design of the high energy bunched beam cooler is still very long.

ACKNOWLEDGMENT

The authors would like to thank members of the EicC design group. We also like to thank H. Zhang for his contribution to the simulation program.

REFERENCES

[1] Daniele P. Anderle *et al.*, “Electron-ion collider in China”, *Frontiers of Physics*, Vol. 16 Issue (6):64701, 2021.

[2] "Electron cooling: theory, experiment, application", *Phys. Rep.* 196, Nos. 3 & 4, 135-297, North-J-Iolland, 1990.

[3] I. Meshkov *et al.*, “BETACOOL Physics Guide”, 2007. `http://betacool.jinr.ru/`

[4] JSPEC on GitHub, `https://github.com/JeffersonLab/ElectronCooling`

[5] V.V. Parkhomchuk, “New insights in the theory of electron cooling”, *Nucl. Instrum. Methods Phys. Res. Sect. A* 441, 2000.

[6] M. Martini, “Intrabeam Scattering in the ACOL-AA Machines”, CERN PS/84-9 AA, 1984.

[7] H. Zhao and M. Blaskiewicz, “Rate redistribution in dispersive electron cooling”, *Phys. Rev. Accel. Beams* 24, 083502, 2021.

ISBN: 978-3-95450-243-1 ISSN: 2226-0374 doi:10.18429/JACoW-COOL2021-P1002

SIMULATION OF TRANSVERSE ELECTRON COOLING AND IBS OF 20 GeV PROTON BEAM AT EICC*

X. D. Yang†, Institute of Modern Physics, CAS, Lanzhou, China

Abstract

The transverse electron cooling and intra-beam scattering processes of 20GeV proton beam were simulated with the help of the code at Electron Ion collider in China. The transverse cooling time were obtained in the different parameter configurations of storage ring, proton beam, electron cooling device and electron beam. The scattering time of proton beam were presented in the cases of different initial emittance and particle number. The final equilibrium transverse emittance were estimated in the cases of different initial emittance and particle number. From the simulated results, the transverse cooling time of 20GeV proton beam is over 100 seconds. The transverse cooling time can be shorten with the help of proper configuration of the parameters.

INTRODUCTION

Based on the HIAF (the Heavy Ion High Intensity Accelerator Facility, approved in 2015 in China), a high luminosity polarized Electron Ion Collider facility in China (EicC) was proposed to study of hadron structure and the strong interaction and to carry out the frontier research on both nuclear and particle physics.

EicC will be constructed in two phases, EicC-I and EicC-II. In the first phase, the proton beam with energy between 15~20GeV will collide with electron beam with energy between 2.8~5GeV in the collider. Both electron and proton beam are polarized. The luminosity will expect to achieve 2~4×$10^{33}$$\mathrm{cm}^{-2}\cdot\mathrm{s}^{-1}$.

In the second phase, the energy of proton will upgrade to 60~100GeV, and the energy of electron beam will increase to 5~10GeV, the luminosity will expect to achieve 1×10^{35}. The primary design and some initial parameters of EicC will be found in the reference [1].

In order to obtain the expected luminosity in collider, the polarized proton beam should be cooled by various cooling methods among the whole energy range. In the case of high intensity high energy proton beam especially, the intra-beam scattering effect should be taken into account in the collider design. Some primary simulation on the transverse electron cooling and intra-beam scattering were presented in this contribution.

SIMULATION OF ELECTRON COOLING

The transverse electron cooling time not only depends on the lattice parameters of the storage ring, the Betatron function, dispersion of the cooling section, such as energy, initial emittance and momentum spread of proton beam , but also on the construction parameters of electron cooling device, the strength of magnetic field, the parallelism of magnetic field in the cooling section, the effective cooling length, and the parameters of electron beam, such as radius, density and transverse temperature of electron beam. These parameters are determined by the storage ring and the technology limitation, on the other hand, they are influenced and restricted each other.

With the help of the electron cooling simulation code SIMCOOL [2, 3], the transverse electron cooling time of proton beam were extensive simulated in various parameters in the EicC, such as proton beam energy, initial transverse emittance, and momentum spread. The influence of the machine lattice parameters-Betatron function, and dispersion function on the cooling time was investigated. The parameters of electron beam and cooling devices were taken into account, such as effective cooling length, magnetic field strength and its parallelism in cooling section, and electron beam current.

Proton Beam Parameters

Left diagram of Fig. 1 shows the transverse electron cooling time as a function of the initial emittance. Right diagram of Fig. 1 gives the dependence of transverse cooling time of the transverse direction on the particle number in the proton beam. In the case of other parameters were fixed, the transverse electron cooling time increases with the initial emittance and slightly decreases with the particle number in the proton beam.

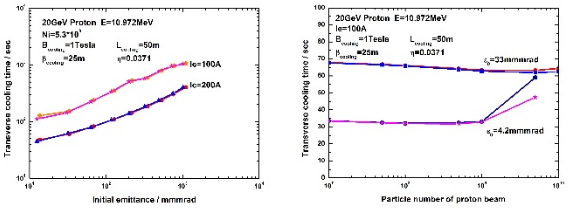

Figure 1: The transverse electron cooling time as a function of the initial emittance (left) and the particle number in the proton beam (right).

Electron Beam Parameters

In order to decrease the transverse cooling time, the current of electron beam and length of cooling section was set as a bigger value. Left diagram of Fig. 2 presents the transverse cooling time as a function of the electron beam current. Right diagram of Fig. 2 indicates the transverse cooling time depends on the transverse temperature of electron beam. In the case of other parameters were fixed, the transverse cooling time decreases with the increasing electron beam current and decreasing transverse temperature of electron beam.

---

* Work supported by NSFC No. 11375245

† yangxd@impcas.ac.cn

ISBN: 978-3-95450-243-1 ISSN: 2226-0374 doi:10.18429/JACoW-COOL2021-P1002

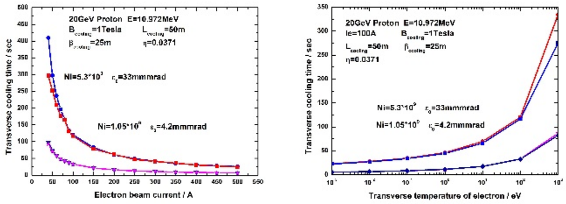

Figure 2: The transverse cooling time as a function of the electron beam current (left) and the transverse temperature of electron beam (right).

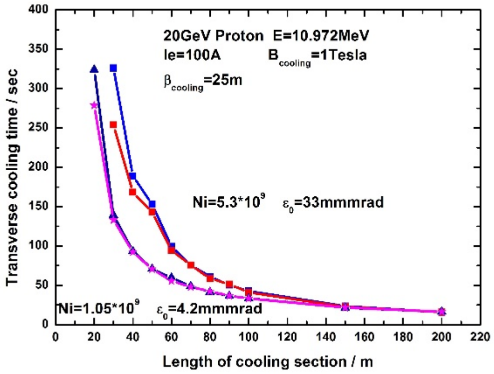

Figure 3: The transverse electron cooling time as a function of the length of the cooling section.

Figure 3 shows the transverse cooling time varies as a function of the length of the cooling section. In the case of other parameters were fixed, the transverse cooling time decreases with the length of the cooling section. The length of cooling section strongly influence the transverse cooling time.

Magnetic Field Parameters

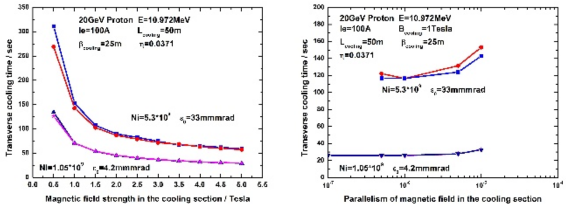

Figure 4: The transverse cooling time as a function of the magnetic field strength (left) and the parallelism of magnetic field (right) in the cooling section.

Left one of Fig. 4 shows the transverse cooling time as a function of the magnetic field strength in the cooling section, and right one of Fig. 4 presents the transverse cooling time as a function of the parallelism of magnetic field in the cooling section. In the case of other fixed parameters, the transverse cooling time decreases with the magnetic field strength in the cooling section. The transverse cooling time decreases with the increasing parallelism of magnetic field in the cooling section. From Fig. 4, one can see the magnetic field strength strongly influence on the cooling time. The cooling time becomes shorter when the magnetic field parallelism is higher in the cooling section.

Storage Ring Parameters

The diagram of Fig. 5 gives the dependence of transverse cooling time on the transverse Betatron function. The transverse cooling time decreases with the Betatron function in the cooling section.

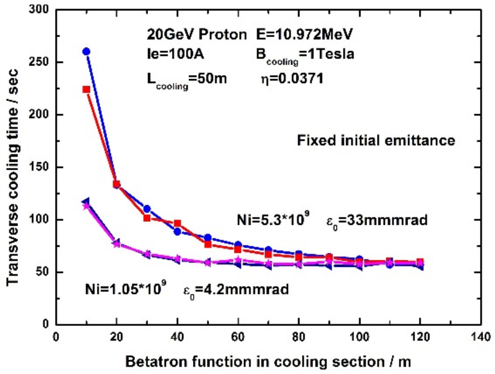

Figure 5: The transverse cooling time as a function of the Betatron function in the cooling section.

Initial Emittance and Particle Number

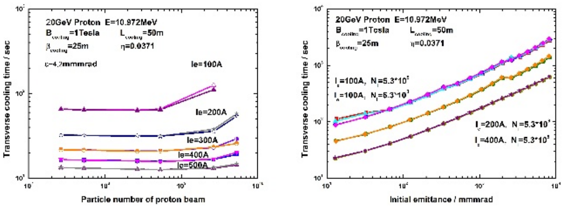

Figure 6: The transverse cooling time as a function of the particle number (left) and initial emittance (right) of proton beam under the cooling with different electron beam current.

The transverse cooling time as a function of the particle number and initial emittance of proton beam were illustrated in the Fig. 6. In the case of other parameters were fixed, the transverse cooling time increases with the increasing of particle number and initial emittance of proton beam.

SIMULATION OF IBS

The luminosity is determined by the quality of proton beam, and the quality of proton beam was determined by the final emittance, momentum spread and longitudinal size.

The ability of electron cooling was determine by the parameters of electron beam, such as electron beam density, temperature of electron and length of cooling section in the storage ring, but also depends on the magnetic parameters in the cooling section.

The effect of intra-beam scattering depends on the particle density of proton beam. It is more serious and important in the situation of high intensity, high energy proton beam.

In order to simulate the intra-beam scattering, the electron beam current was set as zero in the simulation code

SIMCOOL. There is no cooling effect in this case, and only scattering effect in the simulation. The transverse scattering time was derived from the data fitting of simulation results.

In order to compare the simulated results, only one parameter was changed during the simulation, and the other parameters were kept as fixed.

In the case of fixed initial emittance, for the situation of bigger particle number, the proton beam scattered at the beginning, and then cooled, finally keep the emittance constant. The final emittance were different under the cooling by different electron beam current.

Transverse Scattering Time

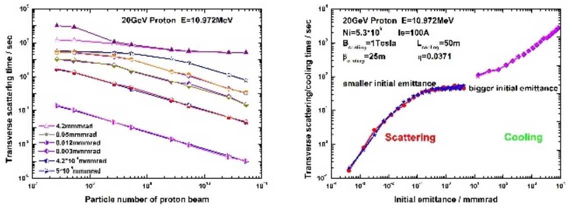

Figure 7: The transverse scattering time as a function of the particle number (left) and initial emittance (right).

The transverse scattering time as a function of the particle number in the proton beam was demonstrated in left of Fig. 7. In the case of fixed other parameters, the transverse scattering time decreases with the increasing particle number in the proton beam.

With respect to a certain particle number in the proton beam cooled by the 100A electron beam, the scattering effect is stronger than the cooling one in the case of smaller initial emittance, the proton beam presents the scattering process, and the scattering of smaller initial emittance is faster than the bigger one.

Final Equilibrium Emittance

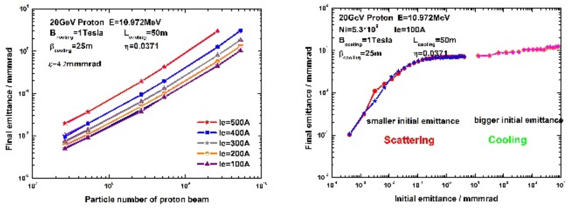

Figure 8: The final equilibrium emittance as a function of the particle number in the case of different electron beam cooling (left) and initial emittance(right).

Left one of Fig. 8 shows the final equilibrium emittance as a function of the particle number in the case of different electron beam cooling. Right one of Fig. 8 presents the final equilibrium emittance as a function of the initial emittance in the proton beam. The final equilibrium emittance was mainly dominated by the particle number in the proton beam.

SUMMARY

From the simulated results, the transverse cooling time of proton beam with 20GeV is over 100 seconds. The transverse cooling time can be shorten with the help of proper configuration of the parameters, such as smaller initial emittance and electron transverse temperature, higher magnetic field strength, parallelism of magnetic field in the cooling section, longer length of electron cooling section, stronger electron beam current, and bigger beta function in the cooling section.

With respect to IBS, the transverse scattering time not only depends on initial emittance, but also depends on the particle number. The final equilibrium emittance was dominated by the particle number in the proton beam.

The emittance, particle number and longitudinal length of proton beam should be optimized and compromise carefully in order to obtain the required luminosity. By the way, the strategy of cooling are important too, such as multi-stage cooling [4] at different energy or different period. The emittance should be cooled to the required value by the stronger electron beam in the first stage, and then the smaller emittance will be maintained by the weaker electron beam.

For the sake of obtaining and keeping the smaller emittance in the case of proton beam with energy 20GeV, the cooling should counteract the scattering at the different situation and period, and provide high quality proton beam for the higher luminosity in the storage ring. The detailed and exact simulation will be necessary for the real lattice design of the EicC storage ring in the future.

In the interest of achieving the required luminosity from physics experiments, the parameters of proton beam, electron cooling device and storage ring should be optimized carefully and compromised each other, and attempt the different configurations from the point of view of realizable technical solutions.

High intensity proton beam and short bunch length was expected to store in a collider with long lifetime and less loss. In order to increase the lifetime of proton beam and decrease the loss, longitudinally modulated electron beam [5] will be attempted to suppress the intra-beam scattering. The traditional DC electron beam in the electron cooler will be modulated into shorter electron bunch with different longitudinal distribution. The stronger cooling was expected in the tail of proton beam and the weaker cooling was performed in the core of proton beam. The proton loss will be decreased and the lifetime will be increased. The intensity of proton beam in the collider will be kept and maintained for long time.

ACKNOWLEDGEMENT

The author would like to thank Prof. V. Parkhomchuk for him to provide the simulation code SIMCOOL and useful guidance in the simulation during this work.

REFERENCES

[1] Cao Xu, Chang Lei, Chang Ningbo, *et al*. “Electron ion collider in China”. *Nuclear Techniques,* vol. 43, no. 2, 2020, p. 020001-1-59. `DOI: 10.11889/j.0253-3219.2020.hjs.43.020001`

[2] Vasily Parkhomchuk, Ilan Ben-Zvi, “Electron cooling for RHIC”, BNL C-A/AP/47, April 2001.

[3] A.V. Fedotov, I. Ben-Zvi, Yu. Eidelman, et al, “Simulation of high-energy electron cooling”, in *Proceedings of 2005 Particle Accelerator Conference*, Knoxville, Tennessee, USA, paper TPAT090, pp. 4251-4263.

[4] H. Zhang, Y. Zhang, Ya. Derbenev, *et al*. “Multi-stage electron cooling scheme for JLEIC”, in *9th International Particle Accelerator Conference IPAC2018*, Vancouver, BC, Canada, paper MOPML006, pp. 397-399. `doi:10.18429/JACoW-IPAC2018-MOPML006`

[5] X. D. Yang, L. J. Mao, J. Li, *et al*. “Investigation on the suppression of intra-beam scattering in the high intensity heavy ion beam with the help of longitudinal multi-bunch chain of electron”, in *Proc. 11th Workshop on Beam Cooling and Related Topics*, Bonn, Germany, Sep. 2017, paper TUP14, pp.58-60. `doi:10.18429/JACoW-COOL2017-TUP14`

ISBN: 978-3-95450-243-1 ISSN: 2226-0374 doi:10.18429/JACoW-COOL2021-P1005

COMPARISON OF AVAILABLE MODELS OF ELECTRON COOLING AND THEIR IMPLEMENTATIONS

A. Borucka*[1], D. Gamba, A. Latina, CERN, Geneva, Switzerland
[1]also at Warsaw University of Technology, Warsaw, Poland

Abstract

Modelling of the electron cooling process is complex and challenging. The simulation needs to include elements like ions, plasma of electrons, the thermal effects of electrons and the influence of the magnetic field. In this work, the performance of three available tools, namely RF-Track [1], Betacool [2], and JSPEC [3], are discussed taking into account only the cooling and neglecting any heating effect. The friction force and cooling times are studied in a wide range of different parameters presenting the main behaviour of the available models together with the limitations of particular simulation codes. Furthermore, a qualitative comparison with experimental data is performed.

INTRODUCTION

The study is focused on the dependence of the friction force and of the cooling time on crucial parameters. A short introduction of the analysis is presented in this paper, while details can be found in [4].

Several simulation codes and models of electron cooling implementation have been used for this analysis. The key aspect of each simulation software and model are presented in the following.

RF-Track

RF-Track [1] is a tracking code developed at CERN. Here, electron cooling is modelled on the basis of the description given in Ref. [5], in which the force is expressed as the sum of unmagnetized and magnetised components:

$$\vec{F} = -\frac{4\pi n_e K^2}{\mu}\left\{F_{\text{unmagnetized}} + F_{\text{magnetized}}\right\}. \tag{1}$$

The unmagnetized part is implemented as:

$$F_{\text{unmagnetized}} = L_F \iiint \left[\frac{\vec{U}}{U^3}\right] f(\vec{v}_e)d\vec{v}_e \tag{2}$$

whereas three different versions of $F_{\text{magnetized}}$ have been implemented due to ambiguities in the description provided in [5]:

RF-Track A

$$L_M \iiint \left[\frac{U_{B\perp}^2}{U_B^5}\left(\vec{U}_{B\parallel}^5 + \frac{\vec{U}_{B\perp}}{2}\left(1 - \frac{U_{B\parallel}^2}{U_{B\perp}^2}\right) f\left(v_e\right)dv_e\right)\right] \tag{3}$$

RF-Track B

$$L_M \int \left[\frac{U_{B\perp}^2}{U_B^5}\left(\vec{U}_{B\parallel}^5 + \frac{\vec{U}_{B\perp}}{2}\left(1 - \frac{U_{B\parallel}^2}{U_{B\perp}^2}\right)\right)\right] f\left(v_{e\parallel}\right)dv_{e\parallel} \tag{4}$$

RF-Track C

$$\int \left[L_A\frac{\vec{U}_B}{U_B^3} + L_{M2}\frac{U_{B\perp}^2}{U_B^5}\left(\vec{U}_{B\parallel}^5 + \frac{\vec{U}_{B\perp}}{2}\left(1 - \frac{U_{B\parallel}^2}{U_{B\perp}^2}\right)\right)\right] f\left(v_{e\parallel}\right)dv_{e\parallel} \tag{5}$$

with L being the so called Coulomb logarithms:

$$L_F = \frac{1}{2}\log\left(1 + \frac{r_F^2}{r_{\text{min}}^2}\right),\quad L_M = \log\frac{r_{\text{max}}}{r_L},$$

$$L_{M2} = \log\frac{r_{\text{max}}}{r_F},\quad L_A = \frac{1}{2}\log\left(1 + \frac{r_L^2}{r_F^2}\right)$$

based on the following impact parameters:

$$r_L = \frac{\sqrt{V_{e\perp}^2 + \Delta_{e\perp}^2}}{\omega_e},\quad r_F = \frac{\sqrt{U_{B\parallel}^2 + \Delta_{e\parallel}^2}}{\omega_e},$$

$$r_{\text{min}} = \frac{K}{\mu(U^2 + \Delta_e^2/3)},\quad r_{\text{max}} = \min\left(r_a, \lambda_D\sqrt{1 + \frac{U^2}{\Delta_e^2/3}}, U\Delta t\right)$$

where $\vec{U}$ is the velocity difference between ions and mean electron velocity, and Δ_e is the electron temperature. Detailed meaning of all symbols is provided in [4].

BETACOOL

Betacool [2] is a widely used code for simulating beam dynamics developed at JINR. It includes a broad-range of effects that can be used and few models of electron cooling:

Parkhomchuk It is the simplest and commonly used model described by the following semi-empirical formula:

$$F = -4\frac{Z^2 e^4 n_e}{m}\log\left(\frac{b_{\text{max}} + b_{\text{min}} + \rho_c}{b_{\text{min}} + \rho_c}\right)\frac{\vec{U}}{(U^2 + v_{\text{eff}}^2)^{3/2}} \tag{6}$$

with impact parameters:

$$b_{\text{max}} = \frac{v_i}{1/\tau_{\text{flight}} + \omega_p},\quad b_{\text{min}} = \frac{Ze^2}{m}\frac{1}{U^2 + v_{\text{eff}}},\quad \rho_c = \frac{cmv_\perp}{eB}$$

A key parameter of this model is v_{eff}, the effective velocity, which is a tuning parameter that can be used to take into account magnetic field line perturbations and other imperfections and it can help to fit the simulation to actual results.

Debrenev-Skrinsky-Meskov It assumes three types of collisions – fast, adiabatic and magnetized, depending on the value of impact parameter with respect to the Larmor radius (r_L). The role of those interactions depends on the relative velocities of electrons and ions, which defines three regions of velocities and impact parameters. This model allows choosing between asymptotic and numerical approaches [2]. After first short tests the asymptotic version was discarded because of nonphysical discontinuities, and therefore not mentioned in this work.

---

* agnieszka.elzbieta.borucka@cern.ch

ISBN: 978-3-95450-243-1 ISSN: 2226-0374 doi:10.18429/JACoW-COOL2021-P1005

Toepffer This is a model of binary collisions assuming three types of interactions – fast collisions at impact parameters less than the radius of electron rotation, collisions with "tight" helices and collisions with "stretched" helices. Details on the mathematical form of the force can be found in [6]. According to the model description in the Betacool user manual and source code, this model is the one that resembles most what is implemented in RF-Track.

JSPEC

JSPEC [3] is a package developed by Jefferson Lab (JLab) for electron cooling simulations. At least three major version of this code has been found and used in this work: JSPEC and JSPEC2 [3] originally by JLab, and RadiaSoft's version [7,8]. All versions implement the Parkhomchuk model, which was used in this study and for which all versions gave comparable results.

FORCE COMPARISON

The force on a single ion was computed as a function of velocity difference between ion and mean electron beam velocity. In the case of the longitudinal force, the scan was performed over the longitudinal velocity difference while the transverse one was set to zero. In the case of the transverse force, it was the other way round. Parameters used in these simulations were chosen to match the parameters of LEIR (CERN):

- Ions: A:208, Q=+54, K_0=862.68 MeV, #10000
- Electrons: uniform distribution, I=0.6 A, $T_\perp$=0.1 eV, $T_\parallel$=0.01 eV, r=25 mm, $K_0(e^-)$=2.3 keV
- E-Cooler: L=2.5 m, B=0.075 T

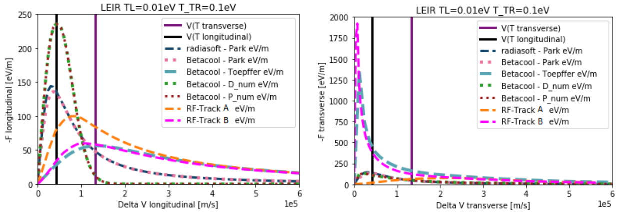

Figure 1: Longitudinal (left), and transverse (right) force on single ion as a function mean electron and single ion velocity difference for all considered models.

Figure 1 shows the cooling forces for each model. The velocities corresponding to electron temperatures are indicated by vertical lines, calculated as $v = c\sqrt{\frac{T}{m_e}}$. Those plots highlight considerable differences and similarities between the different models. The transverse force of RF-Track A is much weaker in comparison to all other models. It suggests that RF-Track A does not consider all physical phenomena. The Toepffler model from Betacool and RF-Track B behave similarly and were considered as the closest to expectation. RF-Track C, not shown in Fig. 1, has a behavior similar to RF-Track B.

FORCE SCAN

To study the behaviour of the models and their performance limits, a set of simulations were performed over a wide range of parameters. Figure 2 presents the peak value of the force as a function of magnetic field and transverse electron temperature.

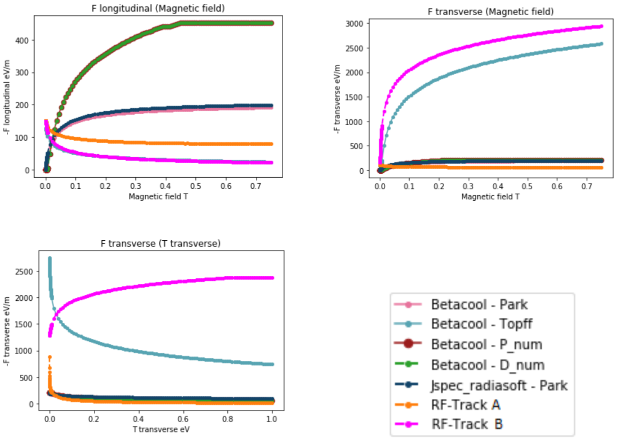

Figure 2: Friction force peak value as a function of electron cooler solenoid field and transverse electron temperature.

Figure 2 (top-left) presents the longitudinal force scan as a function of the solenoid field. There are two separate groups of models: for one the maximum value of force increases with the magnetic field, for the second one it decreases. There is no straightforward reason to decide which behaviour is correct. In this plot the RF-Track B and Toepffer model strongly agree with each other. However, one should note that by setting the transverse velocity difference to zero in Eq. (4) for RF-Track B one removes the magnetized component of the force.

Figure 2 (top-right) shows the dependence of the transverse force on the magnetic field. Here the Toepffer model and RF-Track B have much stronger dependence (up to a factor 10) than the other models.

The scan of transverse force as a function of transverse temperature is presented in Fig. 2 (bottom-left). Although the RF-Track B seems to fit the Toepffer model implemented in Betacool quite well in all previous scans, the behavior of RF-Track B presented on this plot is opposite with respect to all other models, including RF-Track A.

COOLING TIME SCAN

In order to study the influence of the main cooler parameters on the cooling rate, a set of tracking simulations was performed and results are presented in Fig. 3. The scans were performed by changing one of the considered parameters. Cooling time (τ) was defined as the time to reach 20% of the initial emittance, i.e. $\epsilon(\tau) = \epsilon_0/5$.

For the studied parameters, the cooling time is generally longer in the case of Betacool, but for magnetic fields higher than about 0.5 T. RF-Track A shows an unexpected strong dependence on transverse temperature. The scan of the

ISBN: 978-3-95450-243-1 ISSN: 2226-0374 doi:10.18429/JACoW-COOL2021-P1005

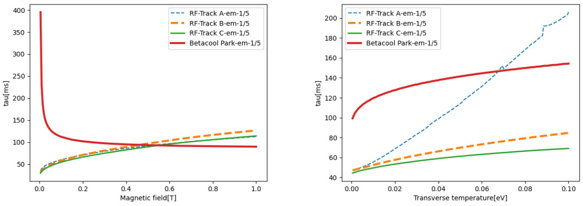

Figure 3: Transverse cooling time as a function of transverse electron temperature (Left) and solenoid field (Right).

magnetic field shows an opposite trend between models, which is compatible with the force analysis in the previous section.

EXPERIMENTAL RESULTS

A set of simulations was performed to reproduce experimental results of cooling time measurements obtained in 1996 on LEAR [9]. Those measurements present the influence of lattice functions at the e-cooler location on the cooling time. Four different machine configurations were measured with lattice functions presented in Table 1. The remaining parameters were specified based on the data from the paper [9]: $\epsilon_0 = 10$, $dp = 0.25$‰, $I = 350\,\mathrm{mA}$, $B = 0.06\,\mathrm{T}$, $L = 1.5\,\mathrm{m}$. As the electron temperatures were not clearly defined, temperatures of $T_\perp$=0.1 eV, $T_\parallel$=0.1 eV were chosen. In these studies the cooling time is defined as: $\epsilon(\tau) = \epsilon_0/10$ as in [9].

The obtained results are presented in Fig. 4. The shape of the dependence of the cooling time on the optics function is comparable. However, the cooling time scales between simulations and measurement are considerably different, especially for Betacool which predicts a factor of about 5-10 slower cooling. This discrepancy can be due to several reasons, for example the absence of heating effects in all simulations; the use of a different definition of beam emittance: in the measurements most likely the emittance was measured from a Gaussian fit of the transverse beam profile, while in simulations this would not be possible due to the un-physical generation of a dense core, and clearly the different model of the cooling force used in the two codes.

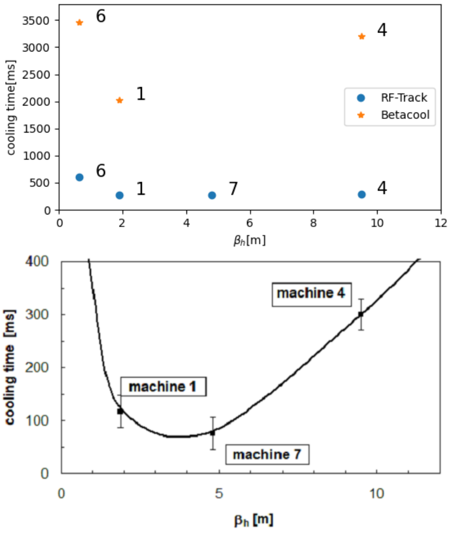

Figure 4: Top: Simulated cooling times for each machine. Bottom: experimental results [9]

Table 1: Lattice functions of measured LEAR machines.

Machine	1	4	6	7
β_H [m]	1.9	9.5	0.65	4.8
β_V [m]	6.4	10.5	5.5	5.0
D[m]	3.6	0	0	5.0

Figure 5 (left) presents the evolution of the momentum distribution in time in the form of a waterfall plot for RF-Track C simulation including e^- space-charge and ions dispersion effects for LEIR e-cooler parameters (but still neglecting any heating effects). This can be qualitatively compared to a measurement taken during the recent recommissioning of the Antiproton Decelerator (AD) [10], shown in Fig. 5 (right). Despite the different ions and e^- parameters (in AD I_{e^-}=2.4 A, $K_0(e^-)$=25.5 keV), it is interesting to observe that both graphs show the same behaviour: the energy of the whole beam increases and then slowly tends to a central edge. This behavior was tracked back to e^- space-charge effects in the simulations.

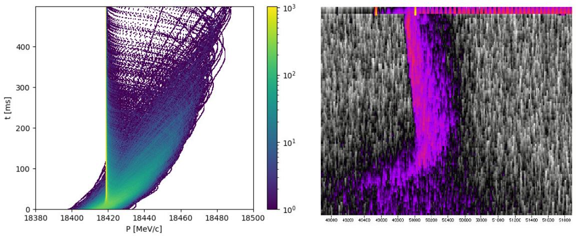

Figure 5: Beam momentum distribution evolution in time simulated with RF-Track C (left) and measured in AD (right) [10].

CONCLUSION

Different models and implementations of electron cooling were compared and tested for a wide range of parameters. Despite the substantial differences observed, it is believed that the latest implementation of e-cooling in RF-Track, model "C", is suitable for future studies. For the presented studies all heating effects (e.g. intra-beam scattering) were neglected, therefore the final distributions of ions include non-physically dense cores. Still, qualitative comparisons with previous experiments at LEAR and observations at AD show that the underlying physics is captured.

The next step will be to consider heating effects, like space-charge and intra-beam scattering, and to compare simulations with new measurements such to increase the predictive power on the e-cooling process in all CERN e-coolers. The different behavior observed between RF-Track and Betacool as a function of e-cooler magnetic field is puzzling. This could be an additional topic of study with experimental measurements in the future.

REFERENCES

[1] A. Latina, "RF-Track Reference Manual", CERN, Geneva, Switzerland, 2021, `https://doi.org/10.5281/zenodo.4580369`.

[2] I. Meshkov *et al.*, "Physics guide of BETACOOL code Version 1.1", 2006, BNL Tech Note C-A/AP/#262.

[3] "JSPEC2 git repository", `https://github.com/JeffersonLab/ElectronCooling`

[4] A. Borucka, D. Gamba, A. Latina, "Benchmark of e-cooling simulations with RF-Track", CERN, Geneva, Switzerland, Nov 2021, report CERN-ACC-NOTE-2021-0031 (unpublished).

[5] H. Nerisisyan, C. Toepffer, G. Zwicknagel, "Interactions between charged particles in magnetic field", *Springer ed.*, ISBN 9783540698531, 2007.

[6] C. Toepffer, "Scattering of magnetized electrons by ions", *Phys. Rev. A*, vol. 66, no. 2, p. 022714, Aug. 2002.

[7] JLab, RadiaSoft, "JSPEC online" `https://www.sirepo.com/jspec#/simulations`

[8] JLab, RadiaSoft, "Radiasoft JSPEC git repository" `https://github.com/radiasoft/electroncooling`

[9] J. Bosser *et al.*, "Experimental Investigation of Electron Cooling and Stacking of Lead Ions in a Low Energy Accumulation Ring", CERN, Switzerland, May 1999, report CERN-PS-99-033-DI.

[10] D. Gamba *et al.*, "AD/ELENA electron cooling experience during and after CERN Long Shutdown (LS2)", *these proceedings*, Novosibirsk, Russia, Oct. 2021, Paper S503.

ISBN: 978-3-95450-243-1 ISSN: 2226-0374 doi:10.18429/JACoW-COOL2021-P1006

DESIGN OF THE SRING ELECTRON TARGET

J. Li*, L. J. Mao, X.D. Yang, J. C. Yang, M.T. Tang, L. X. Zhao, X. M. Ma, T. L. Yan, F. Ma, X. P. Sha, Y. B. Zhou, H. J. Lu, G. Wang, G.D. Shen, Z. K. Huang, H.B. Wang, S. X. Wang, W.Q. Wen, X. Ma
Institute or Modern Physics, CAS, Lanzhou, China

Abstract

An electron target is proposed for high precision experimental measurement at the SRing (Spectrometry Ring) of HIAF (High Intensity heavy ion Accelerator Facility). It provides low temperature electron beam with a few meV for DR (Dielectronic Recombination) experiments at the energy of 1-80 keV. For such a low temperature, the conventional method is adopted by magnetic adiabatic expansion with a factor of 30 after acceleration within 1.2T longitudinal magnetic field at gun section. In this paper, the design optimization of the electron target is introduced.

INTRODUCTION

The Spectrometry ring (SRing) is an in-building dedicated experimental storage ring of the accelerator complex High Intensity heavy-ion Accelerator Facility (HIAF) [1]. It is designed to operate in four modes of the isochronous for time-of-flight nuclei mass measurement, of the internal target for gas-jet experiment, of the normal for Schottky nuclei mass measurement and atomic spectrometry study, and of the stacking. Collision of storage electron-cooled (E-cooled) ions with the cold electron beam is proposed at the SRing for Dielectronic Recombination (DR) spectroscopy measurement of Li-like, H-like, and He-like highly charged heavy ions when fruitful results have been obtained at HIIRFL-CSR electron cooler [2, 3]. Figure 1 shows layout of the SRing.

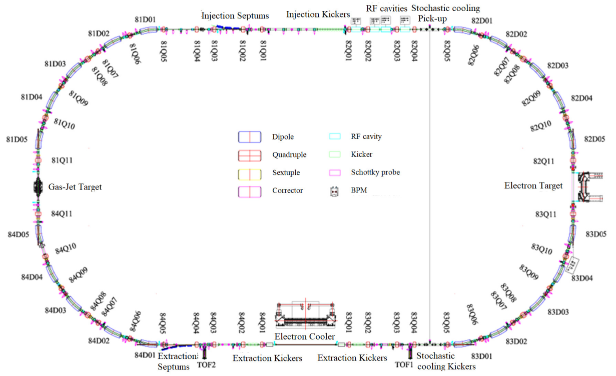

Figure 1: Layout of the Spectrometry Ring.

An electron-target (E-target) is dedicated to the DR experiments. It merges the cold electron beam of transverse temperature $kT_{e\perp}$ 5 meV and longitudinal one $kT_{e\parallel}$ 0.1 meV with the circulating e-cooled ion beam within 2.24 m length the target section. Electrons start from a 10 mm thermionic cathode, and accelerated to the energy range of 10-80 keV within the 1.2 T guiding magnetic field. Then the electron beam get the transverse temperature reduced by a transverse expansion with a factor of 30 along the guiding field. After transition through magnetic bending coils in the toroid, electrons are merged with the circulating highly charged ions in the target solenoid. Collisions between cold electrons and e-cooled storage ions make DR spectrometry investigation possible. After interaction with ions in the target section, the electrons are bent away from the circulating ion beam through electron plates in the Toroid, and finally dumped into the collector after deceleration.

Table 1: Main parameters of SRing and E-target

SRing Nor-2 optics	
Circumference	277.3 m
Typical ions	$^{197}Au^{(76-78)+}$,$^{238}U^{(89-92)+}$
Beam Intensity	$10^4 - 10^8$
Rigidity	3.5-15 Tm
Energy	85-835 MeV/u ($^{238}U^{92+}$)
Accepted ϵ_h/ϵ_v, $\delta p/p$	120/30 $\pi mmmrad$, ±1.1%
E-cooled ϵ_h/ϵ_v, $\delta p/p$	0.2/0.2 $\pi mmmrad$, $\pm 1 \cdot 10^{-4}$
E-Target parameters	
Electron energy	10-80 keV
$kT_{e\perp}$ in experiment	5 meV
$kT_{e\parallel}$ in experiment	0.1 meV
n_e in experiment	$2 \cdot 10^6$ cm^{-3}
Cathode diameter	10 mm
Expansion factor	30
B_s at target	0.04 T
B_s at gun/collector	1.2/0.2 T
Cooled beam σ_x/σ_y	4.7/3.7mm
Vacuum pressure	$1 \cdot 10^{-9}$Pa
Aperture through target	275 mm
$\beta_x/\beta_y, D_x$ at target	18 m/17 m, 4.7 m
Target solenoid length	2.24 m
E-target total length	5.5 m
E-target orientation	horizontal

For DR experiments, the SRing will operate in the Nor-2 optics mode within the magnetic rigidity 3.5-15 Tm. As a feature of the e-target, ion beam will been cooled down with $\sigma_x/\sigma_y = 4.7/3.7mm$ at target section, that makes it possible for the colder electrons in a small radius to collision with the e-cooled ions.

Besides, three isochronous modes are designed at SRing and secondary beam in target section has the largest horizontal envelope 261 mm when the transition energy $\gamma_{tr} = 1.43$. This limit the minimal aperture at the target section. In

---

* lijie@impcas.ac.cn

additional, available height in SRing tunnel limit e-target orientation to horizontal. The main parameters of SRing and E-target are summarized in Table 1.

MAGNETIC FIELD SYSTEM

In order to reduce the electron beam temperatures as much as possible and improve the technical feasibility of the e-target, we redesigned the magnetic field at gun section. It focuses on reducing the longitudinal temperature by accelerating electrons within 1.2 T gun solenoid and thus shortening the length of acceleration tube to 0.46 m from 1.2 m in the old design [4]. Meanwhile, the expansion magnetic field is also optimized at the junction to Toroid. Figure 2 shows the axial field B_s distribution and overall coils arrangement along the electron beam orbit coordinate s.

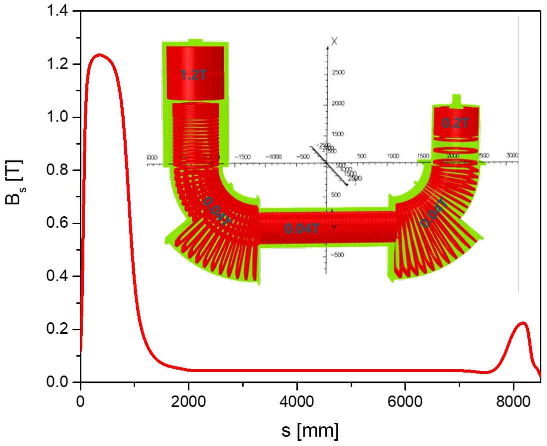

Figure 2: Axial magnetic field variation along electron trajectory and overall arrangement of coils from gun to collector.

The electron gun solenoid consists of two identical normal-conducting coils with bore diameter 220 mm and total length 0.96 m. The 1.2 T axial magnetic field covers a range of 0.5 m for electrons generation and acceleration. The expansion solenoid consist of 20 coils and decrease the magnetic field to 0.04 T from 1.2 T. The two 90° Toroids consist of 40 coils and have the axial fields 0.04 T with a distortion requirement less than 1%. The optimized field in target solenoid is also 0.04 T but with straightness requirement less than $1 \cdot 10^{-4}$ within the effective length 1.6 m. The magnetic field increases gradually in transition toward the collector. It reaches a maximum 0.2 T at entrance of the collector cup and then drops to 0.003 T at the bottom.

ADIABATICITY PARAMETERS AND ELECTRON TEMPERATURE

To reduce heatings of electron beam caused by the radical electric field in acceleration and variation of the magnetic field during expansion, the conventional adiabaticity approaching is used to suppress these affects [5–7] . Along the trajectory of electron beam, the acceleration section in the coordinate interval of 0.5-1.0 m, and the expansion is at range of 1.0-2.2 m. Figure 3 shows the dependence of longitudinal acceleration parameter ξ_{acc} and transverse expansion α_{exp} upon the axial magnetic field B_s and axial electric fields E_s along the electron trajectory coordinate s.

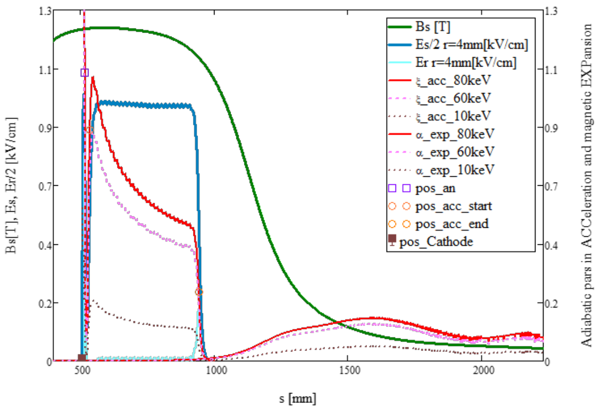

Figure 3: Parameters variation for longitudinal acceleration (0.5-1.0 m) and transverse expansion (1.0-2.2 m) at the minimal energy 10 keV (brown dot curve), the maximal 80 keV (red solid curve) and 60 keV (pink dashed curve) along the electron orbit coordinate. In additional, positions of cathode, anode, acceleration tube are also marked by block symbols.

Adiabatic Acceleration

The longitudinal adiabaticity means the relative energy change of electron should be faster than the electron plasma relaxation time $1/\omega_p$ in acceleration, i.e. the parameter $\xi_{acc} = (1/\omega_p) \cdot (1/E_k)|dE_k/dt|$ is smaller than 1. Here, E_k is kinetic energy and ω_p denotes plasma frequency of electron. The acceleration parameters in Fig. 3 give the maximum at entrance of acceleration tube with 0.2, 0.8 and 1.04 at energies of 10 keV, 60 keV and 80 keV respectively.

In additional, calculation shows the longitudinal temperature is not very dependent on the acceleration parameter [8] with a dependence of 2.2 μeV/0.1 near 1.04 at 80 keV.

Adiabatic Expansion

The transverse adiabaticity means the relative change step of magnetic field is larger than the cyclotron length λ_c when expanding electron beam along the axial, i.e. the expansion parameter $\alpha_{exp} = (\lambda_c/B_s) \cdot |dB_s/ds|$ is smaller than 1. The expansion parameters in Fig. 3 give the maximum in the middle of transition section with 0.05, 0.14 and 0.16 at energies of 10 keV, 60 keV and 80 keV respectively.

Electron temperatures

Using the above design of magnetic and electric field and other typical parameters from the two HIRFL-CSR coolers, we calculate the electron temperatures change with kinetic energy at the target section. Figure 4 shows the result within the overlap area limited by the e-cooled ion beam. They meet the design in Table 1.

ISBN: 978-3-95450-243-1 ISSN: 2226-0374 doi:10.18429/JACoW-COOL2021-P1006

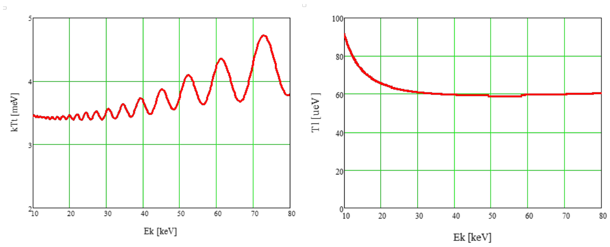

Figure 4: Transverse temperature kTt and longitudinal kTl variation with kinetic energy within overlapped area.

ELECTRON GUN AND COLLECTOR

Since 200 mA uniform profile electron beam at is required by DR experiment, a thermionic gun of two-electrode Pierce type are adopted. The cathode is flat with 10 mm diameter and will work at 750 °C with 1.8 μP perveance. The anode has a horn-shaped structure with 10 mm distance from cathode. The overall cross-section of electron gun and acceleration tube is shown in Fig. 5.

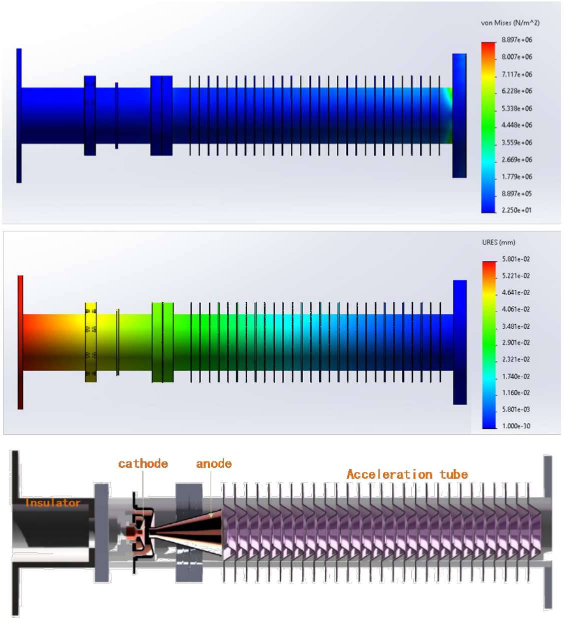

Figure 5: Internal structure (bottom), stress (top) and deformation (middle) of electron gun and acceleration tube.

Besides, the stress and deformation are also evaluated because of horizontal orientation. The results shows that when unsupported, the maximum von Mises stress 32 Mpa locates at the root of acceleration tube, which is smaller than the criterion 8.9 Mpa for ceramic, and the maximum deformation 0.06 mm at the top of electron gun is within acceptable range as well.

The collector electrodes consist of anode, suppressor, and collection cup. It is almost a copy HIRFL-CSR cooler except for minor modifications upon orientation change. In addition, since different deflection of electrostatic and magnetic are used in the two Toroids, the collector secondary emission coefficient will has the order of 1-2 $\cdot 10^{-3}$. Figure 6 shows the collector structure and coils arrangement.

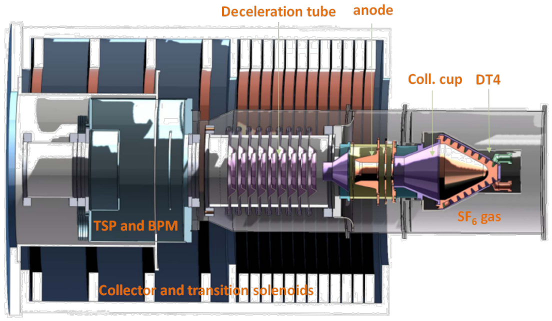

Figure 6: Structure of collector and transition sections.

CONCLUSION

The acceleration and magnetic expansion are optimized for a lower temperatures of electron beam and the improvement at technical feasibility when the SRing e-target is oriented horizontally. The calculated temperature at target section meet the requirement. Some confirmed components have been processed while some detailed optimization is still in progress.

ACKNOWLEDGEMENTS

We sincerely thank the e-cooling group at Budker Institute of Nuclear Physics. Many technical and physical designs of the E-target inherit HIRFL-CSR e-coolers. We also learn a lot from other electron coolers and e-targets around.

REFERENCES

[1] B. Wu *et al.*, “The design of the Spectrometer Ring at the HIAF”, *Nucl. Instr. and Meth. A*, vol. 881, p. 27-35, 2018.

[2] V. Bocharov, *et al.*, ”HIRFL-CSR electron cooler commissioning”, *Nucl. Instr. and Meth. A*, Vol.532, p. 144-149, 2004.

[3] Z.K. Huang *et al.*, “Dielectronic recombination experiments at the storage rings From the present CSR to the future HIAF”, *Nucl. Instr. and Meth. B*, vol. 408, p. 135-139, 2017.

[4] J. Li *et al.*, “Preliminary Design of Electron Target for SRing at HIAF”, *Proceedings of COOL 2017*, p. 40-43, 2017.

[5] T. Tanabe, *et al.*, ”A liquid-helium-free superconducting electron cooler at the storage ring TARN II, *Nucl. Instr. and Meth. A*, Vol.441, p. 326-328, 2000.

[6] H. Danared, *et al.*, ”Studies of electron cooling with a highly expanded electron beam”, *Nucl. Instr. and Meth. A*, Vol.441, p. 123-133, 2000.

[7] F. Sprenger, *et al.*, ”The high-resolution electron–ion collision facility at TSR”, *Nucl. Instr. and Meth. A*, Vol.532, p. 298-302, 2004.

[8] T. SchmoKöller, *et al.*, ”Numerical simulation of the adiabatic acceleration ofelectron beams TSR”, *Nucl. Instr. and Meth. A*, Vol.441, p. 50-53, 2000.

[9] A. Bubley *et al.*, “Low Energy Electron Cooler for the NICA Booster”, *Proceedings of COOL 2017*, p. 22-24, 2017.

ISBN: 978-3-95450-243-1 ISSN: 2226-0374 doi:10.18429/JACoW-COOL2021-P1008

ELECTRON COOLING USING A PULSED AND DITHERING BEAM FROM AN ELECTROSTATIC ELECTRON COOLER

H. Wang, M. W. Bruker, S. Benson, A. Hutton, K. Jordan, T. Powers, R. Rimmer, T. Satogata,
A. Sy, S. Wang, H. Zhang, Y. Zhang, Jefferson Lab, USA
F. Ma, J. Li, X. M. Ma, L. J. Mao, X. P. Sha1, M. T. Tang1, J. C. Yang,
X. D. Yang, H. Zhao, H. W. Zhao, Institute of Modern Physics, China

Abstract

In this paper we report results of an experimental study of a pulsed-beam electron cooler. We have found the effects of the electron bunch length and longitudinal ion focusing strength on the temporal evolution of the longitudinal and transverse ion beam profile and demonstrate the detrimental effect of timing jitter as predicted by the space-charge theory and simulations.

Our experiment has suggested the need of further investigations into specific aspects of bunched cooling such as synchro-betatron coupling and phase dithering effects of using a relative shorter electron bunch to cool a longer ion bunch.

INTRODUCTION

Electron cooling continues to be an invaluable technique to reduce and maintain the emittance in hadron storage rings, for example the US Electron-Ion Collider (EIC) and the Electron-Ion Collider in China (EICC) where stochastic cooling is inefficient in cooling the proton beam and radiative cooling is negligible. Extending the energy range of electron coolers beyond what is feasible with a conventional, electrostatic approach necessitates the use of RF fields for acceleration and, thus, a bunched electron beam. To experimentally investigate how the relative time structure of the two beams affects the cooling properties, we have set up a pulsed-beam cooling device by adding a synchronized pulsing circuit to the conventional electron source of the main Cooler Storage Ring (CSRm) cooler at Institute of Modern Physics (IMP) in China. The experiment conducted in December 2019, using both synchronized [1] and modulated synchronization of electron pulses to the ion beam bunches. This "Dithering" technique modulates the electron bunch arrival time relative the ion revolution frequency by using a shorter electron bunch to cool a longer ion bunch. It is sometimes called "longitudinal painting" in some references.

EXPERIMENT SETUP

Table 1 lists the experimental parameters for both pulsed beam and dithering beam cases. An electron cooler and an RF cavity are placed in the dispersion-free sections in the CSRm ring at Institute of Morden Physics (IMP). The active length of the electron cooler is 3.4 m. The RF voltage ramped from 0.6 to 2 kV in the frequency range of 0.25 to 1.7 MHz. Figure 1 illustrates arrival time Δt verses real time t with a triangle wave variation. The modulation hardware delays or advances the phase of the signal with respect to the reference signal V_{ref} by an amount of $asin(V_{mod}/V_{ref})$ with V_{mod} being the instantaneous value of the modulating voltage. The magnitude of phase change is determined by the reference voltage and was kept constant in the experiment at a value of about 600 ns peak-to-peak. This corresponds to approximately +/- 40° of phase with respect to the reference signal which occurs at 2 × 191.5 kHz. The modulation frequency was changing from 100 Hz to 1000 Hz during the experiment.

Table 1: Beam and Instrumentation Parameters

ion beam	
particle type	$^{86}\mathrm{Kr}^{25+}$
beam current	< 100 µA
rest mass	930.5 MeV/nucleon
kinetic energy	5.0 MeV/nucleon
β	0.103
γ	1.005
revolution frequency f_{rev}	191.5 kHz
harmonic number h	2
RF voltage V_{RF}	0.6–2 kV
electron cooler	
acceleration voltage	2.7 kV
positive grid voltage	50 V
negative grid voltage	–551 V
peak current	30 mA
pulse length	> 100 ns

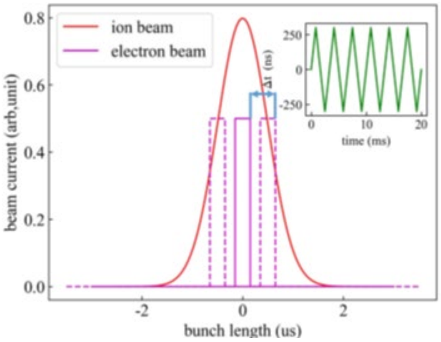

Figure 1: Experimental setup for the longitudinal phase modulation using a triangle waveform. The example here uses a 300 ns square electron pulse to cool an ion beam with a 0.5 µs rms bunch length. The modulation amplitude is 300 ns with frequency of 300 Hz.

After a fixed-frequency experiment with Δt=0 during which there was almost no beam loss for Krypton bunch

---

* This work was supported jointly by U.S. DOE Contract No. DE-AC05-06OR23177 and the National Natural Science Foundation of China, No. 11575264. This experiment was also supported by the International Partnership Program of Chinese Academy of Sciences, Grant No. 113462KYSB20170051,

haipeng@jlab.org

ISBN: 978-3-95450-243-1 ISSN: 2226-0374 doi:10.18429/JACoW-COOL2021-P1008

cooling, the modulation was applied. A beam diagnostic measurement cycle was set in 50 s. Initially, the ions were injected by the SFC and accumulated into CSRm in multi-turn injection with the help of DC cooling. A coasting beam of 10^8 particles was obtained after a 10 s accumulation. After additional DC cooling of 2 s, the DC electron beam was turned off. Then the beam emittance and momentum spread blew up within 3 s due to intra-beam scattering (IBS) heating. The RF system was then turned on to adiabatically form 2 bunches. The capture time was 2.5 s. The modulated electron bunches were then turned on for ion bunch cooling. The longitudinal ion beam profile was measured with a beam position monitor [2] (BPM) and the transverse beam size was measured by an ionization profile monitor [3] (IPM). In addition, a DC beam Current Transformer monitor (DCCT) and a spectrum analyser (SA) connected to a Schottky pickup [4] were used to record the beam current and to observe the process from injection to the end of cooling [1].

INITIAL DATA ANALYSIS

It was clearly observed that the ion beam bunch length was reduced and the peak current was increased by the modulated electron bunches indicating some cooling. However, the beam loss was severe. As shown in Fig. 2, the beam loss increases monotonically as a function of the modulation frequency. Figure 3 shows the cooling processes for a different electron bunch length with the same modulation frequency. The cooling rate is higher for a longer electron pulse and the ion beam loss is reduced.

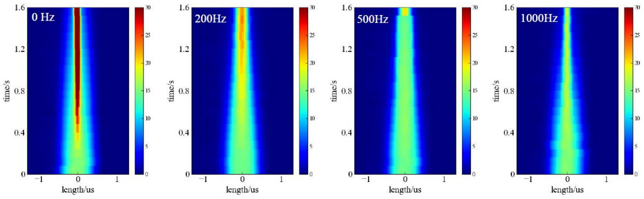

Figure 2: Evolution of longitudinal beam profile of bunched ion beam from bottom to top during the cooling process measured at different modulation frequencies for the 300 ns electron bunch length. Colour code indicates the bunch peak current with a maximum of 30 mA.

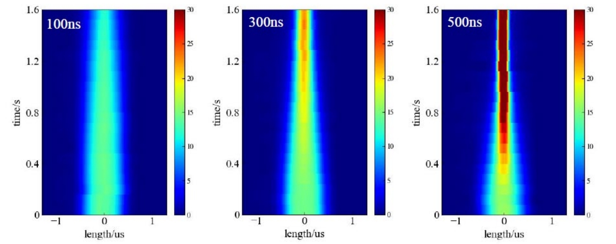

Figure 3: Same process as Fig. 2 for a different electron pulse length for a fixed 200 Hz modulation frequency.

Another measure is to calculate integrated charge on the BPM. So normalized to initial total charge, the percentage of particle loss can be calculated as shown in Fig. 4, the higher modulation frequency, the larger jittering time in synchronization, and the more beam loss. Calculated jittering time is about 2.7 ns at 100 Hz modulation frequency.

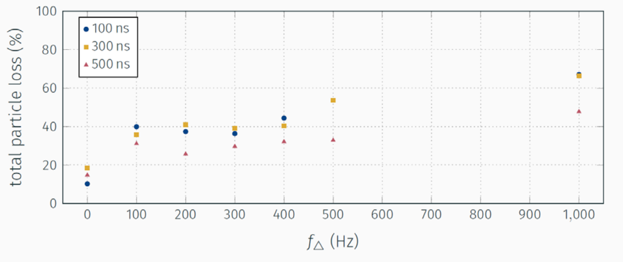

Figure 4: Measured Kr beam loss from the BPM signal as function of modulation frequency.

SIMULATIONS OF BEAM LOSS

To understand this beam loss mechanism, two independent tracking simulation codes have been developed at IMP [5] and JLab [6]. The CSRm beam transport matrices are obtained from MAD-X deck. Both codes include analytical models of magnetized electron friction force cooling, intra-beam scattering, the space charge kicks from the electron beam edges in the cooler, and ion synchrotron motion. They are all are similar to the BETACOOL and JSPEC codes [7-9].

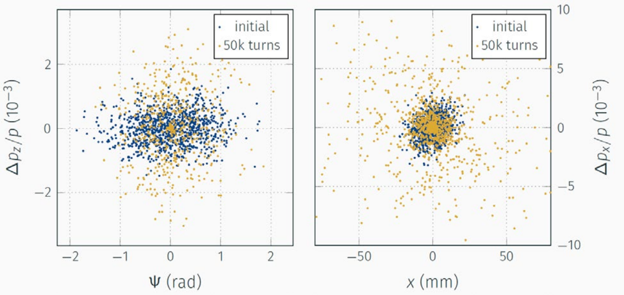

Figure 5: JLab tracking simulation indicates the longitudinal and horizontal emittance coupling and growth after 50000 turns. The model assumes 1/3 of bunches randomly kicked with an edge shift in Δt = 50 ns, and an ensemble of 1000 ions with the initial emittance.

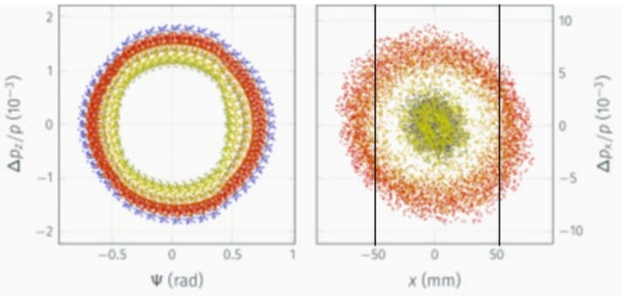

Figure 6: Phase space of single ion tracking with same conditions as Fig. 5. The ions can be lost on the ±50 mm beam pipe aperture.

A large space-charge tune shift (Eq. (1) from [10]) at low energy can cause emittance growth (heating) and then further beam loss due to a synchro-betatron coupling resonance. The emittance growth time in our experiment for a typical 20 ns arrival jitter is ∼0.34-0.66 s due to the very low β^2 and γ^3. We have estimated a fluctuation of 1% of rms peak current at 30 mA in our experiment for a typical 20 ns arrival jitter is ∼0.34-0.66 s. Emittance growth cannot be easily avoided at k=0, dc like, 30 mA in synchro-betatron resonance with such a large space charge tune shift.

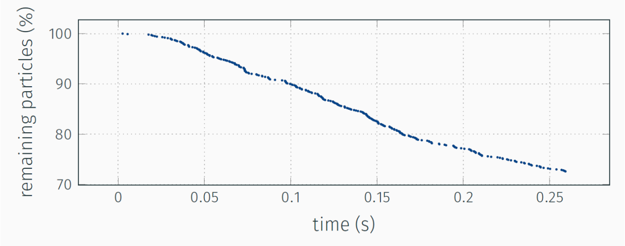

Figure 7: Beam aperture loss during the dithering cooling process by the tracking simulation in Fig. 6.

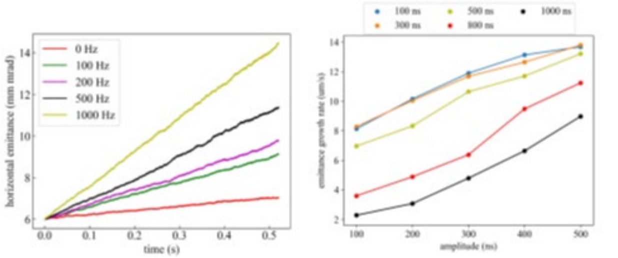

Figure 8: IMP tracking simulations of emittance growth rates. Modulation amplitude is 300 ns. Left: Effects of modulation frequency, pulse length is 500 ns; Right: Effects of electron pulse length, the modulation frequency is 500 Hz.

Further analysis and simulation models need to be studied to explore the third Q_z tune spread in 6D phase space with the RF focusing, the e-pulse edge kicking and their coupling effects to the transverse emittance. A preliminary simulation indicated, as in Fig.10, that the transverse tunes get spread out when the e-beam current increases, crossing several resonance lines. However, for a higher energy cooler like the Low Energy RIC electron Cooling (LEReC), the space charge tune shift has been reduced by 104 times. The synchro-betatron coupling can tolerate up to k=4_{th} order resonances [10].

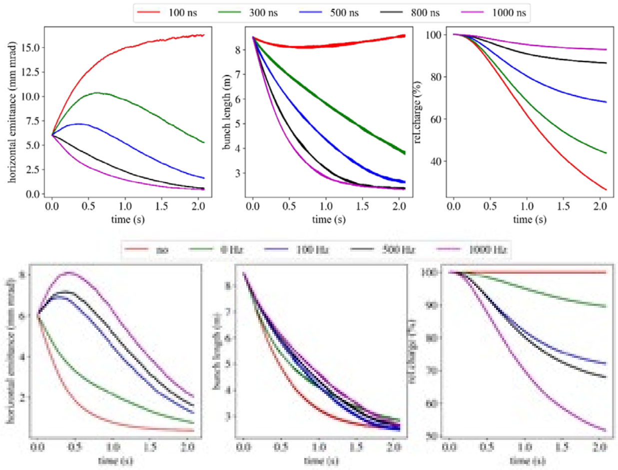

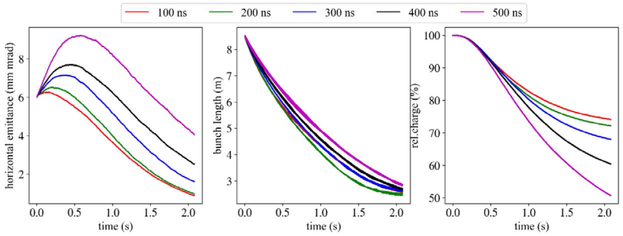

Figure 9: Ion beam emittance grown rate during the cooling process. Top: for different electron pulse lengths with 500 Hz mod. freq. and 300 ns mod. amp.; Middle: for different modulation frequencies with 300 ns mod. amp. and 500 ns e-pulse length; Bottom: for different mod. amp. with 500 Hz mod. freq. and 500 ns e-pulse length. From left to right are the emittance, bunch length and beam loss. verses cooling time respectively.

More precise triggering control of the HV pulsing system and an improved beam diagnostic system are needed at CSRs, IMP. Experiments at higher energy like at the CSRe, IMP will be useful for a further scaling law study of future EIC Strong Hadron Cooling (SHC) machine including the simulation support to understand those data.

$$\Delta\nu_{\text{peak},x/y} = \frac{N_{\text{e}} r_0 L_{\text{cool}}}{(2\pi)^2 Q_{x/y} f_{\text{rev}} \sqrt{2\pi}\sigma_{\text{e}} \gamma^3 \beta^2 a_{\text{e}}^2} \qquad (1)$$

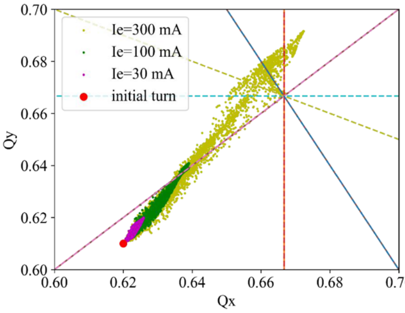

Figure 10: The transverse turn spread of the CSRm ring with the space charge effect from the electron beam. The e-pule length is 500 ns with different peak currents.

CONCLUSION

Pulsed electron bunches generated in a DC cooler to cool a RF focused krypton bunches in experiments at CSRm, IMP, have demonstrated cooling. However a dithering experiment has indicated a larger ion beam loss. Simulations and analytical calculations have indicated that space-charge kicks at random points in the synchrotron motion cause a large resonance coupling, leading to transverse emittance growth and then beam loss. Such large space-charge tune shift is dominated at low energy cooling in this experiment. Further studies for the RF based on higher energy cooler need to be done. Much slower dithering within a longer IBS lifetime of higher energy proton storage ring like EIC could potentially save electron linac cost like an Energy Recovery Linac (ERL) for the alternative solution to the proton cooling.

REFERENCES

[1] M. Bruker *et al.,* "Demonstration of electron cooling using a pulsed beam from an electrostatic electron cooler", *Phys. Rev. Accel. Beams,* vol. 24, 012801, 2021. `doi:10.1103/PhysRevAccelBeams.24.012801`

[2] P. Forck, P. Kowina, and D. Liakin, "Beam position monitors", in CERN Accelerator School: Beam Diagnostics, CERN, Geneva, 2009, pp. 187–228.

[3] H.-M. Xie, *et al.,* "A non-invasive ionization profile monitor for transverse beam cooling and orbit oscillation study in HIRFL-CSR", *Nuclear Science and Techniques* 31, 40, 2020.

[4] P. Forck, P. Kowina, R. Singh, and M. Wendt, "Tutorial on Beam Measurements using Schottky Signal Analysis", in *International Beam Instrumentation Conference*, Grand Rapids, 2017.

[5] F. Ma, *et al.,* "Beam Cooling by a Bunched Electron Beam with Phase Modulation", unpublished.

[6] M. W. Bruker *et al.*, "Demonstration of Electron Cooling using a Pulsed Beam from an Electrostatic Electron Cooler", in *Proc. 12th Int. Particle Accelerator Conf. (IPAC'21)*, Campinas, Brazil, May 2021, pp. 1827-1830. `doi:10.18429/JACoW-IPAC2021-TUPAB181`

[7] I. Meshkov, A. Sidorin, A. Smirnov, G. Trubnikov, R. Pivin, BETACOOL Physics Guide, `http://lepta.jinr.ru/betacool`

[8] H. Zhang, J. Chen, H. Huang, R. Li, L. Luo, and Y. Zhang, "Development of the Electron Cooling Simulation Program for JLEIC", in *Proc. of International Particle Accelerator Conference (IPAC'16),* Busan, Korea, May 8–13, 2016, p. 2451. `doi.org/10.18429/JACoW-IPAC2016-WEPMW014`

[9] JSPEC on GitHub, `https://github.com/JeffersonLab/ElectronCooling`

[10] G. Wang, "Ion Emittance Growth due to Focusing Modulation from Slipping Electron Bunch", *BNL Tech Rep*. No. C-A/AP/536, 2015.

ISBN: 978-3-95450-243-1 ISSN: 2226-0374 doi:10.18429/JACoW-COOL2021-P1010

OPTIMIZATION OF THE ELECTRON EMISSION FROM CARBON NANOTUBES FOR ELECTRON COOLING IN ELENA

B. Galante[1, 2, 3*], G. A. Tranquille[1], C. P. Welsch[2, 3], J. Resta López[2, 3, 4]
[1] CERN, Geneva, Switzerland
[2] The University of Liverpool, Liverpool, United Kingdom
[3] The Cockroft Institute, Sci-Tech Daresbury, Warrington, United Kingdom
[4] ICMUV-Institute of Materials Science, University of Valencia, Spain

Abstract

Electron cooling guarantees beam quality in low energy antimatter facilities. The ELENA e-cooler permits to reduce the emittance blow-up of the $\bar{p}$ beam, thus delivering highly focused and bright beams at the unprecedented low energy of 100 keV to the experiments. To have a “cold” beam at such low energy, the electron gun must emit a mono-energetic and relatively intense electron beam. Efficient cooling can be achieved with a 5 mA electron beam having transverse energy spread $<$ 100 meV and longitudinal energy spread $\sim$ 1 meV. The thermionic gun used in operation limits the cooling performances due to a relatively high transverse energy of the emitted beam ($>>$ 100 meV). An optimization of the e-gun is being studied, aiming to develop a cold cathode gun based on carbon nanotubes (CNTs). The use of CNTs implies the need of an extracting grid to allow for a stable and uniform emission, although the grid’s features are critical to control the electron beam properties.

INTRODUCTION

In field emission the electron extraction is achieved applying a strong electric field between a cathode and an anode. The high intensity of the electric field necessary to enable significant emission has always hindered the use of field emitting cathodes. The arise of tip-like nano-structures has paved the way to field enhancement, so that it is now possible to extract large currents, in the order of many mA, with an electric field in the order of a few V/μm. CNTs are considered among the best field emitters because of their chemical stability, the possibility of mass production with scalable techniques and the large currents that they can emit and withstand [1, 2]. The major issues that have limited their use in operation are related to emission stability and lifetime. In ELENA, CNTs would be required to stably emit for hundreds or even thousands of hours without significant signs of degradation. In our previous work we investigated the best conditioning process necessary to ensure optimal emission stability and a lifetime that is compatible with operational use. If CNTs are operated in optimal conditions and trained appropriately, they can emit for hundreds of hours without significant degradation while emitting current densities of about 2 mA/cm^2; a value that would suffice for the requirements of ELENA’s e-gun, e.g. 5 mA [3, 4]. An emission for more than 1500 hours has been proved for a CNT array, testing it in both DC and switching mode [5, 6]. In order to extract electrons from a large area cathode while obtaining an homogeneous emission an extracting grid becomes necessary. For this reason, a thorough study of the grid effect is essential for tuning the electron beam features according to the requirements. Although in this work we are aiming at using CNTs, this study still holds in the case of any field emitting cathode and in general to any case where an extracting grid is deemed necessary.

EXPERIMENTS

Several grid parameters can affect the beam properties. The grid distance from the cathode defines the voltage to be applied on the grid in order to get the desired electric field. The hole size severely affects the beam properties because of the distortion of the field lines within the hole. The relation between hole size and the pitch determines the transmittance of the grid. Additionally, the hole shape and holes arrangement must be devised cleverly in order to maximize the grid’s transmittance. Finally, the feasibility of physically manufacture the desired grid according to the current technology must be taken into account. We have started analysing six different grid types: Grid 250 – 50. Hole size: 250 μm, Pitch size: 50 μm. Grid 200 – 40. hole size: 200 μm, pitch size: 40 μm. Grid 150 – 30: hole size: 150 μm, pitch size: 30 μm. Grid 100 – 20: hole size: 100 μm, pitch size: 20 μm. Grid 50 – 10: hole size: 50 μm, pitch size: 10 μm. Grid 25 – 5: hole size: 25 μm, pitch size: 5μm. The latter represents what is most likely the smallest grid which is possible to realise at the time of writing. All grids are devised to have squared holes in order to maximize the holes packing and consequently the transmittance. The pitch is hereby defined as the solid spacing between each hole.

All simulations are conducted with the software CST Studio and the simulation design allows for straight field lines in the whole emission region. The only source of field lines distortion is represent by the grid. The main simulation types are two and both have the layout illustrated in Fig. 1.

Simulation 1. Parametric simulation of the electron beam varying the grid distance from 0.4 to 5 mm with a step width of 0.2 mm. The electric field is kept constant. The initial beam energy is set to 0.1 eV in order to run a critical test for all grids. We were then able to derive the maximum deviation % of the voltage along the grid and the beam offset, "r" (calculated via the CST built-in "Envelope" option), which represents the difference between the radii of the emitted

---

* bruno.galante@cern.ch

ISBN: 978-3-95450-243-1 ISSN: 2226-0374 doi:10.18429/JACoW-COOL2021-P1010

beam and the beam hitting the anode.

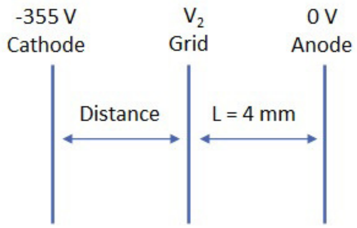

Figure 1: Simulation layout. Triode configuration: cathode, grid, anode. Cathode voltage: −355 V (the electron beam energy for the higher plateau in ELENA's e-cooler); anode voltage: 0 V. The grid voltage varies according to the distance and in order to keep a constant electric field of 2 V/μm. The emission is "Field Induced" with the parameters "a" and "b" of the Fowler-Nordheim equation derived from experimental results [6].

Simulation 2. Double parametric simulation varying the grid distance from 0.6 mm to 2 mm with 0.2 mm step width and the initial beam energy from 0 eV to 0.1 eV with 0.025 eV step width. Data analysed: beam offset.

In both cases we calculated the maximum transverse energy of the beam with the following formula:

$$E_{tr} = \frac{V_2^2 r^2}{2L^2\left(\sqrt{2(V+355)} - 26.646\right)^2} \tag{1}$$

RESULTS AND DISCUSSION

From "Simulation 1" we were able to extract several data. We can notice from Fig. 2a and 2b how the beam offset and the voltage deviation % both greatly decrease with the distance and for smaller hole grids. It is also clear from Fig. 2c how the beam offset is dependent on the voltage deviation %. The reason for the increase of the beam offset when the deviation increases is connected to the higher voltage fluctuations in the grid holes, which translates in curvatures of the field lines that consequently provoke the arise of transverse components in the beam trajectory. This trend is reversed increasing the distance, since higher distance translates in smaller voltage fluctuations along the grid. We were also able to quantify the transverse energy increase due to the passage of the beam through the grid using Eq. 1 in order to study its variation for each grid depending on the distance. The results are shown in Fig. 3 This calculation served us to understand whether the use of any of the investigated grids can fulfill our purpose considering our required beam transverse energy spread. From the inset in Fig. 3 we can assess that the only feasible grids are 50 – 10 and 25 – 5 at distances greater than 1 mm. All other grids add a transverse kick that is too high at every feasible inter-electrode distance. For this reason we focused the remaining simulations on the grid 50 – 10. In "Simulation 2" we studied how the beam offset and the beam transverse energy due to the grid change if the initial beam energy varies. The simulation is ran on the grid 50 – 10. The results are shown in Fig. 4. From Fig. 4a we can notice that the beam offset decreases with the distance for every possible initial beam energy. The beam offset greatly increases when the initial beam energy increases, independently from the grid distance. From calculations of the transverse energy, Fig. 5, we can further notice that for smaller initial beam energy the additional beam transverse energy due to the grid is less significant. As expected, the transverse energy due to the grid and the total transverse energy both decrease when the grid distance increases.

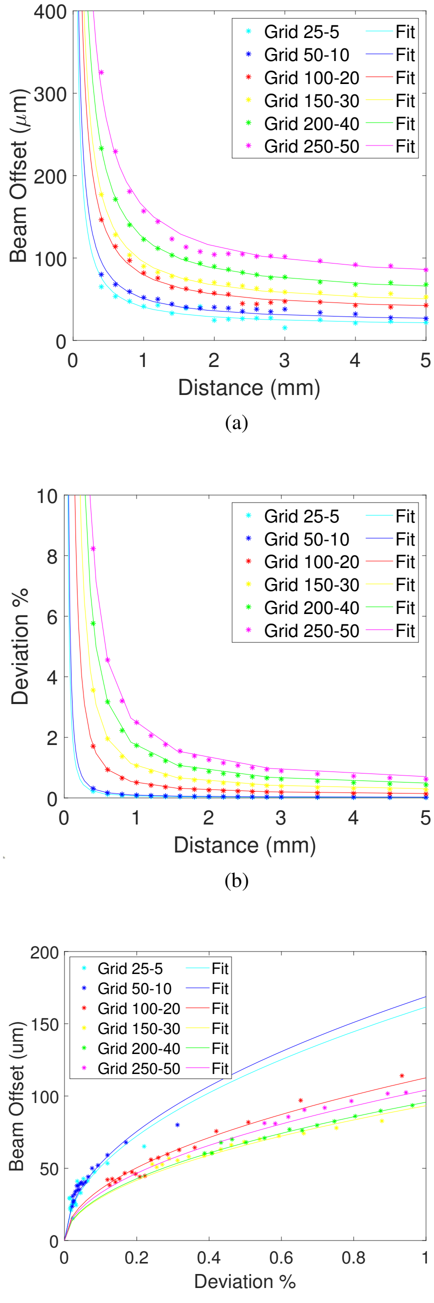

(a)

(b)

(c)

Figure 2: (a) Grid distance vs Beam Offset. (b) Grid distance vs Maximum voltage deviation %. (c) Maximum voltage deviation % vs Beam offset. All fits are done with a power equation of the type: $y = ax^b + c$.

ISBN: 978-3-95450-243-1 ISSN: 2226-0374 doi:10.18429/JACoW-COOL2021-P1010

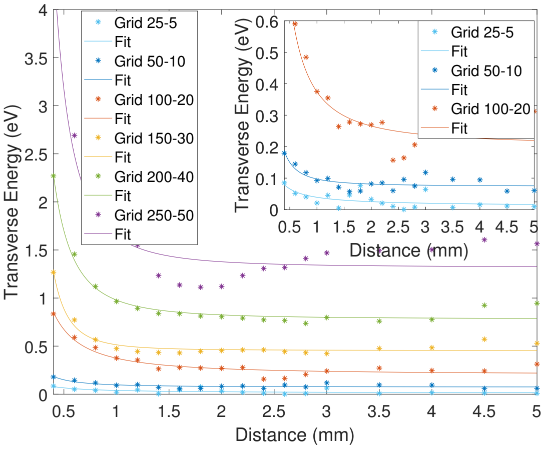

Figure 3: Grid distance vs Transverse energy due to the grid. Inset: magnification for better visualizing the behaviour of the grids 100 – 20, 50 – 10, 25 – 5. All fits are done with a power equation of the type: $y = ax^b + c$.

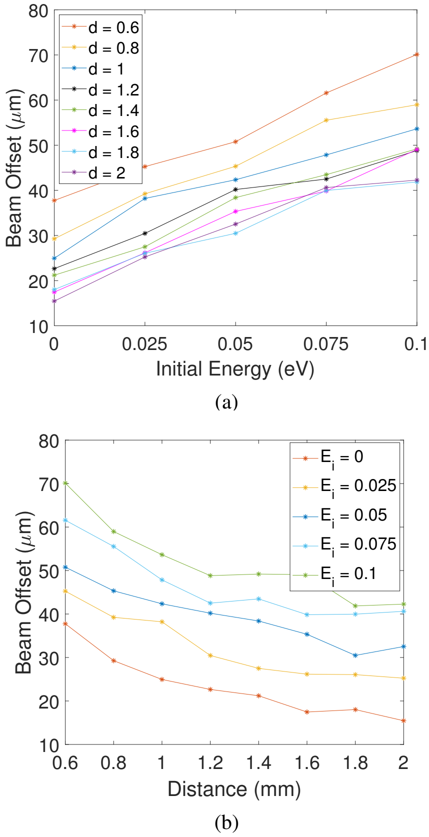

Figure 4: (a) Initial beam energy vs Beam offset, for different grid distances. (b) Grid distance vs Beam offset, for different initial beam energies.

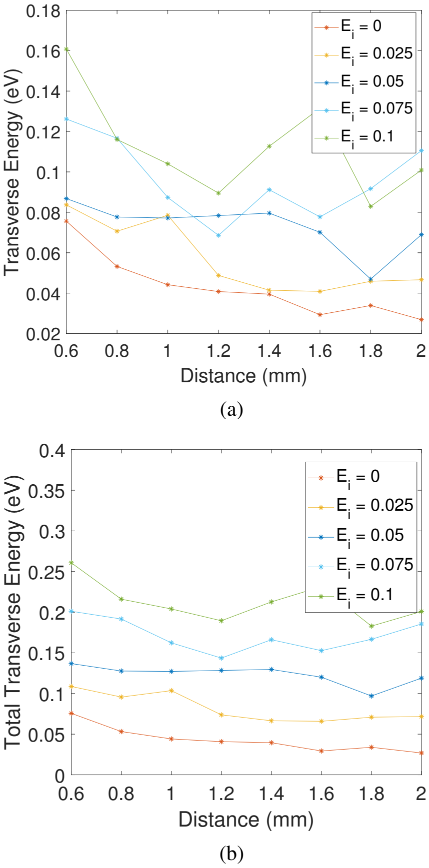

Figure 5: (a) Grid distance vs Transverse energy due to the grid, for different initial beam energies. (b) Grid distance vs Total transverse energy after passing the grid, for different initial beam energies.

CONCLUSIONS

The grid severely affects the beam properties and must be chosen carefully. The results achieved show how a grid 50 – 10 can provide a beam with transverse energy of less than 0.1 eV if the grid distance is > 1 mm and if the initial beam energy is ≤ 0.025 eV. These represent very strict requirements, but prove that the use of a grid is feasible. The grid 25 – 5 would provide for significantly improved beam properties since the impact of such grid on the transverse energy seems to be of less than half compared to the 50 – 10 grid, as suggested by the study in Fig. 3. Further tests are required to finalize the gun layout and a measurement of the CNT electron beam energy is necessary. This grid study gives important results for designing any gun or device involving an extracting grid and served us to determine the conditions for which a CNT-based gun is feasible for the ELENA e-cooler considering the actual state of technology.

ACKNOWLEDGEMENTS

AVA has received funding from the European Union's Horizon 2020 research and innovation program under the Marie Skłodowska-Curie grant agreement No 721559.

Javier Resta acknowledges support by the Generalitat Valencia under grant agreement CIDEGENT/2019/058.

REFERENCES

[1] Yahachi Saito. *Carbon Nanotube and related field emitters: Fundamentals and applications*. Wiley-VCH, 2010. ISBN: 978-3-527-32734-8.

[2] C.Li, Y.Zhang, M.Mann, D.Hasko, W.Lei, B.Wang, D.Chu, D.Pribat, G.Amaratunga, and W.I.Milne. "High emission current density, vertically aligned carbon nanotube mesh, field emitter array.", *Applied Physics Letters* 97, 113107, 2010.

[3] S.Maury, W.Oelert, W.Bartmann, P.Belochitskii, H.Breuker, F.Butin, C.Carli, T.Eriksson, S.Pasinelli, and G.Tranquille. "ELENA: the extra low energy anti-proton facility at CERN." *Hyperfine Interact* 229, 2014.

[4] G.Tranquille, A.Frassier, and L.Joergensen. "The ELENA electron cooler: parameter choice and expected performance." *Hyperfine Interact* 229, 2014.

[5] B. Galante, G. A. Tranquille, M. Himmerlich, C. P. Welsch, and J. Resta López. "Stability and lifetime study of carbon nanotubes as cold electron field emitters for electron cooling in the CERN extra low energy antiproton ring." In *Phys. Rev. Accel. Beams* 24.113401, 2021. DOI: `10.1103/PhysRevAccelBeams.24.113401`.

[6] B. Galante, G. A. Tranquille, C. P. Welsch, O. Apsimon, and J. Resta López. "Carbon nanotubes as cold electron field emitters for electron cooling in the CERN Extra Low ENergy Antiproton (ELENA) ring." *IPAC21 Proceedings,*2021.

ISBN: 978-3-95450-243-1 ISSN: 2226-0374 doi:10.18429/JACoW-COOL2021-P2002

SUSPENDED GROUND MICROSTRIP COUPLED SLOTLINE ELECTRODE FOR STOCHASTIC COOLING

S. Wunderlich*, C.Peschke, GSI, Darmstadt, Germany

Abstract

An alternative design of a slotline electrode has been developed and simulated. In contrast to the planar slotline pick-up designed for FAIR CR and the slot-ring electrode built by FZJ for FAIR HESR, the presented design uses suspended microstrip lines for the coupling to a planar slotline. This has some advantages and disadvantages for kicker and pick-up applications in respect of losses, power handling, and mechanical aspects.

INTRODUCTION

At the moment there are two different electrode designs foreseen for the FAIR Collector Ring (CR), one planar slotline electrode as plunging pickup [1] (also called PU17) and the well-known Forschungszentrum Jülich (FZJ) slot-ring electrode design [2] as kicker (see Fig. 1).

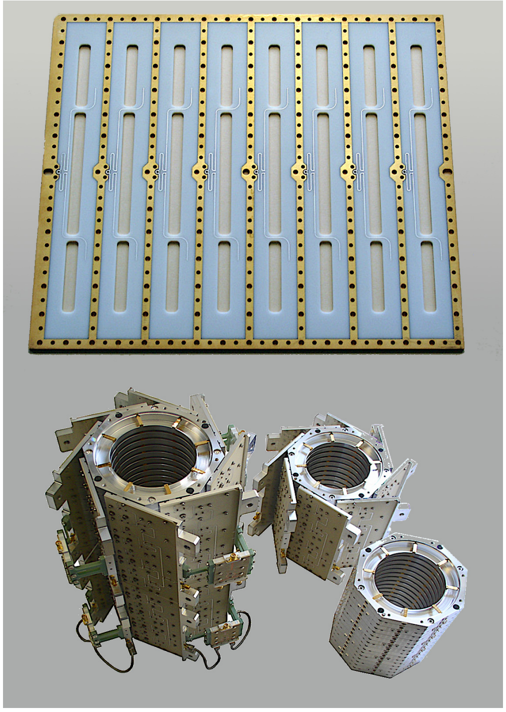

Figure 1: Top: Planar slotline electrode PU17 combiner (non beam) side. Bottom: FZJ slot-ring kickers (for FAIR HESR [2]).

All electrodes are optimized for antiprotons (pbars) at a velocity factor of $\beta = 0.97$ (3 GeV), but should also be functional for rare isotope beams (RIBs) at $\beta = 0.83$ (740 MeV/u) within the CR stochastic cooling band $f = 1$ to 2 GHz and $f = 2$ to 4 GHz for the HESR, respectively.

Design Comparison

Both designs exhibit high impedances, flat frequency response and large beam apertures. Whereas the FZJ design is especially suited as a kicker due to its robust design and large structures, PU17 is less suited as kicker because of the fine microstrip structures on the non beam side (see Fig. 1), which can only handle a limited amount of power. An additional disadvantage of PU17 is the thick 1.905 mm Al_2O_3 ceramic, which is expensive and difficult to manufacture.

The FZJ slot-ring kicker is—due to its mechanical design—not able to be used as plunging pick-up. Whereas PU17 is especially designed for plunging operation, with beneficial factors like planar structures and low mass.

Since every slot of PU17 is housed in its own compartment, and thereby isolated from its neighboring slots, it is possible to inject a test signal into each slot—via an additional coupling loop—for testing without beam. This feature is not foreseen for the FZJ kicker.

Conclusion

While PU17 has some advantages, there is also the inherent disadvantage of not being able to be used as kicker and the fact that it uses thick Al_2O_3 ceramic, which not only increases cost but also lowers manufacturing quality. Thereby increasing risk of failure and lowering performance characteristics, i. e. non constant characteristic impedance and high resistive losses along its microstrip structures.

Therefore, it was decided to start a new development of a slotline electrode with suspended ground technology.

NEW DEVELOPMENT

The original slotline electrode design PU17 was used as a starting point to create a new suspended ground design PU18. Suspended ground microstrip lines experience a significantly lower effective dielectric constant ε_{eff}, thus the mechanical dimensions of the structures have to become larger to exhibit the same characteristic impedance Z_0. This results not only in reduced ohmic losses but also in reduced thermal resistance along the microstrip lines. Furthermore, suspended ground structures tend to have lower dielectric losses and less dispersion effects.

Design

A 6 mm wide slot line milled thru aluminum sheet, perpendicular to the beam, is used as a coupling element between beam (compartment) and an internal suspended coupling bridge. The coupling bridge itself is placed in a distance of ~ $\lambda/4$ to the end of the slotline, it is designed as a spring element which holds two suspended ground printed circuit boards (PCBs) with 635 µm Al_2O_3 substrate in their

---

* S.Wunderlich@gsi.de

place. At the same time, it electrically connects both PCBs. One PCB contains a Wilkinson power combiner, which merges the two coupling elements (bridges) of one slot into one signal. The output of the Wilkinson is connected to a coaxial 50 Ω feed port. The other PCB contains a ~ $\lambda/4$ open end microstrip line for matching.

Every slot is housed in a separated hollow aluminum body, which provides some isolation between the single slots. The distance between slot center to slot center is $\Delta z = 25$ mm. Beam compartment (aperture) size is $A = 230\,\mathrm{mm} \cdot 140\,\mathrm{mm}$ (WxH). Ferroxcube 4S60 ferrites are placed along the outer wall for providing unwanted mode damping and isolation between beam compartment and outer vacuum chamber. Figure 2 shows a sketch of the new PU18 design.

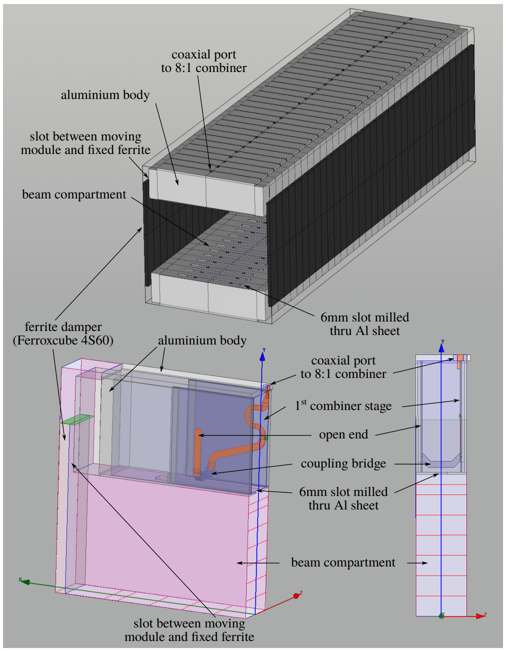

Figure 2: Top: 33 cell structure in vertical orientation (CST). Bottom: One quarter of one cell (HFSS).

Properties

Advantages compared to old PU17:

- The reduction of the Al_2O_3 ceramic thickness from 1905 µm to 635 µm does reduce production cost drastically and reduces production risks.
- The width of the microstrip structures increase from 0.19 mm to 3.9 mm. Thereby reducing resistive losses and thermal resistance along the microstrip line.

Advantages compared to FZJ slot-ring design:

- The new structure allows plunging operation.
- The injection of test signals—via additional coupling loops—for testing without beam is possible.

Disadvantages and potential risks of new PU18 :

- The coupling bridge, only pressed against its contact points by its own spring force, is a potential point of failure, which has to be thoroughly tested under different conditions like cryogenic temperatures and plunging operation.
- This holds also true for the PCBs which are only hold in place by the spring force of the coupling bridge.
- One intrinsic drawback of using Al_2O_3 ceramics is the unevenness of the substrate, negatively influencing mechanical and RF parameters.
- Since the PCB substrates no longer lie flat on the aluminum body—because of the suspended ground—there is an increased thermal resistance between the microstrip structures and the aluminum body. Therefore, it is not yet sure if the new electrode design is able to be used as kicker.
- It is not yet tested how much the ferrites along the outer wall are heated by the radiated field.

Simulation Parameter

In order to get a high confidence level of the results it was decided to use two different simulation programs with different solvers for the simulation:

- HFSS with a frequency domain solver, single cell with periodic boundaries and tetrahedral mesh.
- CST with a time domain solver, 57 cell structure and hexahedral mesh. Where only the mid port No. 29 was used as stimulus, all other ports as passive loads.

SIMULATION RESULTS

Theory

All simulation results are using the kicker circuit convention derived in [3] for the longitudinal shunt impedance:

$$R_{\|} = \frac{|V|^2}{2 \cdot \overline{P}_{in}} \tag{1}$$

where $\overline{P}_{in}$ is the root mean square (RMS) input power and V is the complex beam voltage defined by:

$$V = \int E_z(z) \cdot e^{j\omega \frac{z}{\beta c_0}} dz \tag{2}$$

with E_z the complex z-component of the electric field along the mid-line of the structure—the line through the center of the beam compartment at: $y = 0$ and $x = 0$. c_0 is the speed of light in vacuum and $\int dz$ the line integral along the z-axis.

The phase of the beam voltage is defined by:

$$\varphi(f) = Arg(V) = Arg(K_{\|}) \text{ with } K_{\|} = \frac{V}{V_k} \tag{3}$$

where V_k is the real valued terminal voltage at the input port and $K_{\|}$ the kicker constant.

The non-linear phase variation of the beam voltage V is defined by the following expression:

$$\begin{aligned} \Delta\varphi = \varphi(f) - \varphi_{aff}(f) &= \varphi(f) - \quad \varphi_{lin}(f) \quad - \varphi_c \\ &= \varphi(f) - 360° \cdot \tau_{\varphi} \cdot f \ - \varphi_c \end{aligned} \tag{4}$$

with $\varphi_{aff}(f)$ being the affine linear least square fit of the unwrapped beam voltage phase, consisting of a linear part $\varphi_{lin}(f)$ and a constant part φ_c, where the linear part can also be expressed by the constant phase delay τ_φ.

Longitudinal Shunt Impedance and Non-linear Phase Response

Figure 3 shows the results of the CST and HFSS simulation for antiprotons. We see a good agreement between both solver methods. The minimum shunt impedance is ~ 610 Ω/m at 2 GHz and a maximum value of ~ 1580 Ω/m at 1 GHz. Non-linear phase variation is within an upper limit of +6.3° and a lower limit of −10.1°.

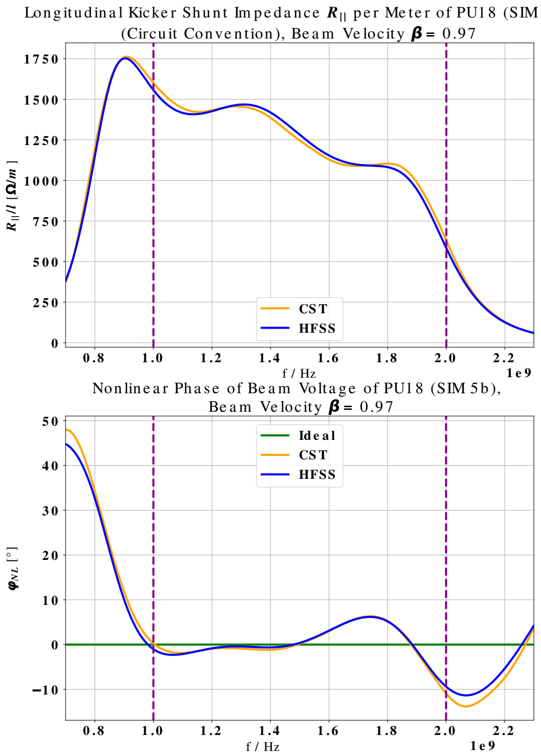
Longitudinal Kicker Shunt Impedance $R_{||}$ per Meter of PU18 (SIM 5b), (Circuit Convention), Beam Velocity β = 0.97

Nonlinear Phase of Beam Voltage of PU18 (SIM 5b), Beam Velocity β = 0.97

Figure 3: Comparison between CST and HFSS.

Figure 4 shows the results of the CST simulation for antiprotons and rare isotopes. Since the structure is optimized for antiprotons, some degradation in the performance of RIBs is expected. At 1 GHz we see a reduction from 1601 Ω/m to 914 Ω/m (−42.94 %). At 2 GHz we see a reduction from 634 Ω/m to 219 Ω/m (−65.53 %). The non-linear phase variation stays virtually the same, which was expected.

CONCLUSION

A new type of slotline electrode with suspended ground coupling elements for stochastic cooling purposes was developed and simulated. Simulation results show high sensitivity and flat frequency response in the targeted bandwidth, especially for antiprotons at high velocity.

While the new electrode shows promising simulation results, there are still open questions regarding mechanical reliability of the structure and suitability as kicker electrode in terms of power handling capabilities. Therefore, it is planned to perform additional simulations and to construct a prototype module. With the available (non cryogenic) vacuum test chamber for plunging electrodes it is possible to test the prototype under realistic operation conditions. A computer controlled three-dimensional near-field measurements probe can be used to verify the simulation results.

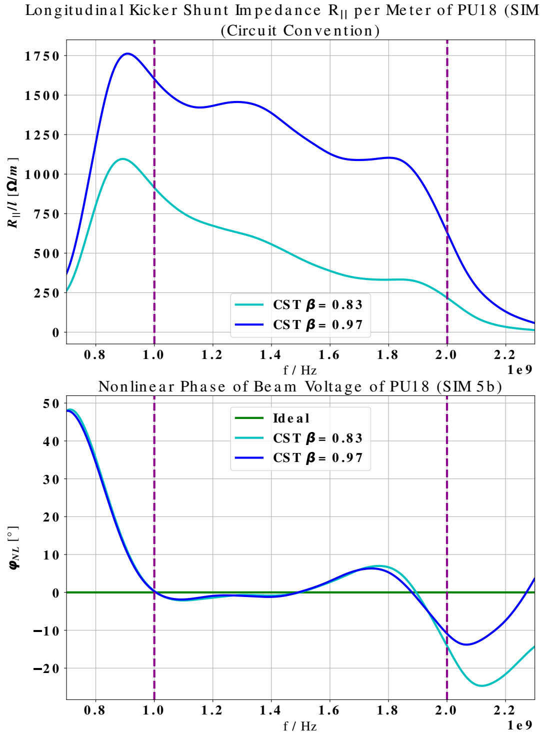
Longitudinal Kicker Shunt Impedance $R_{||}$ per Meter of PU18 (SIM 5b), (Circuit Convention)

Nonlinear Phase of Beam Voltage of PU18 (SIM 5b)

Figure 4: Comparison between RIBs and pbars in CST.

ACKNOWLEDGEMENTS

The authors thank Bernd Breitkreutz from FZJ for performing the first extensive CST PU18 shunt impedance and non-linear phase response simulation and calculation, for providing the CST evaluation software and for many helpful discussions and advice.

REFERENCES

[1] C. Peschke, U. Jandewerth, F. Nolden, P. Petri, and M. Steck, “Prototype pick-up module for cr stochastic cooling at fair,” in *Proc. 7th Workshop on Beam Cooling and Related Topics (COOL’09)*, Lanzhou, China, JACoW Publishing, Aug. 2009, pp. 130–133.

[2] R. Stassen, B. Breitkreutz, T. Katayama, N. Shurkhno, H. Stockhorst, and L. Thorndahl, “First experiences with hesr stochastic cooling system,” en, *Proceedings of the 8th Int. Particle Accelerator Conf.*, vol. IPAC2017, Denmark, 2017. DOI: `10.18429/JACOW-IPAC2017-TUPVA085`.

[3] D. A. Goldberg and G. R. Lambertson, “Dynamic devices. a primer on pickups and kickers,” AIP, 1992. DOI: `10.1063/1.41979`.

ISBN: 978-3-95450-243-1 ISSN: 2226-0374 doi:10.18429/JACoW-COOL2021-P2003

CONTROL FEATURES OF THE PLUNGING PICK-UP ELECTRODES WITH REAL TIME DIGTAL DATA PROCESSING

R. Hettrich[†], R. Böhm, C. Dimopoulou, C. Peschke,
GSI Helmholtzzentrum für Schwerionenforschung GmbH, Darmstadt, Germany

Abstract

The Pick-Up electrodes of the CR Stochastic cooling system can be positioned very precisely and fast. In the normal operating state, a function without jerk provides the set values for an underlying position control loop. Moving the electrodes however with the drives within a narrow tank can be very challenging. For installation and service, we need a manual control facility, which allows to steer the mobile drive rods slowly to the electrodes. Hence eight hand wheels, one at each drive, will make manual positioning of each. A bus-shaped network from several wheel-controllers to a central computer was implemented. A smooth and data saving transmission can be achieved by applying approved techniques from real time data processing. The equipment of analogue drive systems with digital regulation and controls allows to change the proportion between drive distance and angle of rotation of a hand wheel only by means of software.

OPERATIONAL CONCEPT FOR THE CR PLUNGING PICK-UP ELECTRODES

The CR plunging Pick-Up electrodes are moved at cryogenic temperatures within a vacuum tank. They are propelled by linear motors outside this tank, vacuum sealed by bellows. Pre-compressed springs slightly overcompensate the vacuum force, thus avoid dropping the electrodes into the beam axis in case of a power failure. But using this drive construct for fast and precise movements requires damping the inherent resonance of a heavy mass with a strong spring. The solution is a control loop consisting of the motor, the moving payload, the motor controller, a position sensor and a regulator, whose set values can be forced due to almost any desired function [1]. A movement profile can be defined as a periodic function. This can be considered as the future "**automatic mode**". The digital design of the motor controller and the position sensor allowed to implement a digital regulator completely in software. This offers the opportunity to feed the regulator's set values for a desired position by any actuator with a convenient digital interface to the controlling computer. Thus the control software had been supplemented by two additional branches. The first can be considered as "**adjustment mode**" in order to set up the positon control loop. The second can be called "**manual mode**" and provides the input of a man-machine interface for a real time control of the drives. A stepping motor with a special interface hardware was equipped with a hand wheel, linked to the control computer and used as high resolution incremental encoder. While the hand wheel gets twisted, the pulses are counted and transferred to a controlling computer, which accumulates them to an absolute position set value for the underlying control loop. A change of the ratio between the turned wheel angle and the advance of the carriage is carried out classically by a gear transmission. The fully digital implementation allows the change of it without any additional mechanics – just by multiplying the motor pulses with another factor. Thus, each counted pulse has to be assigned to an actual distance, let's assume 100 µm. A continuous turn of the wheel results in a stairway-shaped function, whose steps have a minimum height and whose length lasts always one millisecond. The basic sampling frequency of 1 kHz is given by the motor controller and resides in the audible range. Decreasing the step size down to a few microns can avoid visible jumps, but due to the logarithmic sense of the human ear, the discrete steps remain audible. Thus, this raw kind of counting procedure ends up in a very unpleasant sound, approximately like a rusted machine without any grease. In order to overcome this, an equidistant choice of sampling points was connected by consecutive cubic spline interpolations. Then the ugly sound turned into gentle clicks.

This initial three-mode concept was enhanced from one to eight control channels by digital addressing and transmission techniques, shown on top of Fig. 1. It is proven with up to two manually controlled drives working virtually in parallel. The manual control feature was designed to facilitate all kinds of assembling, service and maintenance tasks. It is not intended for operation with beam.

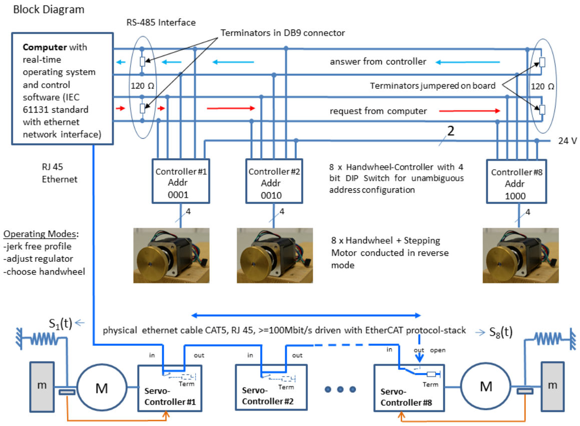

Figure 1: Linear drive control scheme for CR stochastic cooling pickup tanks, supplemented by eight addressable rotary encoders, attached to a four-wire RS-485 bus.

---

† r.hettrich@gsi.de

ISBN: 978-3-95450-243-1 ISSN: 2226-0374 doi:10.18429/JACoW-COOL2021-P2003

THE USE OF A STEPPING MOTOR AS ROTARY ENCODER

Turning the cross section of a coil within the flux of a permanent magnet induces an alternating voltage between both ends of the coil. Its amplitude and frequency grow proportional with the rotational speed. Therefore, the turning angle can be determined by counting the alterations of the voltage. To alleviate the counting process, a simple analogue electronic integrator can be connected to the coil, thus eliminating the dependence of the amplitude on the rotational frequency. The result is a sine wave with a constant amplitude and varying frequency. Provided a simple OP integrator is used, the circuit can be matched empirically by decreasing the characteristic capacitor until the generated signal just covers the full range of the supply voltage. Putting a full range sinewave signal to a Schmitt trigger, generates a full range square wave. An edge-triggered flip-flop can count the number of pulses. A cyclic read request from the controlling computer fetches the values and resets the flip-flop. The accumulation is done by the controlling computer. This explanation is simple, but it does not yet cover the sense of rotation. To resolve the direction information, an additional signal from a further coil is needed, which is oriented exactly 90° twisted in relation to the motor spindle. The outgoing voltages of a 2-phase stepping motor conform to this condition. The inductor magnet of the motor consists of twisted toothed wheels, one step of the motor corresponds to 1.8°. Provided that the logical evaluation is done by a microcontroller, the preceding hardware had just to be doubled. Two µC-inputs sample the information. A block diagram for the controller hardware is shown in Fig. 2. Its occurrence is eightfold per Pick-Up tank.

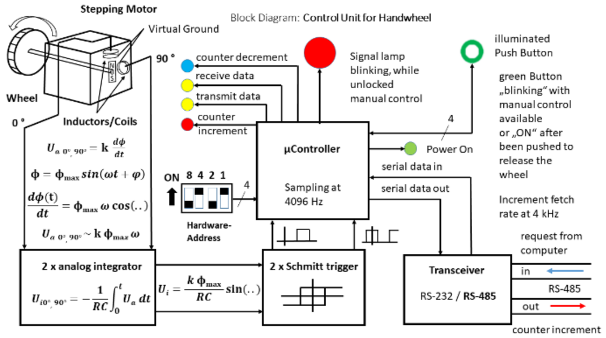

Figure 2: The structural components of a single manual control hardware with their distinctive signals.

The transmission to the controlling computer is done by a bus transceiver, which aligns the digital signals to the RS-485 standard. A four-bit hardware address can be adjusted on the controller board. It will be read by the microcontroller immediately after "switch on". Henceforward the controller only responds to requests directed to its own address. The microcontroller additionally serves as controller for some basic functions: Optical warning about dangerous movement, indicating several states via LEDs for power, for transmission, for wheel rotation direction, locking the manual control option via a dedicated release button. Figure 3 illustrates the full evaluation of the conditioned motor signals.

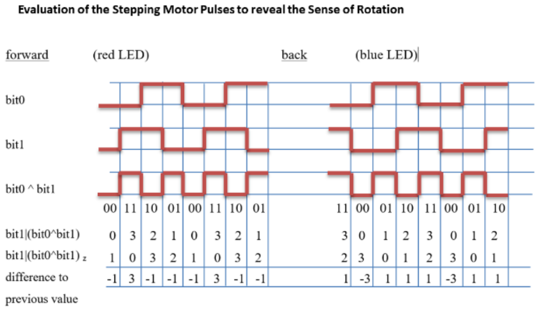

Figure 3: Evaluation of the stepping motor pulses to reveal the sense of rotation.

Assuming that the "bit0" signal is derived from the 0°-coil and the "bit1" signal is derived from the 90°-coil of the motor, a turn forward generates "bit1" 90° before "bit0" and a turn backward generates it 90° after "bit0". Combining bit0 with bit1 via an XOR (or ^) operation delivers a signal, that has twice the frequency as the one from the original coil. When this signal is added to the original one from bit1 by a logical OR-function, a two-digit binary number in the range [0, 3] arises. Turning forward generates a falling sequence [3, 2, 1, 0] and turning backward generates a rising sequence [0, 1, 2, 3]. The line "bit1|(bit0^bit1)" shows the possible values of the actual sampling. The line "bit1|(bit0^bit1) $_z$" shows the corresponding values taken one sample before. Subtracting the previous from the actual values always delivers: -1 or 3 while the wheel turns forward. It delivers 1 or -3 when the wheel turns backward. Equations (1), (2) and (3) show the algorithm, which derives itself from the last line of the above-mentioned table.

$$\begin{aligned} \text{difference} := {} & (\text{bit1}(1) \mid (\text{bit0}(1) \text{ XOR } \text{bit1}(1))) \\ & - (\text{bit1}(0) \mid (\text{bit0}(0) \text{ XOR } \text{bit1}(0)))\,. \end{aligned} \tag{1}$$

$$\text{increment} := \{ \begin{array}{l} +1 \text{ for difference} = -1 \text{ or } +3, \\ -1 \text{ for difference} = +1 \text{ or } -3, \\ \;\;0 \text{ for difference} = 0 \text{ or } 2/{-2} \,\}\,. \end{array} \tag{2}$$

$$\text{counter} := \text{counter} + \text{increment}\,. \tag{3}$$

The collection of digits is outlined in Fig. 4.

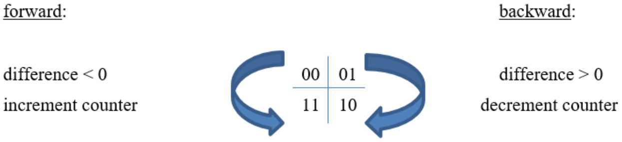

Figure 4: Illustration of the encoder algorithm.

The hardware sampling frequency is set to 4096 Hz in the µcontroller firmware. New increments are fetched every 0.25 millisecond. This corresponds to a transmission rate of 4 kHz and is set up as basic clock within the real time software on the superior control computer.

SUPPRESSING THE STEP FUNCTION OF THE DIGITAL SAMPLING PROCESS BY CUBIC SPLINE INTERPOLATION

A facility of a manual control of each single drive with its dedicated wheel was developed, so that a preferably high number of drives can be used virtually in parallel. Each wheel generates 200 pulses per turn. These pulses are collected by a control computer via a serial bus. Eight wheel controllers and the superior computer are attached to two twisted pair lines. The computer consecutively sends addressed requests to the wheel controllers, which answer with their increments. Between two answered requests from different wheels, the prior controller has to free the bus by switching its output into a high impedance state and the following controller has to occupy the bus by switching its output on. Due to the limited transfer rate of the serial RS-485 interface to 115200 bits/s, a rate of 4000 bus transmissions per second could not be exceeded. A virtual parallel operation would need 8 bus transmissions for sampling two drives. Thus the parallel update rate for each drive drops to (4000/8) s^{-1}=500 per second and below the basic sampling frequency of the motor controller of 1 kHz. The application of these values to the position control loop would result in a stairway-shaped function with higher and longer steps than described above for the "manual control mode". To avoid the scratching sound, only every forty-fifth accumulated value was transferred to the underlying position control loop. The missing values in between were calculated by a consecutive cubic spline interpolation in such a way, that each section between the remaining nodes fits seamlessly to the next. The drives follow with a time lag of 45 milliseconds, which appears just to be in real time. Provided that four pairs of $y_0(x_0)$, $y_1(x_1)$, $y_2(x_2)$, $y_3(x_3)$ are known with an incoming slope $s_0'(x_0) = b_0 = \alpha$, a three order polynomial with no output bend $s_3''(x_3) = 2\ c_3 = 0$ can be found, which connects all nodes in a smooth, jerk-free way. Figure 5 shows a graphical representation.

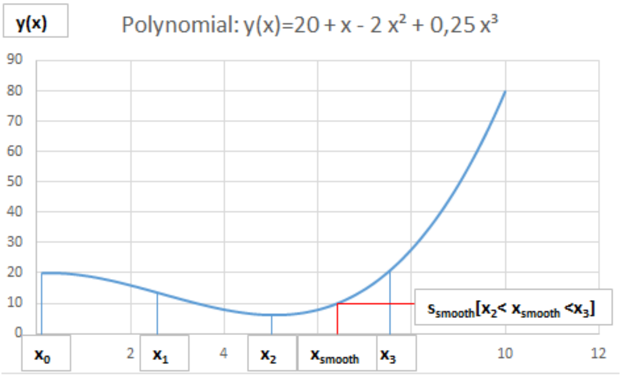

Figure 5: Example of a three-order polynomial.

Assuming that the first three nodes are stored in the past, the polynomial

$$s_2(x) = a_2 + b_2\ (x - x_2) + c_2\ (x - x_2)^2 + d_2\ (x - x_2)^3. \quad (4)$$

with c_1, c_2, c_0, d_1, d_0, b_2, b_1, $b_0=\alpha$ and $a_2=y_2(x_2)$ can be used to calculate a continuous sequence between $[x_2, x_3]$, which fits seamlessly to the previous ones. This method can be applied in real time by exploiting the four past samples to calculate the coefficients of a three order polynomial just before the next sequence starts. But the limitation is a latency time (x_3-x_2) until the drive follows.

The algorithm is derived from the following equations and their known conditions with i=[0..2], j=[0..3]:

$$s_i(x) = a_i + b_i\ (x - x_j) + c_i\ (x - x_j)^2 + d_i\ (x - x_j)^3. \quad (5)$$

$$s_i(x_j) = s_{i+1}\ (x_{j-1}), \quad j \neq 0. \quad \text{points fit} \quad (6)$$

$$s_i'(x_j) = s_{i+1}'\ (x_{j-1}), \quad j \neq 0. \quad \text{slopes fit} \quad (7)$$

$$s_i''(x_j) = s_{i+1}''\ (x_{j-1}), \quad j \neq 0. \quad \text{bends fit} \quad (8)$$

$$s_i'(x_0) = b_0 = \alpha. \quad \text{entrance slope given} \quad (9)$$

$$s_i''(x_3) = 2\ c_3 = 0. \quad \text{no output bend} \quad (10)$$

The Algorithm as final Result

(**start point**) Memorize 4 consecutive values of [position, timestamp]: $[y_0, x_0]$, $[y_1, x_1]$, $[y_2, x_2]$, $[y_3, x_3]$

Calculate 3 distances between these 4 points: $h_0=x_1-x_0$, $h_1=x_2-x_1$, $h_2=x_3-x_2$, let the slope be $\alpha = 0$ at start

After a convenient interval of time [e. g. 45 milliseconds], a new position value with the latest increment from the wheel has been accumulated: $[y_{3new}, x_{3new}]$:

(**entry point**) set $y_0 = y_1$, $y_1 = y_2$, $y_2 = y_3$, $y_3 = y_{3new}$
set $h_0 = h_1$, $h_1 = h_2$, $h_2 = x_{3new} - x_3$,
ignore if equally spaced,
set $a_0=y(x_0) =y_0$, $a_1=y(x_1) =y_1$, $a_2=y(x_2) =y_2$, $a_3=y(x_3) =y_3$
calculate:

$$c_1 = \frac{3\left[(-3)\frac{(a_1-a_0)}{h0}(h_1+h_2) + 2\frac{(a_2-a_1)}{h_1}\left(\frac{3}{2}h_1+h_2\right) - \frac{(a_3-a_2)}{h_2}\ h_1 + \alpha\,(h_1+h_2)\right]}{2\,(2\,h_1+\frac{3}{2}h_0)\,(h_1+h_2) - h_1^2} \quad . (11)$$

$$c_2 = \frac{3\left[\frac{3}{2}\frac{(a_1-a_0)}{h0}\ h_1 - 3\ \frac{(a_2-a_1)}{h_1}\left(h_1+\frac{1}{2}h_0\right) + \frac{(a_3-a_2)}{h_2}\ \left(2\,h_1+\frac{3}{2}h_0\right) - \frac{1}{2}\alpha\,h_1\right]}{2\,(2\,h_1+\frac{3}{2}h_0)\,(h_1+h_2) - h_1^2} \quad . (12)$$

$$d_2 = -\ \frac{c_2}{3\ h_2}\ . \quad (13)$$

$$b_2 = \frac{a_3-a_2}{h_2} - \frac{2}{3}h_2c_2\ . \quad (14)$$

$$b_1 = \frac{a_2-a_1}{h_1} - \frac{h_1}{3}(c_2+2\,c_1)\ . \quad (15)$$

$$a_2 = y_2\ . \quad \text{(already known)} \quad (16)$$

use $\alpha = b_1$ as input slope for the following iteration.

Calculate $y(x) = s_2(x)$ in $[x_2 < x < x_3]$ due to Eq. (4) and apply to the drives. The sliding carriage will follow without jerk or unpleasant sound.

RETURN to (**entry point**) and repeat the loop as long as needed …

REFERENCES

[1] R. Hettrich *et al.*, "Latest News from Stochastic Cooling Developments for the Collector Ring at FAIR", in *Proc. 11th Workshop on Beam Cooling and Related Topics (COOL'17)*, Bonn, Germany, Sep. 2017, pp. 64-67. `doi:10.18429/JACoW-COOL2017-TUP16`

[2] Arndt Brünner, "Kubische Splines", `https://www.arndt-bruenner.de/mathe/scripts/kubspline.htm`

ISBN: 978-3-95450-243-1 ISSN: 2226-0374 doi:10.18429/JACoW-COOL2021-P2004

A NEW ELECTRON COOLER FOR THE CERN ANTIPROTON DECELERATOR (AD)

G. Tranquille†, J. Cenede, A. Frassier, N. S. Chritin, Y. M. Coutron, A. Sinturel, J. A. Ferreira, L. von Freeden, H. Bajas, L. V. Jorgensen, CERN, Geneva, Switzerland

Abstract

The current electron cooler at the Antiproton Decelerator (AD) at CERN was built in the second half of the 1970s and is thus well over 40 years old. It was built for the Initial Cooling Experiment (ICE) where stochastic and electron cooling were tested to ascertain the feasibility of using these techniques to generate high intensity antiproton beams for the SPpS. The ICE electron cooler was subsequently upgraded and installed in LEAR (Low Energy Antiproton Ring) to help generate intense beams of antiprotons at low energies. After the stop of the anti-proton physics at LEAR in 1996 and two years of studies of electron cooling of Pb ions, the electron cooler was moved to the AD where it has been in use ever since.

With the new ELENA ring becoming operational, a major consolidation project has been launched to extend the lifetime of the AD and as a part of this a new electron cooler for the AD is being built. In this paper, we describe some of the design considerations and challenges of this project as well as the expected gains in terms of cooling performance.

INTRODUCTION

Since the completion of the LEAR physics program a simplified scheme using a modified AC (antiproton collector) as a decelerator (AD) was implemented at CERN to deliver antiprotons to experiments at an energy of 5.3 MeV. The scheme relies on stochastic and electron cooling to efficiently decelerate and extract high brightness beams to the experimental zones. With the recent addition of the ELENA ring to the CERN antimatter complex and an electron cooler with more than 40 years of operation [1], it was decided that a new cooler should be built to ensure reliable operations for the next 20 years.

Table 1: Main Parameters of the new Electron Cooler

	Value	Comment
E_e	68 keV	Cooling at 500 MeV/c
B_{gun}	2400 G	Expansion factor 2
Ie@68keV	3.5 A	
Ie@3keV	0.45 A	Factor 4 more current

The new device (Fig. 1) has been designed to cool antiprotons at a considerably higher energy than what is presently possible. Cooling at a higher energy will limit the adiabatic blow-up of the emittance of the circulating beam by a factor of three making the cooling of this “hot” beam more efficient. The cooler will also have an electron beam expansion system to obtain an electron beam with a reduced transverse energy for efficient and faster cooling of the circulating beam. It will be installed horizontally allowing easier access to the device for maintenance and repairs. Some of the main parameters and the potential gains of the new cooler are given in Table 1.

ELECTRON GUN

A high perveance electron gun capable of operating up to 80 kV is presently under design (Fig. 2). It is based on a study of various gun optics (Fig. 3) performed some years ago [2] and incorporates some ideas inspired by the decelerating tube of the Gbar experiment at CERN [3]. With a four times higher perveance, the gun will be able to deliver up to 450 mA of electron current for cooling at the lowest energy plateau of 5.3 MeV. At the top energy for electron cooling, the current will be limited to 3.5A.

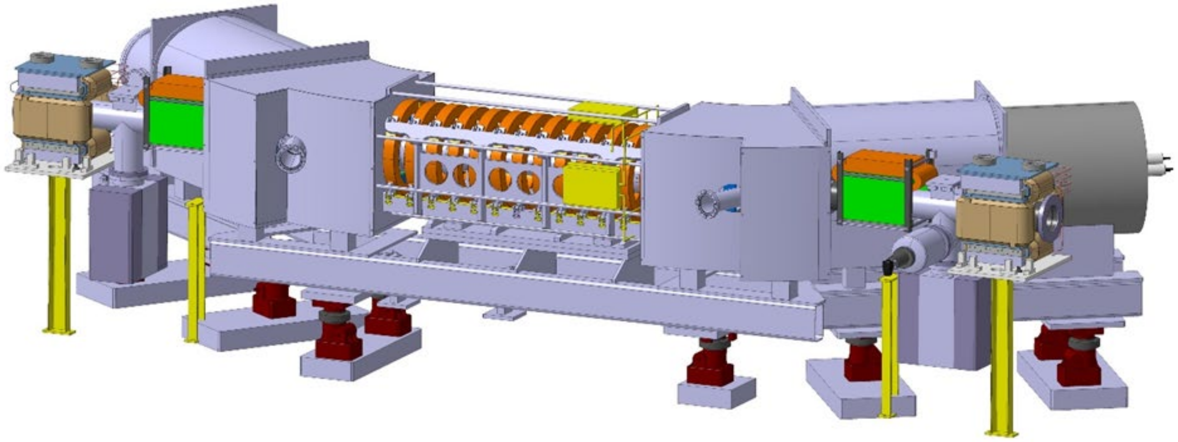

Figure 1: Mechanical design of the new AD electron cooler.

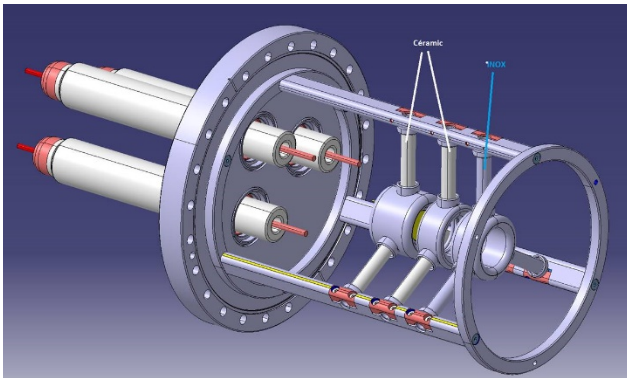

Figure 2: The new electron gun design.

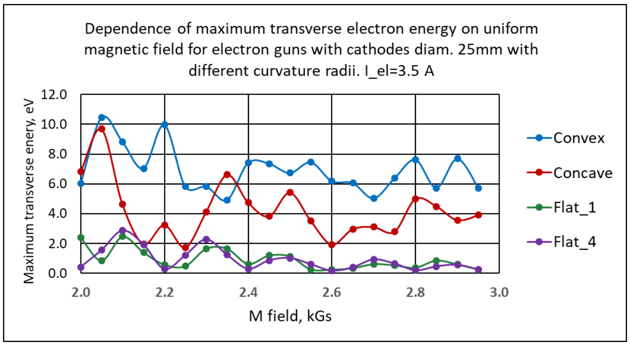

Figure 3: Maximum electron beam transverse temperature for different cathode configurations.

MAGNETIC SYSTEM

Apart from the expansion solenoid and the two transition solenoids, the magnetic system of the new cooler will be constructed using short "pancake" coils (Fig. 4). This has the advantage that the local field errors can be easily corrected by the adjustment of the individual coils [4]. The return flux of the field is insured by a set of iron rods running alongside the coil assembly. Magnetic field calculations with Opera [5] have shown that there is no substantial difference in the magnetic field quality between the rods or a full shield (Fig. 5). In the final design additional shielding will be installed around the toroids and gun/collector solenoids to avoid any external magnetic fields perturbing the electron beam in these regions.

The magnetic field of the current AD electron cooler was measured twice, the first time in 1984 and again in 1997 and those measurements show that the transverse field in the drift region is only at the level 2×10^{-3} compared to the longitudinal field. The new cooler has been designed to have a transverse magnetic field that is much better than this with a specification value of better than 5×10^{-4}. This could potentially shorten the cooling time and result in a lower final temperature of the antiproton beam.

The new cooler will also feature compact orbit correctors similar to what was built for the ELENA electron cooler, this saves space and, by being as close as possible to toroid regions of the cooler, will help minimize the orbit excursions of the circulating beam of antiprotons.

We have also decided to combine the installation of the new electron cooler with moving some of the magnets close to the electron cooler section in the current AD set-up. At the moment on each side of the electron cooler there is a quadrupole triplet in between the electron cooler and the compensation solenoids. With active optics elements in between the drift region solenoidal field and the compensation solenoids, the compensation cannot be complete and the result is increased coupling in whole of the AD.

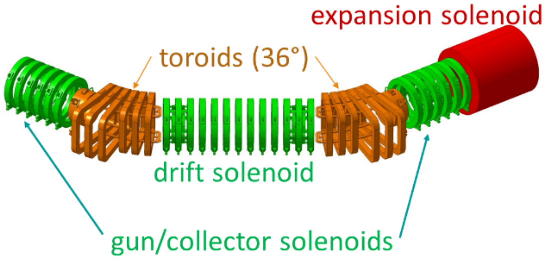

Figure 4: The magnetic system of the new cooler.

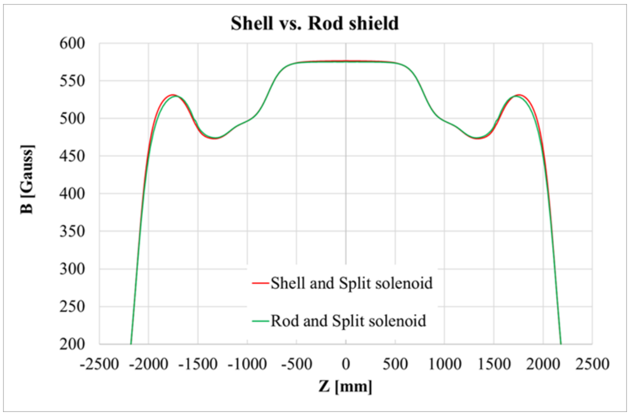

Figure 5: Comparison of the magnetic field for "pancake" coils with iron bars or full shield for the return flux.

COLLECTOR

Recent failures on the current AD electron beam collector has meant that the design and construction of the new collector needed to be mechanically compatible with the present setup. This is to make sure we have a spare collector available should the current collector run into problems before the installation of the new electron cooler. The current design of this new collector (Fig. 6) has suffered some HV breakdowns and the design is under review to better understand the exact causes of these breakdowns and hence mitigate them.

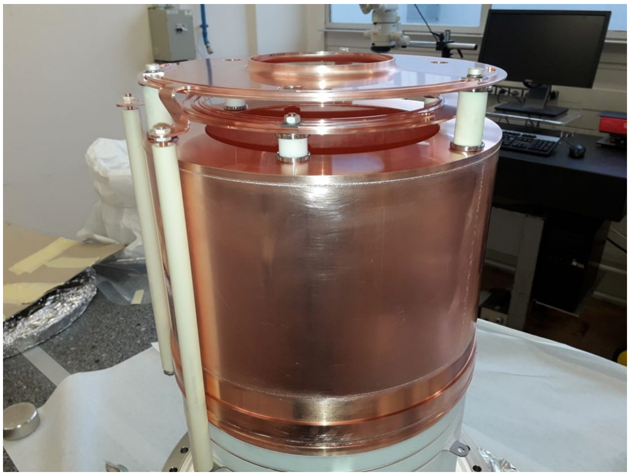

Figure 6: Electron beam collector.

VACUUM SYSTEM

The vacuum is fully designed and is shown on Fig. 7. All the elements will be made from vacuum fired 316LN stainless steel and be fully bakeable up to 350°C. In order to reach the desired vacuum level below 10^{-11} mbar, both toroid chambers, central drift vacuum chamber and pick-up bodies will be NEG coated [6] and additional NEG strips [7] will be placed at the gun exit and the collector entrance. Two vacuum ports are foreseen on the toroid chambers for vacuum instrumentation and additional pumping.

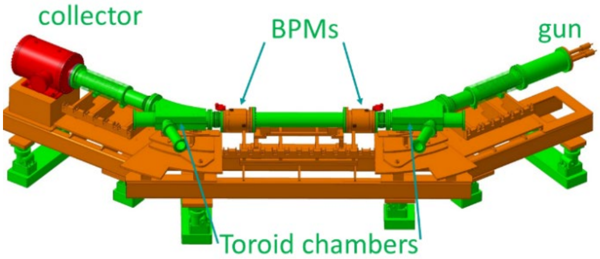

Figure 7: The vacuum envelope and support system.

SCHEDULING

The design of the new AD electron cooler is well advanced. The vacuum and support structures will go into production early in the new year.

The magnetic system is expected to go for tender in the first half of 2022. All parts are expected to be ready for assembly by the end of 2023. The assembly, testing and full validation of the new AD electron cooler is expected to take place in our test area during 2024. The cooler will be installed in the AD ring during CERNs next Long Shutdown (LS3) which is currently scheduled for 2025.

CONCLUSION

CERN Antiproton Decelerator is undergoing a big consolidation to make it fit to run for another 20 years. As part of this effort it has been decided to build a new electron cooler for the AD. The current electron cooler, which has been in use with great success for almost 45 years, will be retired, . It has served as an operational electron cooler on both ICE, LEAR and the last more than 20 years at the AD.

The new electron cooler will feature a range of what has been learned in the field over the last 50 years. Thus, it will make use of an expansion coil around the e-gun to reduce the transverse temperature of the electron beam. It will also feature a substantially better magnetic field in the drift region, better diagnostics, compact orbit correctors and much better vacuum. It is difficult to predict any improvements that might come from this, but perhaps it will be possible to reduce the time needed on each of the two electron cooler plateaus at the AD, thus perhaps reducing the AD cycle time, as well as possibly reaching a lower final temperature of the antiproton beam. The magnet reshuffling in the vicinity of the new electron cooler, to be done at the same time as the installation of the new electron cooler, should make the AD optically simpler by reducing coupling in the whole ring.

REFERENCES

[1] G. Tranquille, “40 Years of Electron Cooling at CERN”, in *Proc. 9th Int. Particle Accelerator Conf. (IPAC'18),* Vancouver, Canada, Apr.-May 2018, pp. 69-72. `doi:10.18429/JACoW-IPAC2018-MOZGBF3`

[2] Alexander Pikin, private communication.

[3] A. Husson *et al.,* “A pulsed high-voltage decelerator system to deliver low-energy antiprotons”, *Nucl. Instr. Meth. A*, Vol. 1002, 2021, 165245, `doi:10.1016/j.nima.2021.165245`

[4] A. Bubley, V. Panasyuk, V. Parkhomchuk ,V. Reva, “Optimization of the Magnet System for Low Energy Coolers”, *in COOL'2007*, Bad Kreuznach, Germany, paper THAP04 `https://accelconf.web.cern.ch/cl07/PAPERS/THAP04.PDF`

[5] H. Bajas, private communication.

[6] C. Benvenuti, P. Chiggiato, P. Costa Pinto, A. Escudeiro Santana, T. Hedley, A. Mongelluzzo, V. Ruzinov, and I. Wevers, *Vacuum* 60, 57, 2001.

[7] C. Benvenuti and P. Chiggiato, *Journal of Vacuum Science & Technology A* 14, 3278, 1996.

ISBN: 978-3-95450-243-1 ISSN: 2226-0374 doi:10.18429/JACoW-COOL2021-P2005

TESTS OF THE GUN PROTOTYPE FOR THE ELECTRON COOLING SYSTEM OF THE NICA COLLIDER

A.P. Denisov, M.I. Bryzgunov, A. Bubley, V. Chekavinskiy, A.D. Goncharov, A. Ivanov, V.V. Parkhomchuk, A. Petrozhitskii, V.B. Reva, E.R. Urazov[1], BINP SB RAS, Novosibirsk, Russia
[1]also at Novosibirsk State University, Novosibirsk, Russia

Abstract

The efficiency of the electron cooling depends on the electron beam quality produced be the electron gun. The characteristics of the electron gun were tested on the test bench with the linear transport channel. For the beam diagnostics, we used beam position monitors alongside with the W-Re wire sensor for 1-D quantitative profile measurements. We also used a high-definition CCD camera with high sensitivity for qualitative 2-D measurements of the electron density distribution via the wire thermal radiation.

INTRODUCTION

This work is related to the new electron cooling system, developed for the NICA collider facility, located in Dubna.

Unlike the previous electron cooling systems manufactured in the Budker Institute [1], the NICA collider requires the electron beam with higher current density for the effective cooling. Meanwhile, the size of the electron beam is not required to be as large as in the previous systems. Therefore, we decided to develop a new electron gun.

ELECTRON GUN

The electron gun we developed and tested is based on the Pierce optics with the shield electrode placed near a flat BaO cathode and with an additional four-sector control electrode [2] (Fig. 1).

The anode controls the overall emission, whereas the control electrode controls the emission from the edges of the cathode. This allows us to change the electron current density distribution of the beam. Also an auxiliary electrode is introduced, which controls the output energy of the electron beam on the desired distance from the anode.

To prevent the beam from expanding due to the space charge the gun is emerged into the longitudinal magnetic field.

The geometry, position and voltages of the electron gun electrodes were calculated in an iterative manner using the SAM software developed at BINP [3] in order to minimize the amplitude of Larmour oscillations. The parameters of the electron gun are in Table 1.

Table 1: Parameters of the Electron Gun

Parameter	Value
Anode voltage, kV	0-20
Control electrode voltage, kV	-3..+3
Electrons output energy, keV	1-30
Cathode / Electron beam diameter, cm	1
Electron current density, A/cm^2	0..1.5
Magnetic field, G	900-1000

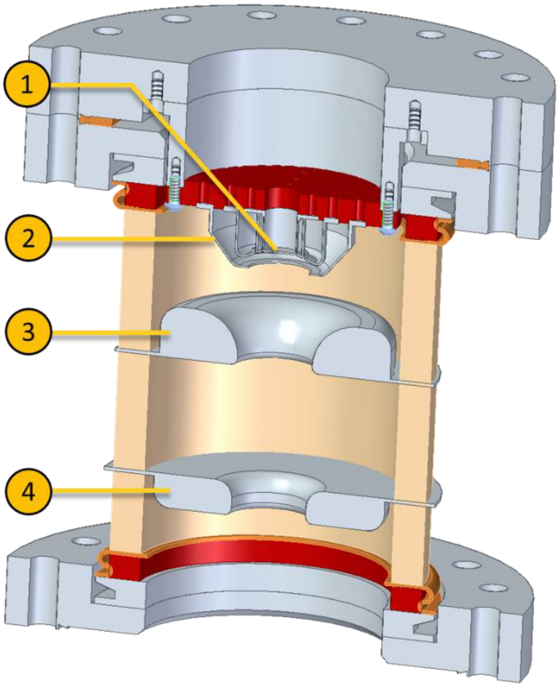

Figure 1: A design of the electron gun based on the Pierce optics. The gun includes a cathode (1), a control electrode (2), an anode (3) and an auxiliary electrode (4) for setting the electrons output energy.

TEST STAND

For testing the electron gun and developing the beam diagnostics techniques the test stand with a linear structure was assembled (Fig. 2 and Fig 3). It bases on the test stand used for testing the electron gun for the EC-300 electron cooling system. It includes the magnetic coils for providing a longitudinal magnetic field about 900-1000 Gauss along the beam transport channel.

The modified version of the test stand has a longer transport channel for the electron beam. Additional coils create the longitudinal magnetic field for the gun and collector. Magnetic coil correctors allow shifting the electron beam in the transverse direction. Additional magnetic coils placed in the centre of the transport channel change the longitudinal magnetic field locally in order to control the Larmour oscillation phase.

We also added a beam diagnostics chamber for measuring the beam position and beam current density profile. The electrons energy is up to 30 keV.

Figure 2: A photo of the test stand for the electron gun.

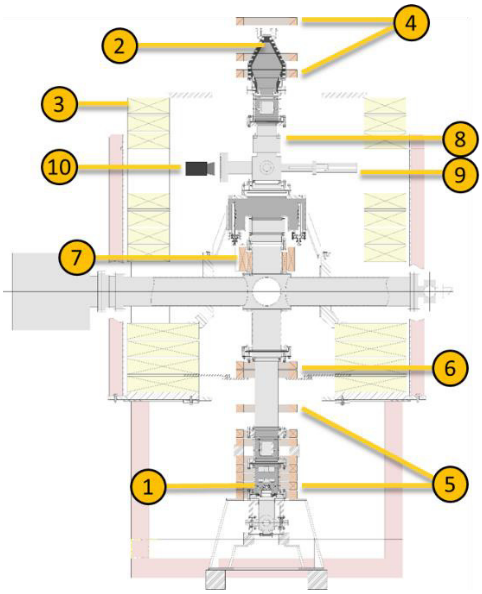

Figure 3: The schematic layout of the test stand. The layout includes the electron gun (1), the collector (2), the coils creating the magnetic field in the transport channels (3), coils for adjusting the magnetic field around the collector (4), coils for adjusting the magnetic field around the electron gun (5), coils for adjusting the Larmour oscillation phase (6), coils for shifting the beam in the transverse direction (7), beam diagnostics chamber (8), a vacuum feedthrough (9), a CCD camera (10).

The diagnostics chamber (Fig. 4) includes the electrostatic Beam Position Monitor (BPM), a channel for the wire-based beam profile sensor placed on a movable holder and a channel with a vacuum feedthrough.

The BPM measures the position of the beam, necessary for performing the profile scanning. It also allows us to measure the shape of the beam.

The window is necessary for the measurements of the thermal radiation of the wire. Such measurements can be used to restore the 2D profile, while the current measurements alone can provide only 1D profiles.

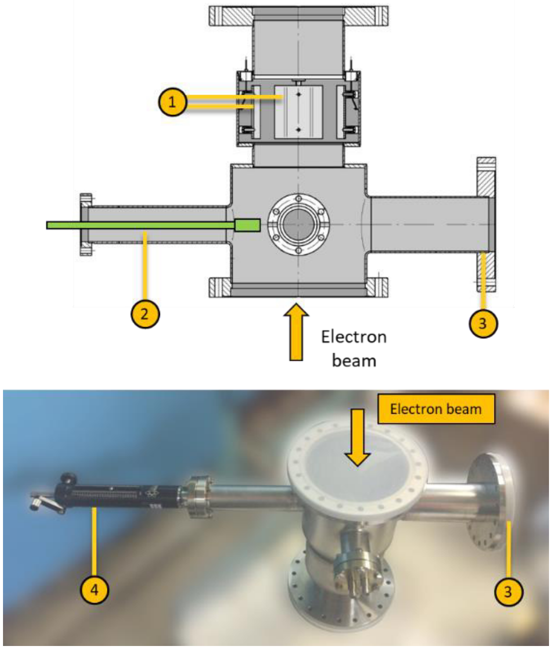

Figure 4: The beam diagnostics chamber. It includes an electrostatic BPM (1), the wire sensor attached to the movable holder (2), a viewport (3), the vacuum feedthrough (4).

For measuring the electron beam profile, we use a wire-based profile sensor (Fig. 5). The wire is 25 μm in diameter and made of W-Re alloy (85%/15%).

The wire sensor is placed on the movable holder. The vacuum feedthrough changes the position of the wire sensor roughly. The beam profile scanning is performed by changing the position of the electron beam using the magnetic coils correctors.

When the wire is heated, its length increases. To prevent the wire from sagging the flexible bronze plate is used, which pulls the wire.

The current is measured through the shunt connected through wires to the rigid plate and the U-shaped part of the holder.

This design allow us to let the current from the external power supply through the wire in order to heat it. By letting the known amount of current through the wire sensor, we can establish the dependency between the power emitted from the wire and the CCD camera signal. In other word, it is necessary for calibrating the camera. It also allows us to preliminary clean the wire sensor from any organic materials.

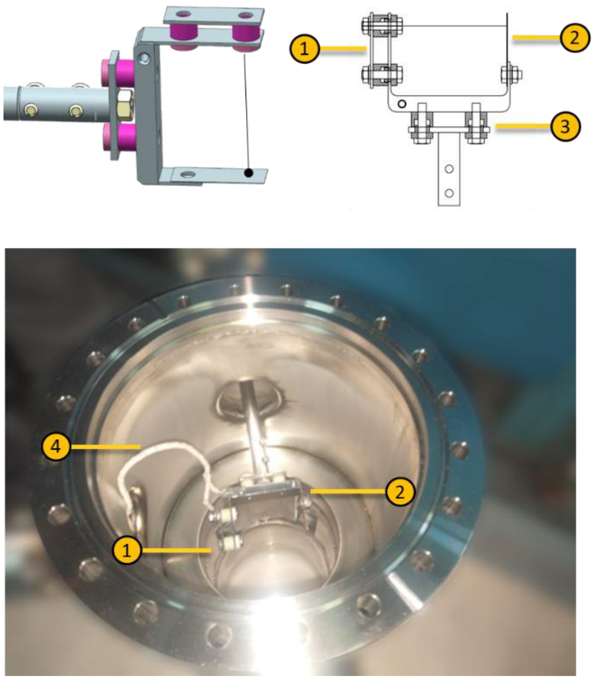

Figure 5: The wire sensor for beam profile measurements. (1) and (2) are rigid and elastic plates for attaching the wire for profile measurements. (3) is insulation for preventing the electrical current flow through the holder and the vacuum feedthrough. (4) Wires for measuring the current absorbed by the sensor.

MEASUREMENTS OF THE ELECTRON BEAM PROFILE

In this section, we want to share some results of the experiments conducted with the electron beam on the test stand.

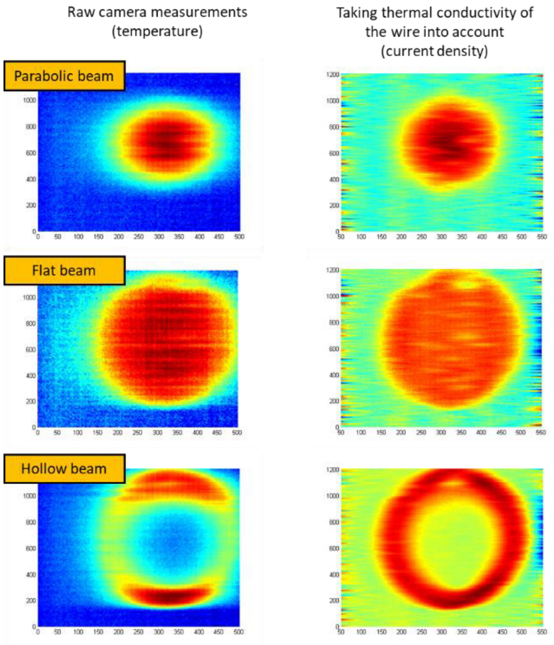
Raw camera measurements (temperature)

Taking thermal conductivity of the wire into account (current density)

Figure 6: Qualitative beam profiles restored from the CCD camera measurements.

The list of conducted experiments includes the calibration of the wire sensor (analysing the secondary emission, and the CCD camera signal) one-dimensional current profile measurements and two-dimensional profile measurements based on the sensor thermal radiation.

The firs experiment also included the beam shapes measurements using the BPM. The control electrode have four sectors. The potential of each electrode can be slightly modulated in time, resulting in the modulations of the current density on different sides of the beam. BPM can register these modulations and provide us the information about the beam position, its shape and the beam rotation around its axis for different values of the longitudinal magnetic field.

Figure 6 shows the results of the beam profile measurements using the CCD camera. Due to the thermal conductivity, an electron beam heats up not only the part of the wire where it is absorbed, but also its adjacent parts. Therefore, the signal from the camera does not match the actual distribution of the current density.

We can associate the current distribution with the measured temperature using the steady-state form of the heat equation:

$$T''(x) = A \cdot j(x) + B \cdot T^4(x) + C$$

We assume that we do not know the exact values of the coefficients of the heat equations. However, we can estimate them by applying restoration procedure for simple cases, for example for restoring the profile of a small beam, for which the actual size is much smaller than the heated area of the sensor. The examples of the restored beam current distributions is in Fig. 6 (the right column).

CONCLUSION

The further experiments require the upgrades for the gun electronics in order to modulate the electron beam current. The 1 A beam with electron energies 1-10 keV can break the wire sensor. By modulating the beam current, we can effectively decrease the average power absorbing by the wire sensor.

One of the experiments to be conducted is measuring the amplitude of the Larmour oscillations at the edge of the beam, by measuring the oscillations of the outer size of the beam.

We also look forward for improving the method of restoring the beam current density distribution using the CCD camera measurements.

REFERENCES

[1] V. V. Parkhomchuk, A. N. Skrinsky, “Electron cooling: 35 years of development”, UFN, vol. 170, no 5, pp. 473-493, 2000.

[2] A. P. Denisov *et al.*, “Design of a compact electron gun for the high-voltage electron cooling system of the NICA collider”, in *Proc. of COOL19*, Novosibirsk, Russia, September 2019, paper MOA02, pp.18-21.

[3] A. Ivanov, M. Tiunov, “UltraSAM – 2D code for simulation of electron guns with ultra high precision”, in *Proc. of EPAC 2002,* Paris, France, 2002, pp. 1634-1636.

ISBN: 978-3-95450-243-1 ISSN: 2226-0374 doi:10.18429/JACoW-COOL2021-P2006

CASCADE TRANSFORMER FOR HIGH VOLTAGE COOLER

V.V. Parkhomchuk, M.I. Bryzgunov, A.D. Goncharov, A.A. Denisov, V.A.Polukhin,
A.A. Putmakov, V.B. Reva, D.N. Skorobogatov, Budker INP, Novosibirsk, Russia

Abstract

Experience of using the different systems for powering the high voltage coolers are discussed. The acceleration and deceleration tube need the electric power for operating. At BINP several different power transferring systems were used. The multistage cascade transformers, and the system based on the turbo generators powered by the compressed gas flow.

HIGH VOLTAGE COOLER

The electrons in the electron cooling section should have the low temperature in the rest frame of the electron beam. For this we use strong focusing by the magnetic fields not only in the cooling section but in the entire transport channel of the electron beam, in the acceleration tube and near the electron gun. The last two parts of the electron cooling systems require to supply enough electric power in order to create the necessary magnetic field and also to power the gun and collector electronics.

Figure 1 shows the design of the cascade transformer which will be used for the high-voltage electron cooling system for the NICA collider [1].

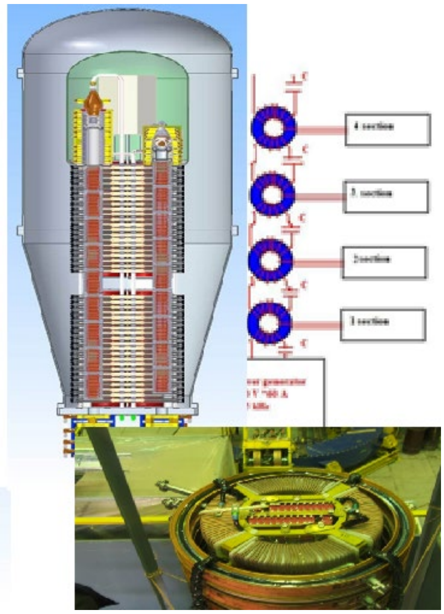

Figure 1: The design of cooler and power supply.

The cascade transformer design is similar to the design of the acceleration tube. The transformer consists of alternating ceramic and metal rings. Inside the metal ring there is a magnetic circuit with two high-voltage sectioned windings and one winding under the potential of the magnetic core to power the electronics of the high-voltage section. One high-voltage winding serves to transfer power to the next stage up, the other winding for communication with the lower section of the transformer [2].

The parameters of the cascade transformer section are presented in the Table 1.

Table 1: Parameters of a Single Section of the Cascade Transformer

Parameter	Value
Diameter of the magnetic core (outer/inner), mm	280/200
Thickness, mm	20
Mass, kg	4.8
Operational magnetic field, T	0.25
Power losses in the yank, W/kg	12
Coils current (r.m.s.), A	≤ 50
Voltage (r.m.s.), V	≤ 700
Transferred power, kW	≤ 35
Power losses, kW	7
Number of turns	28
Mass of the wires, g	230
Wires cross section, mm^2	5.8
Wires resistance, Ohm	0.015

A NEW DESIGN OF THE CASCADE TRANSFORMER

A prototype of a new cascade transformer consists of three magnetic core rings connected by eight parallel turns for communication was obtained from the manufactory and tested (Fig. 1). When making measurements (according to point 2), the input winding W1=32 turns, the first lower magnetic circuit is powered by a voltage generator (U gen)with a frequency of 25 kHz. The output winding W2=32 turns, a load with a resistance R=62 ohms is connected to the third upper magnetic circuit, and with an overall dissipation power of up to 3000W.

To calculate the coupling coefficient of two pairs of connected cascades, the input inductance of the transformer was measured in two modes-with the secondary winding of the transformer open and shorted: Inductance Lopen=15.5 mH Inductance Lshort=56 uH. The calculated coupling coefficient for one pair of cascades is equal to: Kc=0.9991.

Measurement of the voltage transfer coefficient to the load: A measuring current transformer with a current transfer coefficient of 75/1 is included in the loads circuit.

The voltages on the input W1(Ugener)and output W2 (ULoad) windings of the cascade transformer are measured using an oscilloscope in the rms cycle voltage measurement mode for a period.

ISBN: 978-3-95450-243-1 ISSN: 2226-0374 doi:10.18429/JACoW-COOL2021-P2006

During the operation (about 40 minutes) of the cascade transformer in the power transfer mode of 2.7 kW to the load, the transformer cores were heated to 30 degree Celsius. The ambient air temperature was 23 degrees Celsius.

Later, a new transformer was manufactured in a complete set and delivered for the Chinese project CSRe (see Fig. 2).

Figure 2: A photo of the prototype of the cascade transformer based on a distributed windings.

TRANSFERRING THE POWER USING TURBO GENERATORS

Compressed gas is an ideal carrier of stored power from the ground potential to the high-voltage parts of the electron cooling system. We use a turbo generator to convert the power stored in the compressed gas into the electrical power which we can further use [3].

The same concept is utilized in the Accelerator Mass Spectrometer (AWS) facility, and it has been operating successfully for years. The photo of the turbo generator used in the AWS is in the Fig. 3.

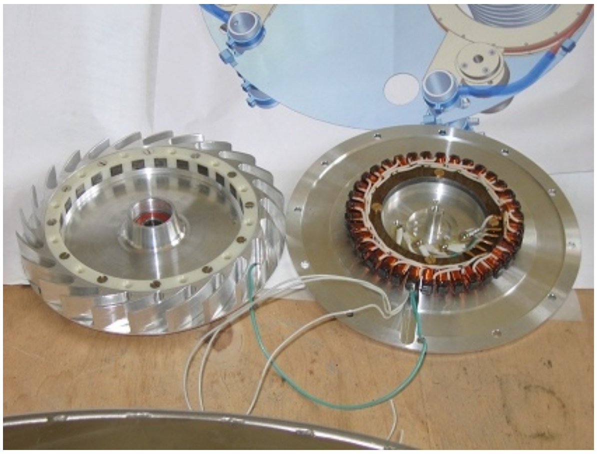

Figure 3: A photo of the internals of the turbo generator.

CONCLUSION

The methods of energy transfer from ground potential to high voltage are under active development in the Budker INP. All methods have both advantages and disadvantages and should be chosen in dependence of system requirements.

ACKNOWLEDGEMENTS

We want to thank our colleagues A.A. Lomakin, N.P. Protopopov, N.P. Zapyatkin, D.L. Stebaylo, V.N. Voronin, V.V. Efimennko for helping us with preparing the test stand and operating it.

REFERENCES

[1] M. I. Bryzgunov, *et al.*, “High voltage electron cooling system in the NICA collider”, presented at COOL’21, Novosibirsk, Russia, November 2021, paper S102, this conference.

[2] Mao Lijun, ”Development of Electron Cooler Components for HIAF Accelerator”, presented at COOL’21, Novosibirsk, Russia, November 2021, paper S103, this conference.

[3] Kurt Aulenbacher *et al.*, “Future developments for the HESR Cooler prototype at Helmholtzinstitut Mainz”, presented at COOL’21, Novosibirsk, Russia, November 2021, paper S501, this conference.

ISBN: 978-3-95450-243-1 ISSN: 2226-0374 doi:10.18429/JACoW-COOL2021-P2008

IMPROVEMENTS TO SIMULATIONS OF MICROBUNCHED ELECTRON COOLING FOR THE EIC*

W. F. Bergan[†], Brookhaven National Laboratory, Upton, NY, USA

Abstract

Microbunched electron cooling (MBEC) is a promising new technique for cooling dense hadron beams. It operates by copropagating the hadron beam with a beam of electrons, during which time the hadrons induce an energy modulation on the electrons. This is amplified, turned into a density modulation, and acts back on the hadrons in order to give them energy kicks which tend to reduce their initial energy spread and emittance. We plan to use this technique to cool the proton beams at the Electron-Ion Collider (EIC). In order to better understand the process, we have expanded on our simulation codes of cooling times and saturation effects, allowing us to explore such issues as variable Courant-Snyder parameters within the lattice elements.

MICROBUNCHED ELECTRON COOLING THEORY

In order to cool the dense proton beams in the future Electron-Ion Collider (EIC), we plan to make use of microbunched electron cooling (MBEC) [1]. The theory of MBEC was first developed in [2] and expanded upon in [3–6], and full details can be found therein. The main idea is that the hadrons which one wishes to cool are copropagated with an electron bunch in a straight "modulator" section, where the hadrons induce an energy perturbation in the electron beam. The electrons and hadrons are then separated. The electron beam passes through an amplification section, where its energy perturbation is amplified and transformed into a density perturbation. The hadrons pass through a chicane with non-zero R_{51}, R_{52}, and R_{56} values, so that its delay depends on its initial energy and transverse offsets. In the "kicker" section, the hadrons and electrons again copropagate, and the density perturbations in the electron beam provide energy kicks to the hadrons, with the kick magnitude as a function of hadron delay defined by a wake function. By adjusting the hadron optics appropriately, we can arrange for these kicks to on average cool the hadrons longitudinally and transversely. A diagram of the setup is shown in Fig. 1. Parameters used for this paper are shown in Tab. 1, with the quoted Courant-Snyder parameters evaluated at the center of the appropriate element.

WAKE SENSITIVITY TO VARYING OPTICS

We had noticed that the density perturbations in the electron beam can become comparable to the total electron density, and so saturation effects cause deviations from the linear cooling theory. To account for this effect, we have developed a one-dimensional simulation code to track hadron and electron macroparticles through the elements of the cooling section using a cloud-in-cell formalism [7] and empirically determine the effective hadron wake function. Details of this simulation code may be found in [8].

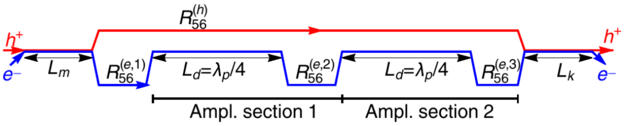

Figure 1: Layout of the MBEC cooler. Figure from [4].

Of particular note here is that the previous version of the code made the simplifying assumption that the beam sizes of the electrons and hadrons did not change within the accelerator elements, so that the inter-particle forces only had to be computed once for each element. This is of course not the case in reality, where beta functions of the electrons and hadrons will evolve within the modulator, amplifier straights, and kicker. We assume that the electrons are focused by a simple FODO scheme in each element and that the hadrons experience a drift in the modulator and kicker straights, as illustrated in Fig. 2 and Fig. 3.

We run the simulation code in two separate configurations. First, we run a detailed simulation in which we take 1m steps in the modulator and 10cm steps in the amplifiers and kicker,[1] re-evaluating the beam sizes and electron/electron and electron/hadron interaction functions at each step. We also run a simulation similar to what we had done previously, where we average the beta functions and dispersions across each element for each particle species and use these to create constant beam sizes and interaction functions in each element. We then track the macroparticles in 1m steps. Using 100 random noise seeds, we obtain the effective wake functions from these two methods, as shown in Fig. 4. We see that the use of average Courant-Snyder parameters in an element gives essentially the same result as doing the full detailed tracking.

INSENSITIVITY OF LOCATION OF ENERGY KICK

We have also developed a turn-by-turn code to simulate the multi-turn cooling dynamics in detail. This tracks hadron macroparticles in the bunch through a simplified lattice consisting of the modulator, kicker, and RF section, so that synchrotron motion may be included. Details of the code may be found in [9]. Each turn, each hadron macropar-

---

* Work supported by Brookhaven Science Associates, LLC under Contract No. DE-SC0012704 with the U.S. Department of Energy.

[†] wbergan@bnl.gov

[1] A smaller step size was chosen in those elements due to the faster variation in the electron beta functions.

ISBN: 978-3-95450-243-1 ISSN: 2226-0374 doi:10.18429/JACoW-COOL2021-P2008

Table 1: Parameters for Longitudinal and Transverse Cooling

Case	**275 GeV**
Protons per Bunch	6.9e10
Proton Bunch Length (cm)	6
Proton Emittance (x/y) (nm)	11.3 / 1
Proton Fractional Energy Spread	6.8e-4
Electron Normalized Emittance (x/y) (mm-mrad)	2.8 / 2.8
Electron Bunch Charge (nC)	1
Electron Bunch Length (mm)	7
Electron Fractional Energy Spread	1e-4
Horizontal/Vertical Proton Betas in Modulator and Kicker (m)	40 / 60.2
Horizontal/Vertical Electron Betas in Modulator (m)	40 / 25
Horizontal/Vertical Electron Betas in Kicker (m)	4 / 4
Modulator and Kicker Lengths (m)	39
Number of Amplifier Drifts	2
Amplifier Drift Lengths (m)	43
R56 in First Two Electron Chicanes (cm)	0.50
R56 in Third Electron Chicane (cm)	-1.15
R56 in Proton Chicane (cm)	-0.226
Proton Horizontal Phase Advance (rad)	5.446
Proton Horizontal Dispersion in Modulator & Kicker (m)	1.36
Proton Horizontal Dispersion Derivative in Modulator/Kicker	-0.0146 / 0.0146
Electron Betas in Amplifiers (m)	1.00
Horizontal / Longitudinal IBS Times (hours)	2.0 / 2.9
Horizontal / Longitudinal Cooling Times (hours)	1.9 / 3.0

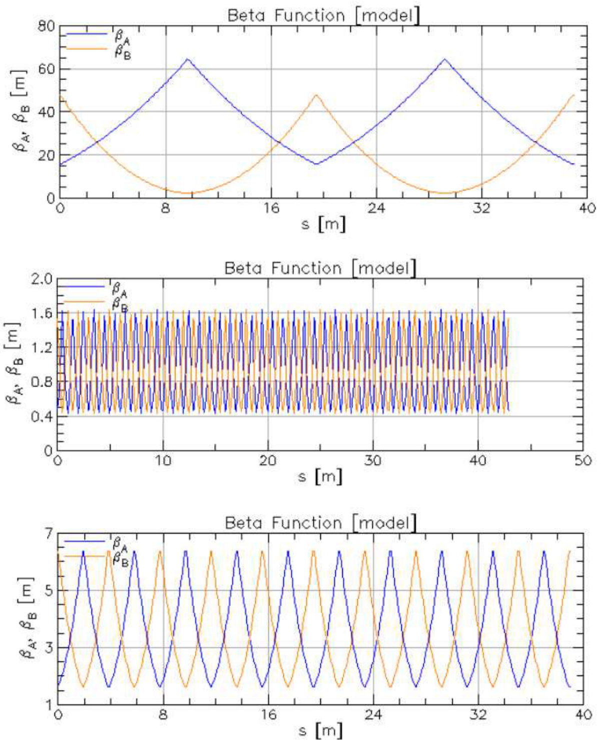

Figure 2: Electron optics in the modulator (top), amplifiers (middle), and kicker (bottom). Dispersions are all near 0.

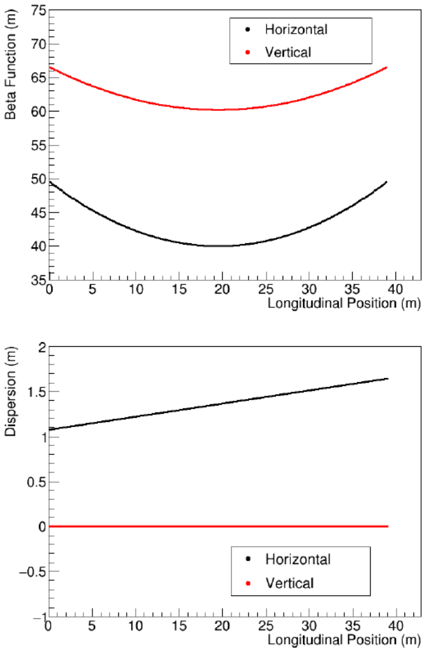

Figure 3: Hadron optics functions in the kicker. The modulator is a mirror image.

ticle receives at the kicker element both a coherent kick, computed from the wake function and the hadron's delay in traveling from modulator to kicker, and a random diffusive kick, with characteristic amplitude set by the size of the wake and local density of electron and hadron beams. Although both kicks are simulated as occurring at the kicker

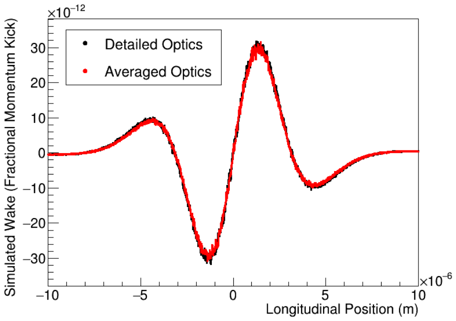

Figure 4: Comparison of effective wakes from the detailed and averaged cloud-in-cell simulations. No significant difference is seen, indicating that re-evaluation of the beam size and interaction functions at each simulation step is not necessary for accurate results.

center, in reality, they will act on the hadron continuously throughout its passage through the kicker. We therefore wish to know what effect this simplification may cause.

A simple analysis shows that, in the absence of dipoles, the effect of an energy kick on a proton's transverse action is independent of the location within the kicker where said kick takes place.

A proton's action is given by

$$J = \frac{1}{2}[\beta(x' - D'\delta)^2 + 2\alpha(x - D\delta)(x' - D'\delta) + \gamma(x - D\delta)^2] \quad (1)$$

where δ is the proton's fractional momentum deviation, and the other variables are standard Courant-Snyder parameters, dispersions, and phase-space coordinates. A small energy kick gives a change in action

$$\begin{aligned}\Delta J = [&-D'\beta(x' - D'\delta) - D\alpha(x' - D'\delta) \\ &- D'\alpha(x - D\delta) - D\gamma(x - D\delta)]\Delta\delta\end{aligned} \quad (2)$$

This may be rewritten as

$$\Delta J = [-\vec{x}^T \mathbf{B}\vec{D} + \mathcal{H}\delta]\Delta\delta \quad (3)$$

where $\mathcal{H}$ is the usual dispersion invariant and

$$\begin{aligned}\vec{x} &= \begin{bmatrix} x \\ x' \end{bmatrix} \\ \vec{D} &= \begin{bmatrix} D \\ D' \end{bmatrix} \\ \mathbf{B} &= \begin{bmatrix} \gamma & \alpha \\ \alpha & \beta \end{bmatrix}\end{aligned} \quad (4)$$

Under the operation of a transfer matrix $\mathbf{M}$, which does not include any dipoles, it can be shown that

$$\begin{aligned}\mathcal{H} &\to \mathcal{H} \\ \vec{x} &\to \mathbf{M}\vec{x} \\ \vec{D} &\to \mathbf{M}\vec{D} \\ \mathbf{B} &\to (\mathbf{M}^T)^{-1}\mathbf{B}\mathbf{M}^{-1}\end{aligned} \quad (5)$$

It immediately follows that, to leading order in $\Delta\delta$, Eqtn. 3 will be invariant as we move along the kicker.

Similarly, we may examine the effect on diffusion. Taking the quadratic term in the change in action, we see that

$$\Delta J = [\beta D'^2 + 2\alpha DD' + \gamma D^2]\Delta\delta^2 = \mathcal{H}\Delta\delta^2 \quad (6)$$

which is again invariant as we move through the kicker.

Therefore, the effect of both the cooling and diffusive energy kicks on the hadron's transverse action will be the same wherever the hadron is within the kicker, and so it is safe to take the full kick as happening at the center in our cooling simulations. This is borne out by simulations.

CONCLUSION

We have expanded on our simulations of the MBEC process to incorporate realistic optics into the modulator, kicker, and amplifier sections, and have verified that this addition does not significantly change the results of the basic MBEC theory.

ACKNOWLEDGEMENT

We would like to thank Chris Mayes for his assistance in the implementation of this code in Python. We would also like to thank Erdong Wang, Steve Peggs, Panos Baxevanis, Mike Balskiewicz, and Gennady Stupakov for many useful discussions.

REFERENCES

[1] Electron-ion collider at Brookhaven National Laboratory, conceptual design report 2021, `https://www.bnl.gov/EC/files/EIC_CDR_Final.pdf`

[2] D. Ratner, "Microbunched electron cooling for high-energy hadron beams", *Phys. Rev. Lett.*, vol. 111, p. 084802, Aug. 2013.

[3] G. Stupakov, "Cooling rate for microbunched electron cooling without amplification", *Phys. Rev. Accel. Beams*, vol. 21, p. 114402, Nov. 2018.

[4] G. Stupakov and P. Baxevanis, "Microbunched electron cooling with amplification cascades", *Phys. Rev. Accel. Beams*, vol. 22, p. 034401, Mar. 2019.

[5] P. Baxevanis and G. Stupakov, "Transverse dynamics considerations for microbunched electron cooling", *Phys. Rev. Accel. Beams*, vol. 22, p. 081003, Aug. 2019.

[6] P. Baxevanis and G. Stupakov, "Hadron beam evolution in microbunched electron cooling", *Phys. Rev. Accel. Beams*, vol. 23, p. 111001, Nov. 2020.

[7] R.W Hockney and J.W Eastwood, *Computer simulation using particles*. New York, NY, USA: Taylor & Francis, 1988.

[8] W. F. Bergan, “Plasma simulations for an MBEC cooler for the EIC”, presented at IPAC’21, Campinas, Brazil, May 2021, paper TUPAB180, pp. 1823-1826.

[9] W. F. Bergan, P. Baxevanis, M. Blaskiewicz, E. Wang, and G. Stupakov, “Design of an MBEC cooler for the EIC”, presented at IPAC’21, Campinas, Brazil, May 2021, paper TUPAB179, pp. 1819-1822.

A PERTURBATIVE TECHNIQUE FOR 3D MODELING OF THE MICROBUNCHED ELECTRON COOLING CONCEPT*

I.V. Pogorelov†, D.L. Bruhwiler, C. Hall, RadiaSoft LLC, Boulder, CO, USA
G. Stupakov, SLAC, Menlo Park, CA, USA

Abstract

Because the efficacy of conventional electron cooling falls off rapidly with energy, reaching the required cooling time at collision energies targeted by the Electron-Ion Collider (EIC) design [1] can be challenging. A possible solution is offered by cooling schemes that are based on fundamentally different approaches such as microbunched electron cooling (MBEC) [2]. Regular particle-in-cell (PIC) simulations in the parameter regime of the EIC cooling system would require a prohibitively large number of particles to resolve the evolution of the ion-imprinted phase space density modulation. We explored a solution to this problem by developing and implementing in the code Warp a computational approach based on two perturbative techniques, the beam-frame δf method and a variant of the distribution difference (DD) technique. To model the dynamics of the ion-seeded modulation in the MBEC chicanes, we developed an approach that combines the DD and quiet start techniques with analysis of correlations between the divergence of pairs of DD trajectories and their location within the e-beam. We have also prototyped in Warp the computation of the time-dependent 3D wakefield in the MBEC kicker.

δf SIMULATION OF THE MODULATOR SECTION

We have prototyped the δf algorithm [3–5] for modeling the ion-induced modulation dynamics in the modulator section of the EIC cooler, assuming a single-chicane MBEC layout [2, 6] for this initial investigation. In the δf-PIC approach, the phase space density f of the electron beam is decomposed into the sum of (i) the background distribution f_0, assumed to be an analytically known function of the phase space variables and time, and (ii) the perturbation δf which is represented by variable-weight macroparticles whose weights w and phase space coordinated evolve in response to the perturbing influence (e.g., the ion) and the background. Two key aspects of the dynamics in the modulator are the interaction of the δf particles with the ion and the space charge forces associated with the e-beam density modulation. It is therefore advantageous to work in the beam frame where the relevant dynamics are non-relativistic and an electrostatic field solver can be used. We have developed a hybrid formulation of the δf algorithm, where the phase space coordinates and weights of the δf particles evolve in the beam frame, while the background distribution f_0, whose gradients enter the evolution equations, is given in terms of the *beam-frame* phase space coordinates and the Twiss parameters of the e-beam specified in the lab frame. Such formulation allows us to include in simulations the effects of focusing quadrupoles on the electron beam dynamics. This is important for modeling the actual cooler lattice that includes multiple quadrupole focusing sections, because the transverse-to-longitudinal coupling in the quads can perturb the electrons' longitudinal momentum modulation imprinted by the ion.

We take $f_0(s)$ to mean the background e-beam distribution evolving in response to the external focusing magnet fields as well as (for non-emittance-dominated beams) the bulk space charge self-force. The growth of the perturbation $\delta f(s)$ is then due to the beam-frame Coulomb field of the ion and the Coulomb field of the ion-induced electron density perturbation, the latter expected to be a small fraction of the field of the ion in the parameter regime of the EIC cooler modulator section. We employ an approximation that f_0 is separable in x, y, and the longitudinal phase space coordinates:

$$f_0(s; x, x', y, y', z, v_z) = f_0^{(x)}(s, x, x') f_0^{(y)}(s, y, y') f_0^{(z)}(s, z, v_z) \tag{1}$$

with $f_0^{(x)}$ and $f_0^{(y)}$ bi-Gaussian in their respective trace spaces, and $f_0^{(z)}$ constant in z and Maxwellian in v_z, *i.e.*,

$$f_0^{(x)}(s, x, x') = C \exp\left(-\frac{\hat{\gamma}_x(s)x^2 + 2\hat{\alpha}_x(s)xx' + \hat{\beta}_x(s)x'^2}{2\epsilon_x}\right) \tag{2}$$

and similarly for the y trace space.

With the above assumptions, we obtain the δf particle weight evolution equation:

$$\begin{aligned} \frac{dw}{dt} = -\frac{1}{f_0}(1-w)\frac{df_0}{dt} = -(1-w)\Bigg(\frac{\partial}{\partial t} + \vec{v}\frac{\partial}{\partial \vec{x}} \\ + \frac{q}{m}(\vec{E}_{total} + \vec{v}\times\vec{B}_{total})\frac{\partial}{\partial \vec{v}}\Bigg)\ln(f_0). \end{aligned} \tag{3}$$

Because we work in the beam frame, the gradients of the f_0 have to be expressed in terms of the beam frame variables (labeled by "b"), and the beam-frame time $t_b = s/\gamma_0\beta_0 c$ is used to parametrize the dynamics. The partial derivatives of f_0 that enter Eq. (3) are given by

$$\begin{aligned} \frac{\partial}{\partial t_b}\ln f_0^{(x)} = -\frac{\gamma_0\beta_0 c}{\epsilon_x}\Bigg[\frac{\hat{\alpha}_x(s)}{\hat{\beta}_x(s)}\left(\frac{\partial\hat{\alpha}_x(s)}{\partial s} + \hat{\gamma}_x(s)\right)x^2 \\ + \frac{1}{\gamma_0\beta_0 c}\frac{\partial\hat{\alpha}_x(s)}{\partial s}xv_{bx} - \frac{\hat{\alpha}_x(s)}{(\gamma_0\beta_0 c)^2}v_{bx}^2\Bigg], \end{aligned} \tag{4}$$

$$\frac{\partial}{\partial x}\ln f_0^{(x)} = -\frac{1}{\epsilon_x}\left[\hat{\gamma}_x(s)x + \frac{\hat{\alpha}_x(s)}{\gamma_0\beta_0 c}v_{bx}\right], \tag{5}$$

---

* Work supported by the U.S. Department of Energy, Office of Science, Office of Nuclear Physics under Award Number DE-SC0020592.

† ilya@radiasoft.net

$$\frac{\partial}{\partial v_{bx}} \ln f_0^{(x)} = -\frac{1}{\epsilon_x}\left[\frac{\hat{\alpha}_x(s)}{\gamma_0\beta_0 c}x + \frac{\hat{\beta}_x(s)}{(\gamma_0\beta_0 c)^2}v_{bx}\right], \quad (6)$$

and similarly for the y trace space. For the longitudinal phase space, one only needs the derivative with respect to velocity:

$$\frac{\partial}{\partial v_{bz}} \ln f_0^{(z)} = -\frac{v_{bz} - \langle v_{bz}\rangle(s)}{\sigma^2_{v_{bz}}(s)}. \quad (7)$$

After implementing the discrete-time version of the above equations in Python and performing initial testing, the δf algorithm has been implemented in the particle-in-cell code Warp [7–9]. Warp's use of a Python layer to setup and interface with Fortran code that performs the computationally intensive simulations simplifies the adding of new features such as δf. The δf algorithm was implemented on the Python level using vectorized operations over the particle and field data (Warp's particle and field interfaces at the Python level inherit from NumPy) to ensure that the code still maintains reasonable performance. Most of the algorithm is trivially parallelizable with the exception of the weight calculation which does require some MPI communication between ranks holding particle data to compute the ensemble quantities. The parallel performance of the resulting code was examined on RadiaSoft's internal servers and found to be quite good, in terms of both weak and strong scaling.

To use δf PIC in Warp there is a base `DriftWeightUpdate` that allows users to input initial conditions for the electron bunch and set ion charge, position, and velocity. This class handles update of the background beam properties and field calculations during each step. Field calculation can either be performed from an analytic calculation for the ion's field or by introducing an ion macroparticle into the simulation that deposits to the grid during the PIC cycle. A second, inherited class `SpaceChargeDriftWeightUpdate` is also provided that solves the coupled envelope evolution including a space charge term and can be used for a coasting beam with space charge.

Because the beam-frame transit time in the MBEC modulator is a small but non-negligible fraction of the plasma period, the ion induces both energy and density modulation in the electron phase space distribution, the energy modulation being of primary interest. Using the modulator and beam parameters considered at the time, we performed 3*D* Warp δf simulations of the modulator and compared the energy modulation results to the predictions of 1D theory for the same parameters, calculated in [6]. Shown in Fig. 1, the agreement is quite good, with the simulation showing slightly lower peak modulation, which is probably due to the finite electron temperature in our simulation as opposed to a cold electron beam assumed by a theoretical 1D model.

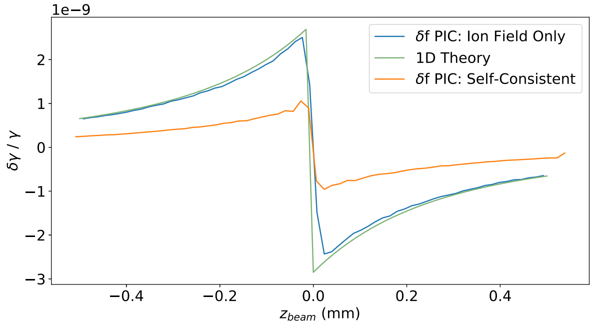

Figure 1: Comparison of energy modulation from a δf PIC simulation and 1D theory.

COMPUTATION OF THE DENSITY MODULATION AND THE WAKEFIELD

A perturbative approach to modeling the conversion of the energy modulation into a density modulation in an MBEC amplifier chicane that we prototyped is based on a combination of the quiet start and a variant of the DD techniques. Similar to other DD variants, pairs of electron macroparticles are used, with one particle in each pair not affected by the source(s) of the perturbation and the other interacting with the perturbing agent. The quiet-start aspect of the approach is in arranging such pairs to smoothly sample the distribution in position and *thermal* velocity space at the entrance to the chicane. Both particles in each pair arrive at their positions at the entrance to the chicane by moving along the unperturbed trajectories, but one particle in each pair keeps track of the accumulated velocity modulation (on top of its thermal velocity) due to the interaction with the ion in the modulator. R_{56} of the chicane converts this velocity modulation into a difference δz in longitudinal positions of the perturbed and unperturbed pair-particles after the chicane, resulting in a density modulation. This is illustrated here for the case of a transversely cold e-beam with longitudinal thermal momentum distribution sampled by 5 points (quintuples of blue dots in Fig. 2) and the initial conditions uniformly sampling a line of "impact parameter" $b = 1.0 \times \sigma_x$ parallel to the z axis, the ion being at rest at the coordinate system origin. (We use $\sigma_x = 0.7$ mm, $\sigma_\gamma/\gamma = 1. \times 10^{-4}$, $\gamma_0 = 313$, and $R_{56} = 1.4$ cm, the same values as in [6].) The average value of δz at each z after the chicane, $\langle\delta z(z)\rangle$ (the green line in Fig. 2, with a hypothetical $\sigma_\gamma/\gamma = 0$ case shown for comparison in red) can then be used to calculate the relative modulation of the line density of the electrons:

$$\delta\lambda/\lambda_0 = -d/dz(\langle\delta z(z)\rangle). \quad (8)$$

The result is shown in Fig. 3. For a round Gaussian beam with the lab-frame linear number density $\lambda_0 = 6.25 \times 10^{11}$ m^{-1} corresponding to the $I_e = 30$ A and other parameters as above, this density modulation would result in a longitudinal on-axis wakefield $E_z(z)$ shown in Fig. 4. An actual calculation (as distinct from the simplified illustrative example here) should partition the e-beam in transverse coordinate space and use $\lambda_0(x, y)$ appropriate for the actual transverse density profile of the e-beam to compute $\delta\lambda(x, y, z)$, which is then used as the source for computing the wake field. We note that the technique described in this section can be used with an arbitrary time-dependent, 3D source of perturbation, *e.g.*, a moving ion and an electron density modulation developing in the modulator in response to the ion.

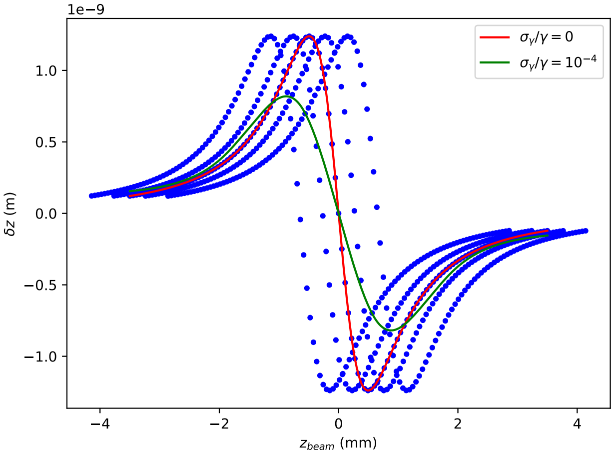

Figure 2: Calculation of $\langle\delta z(z)\rangle$ after the chicane (see text).

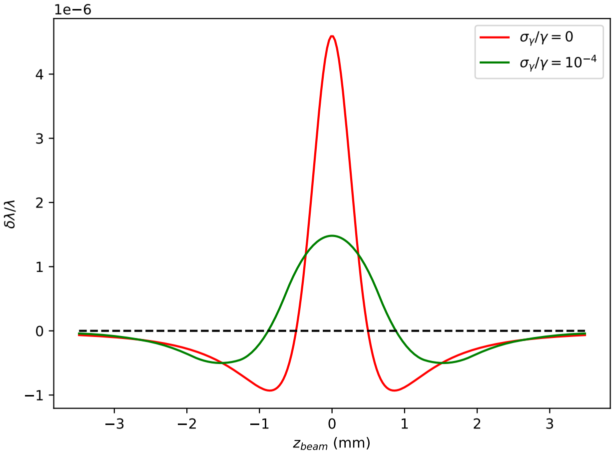

Figure 3: Longitudinal relative density modulation after the first chicane (beam frame z).

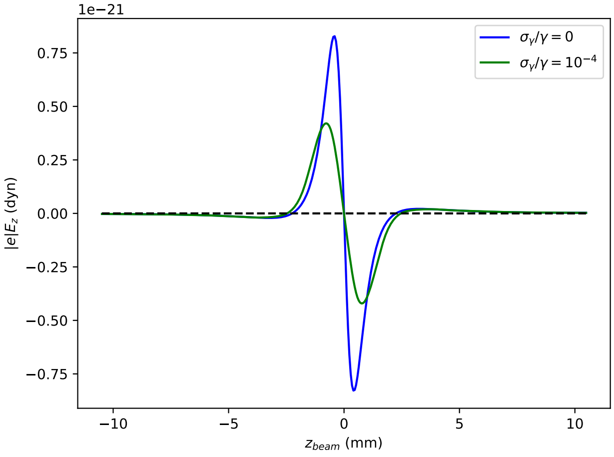

Figure 4: On-axis wake field for the longitudinal charge modulation as in Fig. 3 and a Gaussian transverse density profile (beam frame z).

In order to compute the $3D$, time-dependent wakefield generated in the kicker (or an amplifier cascade drift) by the evolving density modulation out of the chicane, we implemented in Warp the following approach. We assume that the local unperturbed background e-beam density is constant over the spatial scales on which the density modulation develops, leaving out the background E-field. Regions of positive $\delta\lambda(x, y, z)$ are then sampled by electron macroparticles, and positron-like macroparticles are used to sample negative $\delta\lambda$ regions. These are used as a source term, as the beam traverses the kicker and evolves, for solving the Poisson equation in Warp in the beam frame on a $3D$ Cartesian grid, so as to find the 3 time-dependent E-field components on the grid. For a transversely cold beam we benchmarked the implementation against the $1D$ longitudinal wake result in [6]. Fig. 5 shows an example of the wake computation in Warp with this approach for the parameters of benchmarking simulations as above, except allowing the beam to freely expand in the 40-meter long kicker. The figure shows snapshots of the beam-frame on-axis $|e|E_z(z)$ at times corresponding to $s = 0.7$, 14.4, and 36.1 m into the kicker.

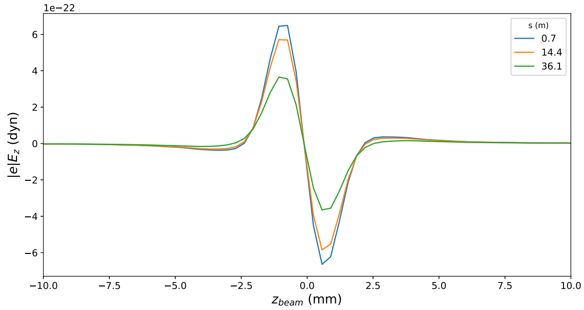

Figure 5: On-axis longitudinal wake computed in Warp at 3 positions in the kicker, for a transversely expanding beam.

REFERENCES

[1] Electron-Ion Collider at BNL. Conceptual Design Report. `https://www.bnl.gov/ec/files/EIC_CDR_Final.pdf`

[2] D. Ratner, *"Microbunched Electron Cooling for High-Energy Hadron Beams," Phys. Rev. Lett.* **111**, *084802*, 2013.

[3] S.E. Parker and W.W. Lee, *"A fully nonlinear characteristic method for gyrokinetic simulation," Phys. Fluids B* **5**, *78* 1992.

[4] G. Hu and J.A. Krommes, *"Generalized weighting scheme for δf particle-simulation method," Phys. Plasmas* **1**, *863,* 1994.

[5] N. Xiang *et al.*, *"Low-noise electromagnetic δf particle-in-cell simulation of electron Bernstein waves," Phys. Plasmas* **13**, *062111,* 2006.

[6] G. Stupakov, *"Cooling rate for microbunched electron cooling without amplification," Phys. Rev. AB* **21**, *114402,* 2018.

[7] Warp, `https://bitbucket.org/berkeleylab/warp`

[8] D.P. Grote, A. Friedman, J.-L. Vay, I. Haber, *"The WARP Code: Modeling High Intensity Ion Beams," AIP Conf. Proc.* **749**, *55,* 2005.

[9] J.-L. Vay, D.P. Grote, R.H. Cohen and A. Friedman, *"Novel methods in the Particle-In-Cell accelerator Code-Framework Warp," Comput. Sci. Disc.* **5**, *014019,* 2012.

13th Workshop on Beam Cooling and Related Topics COOL2021, Novosibirsk, Russia JACoW Publishing
ISBN: 978-3-95450-243-1 ISSN: 2226-0374 doi:10.18429/JACoW-COOL2021-P2010

FEATURES OF THE PICKUP DIAGNOSTIC AT LOW ENERGY IN THE COOLER OF NICA BOOSTER

V.B. Reva, M.I. Bryzgunov, V.V. Parkhomchuk,
BINP, Novosibirsk, Russia

Abstract

This work deals with an experimental study of changes in the amplitude of the sum signal induced at pickup stations, which can be associated with the formation of space charge waves arising along the electron beam. In the case of low electron energies, the space charge of the beam can have a significant effect on the interpretation of the obtained experimental data.

INTRODUCTION

The electron cooling system of the NICA booster is designed to accumulate an ion beam during injection and to cool it after acceleration to a certain intermediate energy. This system was developed and tested at the BINP SB RAS [1]. The maximum electron beam energy in it is 50 keV, which corresponds to an ion energy of 100 MeV / nucleon. The minimum energy of 1.74 keV corresponds to the injection energy. The schematic design of the electron cooler is shown in Fig. 1 and the main specification at the Table 1.

The electron beam is generated by an electron gun immersed into the longitudinal magnetic field. After that the electron beam is accelerated, moves in the toroid magnet to the cooling section where it will interact with ions of Booster storage ring. After interaction the electron beam is decelerated and absorbed in the collector. The centrifugal force in toroid magnets is compensated by the electrostatic plates.

Table 1: Main Specifications of the Cooler.

ions type	from p+ up to $^{197}Au^{31+}$
electron energy, E	1,5 ÷ 50 keV
electron beam current, I	0.2 ÷ 1.0 Amp.
energy stability, $\Delta E/E$	$\le 1\cdot 10^{-5}$
electron current stability, $\Delta I/I$	$\le 1\cdot 10^{-4}$
electron current losses, $\delta I/I$	less than $3\cdot 10^{-5}$
longitudinal magnetic field	0.1 ÷ 0.2 T
inhomogeneity of the field in the cooling section, $\Delta B/B$	$\le 3\cdot 10^{-5}$
transverse electron temperature	≤ 0.3 eV
ion orbit correction:	
residual gas pressure	10^{-11} mbar.

For the effective realization of the electron cooling method, it is necessary to accurate combine both beams inside cooling section. For this purpose, electrostatic sensors or pickup electrodes are used. For position measurements the ion beam must be bunched using the RF system of booster. In order to measure the position of the electron beam, it is modulated with sinusoidal voltage at 3 MHz with amplitude 10 V applied to the control electrode. The magnitude of the electron current modulation is usually much less than the total current of the electron beam. In order to get additional information about the dynamics of the electron beam a system of 4 pickups located along its trajectory is used.

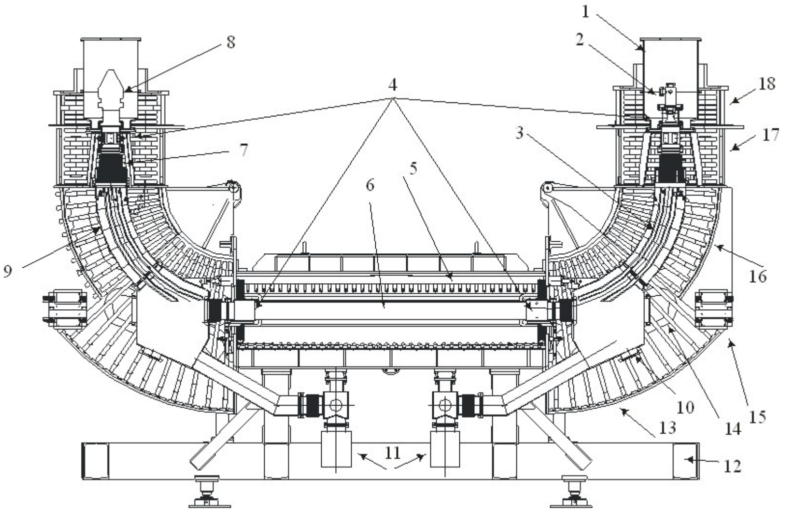

Figure 1: Design of electron cooler for NICA booster. The SF_6 vessel is 1, the electron gun is 2, the electrostatic plate is 3, pickups are 4, cooling section is 5, the vacuum chamber of cooling section is 6, NEG pump is 7, collector is 8, the vacuum chamber of toroid is 9, titanium pump is 10, the ion pumps are 11, the support is 12, the toroid is 13, the correction coil is 14, the corrector of ion beam is 15, the toroid solenoid is 16, the matching solenoid is 17, the gun solenoid is 18.

ISBN: 978-3-95450-243-1 ISSN: 2226-0374 doi:10.18429/JACoW-COOL2021-P2010

At a electron energy of 5 kV and electron current 50 mA the value of sum signal along trajectory was close to constant for different pickups. But with a small value of the electron beam energy of 1.74 kV, a strong decrease in the magnitude of the signals at the far from the gun pickup electrodes was observed (see Fig. 2). At a current of 400 mA, a minimum signal value is observed at the 3-rd pickup electrode and a strong increase almost to the initial value is observed at the 4-th pickup electrode. The most probable cause of this phenomenon may be the propagation of space charge wave along the electron beam with the formation of a standing wave.

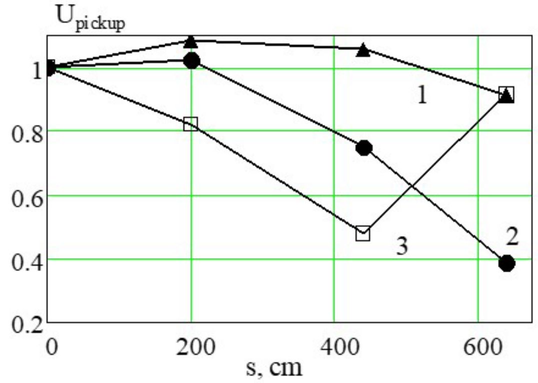

Figure 2: Normalized values of the sum signal along the electron beam trajectory at different electron beam currents: 42mA (1), 167 mA (2), 440 mA (3). The signal is normalized to the amplitude of the signal in the first pickup station. The electron energy is 1.74 keV. For relative calibration between different pickup stations, signal amplitudes were used at an electron energy of 5 keV, when spatial charge waves can be neglected.

AXIAL SYMMETRIC OSCILLATION

At small density of the electron beam the wave-vector of oscillation is $k_s = \omega/u_0$ and the length of wave $\lambda_s = 2\pi/k_s \approx 800$ cm is much larger than electron beam radius. In this case, it is possible to use the long-wave approximation of the longitudinal field. At the same time, it is assumed that the charge density varies slightly along the beam, so one can locally use the approximation of a constant linear density to find the radial electric field.

The exact solution of the linearized equations of hydrodynamics in a longitudinal magnetic field and the Poisson equation is described in [2-5]. The continuity equation, the equation of motion and the Poisson equation can be written as

$$\frac{\partial n'}{\partial t} + div\left(n_0\vec{v'}\right) + \vec{v}_0\nabla n' = 0$$

$$m_e\left(\frac{\partial\vec{v'}}{\partial t} + (\vec{v}_0\nabla)\vec{v'}\right) = e\vec{E} + \frac{e}{c}\left[\vec{v'}\times\vec{B}_0\right],$$

$$\Delta\varphi = -4\pi e n',$$

where the velocity $\vec{v}_0$ takes into account the presence of the azimuthal velocity of electron drift. Using Fourier series expansion for oscillations of space charge potential

$$\delta\phi(r,\theta,s,t) = \sum_{l=-\infty}^{\infty}\sum_{k_s=-\infty}^{\infty}\delta\phi_l(r,k_s)\exp[i(l\theta + k_s s - \omega t)]$$

allows to write Poisson equation as

$$\frac{1}{r}\frac{\partial}{\partial r}r\frac{\partial}{\partial r}\delta\phi_l - \frac{l^2}{r^2}\delta\phi_l + T^2\delta\phi_l = 0,\ 0 < r < a_e \qquad (1)$$

$$\frac{1}{r}\frac{\partial}{\partial r}r\frac{\partial}{\partial r}\delta\phi_l - \frac{l^2}{r^2}\delta\phi_l - k^2\delta\phi_l = 0,\ a_e < r < b. \qquad (2)$$

Here

$$T^2 = k_s^2\frac{\frac{\omega_p^2}{(\omega - k_s u_0 - l\omega_0)^2} - 1}{1 - \frac{\omega_p^2}{\nu^2}}$$

$$\nu^2 = (\omega - k_s u_0 - l\omega_0)^2 - (\Omega + 2\omega_0)^2,$$

$\Omega = eB/(m_e c)$ is cyclotron frequency, ω_0 is angular velocity of the equilibrium rotation of the electron column as a whole

$$\omega_0 = -\frac{\Omega}{2}\left[1 - \left(1 - 2\frac{\omega_p^2}{\Omega^2}\right)^{1/2}\right].$$

In the region $0 < r < a_e$ Eq. (1) has a solution in the form of

$$\delta\phi_l = AJ_l(Tr), \qquad (3)$$

where J_l is a Bessel function of the first kind of order l, remaining finite at $r = 0$ and A is some constant. A similar solution in the outer region Eq. (2) of the electron beam can be written as

$$\delta\phi_l = B\cdot I_l(k_s r) + C\cdot K_l(k_s r) \qquad (4)$$

where the functions K_l and I_l are modified Bessel functions of the first and second kind and B, C are some constants. From the boundary conditions on the surface of the conducting vacuum chamber and on the surface of the beam, it is possible to obtain the dispersion equation in the form [4]

$$k_s a_e\frac{K_l(k_s b)I'_l(k_s a_e) - K'_l(k_s a_e)I_l(k_s b)}{K_l(k_s b)I_l(k_s a_e) - K_l(k_s a_e)I_l(k_s b)} -$$
$$-\left(1 - \frac{\omega_p^2}{\nu^2}\right)Ta_e\frac{J'_l(Ta_e)}{J_l(Ta_e)} = l\frac{\omega_p^2(\Omega+2\omega_0)}{\nu^2(\omega-k_s u_0-l\omega_0)}. \qquad (5)$$

The strokes of the Bessel functions in the equation mean their derivative with respect to the full argument. In an extremely strong magnetic field Eq. (5) can be written

$$k_s a_e\frac{K_l(k_s b)I'_l(k_s a_e)-K'_l(k_s a_e)I_l(k_s b)}{K_l(k_s b)I_l(k_s a_e)-K_l(k_s a_e)I_l(k_s b)} - Ta_e\frac{J'_l(Ta_e)}{J_l(Ta_e)} = 0. \qquad (6)$$

If one consider the azimuthally symmetric case $l = 0$ and use the approximation of long waves

$$k_s b\ ,\ k_s a_e \ll 1,\ a_e = 1\ cm,\ b = 7.5\ cm,$$

one can expand the Bessel functions in the vicinity of zero argument and simplify both terms of Eq. 6

$$k_s a_e\frac{K_l(k_s b)I'_l(k_s a_e)-K'_l(k_s a_e)I_l(k_s b)}{K_l(k_s b)I_l(k_s a_e)-K_l(k_s a_e)I_l(k_s b)} \approx -\frac{1}{\ln(b/a_e)},$$

$$\frac{1}{\ln(b/a_e)} - Ta_e\frac{J_1(Ta_e)}{J_0(Ta_e)} = 0,\ \ T^2 = k_s^2\frac{\omega_p^2}{(\omega-k_s u_0)^2}. \qquad (7)$$

Eq. (7) allows to obtain a solution in both cases for homogeneous and inhomogeneous distribution of space charge fluctuation over the beam cross-section. To do this, one need to find several solutions to this transcendental equation and make the required linear combination from the corresponding perturbation density distributions. In order to find the roots of Eq. 7 it is sufficient to construct the intersection of the graphs of the functions included in the equation.

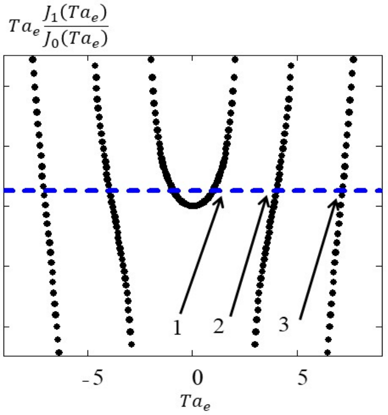

Figure 3: Graphical solution of Eq. 7. Point 1 corresponds to the main radial mode μ_0=0.95, points 2 and 3 correspond to additional solutions of this equation μ_1 and μ_2.

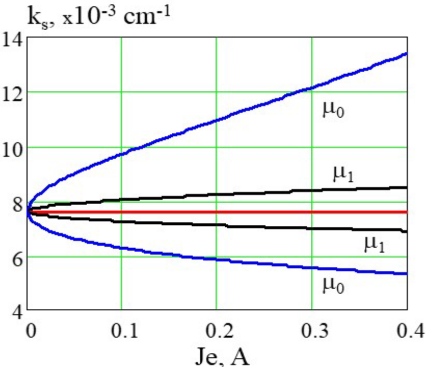

Figure 4: Dependence of the longitudinal component of the wave vector of the wave propagating along and opposite of the flow k_+ and k_- versus the beam current. The curves correspond to the values for the main μ_0=0.95 and the first radial mode with μ_1=3.97. Straight line (red colour) corresponds to the "dispersion equation" of particles without taking into account the space charge k_s=ω⁄u_0.

The dispersion equation corresponding Eq. (7) can be written in the form

$$(\omega - k_s u_0)^2 = \frac{1}{\mu_i^2} k_s^2 a_e^2 \omega_p^2 \qquad (8)$$

Figure 4 shows the longitudinal wave vector dependences on the beam current estimated by Eq. (8).

The difference of dispersion equation for k_+ and k_- wave leads to the evolution of the amplitude of the sum signal along the beam trajectory. Assuming that after the control electrode, the electron density is

$$n'_i(r,t) = \delta n_{i0} f_i(r) \cos(\omega t),$$

then the electron density is

$$n'_i(r,t) =$$

$$= \frac{1}{2} \delta n_{i0} f_i(r) [\cos(\omega t - k_+ s) + \cos(\omega t - k_- s)]$$

at s distance from the place of excitation.

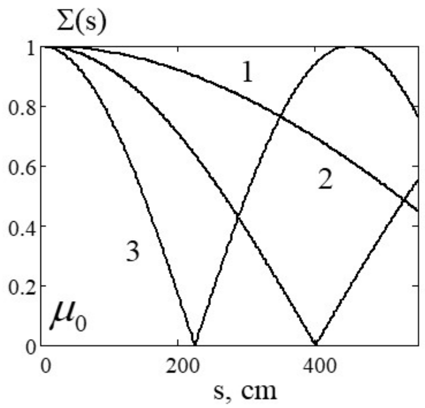

Figure 5: Longitudinal distribution of the amplitude of the sum signal Σ(s) for azimuthally symmetric modes μ_0.

Figure 5 shows the amplitude of pickup signal for the main azimuthally symmetric mode μ_0. In the case of a radially inhomogeneous beam density distribution, the contribution of the mode μ_1 is not very large. The graphs are calculated for different values of the total electron beam current of 50 (1), 150 (2) and 300 (3) mA. In order to calculate the initial electron density n_0, it is taken into account that the energy of the electrons in the beam will differ from the voltage at the cathode by the amount of the "drawdown" potential

$$\Delta\phi = \frac{2J_e}{\beta c} \ln\left(\frac{b}{a_e}\right)$$

caused by the space charge of the electron beam.

One can see that the qualitative behavior of the signals distribution in Figures 2 and 5 is quite similar, so the mechanism described above may explains the observed effect.

CONCLUSION

Electrostatic pickups are one of the main methods for obtaining information about the properties of an electron beam in electron cooling devices. The analysis presented in the article shows that the propagation of spatial charge waves in a sufficiently intense beam should be taken into account when analysing experimental data.

REFERENCES

[1] M. I. Bryzgunov *et al.*, “Status of the Electron Cooler for NICA Booster and Results of its Commissioning”, in *Proc. 12th Workshop on Beam Cooling and Related Topics (COOL'19)*, Novosibirsk, Russia, Sep. 2019, pp. 22-25. `doi:10.18429/JACoW-COOL2019-TUX01`

[2] L. S. Bogdankevich and A. A. Rukhadze. *Sov. Phys. Usp.* 14, 163, 1971.

[3] A. V. Burov, V. I. Kudelainen, V. A. Lebedev *et al.* Preprint BINP No. 89-116 (in Russian).

[4] R. C. Davidson, “Theory of Nonneutral Plasmas”, W. A. Benjamin, Reading, MA, 1974.

[5] M. I. Bryzgunov, V. V. Parkhomchuk and V. B. Reva. “Space-charge waves in the electron beam of the electron cooling system of the NICA booster”, *Physics of Particles and Nuclei Letters*, 2021, Vol. 18, No. 4, pp. 472–480. `DOI: 10.1134/S154747712104004X`

ISBN: 978-3-95450-243-1 ISSN: 2226-0374 doi:10.18429/JACoW-COOL2021-P2010

List of Authors

Bold papercodes indicate primary authors

Institutes List

ANL
Lemont, Illinois, USA
- Zholents, A.

Belgrade Institute of Physics
Belgrade, Republic of Serbia
- Maletic, D.M.

BINP SB RAS
Novosibirsk, Russia
- Batrakov, A.M.
- Bekhtenev, E.A.
- Belikov, O.V.
- Bryzgunov, M.I.
- Bubley, A.V.
- Chekavinskiy, V.A.
- Denisov, A.P.
- Fedotov, M.G.
- Goncharov, A.D.
- Gorchakov, K.
- Gosteyev, V.C.
- Gusev, I.A.
- Ilyin, I.V.
- Ivanov, A.V.
- Karpov, G.V.
- Kondaurov, M.N.
- Kremnev, N.S.
- Mityanina, N.V.
- Panasyuk, V.M.
- Parkhomchuk, V.V.
- Petrozhitskii, A.V.
- Pureskin, D.N.
- Putmakov, A.A.
- Reva, V.B.
- Senkov, D.V.
- Shtro, K.S.
- Skorobogatov, D.N.
- Vakhrushev, R.V.
- Zharikov, A.A.

BNL
Upton, New York, USA
- Bergan, W.F.
- Fedotov, A.V.
- Fischer, W.
- Gu, X.
- Kayran, D.
- Kewisch, J.
- Litvinenko, V.
- Minty, M.G.
- Schoefer, V.
- Seletskiy, S.
- Wang, E.
- Zhao, H.

CASUS
Görlitz, Germany
- Bussmann, M.H.

CERN
Geneva, Switzerland
- Bojtár, L.
- Borucka, A.E.
- Carli, C.
- Caspers, F.
- Cenede, J.
- Dupuy, B.
- Frassier, A.
- Galante, B.
- Gamba, D.
- Höfle, W.
- Jørgensen, L.V.
- Latina, A.
- Louwerse, R.
- Myklebust, V.R.
- Oliveira, J.C.
- Ponce, L.
- Rey, S.F.
- Sinturel, A.
- Somoza, J.A.F.
- Thorndahl, L.
- Tranquille, G.

Enrico Fermi Institute, University of Chicago
Chicago, Illinois, USA
- Banerjee, N.
- Brandt, J.A.

Fermilab
Batavia, Illinois, USA
- Broemmelsiek, D.R.
- Carlson, K.
- Cathey, B.L.
- Edstrom, D.R.
- Franck, D.
- Jarvis, J.D.
- Lebedev, V.A.
- Nagaitsev, S.
- Obrycki, O.
- Piekarz, H.
- Romanov, A.L.
- Ruan, J.
- Santucci, J.K.
- Stancari, G.
- Stratakis, D.
- Valishev, A.
- Yonehara, K.

FZJ
Jülich, Germany
- Breitkreutz, B.
- Shurkhno, N.
- Stassen, R.

GSI
Darmstadt, Germany
- Andelkovic, Z.
- Bardonner, A.
- Bozyk, L.H.J.
- Böhm, R.M.
- Dimopoulou, C.
- Geithner, W.

- Gorda, O.E.
- Hackler, T.
- Herfurth, F.
- Hess, R.
- Hettrich, R.
- Klammes, S.
- Krantz, C.
- Kühl, T.
- Lestinsky, M.
- Menz, E.
- Peschke, C.
- Reiter, A.
- Roßbach, J.
- Sanchez Alarcon, R.M.
- Schroeder, C.
- Spiller, P.J.
- Steck, M.
- Stöhlker, T.
- Täschner, A.
- Vorobjev, G.
- Winters, D.F.A.
- Wunderlich, S.
- Zhang, C.

HFHF
Frankfurt am Main, Germany
- Nörtershäuser, W.
- Walther, T.

HIJ
Jena, Germany
- Stöhlker, T.

HIM
Mainz, Germany
- Aulenbacher, K.
- Beiser, Th.
- Dietrich, J.

HZDR
Dresden, Germany
- Bussmann, M.H.
- Löser, M.
- Schramm, U.
- Siebold, M.

ICMUV
Paterna, Spain
- Resta-Lopez, J.

IKP
Mainz, Germany
- Aulenbacher, K.

IMP/CAS
Lanzhou, People's Republic of China
- Chen, D.Y.
- Huang, Z.
- Li, J.
- Li, M.
- Lu, H.J.
- Ma, F.
- Ma, X.M.
- Ma, X.
- Mao, L.J.
- Sha, X.P.
- Shen, G.D.
- Tang, M.T.
- Wang, H.B.
- Wang, S.X.
- Wen, W.Q.
- Yan, K.M.
- Yan, T.L.
- Yang, J.C.
- Yang, X.D.
- Yuan, Y.J.
- Zhao, H.W.
- Zhao, H.
- Zhao, L.X.
- Zhou, Y.B.

Institut für Kernphysik, Westfälische Wilhelms-Universität Münster
Münster, Germany
- Weinheimer, C.

IOQ
Jena, Germany
- Stöhlker, T.

JINR
Dubna, Moscow Region, Russia
- Ahmanova, E.V.
- Baldin, A.A.
- Butenko, A.V.
- Kobets, A.G.
- Korovkin, D.S.
- Melnikov, S.A.
- Meshkov, I.N.
- Orlov, O.
- Semenov, S.V.
- Sergeev, A.S.
- Sidorin, A.A.
- Sidorin, A.O.
- Syresin, E.
- Trubnikov, G.V.

JINR/VBLHEP
Dubna, Moscow region, Russia
- Butenko, A.V.
- Gorelyshev, I.V.
- Meshkov, I.N.
- Osipov, K.G.
- Philippov, A.V.
- Sidorin, A.O.
- Syresin, E.

JLab
Newport News, Virginia, USA
- Benson, S.V.
- Bruker, M.W.
- Derbenev, Y.S.
- Hutton, A.
- Jordan, K.
- Krafft, G.A.
- Morozov, V.S.
- Powers, T.

- Rimmer, R.A.
- Satogata, T.
- Sy, A.V.
- Wang, H.
- Wang, S.
- Zhang, H.
- Zhang, Y.

Justus-Liebig-University Giessen, I. Physics Institute, Atomic and Molecular Physics
Giessen, Germany
- Brandau, C.
- Schippers, S.

MPI-K
Heidelberg, Germany
- Wolf, A.

Muons, Inc
Illinois, USA
- Johnson, R.P.

Northern Illinois University
DeKalb, Illinois, USA
- Chattopadhyay, S.
- Dick, A.J.
- Piot, P.

NSU
Novosibirsk, Russia
- Bekhtenev, E.A.
- Ivanov, A.V.
- Kremnev, N.S.
- Reva, V.B.
- Urazov, E.R.

ODU
Norfolk, Virginia, USA
- Dhital, B.
- Krafft, G.A.

ORNL RAD
Oak Ridge, Tennessee, USA
- Lin, F.
- Morozov, V.S.

RadiaSoft LLC
Boulder, Colorado, USA
- Bruhwiler, D.L.
- Hall, C.C.
- Pogorelov, I.V.

SLAC
Menlo Park, California, USA
- Stupakov, G.

STFC/RAL/ISIS
Chilton, Didcot, Oxon, United Kingdom
- Rogers, C.T.

The University of Liverpool
Liverpool, United Kingdom
- Welsch, C.P.

TU Darmstadt
Darmstadt, Germany
- Birkl, G.
- Eizenhöfer, N.
- Horst, M.
- Kiefer, D.
- Langfeld, B.
- Nörtershäuser, W.
- Walther, T.

UMiss
University, Mississippi, USA
- Cremaldi, L.M.
- Hart, T.L.

Universidad Distrital Francisco Jose de Caldas
Bogota, Colombia
- Acosta, J.G.
- Forero, N.L.
- Oliveros, S.J.

University of Chicago
Chicago, Illinois, USA
- Bossard, M.K.
- Kim, Y.K.
- Lobach, I.

Universität Kassel
Kassel, Germany
- Kiefer, N.

Warsaw University of Technology
Warsaw, Poland
- Borucka, A.E.

Westfälische Wilhelms-Universität Münster, Institut für Kernphysik
Münster, Germany
- Buss, A.
- Hannen, V.
- Ueberholz, K.
- Winzen, D.

Xidian University
Xi'an, People's Republic of China
- Zhang, D.

Participants List

Abantika Ghosh, University of Calcutta
John Gabriel Acosta Castillo, Universidad Distrital
Afnan Al Marzouk, NIU/CBB
Oznur Apsimon, The University of Liverpool and Cockcroft Institute
Rudra prasad sangram singh Badal, National institute of science, education and research
Nilanjan Banerjee, The University of Chicago
Apurbalal Bar, University of Calcutta
Thomas Beiser, Helmholtz-Institut Mainz
Stephen Benson, Jefferson Lab
William Bergan, Brookhaven National Laboratory
Dmitriy Berkaev, BINP
Agnieszka Borucka, CERN
David Bruhwiler, RadiaSoft LLC
Maxim Bryzgunov, Budker Institute of Nuclear Physics
Aleksandr Bublei, BINP
Fritz Caspers, CERN/ESI
Jean CENEDE, CERN
Dongyang Chen, Institute of Modern Physics, CAS
Jianhui Chen, SARI
Zhichu Chen, Shanghai Synchrotron Radiation Facility
Emre Cosgun, UNIST
Andrey Denisov, Budker Institute of Nuclear Physics
Yaroslav Derbenev, Jefferson Lab
Juergen Dietrich, HIM, TU Dortmund
Nikolay Dikansky, Budker INP SB RAS
Christina Dimopoulou, GSI
Oleksiy Dolinskyy, GSI
Samira Fatehi, Karlsruhe Institute of Technology (KIT)
Alexei Fedotov, Brookhaven National Laboratory
Wolfram Fischer, Brookhaven National Laboratory
Alexandre Frassier, CERN
Bruno Galante, CERN
Davide Gamba, CERN
Oleksii Gorda, GSI
Ivan Gorelyshev, JINR
Manfred Grieser, Max Planck Institute for Nuclear Physics
Xiaofeng Gu, Brookhaven National Lab
Naveen Gupta, Lovely Professional University
Arthur Halama, FZ-Juelich IKP-4
Regina Heß, GSI
Rainer Hettrich, GSI Helmholtzzentrum für Schwerionenforschung GmbH
Wolfgang Höfle, CERN
Zhongkui Huang, Institute of Modern Physics, CAS
Andrey Ivanov, BINP SB RAS
Eberhard Jaeschke, HZB BESSY II
Jonathan Jarvis, Fermilab
Lars Jorgensen, CERN
Takeshi Katayama, Nihon University
Oleksii Khelemelia, Institute of applied physics NAS of Ukraine
Behzad Khosrowpour, OCE
Young-Kee Kim, The University of Chicago
Sebastian Klammes, GSI Helmholtzzentrum für Schwerionenforschung GmbH
Andrii Kobets, Joint Institute for Nuclear Research
Claude Krantz, GSI
Pankaj Kumar, Indian Institute of Technology, Bombay
Aulenbacher Kurt, Helmholtzinstitut Mainz (HIM)
Maksim Kuzin, Budker INP SB RAS
Andrea Latina, CERN
chao li, DESY
Rui Li, Jefferson Lab
Fanglei Lin, Oak Ridge National Laboratory
Vladimir Litvinenko, Stony Brook University
Sergey Litvinov, GSI Helmholtzzentrum für Schwerionenforschung GmbH (GSI)
Haijiao Lu, Institute of Modern Physics ,CAS
Tianhuan Luo, Lawrence Berkeley National Laboratory
Fu Ma, Institute of Modern Physics
Dimitrije Maletic, Institute of Physics Belgrade
Yuliya Maltseva, BINP
Lijun Mao, Institute of Modern Physics, IMP
Vivek Maradia, PSI
Pedro Martins, CNPEM
Kacper Matuszynski, Teledyne SP Devices
Sergey Melnikov, JINR
Igor Meshkov, JINR
Michiko Minty, Brookhaven National Laboratory
Swarnava Mitra, Birla Institute Of Technology, Mesra
Ivan Morozov, Budker Institute of Nuclear Physics
Patric Muggli, Max Planck Institute for Physics
Mustafa Mumyapan
Sungkyunkwan University
Sergei Nagaitsev, Fermilab/U.Chicago
Alexandr Narkhov, IQComponents
David Neuffer, Fermilab
Philipp Niedermayer, Forschungszentrum Jülich
Sandra Jimena Oliveros Tautiva, Universidad Distrital
Oleg Orlov, JINR
Francis Osswald, CNRS/IN2P3/IPHC
Vitaly Panasyuk, Budker Institute of Nuclear Physics
Vasily Parkhomchuk, BINP
Zohreh Parsa, Brookhaven National Laboratory
Claudius Peschke, GSI
Alexey Petrenko, BINP
Igor Pinayev, BNL
Ilya Pogorelov, RadiaSoft LLC
Oleg Prudnikov, Institute of Laser Physics SB RAS
Javier Resta Lopez, ICMUV-University of Valencia
Vladimir Reva, Budker Institute of Nuclear Physics
Jon Roßbach, GSI
Evgeny Rotov, The Budker Institute of Nuclear Physics
Parva Sadeghi Alavijeh, University of Kashan
Omid Seify, IPM
Sergei Seletskiy, Brookhaven National Laboratory
Vladimir Shiltsev, Fermilab
Dmitry Shwartz, BINP
Alexey Sidorin, JINR
Boris Skarbo, BINP
Dmitry Skorobogatov, BINP
Alexander N. Skrinsky, Budker INP
Giulio Stancari, Fermilab
Rolf Stassen, Forschungszentrum Juelich
Markus Steck, GSI Helmholtzzentrum für Schwerionenforschung GmbH (GSI)
James Storey, CERN
Diktys Stratakis, Fermilab
Gennady Stupakov, SLAC National Accelerator Laboratory
Evgeny Syresin, Joint Institute for Nuclear Research
Aleksei Taichenachev, Institute of laser physics
Lars Thorndahl, CERN, Geneva, Switzerland
Gerard Tranquille, CERN
Melissa Uchida, University of Cambridge
Eldar Urazov, Novosibirsk State University
Alexander Valishev, Fermilab
Erdong Wang, Brookhaven national laboratory
Haipeng Wang, Thomas Jefferson Lab
Hanbing Wang, Institute of Modern Physics, CAS
Wei-Qiang Wen, Institute of Modern Physics, CAS
Danyal Winters, GSI Helmholtzzentrum
Andreas Wolf, Max Planck Institute for Nuclear Physics
Stefan Wunderlich, GSI Helmholtzzentrum für Schwerionenforschung
Xiaodong Yang, Institute of Modern Physics, CAS
Katsuya Yonehara, Fermilab
Cary Yoshikawa, None
Chuan Zhang, GSI
He Zhang, Jefferson Lab
Yuhong Zhang, Thomas Jefferson National Accelertor Facility
Yunbin Zhou, institute of modern physics
Guangyu Zhu, Institute of Modern Physics, CAS